

---

# Cross-section measurement of exclusive $\pi^0$ muoproduction and firmware design for an FPGA-based detector readout

Matthias GORZELLIK



---

Fakultät für Mathematik und Physik  
ALBERT-LUDWIGS-UNIVERSITÄT Freiburg



---

**Cross-section measurement of  
exclusive  $\pi^0$  muoproduction and  
firmware design for an  
FPGA-based detector readout**

---

Matthias GORZELLIK

*Dissertation zur Erlangung  
des Doktorgrades der*

Fakultät für Mathematik und Physik

ALBERT-LUDWIGS-UNIVERSITÄT

Freiburg im Breisgau

Freiburg, März 2018



Dekan:	Prof. Dr. Gregor HERTEN
Leiter der Arbeit:	apl. Prof. Dr. Horst FISCHER
Referent:	apl. Prof. Dr. Horst FISCHER
Korreferent:	Dr. Christian WEISER
Tag der Verkündung des Prüfungsergebnisses:	07.06.2018

Teile dieser Arbeit wurden in folgenden Fachzeitschriften veröffentlicht:

M. Gorzellik, "Measurement of the exclusive  $\pi^0$  muoproduction cross section at COMPASS", 22nd International Spin Symposium, conference proceeding (2016), [arXiv:1702.06293](https://arxiv.org/abs/1702.06293)

**COMPASS Collaboration**, M. Aghasyan et al., "Transverse Extension of Partons in the Proton probed by Deeply Virtual Compton Scattering", submitted to Physical Review Letters (2018)

---



# Contents

<b>Contents</b>	<b>i</b>
<b>List of Figures</b>	<b>v</b>
<b>List of Tables</b>	<b>xi</b>
<b>Physical Constants</b>	<b>xiii</b>
<b>List of Symbols</b>	<b>xv</b>
<b>1 Introduction</b>	<b>1</b>
<b>2 Theoretical context</b>	<b>5</b>
2.1 Generalized Parton Distribution functions . . . . .	5
2.2 Hard Exclusive Meson Production . . . . .	10
2.3 Availability of data . . . . .	15
<b>3 COMPASS experiment</b>	<b>19</b>
3.1 Beam . . . . .	19
3.2 Beam momentum and direction reconstruction . . . . .	20
3.3 Target area . . . . .	20
3.3.1 Target . . . . .	20
3.3.2 Target Time-of-Flight system . . . . .	21
3.4 Spectrometer . . . . .	22
3.4.1 Tracking . . . . .	22
3.4.2 Particle identification . . . . .	23
3.5 Trigger . . . . .	24
3.6 Readout and DAQ . . . . .	27
3.7 GANDALF framework . . . . .	28
3.7.1 GANDALF-module . . . . .	28
3.7.2 TIGER-module . . . . .	29
3.7.3 VXS-backplane . . . . .	30
<b>4 GANDALF-ADC firmware</b>	<b>33</b>
4.1 DSP-FPGA firmware structure . . . . .	34
4.2 ADC mezzanine card (AMC) . . . . .	36
4.3 I <sup>2</sup> C . . . . .	37
4.4 SI chips . . . . .	40
4.4.1 Configuration . . . . .	41
4.4.2 Phase alignment . . . . .	41
4.5 Clocking and clock distribution . . . . .	46

4.6	GANDALF-module configuration and monitoring . . . . .	49
4.6.1	Configuration memory . . . . .	49
4.6.2	Status and general purpose (GP) interface . . . . .	51
4.7	Treatment of ADC . . . . .	52
4.7.1	ADC clock distribution . . . . .	52
4.7.2	ADC bit sampling and bit error monitoring . . . . .	53
4.7.3	Baseline adjustment . . . . .	55
4.7.4	Signal processing and event packaging . . . . .	56
4.8	Readout . . . . .	57
4.8.1	Readout via VME-backplane using S-LINK source card . . . . .	59
4.8.2	Readout via VXS-backplane . . . . .	59
4.8.3	Readout via VME-CPU or USB . . . . .	60
4.8.4	Including the MEM-FPGA . . . . .	60
4.9	Testbench . . . . .	61
<b>5</b>	<b>CAMERA calibration and commissioning</b>	<b>65</b>
5.1	Concepts . . . . .	66
5.2	Calibration . . . . .	67
5.2.1	Radial position calibration . . . . .	68
5.2.2	Longitudinal position calibration . . . . .	70
5.2.3	Time-of-Flight and momentum calibration . . . . .	72
5.3	Data quality and stability . . . . .	73
5.3.1	System synchronization . . . . .	74
5.3.2	Clock ambiguity . . . . .	74
5.3.3	Phase alignment . . . . .	77
5.3.4	Sampling errors of the ADC bits . . . . .	77
5.3.5	Bad spill list and quality flags . . . . .	78
5.4	Start counter . . . . .	81
5.4.1	Calibration . . . . .	82
5.5	Results . . . . .	83
<b>6</b>	<b>Extraction of the exclusive <math>\pi^0</math> muoproduction cross-section</b>	<b>87</b>
6.1	Data . . . . .	87
6.1.1	Luminosity determination . . . . .	88
6.2	The kinematic fit for exclusive $\pi^0$ muoproduction . . . . .	91
6.3	Event selection . . . . .	96
6.3.1	Selection of beam particles and vertices . . . . .	97
6.3.2	Selection of neutral cluster pairs . . . . .	100
6.3.3	Selection of proton tracks . . . . .	101
6.3.4	Exclusivity conditions . . . . .	101
6.3.5	Multiplicity condition . . . . .	103
6.3.6	Cut on $\pi^0$ signal . . . . .	103
6.3.7	Kinematic fit . . . . .	104
6.4	Simulations . . . . .	108
6.4.1	HEPGEN++ . . . . .	109
6.4.2	LEPTO . . . . .	110
6.4.3	Normalization . . . . .	111

6.5	Acceptance . . . . .	117
6.6	Cross-section extraction . . . . .	121
6.6.1	Extraction method . . . . .	121
6.6.2	Extraction of unseparated cross-section . . . . .	124
6.6.3	Extraction of the cross-section as a function of $t$ . . . . .	125
6.6.4	Extraction of the cross-section as a function of $\phi_{\pi^0}$ . . . . .	126
6.6.5	Estimation of uncertainties . . . . .	128
6.6.6	Parameterization of compound Poisson distribution evolution . . . . .	132
6.6.7	Binned maximum likelihood fit . . . . .	133
6.6.8	Bayesian interpretation . . . . .	136
6.6.9	Summary . . . . .	141
6.7	Systematic studies . . . . .	145
6.7.1	Variation of the absolute normalization scale . . . . .	145
6.7.2	Variation of the thresholds of the ECals . . . . .	152
6.7.3	Variation of the acceptance binning . . . . .	153
6.7.4	Variation of the “LEPTO background” normalization . . . . .	157
6.7.5	Impact of the shift in the energy and momentum balance seen with the kinematic fit . . . . .	160
6.7.6	Contamination of exclusive $\omega$ . . . . .	161
6.7.7	Radiative corrections . . . . .	162
6.7.8	Summary . . . . .	163
6.8	Discussion of the results . . . . .	166
6.8.1	Model for GPDs by Goloskokov and Kroll . . . . .	166
6.8.2	Comparison and interpretation with respect to the model for GPDs by Goloskokov and Kroll . . . . .	169
<b>7</b>	<b>Summary and outlook</b>	<b>173</b>
	<b>Acknowledgements</b>	<b>177</b>
<b>A</b>	<b>GANDALF-ADC firmware auxiliary material</b>	<b>179</b>
A.1	Directory structure . . . . .	179
A.2	Simulation . . . . .	179
A.3	Phase alignment . . . . .	182
<b>B</b>	<b>Additional material</b>	<b>187</b>
B.1	Photograph of CAMERA and spectrometer . . . . .	187
B.2	Additional figures for event selection . . . . .	188
B.2.1	Kinematic and exclusive variables before cut on pulls . . . . .	188
B.2.2	Absolute values of pulls for measured quantities . . . . .	190
B.3	Additional material for simulation . . . . .	193
B.3.1	JETSET output for LEPTO event types . . . . .	193
B.3.2	Pull distributions for LEPTO event types . . . . .	194
B.3.3	Acceptance for each extraction bin . . . . .	197
B.4	Additional material for extraction of cross-section . . . . .	211
B.4.1	Resolution effects on virtual-photon flux . . . . .	211

B.4.2	Study of binned maximum likelihood fit using a bootstrap/replica method . . . . .	211
B.4.3	Alternative likelihood using parameterized PDFs . . .	212
B.4.4	MCMC with flat prior . . . . .	214
B.4.5	MCMC result with model curves . . . . .	217
B.5	Various systematic tests . . . . .	217
<b>Acronyms</b>		<b>221</b>
<b>Glossary</b>		<b>225</b>
<b>Bibliography</b>		<b>229</b>

# List of Figures

2.1	Three regions for $x \pm \xi$ . . . . .	6
2.2	Scheme of helicities and the different GPDs . . . . .	8
2.3	Tomography of the nucleon . . . . .	10
2.4	Schematic diagram for the hard exclusive meson production process . . . . .	11
2.5	Schematic diagram of factorization in hard exclusive meson production . . . . .	12
2.6	Definition of angle $\phi$ . . . . .	13
2.7	Cross-section measurement of exclusive $\pi^+$ production by HERMES . . . . .	15
2.8	Cross-section measurement of exclusive $\pi^0$ production by CLAS	17
2.9	Cross-section measurement of exclusive $\pi^0$ production by JLab Hall A . . . . .	18
3.1	Beamline with beam momentum stations and magnets . . . . .	20
3.2	Schematic drawing of the DVCS target . . . . .	21
3.3	Photograph of the CAMERA detector . . . . .	23
3.4	Overview of the COMPASS-II spectrometer . . . . .	24
3.5	Visualization of ECal0 . . . . .	25
3.6	Illustration of the COMPASS trigger system . . . . .	26
3.7	Overview of the COMPASS DAQ . . . . .	28
3.8	Overview of the GANDALF-module transient recorder . . . . .	29
3.9	Overview of the TIGER-module . . . . .	30
3.10	Structure of the double-star bus fabric of the VXS-backplane . . . . .	31
4.1	Overview of the DSP-FPGA firmware <i>oplevel</i> -module . . . . .	34
4.2	Schematic of the analog-to-digital converter (ADC) mezzanine card . . . . .	37
4.3	State machine for operating the I <sup>2</sup> C bus . . . . .	39
4.4	Schematic circuit used for the sweep procedure . . . . .	43
4.5	Example of a sweep measurement . . . . .	44
4.6	Resolution of the phase alignment procedure . . . . .	45
4.7	GIMLI mezzanine cards . . . . .	46
4.8	GANDALF-ADC clock circuitry with fiber GIMLI . . . . .	47
4.9	GANDALF-ADC clock circuitry with VXS GIMLI . . . . .	47
4.10	GANDALF-ADC clock circuitry with copper GIMLI . . . . .	48
4.11	State machine for operating the <i>configuration memory</i> . . . . .	50
4.12	Circuitry for the edge detection of ADC bits . . . . .	54
4.13	State machine of the readout event packing process . . . . .	58
4.14	Overview of the <i>oplevel</i> -simulation-module . . . . .	61

5.1	Schematic view of the CAMERA detector . . . . .	65
5.2	Principle of the Time-of-Flight measurement with the CAMERA detector . . . . .	67
5.3	Target histogram for the radial position calibration . . . . .	68
5.4	Comparison of nominal and calibrated radial position of CAMERA scintillators . . . . .	69
5.5	Comparison of methods to obtain radii of CAMERA scintillators	70
5.6	Predicted longitudinal position versus measured time difference	71
5.7	Target histogram for the longitudinal position calibration . . .	71
5.8	Extracted radial position of scintillators . . . . .	72
5.9	Target histogram for the Time-of-Flight calibration . . . . .	73
5.10	Time-of-Flight calibration constant as a function of run number	75
5.11	Illustration of the clock ambiguity for two GANDALF-ADC modules . . . . .	76
5.12	Histogram for Time-of-Flight calibration constant . . . . .	76
5.13	ADC delay graphs after re-aligning phase . . . . .	77
5.14	Frame with <i>bit-errors</i> . . . . .	78
5.15	Time difference distribution and its FFT for two runs . . . . .	79
5.16	Histogram of time difference FFT integral values . . . . .	80
5.17	Comparison of methods to identify <i>bit-error</i> affected channels	81
5.18	Principle of the Time-of-Flight measurement using CAMERA together with start counter . . . . .	81
5.19	Target histogram for the inter-calibration of start counter and CAMERA outer ring . . . . .	83
5.20	Position resolution of CAMERA . . . . .	84
5.21	Momentum bias and resolution of CAMERA . . . . .	85
6.1	Position of the target center as a function of longitudinal position	89
6.2	Comparison of different determinations of the variable $t$ . . .	94
6.3	Schematic diagram for the hard exclusive meson production process . . . . .	96
6.4	Transverse vertex position . . . . .	98
6.5	Distribution of longitudinal vertex position . . . . .	98
6.6	Distributions for initial and final state muon . . . . .	99
6.7	Distribution of kinematic variables . . . . .	99
6.8	Cluster time as a function of the cluster energy . . . . .	100
6.9	Distribution of exclusivity variables . . . . .	102
6.10	$M_{\gamma\gamma}$ distribution before kinematic fit . . . . .	103
6.11	$M_{\gamma\gamma}$ distributions separated for beam charge and sum . . . . .	104
6.12	Pull distributions for the incoming $\mu$ . . . . .	105
6.13	Pull distributions for the outgoing $\mu$ . . . . .	106
6.14	Pull distributions for the position in ring A of CAMERA . . . . .	106
6.15	Pull distributions for the position in ring B of CAMERA . . . . .	106
6.16	Pull distribution for the magnitude of the momentum of the recoil proton . . . . .	107
6.17	Pull distributions for the higher energetic $\gamma$ . . . . .	107
6.18	Pull distributions for the lower energetic $\gamma$ . . . . .	107

6.19	Distribution of $M_{\gamma\gamma}$ for data, LEPTO and HEPGEN++ normalized to luminosities . . . . .	109
6.20	Pull distributions for data, HEPGEN++ and different event types of LEPTO . . . . .	111
6.21	Distributions of $M_{\gamma\gamma}$ and multiplicity in the normalization procedure . . . . .	112
6.22	Evolution of the $M_X^2$ distribution for different multiplicities . . . . .	113
6.23	Example distribution for normalization method 1 . . . . .	114
6.24	Example distribution for normalization method 2 . . . . .	115
6.25	Example distribution for normalization method 3 . . . . .	115
6.26	Values for the fraction of “LEPTO background” in $\mu^-$ data . . . . .	116
6.27	Values for the fraction of “LEPTO background” in $\mu^+$ data . . . . .	117
6.28	Acceptance as function of $\phi_{\pi^0}$ . . . . .	119
6.29	Acceptance as function of $t$ . . . . .	120
6.30	Number of events as a function of $ t $ . . . . .	125
6.31	Virtual-photon proton cross-section as function of $ t $ with different confidence intervals . . . . .	126
6.32	Number of events as a function of $\phi_{\pi^0}$ . . . . .	127
6.33	Virtual-photon proton cross-section as function of $\phi_{\pi^0}$ with different confidence intervals . . . . .	128
6.34	Poisson bootstrap distributions for $t$ . . . . .	129
6.35	Poisson bootstrap distributions for $\phi_{\pi^0}$ . . . . .	131
6.36	Poisson bootstrap distributions for different values of $\lambda$ . . . . .	132
6.37	Evolution of fit parameters of Poisson bootstrap distributions . . . . .	133
6.38	Virtual-photon proton cross-section as function of $\phi_{\pi^0}$ with BML fit . . . . .	136
6.39	Visualization of the most probable parameter set obtained using MCMC . . . . .	138
6.40	Visualization of the MCMC . . . . .	139
6.41	Virtual-photon proton cross-section as function of $\phi_{\pi^0}$ with Bayesian fit . . . . .	140
6.42	Virtual-photon proton cross-section as function of $ t $ . . . . .	142
6.43	Virtual-photon proton cross-section as function of $\phi_{\pi^0}$ with BML and Bayesian fit . . . . .	143
6.44	Influence on extraction in $t$ through scaling of data . . . . .	146
6.45	Influence on extraction in $\phi_{\pi^0}$ through scaling of data . . . . .	147
6.46	Influence on extraction in $t$ through scaling of flux . . . . .	148
6.47	Influence on extraction in $\phi_{\pi^0}$ through scaling of flux . . . . .	149
6.48	Systematic effect due to ECal threshold . . . . .	152
6.49	Influence on extraction in $t$ through determination of acceptance . . . . .	155
6.50	Influence on extraction in $\phi_{\pi^0}$ through determination of acceptance . . . . .	156
6.51	Influence on extraction in $t$ through scaling of “LEPTO background” . . . . .	158
6.52	Influence on extraction in $\phi_{\pi^0}$ through scaling of “LEPTO background” . . . . .	159

6.53	Invariant mass spectrum for leaking $\omega$ and in dedicated exclusive $\omega$ muoproduction analysis . . . . .	162
6.54	Cross-section as function of $t$ with GK model . . . . .	170
6.55	Cross-section as function of $\phi_{\pi^0}$ with GK model . . . . .	171
A.1	Directory structure of GANDALF-ADC project . . . . .	180
A.2	Relevant DSP-FPGA VHDL implementation files . . . . .	180
A.3	Relevant testbench files . . . . .	181
A.4	State machine for the sweep control process. . . . .	183
A.5	State machine for reading flip-flops in sweep procedure . . . . .	184
A.6	State machine to control the fine shift of the Si5326 clock multiplier chip (further referred to as “SI chip”) . . . . .	185
A.7	State machine to control the coarse shift of the SI chip . . . . .	186
B.1	Photograph of assembled CAMERA detector . . . . .	187
B.2	Distribution of kinematic variables . . . . .	188
B.3	Distribution of exclusivity variables . . . . .	189
B.4	Pull distributions for the incoming $\mu$ . . . . .	190
B.5	Pull distributions for the outgoing $\mu$ . . . . .	190
B.6	Pull distributions for the position in ring A of CAMERA . . . . .	191
B.7	Pull distributions for the position in ring B of CAMERA . . . . .	191
B.8	Pull distribution for the magnitude of the momentum of the recoil proton . . . . .	191
B.9	Pull distributions for the higher energetic $\gamma$ . . . . .	192
B.10	Pull distributions for the lower energetic $\gamma$ . . . . .	192
B.11	JETSET output for a LEPTO type 1 event . . . . .	193
B.12	JETSET output for a LEPTO type 2 event . . . . .	193
B.13	Pull distributions for the incoming $\mu$ . . . . .	194
B.14	Pull distributions for the outgoing $\mu$ . . . . .	195
B.15	Pull distributions for the position in ring A of CAMERA . . . . .	195
B.16	Pull distributions for the position in ring B of CAMERA . . . . .	195
B.17	Pull distribution for the magnitude of the momentum of the recoil proton . . . . .	196
B.18	Pull distributions for the higher energetic $\gamma$ . . . . .	196
B.19	Pull distributions for the lower energetic $\gamma$ . . . . .	196
B.20	Acceptance as function of $\phi_{\pi^0}$ for the 0th $t$ -bin . . . . .	198
B.21	Acceptance as function of $\phi_{\pi^0}$ for the 1st $t$ -bin . . . . .	199
B.22	Acceptance as function of $\phi_{\pi^0}$ for the 2nd $t$ -bin . . . . .	200
B.23	Acceptance as function of $\phi_{\pi^0}$ for the 3rd $t$ -bin . . . . .	201
B.24	Acceptance as function of $\phi_{\pi^0}$ for the 4th $t$ -bin . . . . .	202
B.25	Acceptance as function of $t$ for the 0th $\phi_{\pi^0}$ -bin . . . . .	203
B.26	Acceptance as function of $t$ for the 1st $\phi_{\pi^0}$ -bin . . . . .	204
B.27	Acceptance as function of $t$ for the 2nd $\phi_{\pi^0}$ -bin . . . . .	205
B.28	Acceptance as function of $t$ for the 3rd $\phi_{\pi^0}$ -bin . . . . .	206
B.29	Acceptance as function of $t$ for the 4th $\phi_{\pi^0}$ -bin . . . . .	207
B.30	Acceptance as function of $t$ for the 5th $\phi_{\pi^0}$ -bin . . . . .	208
B.31	Acceptance as function of $t$ for the 6th $\phi_{\pi^0}$ -bin . . . . .	209
B.32	Acceptance as function of $t$ for the 7th $\phi_{\pi^0}$ -bin . . . . .	210

B.33	Resolution effects on virtual-photon flux . . . . .	211
B.34	Poisson bootstrap distributions for MLH fit . . . . .	212
B.35	Poisson bootstrap distributions for MLH fit, using parameterized PDFs . . . . .	213
B.36	Visualization of the most probable parameter set obtained using MCMC with flat prior . . . . .	215
B.37	Visualization of the MCMC with flat prior . . . . .	216
B.38	Cross-section as function of $\phi_{\pi^0}$ with GK model and MCMC result . . . . .	217
B.39	Influence on extraction in $t$ through various studies . . . . .	218
B.40	Influence on extraction in $\phi_{\pi^0}$ through various studies . . . . .	219



# List of Tables

3.1	Properties of CAMERA . . . . .	22
3.2	Properties of various tracking detectors . . . . .	25
4.1	Data format used in the phase alignment procedure . . . . .	45
6.1	Number of beam particles and luminosity . . . . .	90
6.2	Estimation of “LEPTO background” in data . . . . .	117
6.3	Extraction bins in $ t $ . . . . .	125
6.4	Extraction bins in $\phi_{\pi^0}$ . . . . .	127
6.5	Cross-section with statistical and systematical uncertainties in each bin . . . . .	141
6.6	Collection of numbers involved in the cross-section extraction . . . . .	144
6.7	Syst. uncertainty in $t$ , originating from loss of $\mu^+$ data . . . . .	150
6.8	Syst. uncertainty in $\phi_{\pi^0}$ , originating from loss of $\mu^+$ data . . . . .	150
6.9	Syst. uncertainty on param. of fit, originating from loss of $\mu^+$ data . . . . .	150
6.10	Syst. uncertainty in $t$ , originating from determination of flux . . . . .	151
6.11	Syst. uncertainty in $\phi_{\pi^0}$ , originating from determination of flux . . . . .	151
6.12	Syst. uncertainty on param. of fit, originating from determination of flux . . . . .	151
6.13	Syst. uncertainty in $t$ , originating from thresholds for ECals . . . . .	152
6.14	Syst. uncertainty in $\phi_{\pi^0}$ , originating from thresholds for ECals . . . . .	153
6.15	Syst. uncertainty on param. of fit, originating from thresholds for ECals . . . . .	153
6.16	Syst. uncertainty in $t$ , originating from acceptance binning . . . . .	153
6.17	Syst. uncertainty in $\phi_{\pi^0}$ , originating from acceptance binning . . . . .	154
6.18	Syst. uncertainty on param. of fit, originating from acceptance binning . . . . .	154
6.19	Syst. uncertainty in $t$ , originating from normalisation of “LEPTO background” . . . . .	157
6.20	Syst. uncertainty in $\phi_{\pi^0}$ , originating from normalisation of “LEPTO background” . . . . .	157
6.21	Syst. uncertainty on param. of fit, originating from normalisation of “LEPTO background” . . . . .	158
6.22	Syst. uncertainty in $t$ , originating from shift in kinematic fit . . . . .	160
6.23	Syst. uncertainty in $\phi_{\pi^0}$ , originating from shift in kinematic fit . . . . .	160
6.24	Syst. uncertainty on param. of fit, originating from shift in kinematic fit . . . . .	161
6.25	Syst. uncertainty in $t$ , summary . . . . .	163
6.26	Syst. uncertainty in $\phi_{\pi^0}$ , summary . . . . .	164

6.27	Syst. uncertainty on param. of fit, summary . . . . .	165
6.28	Parameters of GK model . . . . .	169
6.29	Modified parameter set of GK model . . . . .	169

# Physical Constants

speed-of-light	$c = 29.979\,245\,8 \text{ cm ns}^{-1}$ (exact)	
fine-structure constant	$\alpha = 0.007\,297\,352\,566\,4(17)$	[1]
proton mass	$m_p = 1.007\,276\,466\,879(91) \text{ g}/(\text{mol} \cdot N_a)$	[2]
muon mass	$m_\mu = 0.105\,658\,371\,5(35) \text{ GeV}/c^2$	[2]
neutral pion mass	$m_{\pi^0} = 0.134\,976\,6(6) \text{ GeV}/c^2$	[2]
Avogadro's constant	$N_a = 6.022\,140\,857(74) \text{ mol}^{-1}$	[1]
density of liquid hydrogen	$\rho_{\text{LH}_2} = 0.070\,37 \text{ g/cm}^3$	[3]



# List of Symbols

General		unit
$\vec{r}_i$	position vector with components $(x_i, y_i, z_i)$ ; subscript $i$ indicates the object (particle) in question	cm
$\vec{a}_i$	transverse position with components $(x_i, y_i)$ ; subscript $i$ indicates the object (particle) in question	cm
$\vec{p}_i$	momentum vector with components $(p_{i,1}, p_{i,2}, p_{i,3})$ ; subscript $i$ indicates the particle in question	GeV/c
$p_i$	magnitude of the momentum of particle indicated by subscript $i$	GeV/c
$S_i$	helicity of particle indicated by subscript $i$	-
$E_i$	energy of particle indicated by subscript $i$	GeV
$\varphi_i$	azimuth angle of particle indicated by subscript $i$	rad
$\theta_i$	polar angle of particle indicated by subscript $i$	rad
Theory and GPD related		
$k$	incident muon four-momentum	GeV/c
$k'$	scattered muon four-momentum	GeV/c
$q = k - k'$	virtual photon four-momentum	GeV/c
$q'$	produced particle four-momentum	GeV/c
$p$	target nucleon four-momentum	GeV/c
$p'$	scattered target nucleon four-momentum	GeV/c
$Q^2 = -q^2$	invariant negative mass squared of virtual photon	$(\text{GeV}/c)^2$
$W^2 c^2 = (p + q)^2$	invariant mass squared of the virtual photon - nucleon system	$(\text{GeV}/c^2)^2$
$\nu = (p \cdot q)/m_p$	energy transfer between incident and final muon	GeV
$y = (p \cdot q)/(p \cdot k)$	fraction of energy transfer between incident and final muon	-
$x_{Bj} = Q^2/(2p \cdot q)$	Bjorken scaling variable	-
$t = (p - p')^2$	Mandelstam variable; square of four-momentum transfer to the proton	$(\text{GeV}/c)^2$
$\xi$	skewness variable of GPDs	-
$-t_0 = \frac{4\xi^2 m_p^2}{1-\xi^2}$	minimal value of $-t$ at given $\xi$	$(\text{GeV}/c)^2$
$H, \tilde{H}, E, \tilde{E}$	parton helicity non-flip GPDs	-
$H_T, \tilde{H}_T, E_T, \tilde{E}_T$	parton helicity flip GPDs	-
$\tilde{E}_T = 2\tilde{H}_T + E_T$	combination of helicity flip GPDs	-
$A_{S_N' S_{q'}, S_N S_q}$	nucleon and parton helicity dependent amplitudes	-

$\mathcal{M}_{S_{\gamma^*}S_N, S_M S_{N'}}$	virtual photon, parton and meson helicity dependent amplitudes	-
$\sigma_{S_N S_N}^{S_{\gamma^*} S_{\gamma^*}}$	polarized photoabsorption cross-sections or interference terms	-
$\phi = \phi_{\pi^0}$	angle between scattering plane and meson production plane	rad
$\varepsilon$	virtual photon polarization factor	-
$\Gamma(Q^2, \nu)$	virtual photon flux	GeV <sup>3</sup> /c <sup>2</sup>
$\sigma_T, \sigma_L, \sigma_{TT}, \sigma_{LT}$	structure functions appearing in meson production cross-section	nb
<b>GANDALF related</b>		
$f_{tcs} = 155.52$ MHz	frequency of the COMPASS TCS system	MHz
$f_{tcs,data} = f_{tcs}/4$	frequency of data modulated on TCS clock	MHz
$f_{ocxo}$	frequency of the oscillator on the copper GIMLI	MHz
$f_{vxs}$	frequency of the VXS DDR link	MHz
$f_{aurora}$	frequency of the aurora bus reference clock	MHz
$f_{adc}$	operating clock frequency for the ADCs on the GANDALF AMC	MHz
$f_{amc} = f_{adc}/2$	operating clock frequency of the logic inside the DSP-FPGA handling ADC readings	MHz
$f_{osc}$	frequency of the oscillator on the GANDALF board	MHz
<b>CAMERA related</b>		
$c_{eff}$	effective speed-of-light in scintillator	cm ns <sup>-1</sup>
$t_{up}$	time of the pulse at the upstream photomultiplier	ns
$t_{dn}$	time of the pulse at the downstream photomultiplier	ns
$k_z$	calibration constant for longitudinal position	cm
$z_A$	longitudinal position in inner scintillator	cm
$z_B$	longitudinal position in outer scintillator	cm
$t_A$	mean-time in inner scintillator	ns
$t_B$	mean-time in outer scintillator	ns
$r_A$	radius of inner ring of scintillator	cm
$r_B$	radius of outer ring of scintillator	cm
$w_A$	width of inner scintillator	cm
$w_B$	width of outer scintillator	cm
$t_{ToF}$	ToF between inner and outer scintillator	ns
$k_t$	calibration constant for ToF	ns
$d$	difference of radii of inner and outer scintillator	cm
$s_{DoF}$	DoF between inner and outer scintillator	cm
$\beta_{raw}$	velocity of particle between inner and outer scintillator relative to speed-of-light	-
$p_{raw}$	momentum between inner and outer scintillator	GeV/c
$d_{sc}$	distance of start counter to vertex	cm
$k_{t,sc}$	calibration constant for ToF	cm

## HEMP analysis related

$t_{cam}$	Mandelstam variable determined using CAMERA	$(\text{GeV}/c)^2$
$t_{spec}$	Mandelstam variable determined using spectrometer («constraint $t$ »)	$(\text{GeV}/c)^2$
$t_{fit}$	Mandelstam variable determined using the kinematic fit	$(\text{GeV}/c)^2$
$t_{mc}$	Mandelstam variable on generator level	$(\text{GeV}/c)^2$
$\eta(Q^2, x_{Bj,})$	radiative corrections for DIS	-
$a(Q^2, x_{Bj,})$	acceptance for DIS	-
$a(Q^2, \nu, t, \phi_{\pi^0,})$	acceptance for exclusive $\pi^0$ muoproduction	-
$\Phi$	flux of beam particles	-
$\mathcal{L}$	integrated luminosity	$\text{nb}^{-1}$
$p_{\perp}$	transverse momentum (here: of the proton)	$\text{GeV}/c$
$M_X^2$	missing mass (or undetected mass) squared	$(\text{GeV}/c^2)^2$
$E_{miss}$	missing energy	$\text{GeV}$
$M_{\gamma\gamma}$	mass of the two photon system	$\text{GeV}/c^2$
$K$	multiplicity; number of combinations of <i>vertex candidates</i> , $\pi^0$ <i>candidates</i> and <i>proton candidates</i> that fulfill the exclusivity conditions	-
$K_{\pi^0}$	multiplicity restricted to $\pi^0$ signal; number of combinations of <i>vertex candidates</i> , $\pi^0$ <i>candidates</i> and <i>proton candidates</i> that fulfill the exclusivity conditions and $M_{\gamma\gamma}$ compatible with $\pi^0$ mass	-
$r_{lepto}$	estimated ratio of SIDIS background in the data	%



---

# 1

# Introduction

---

“Where, oh where is the proton’s spin?” [4]

The article going by this title was issued in a journal in 1988. The title expresses the surprise that one was unable to explain the proton’s spin taking into account the contribution of the spins of valence quarks. Even today, 30 years later, the question of how the proton’s spin is assembled by its constituents, remains unanswered. So, what do we know so far?

In the fifties, the invention of particle accelerators as a source of particles other than cosmic rays introduced a new era of experimental particle physics. By colliding particle beams or impinging a particle beam on a target, the structure of matter could be probed in growing detail. Experiments found evidence for a large number of (unstable) particles they grouped into mesons and baryons. With the quark model, Gell-Mann [5], Zweig [6] and Petermann [7] brought order into the Zoo of particles by introducing non-integer spin elementary particles (three quarks) that act as the building blocks of mesons and baryons. It took time and an even increasing experimental effort to verify and establish the quark model. In the sixties, the SLAC experiment performed deep inelastic scattering (DIS) with an electron beam on protons and found evidence for point-like objects in the proton. Although confirmed in DIS experiments with neutrinos at CERN, these particles were not yet conclusively identified as “the quarks”. Only with the discovery of the  $J/\Psi$  meson in 1974 and the fact that it seamlessly integrated into the quark model through the introduction of a fourth quark, the quark model was raised to wide acceptance.

The quark model as we know of today has grown by another two quarks where the latest one, the top quark, was unambiguously verified in 1995 at the Tevatron.

Once it was established that the fundamental constituents of mesons and baryons are quarks, the content of compound particles was elaborately studied in DIS experiments. In the current picture, mesons and baryons are composed of valence quarks that are embedded in a sea of quarks, antiquarks and gluons. These constituents are usually referred to as partons. A formalism to describe the partonic contents was established by Feynman who introduced density distributions for partons inside the nucleon to describe said DIS experiments at SLAC. These distributions, however, are not calculable by first principles but are determined empirically by measurements of (semi-inclusive) DIS and cross-section measurements of W and Z bosons.

Still, the question begs how the large-scale properties of compound particles, here the properties of the proton, are generated from its constituents. It is known, for instance, that for the proton's rest mass, the rest masses of the partons are almost irrelevant, as they make up only  $\sim 1\%$  of the mass. The bulk of the mass is generated through internal dynamics and interactions between (anti-)quarks mediated by gluons.

Other important properties of the proton are charge and size. On a large scale (*i.e.* in an atom), the proton's charge of +1 (in units of the electron charge) results from the sum of valence quark charges, since the gluons have no charge and the charge of the (anti-)quarks in the sea is neutralized. However, charge and size are (somehow) connected, since the size of objects is (usually) probed within electromagnetic interactions. Thus, elastically probing the proton with an electron, it sees the net charge of the constituents of the proton. Such measurements of the charge distribution, encoded in form factors, allow quoting a charge radius of the proton. There are other options to measure the charge radius such as studying energy levels in atoms. In fact, recently, "What is the true charge radius of a proton?" has become one of the unsolved problems in physics when first results for the charge radius using muonic hydrogen were found incompatible with world data [1, 8].

Coming back to the initial question, the spin- $\frac{1}{2}$  nature of the proton has to be discussed. Naively, one may assume that like the charge, adding the spins of the valence quarks closes this chapter. However, when the EMC experiment at CERN tried to decompose the proton's spin, things turned out to be more complicated. The staggering conclusion, that quarks and antiquarks stem only a very small fraction of the proton's spin finally lead to the article cited at the beginning and started what is sometimes referred to as the "spin crises" [4, 9]. Since then, much effort was put into the determination of individual quark helicity distributions, yet still not inconsistent with the early conclusions. The reasoning, that the missing contribution must be attributed to gluons was first rejected in measurements by COMPASS [10] and remains so in current world data [11].

This leaves only one unknown component - the contribution of the orbital angular momenta of (anti-)quarks and gluons. However, experimental access to this contribution is to-date not known and the question "How do the quarks and gluons carry the spin of protons?" remains another one of the unsolved problems in physics.

Since the late nineties, it became more and more evident that a generalization of the known concepts is needed. As such, generalized parton distribution functions (GPDs) were found to be objects with interesting properties that allow a comprehensive description of the partonic structure of the nucleon. The relevance of GPDs is evident due to their sensitivity to the total angular momentum of partons inside the nucleon [12]. The motivation to study GPDs is even increased by their interpretation in the impact parameter space [13], allowing to generate a tomographic picture of the nucleon and adding another view of the proton's size.

Like Feynman's parton distributions, GPDs are objects to be determined by empirical data. The most prominent processes that are sensitive to GPDs are deeply virtual Compton scattering (DVCS) and hard exclusive meson production (HEMP). Such processes are studied at the COMPASS experiment using a high energetic polarized muon beam with a momentum of  $160 \text{ GeV}/c$  impinging on a  $2.5 \text{ m}$  long liquid hydrogen target. The two staged open field spectrometer and the target time-of-flight system CAMERA allow for the reconstruction of the scattering process by detecting and identifying all involved particles.

This thesis accompanies the progression of the COMPASS experiment from the 2012 DVCS pilot run to the dedicated DVCS data taking period in 2016 and 2017. Based on the data recorded in 2012, the recoil proton detector CAMERA and its readout are thoroughly studied. Methods for the calibration of the detector are developed and executed. The stability of the detector and its readout are assessed. The FPGA firmware of the detector readout is further developed so that a smooth data taking in 2016 and 2017 is accomplished. The status of the FPGA firmware and the improvements are reviewed in great detail.

The 2012 DVCS pilot run data allow the pioneering measurement of the exclusive  $\pi^0$  muoproduction cross-section at COMPASS conducted in the course of the thesis. This particular channel of HEMP is of special interest for different reasons. First, there is few availability of data for exclusive pion production in the DIS region, while COMPASS sits at a unique kinematic spot not accessible by others. Compared to charged pion production,  $\pi^0$  production is theoretically more clean, since here, the pion pole contribution is absent. Additionally, the process is especially sensitive to the weakly constrained transversity GPDs. Beyond that, exclusive  $\pi^0$  muoproduction emerges as one of the major backgrounds in the DVCS measurement that was studied in a companioned thesis. In order to have the most precise measurement of DVCS, a comprehensive knowledge of backgrounds is imperative.

The structure of this thesis is as follows. In Chapter 2, a detailed picture of the formalism for GPDs is drawn and their connection to HEMP is explained. The chapter closes by formulating the exclusive  $\pi^0$  muoproduction cross-section and a discussion of available data. It follows a broad review of the 2012 setup of the COMPASS experiment and an overview over the GANDALF-framework in Chapter 3. A detailed description of the GANDALF-module transient analyzer firmware is given in Chapter 4. Many improvements in the firmware followed by the thorough commissioning and calibration of the CAMERA detector that included studies of the readout which are addressed in the subsequent Chapter 5. Finally, the extraction of the exclusive  $\pi^0$  muoproduction cross-section is outlined in Chapter 6. The chapter closes with an interpretation of the measurement and putting it into the context of a particular model for GPDs. Chapter 7 concludes the thesis with a summary and an outlook.



---

## 2 Theoretical context

---

This chapter is supposed to establish the theoretical context for the experiments studied at COMPASS with regards to GPDs. For this, the theoretical framework for the description of the structure of nucleons using GPDs is outlined. While the fundamental concepts are introduced in Section 2.1 together with important properties of the GPDs, a specific channel that allows accessing GPDs is highlighted in Section 2.2. Measurements of this particular channel using the COMPASS experiment are then subject of Chapter 6.

### 2.1 Generalized Parton Distribution functions

Today, the common description of nucleons comes with form factors that describe the spatial charge distribution of the nucleons and with parton distribution functions (PDFs) that describe the probability to find a parton with a certain longitudinal momentum fraction inside the nucleon (in the infinite momentum frame). Form factors express the matrix elements of currents between unequal nucleon states. For example, choosing appropriate wave forms  $\psi(p)$  and Dirac spinors  $u(p)$  and with  $p$  ( $p'$ ) denoting the nucleon momentum in the initial (final) state [14]

$$\langle p' | \bar{\psi}(0) \gamma^\mu \psi(0) | p \rangle = \bar{u}(p') \left[ F_1(t) \gamma^\mu + i \frac{1}{2m_p} F_2(t) \sigma^{\mu\nu} \Delta_\nu \right] u(p),$$

with  $t$  the square of four-momentum transfer to the nucleon,  $\gamma^\mu$  and  $\sigma^{\mu\nu}$  the gamma respectively Pauli matrix,  $m_p$  the mass of the nucleon and  $\Delta_\nu$  the covariant derivative. Here,  $F_1$  and  $F_2$  correspond to the Dirac and Pauli electromagnetic form factors.

In light-cone coordinates and in the infinite momentum frame, the definition of PDFs follows from the Fourier transform of matrix elements between equal nucleon momenta. For instance, the unpolarized quark distribution  $q(x)$  is obtained with [14]

$$q(x) = \frac{1}{2p^+} \int \frac{dz^-}{2\pi} e^{ixp^+z^-} \langle p | \bar{\psi}(0) \gamma^+ \psi(z) | p \rangle |_{z^+=z_\perp=0},$$

where  $x$  is the longitudinal momentum fraction carried by the parton. Different PDFs follow by inserting other gamma matrices than  $\gamma^+$ .

GPDs appear by generalizing the above concepts. They simultaneously describe the spatial and the momentum distribution of the partons inside a nucleon. Their leading twist definition follows from the matrix elements of

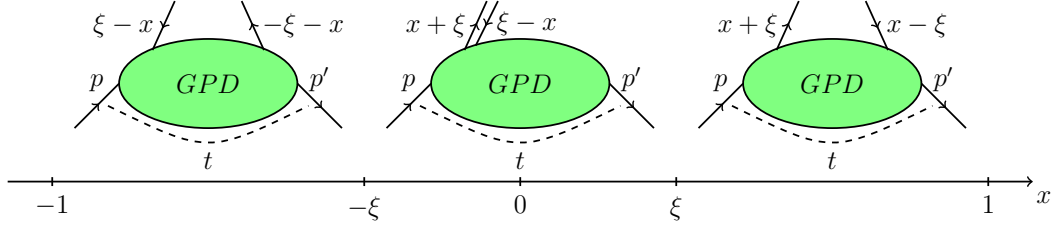


FIGURE 2.1: The three different regions for the momentum  $x \pm \xi$ .

gluon and quark field operators between unequal nucleon states. The quark GPDs for flavor  $q$  are generated by [15]

$$F_{\Gamma}^q(x, \xi, t) = \frac{1}{2} \int \frac{dz^-}{2\pi} e^{ixP^+z^-} \langle p', S_{N'} | \bar{\psi}(-z/2) \Gamma \psi(z/2) | p, S_N \rangle |_{z^+ = \bar{z}^+ = 0},$$

where  $\Gamma$  represents one of the gamma matrices. The helicity of the nucleon is denoted by  $S_N$  ( $S_{N'}$ ) in the initial (final) state and  $P = \frac{1}{2}(p + p')$  while the fractional momentum  $\xi$  is explained later. With this,  $F_{\gamma^+}$  defines the GPDs  $H$  and  $E$  while  $F_{\gamma^+\gamma^5}$  defines the GPDs  $\tilde{H}$  and  $\tilde{E}$ . Finally,  $F_{\sigma+i\gamma^5}$  generates the GPDs  $H_T$ ,  $\tilde{H}_T$ ,  $E_T$  and  $\tilde{E}_T$ . The same quantities follow for gluons using appropriate operators [15]. The GPDs denoted by  $H$ ,  $\tilde{H}$ ,  $E$ ,  $\tilde{E}$  are parton helicity conserving (chiral even), while for  $H_T$ ,  $\tilde{H}_T$ ,  $E_T$ ,  $\tilde{E}_T$  the parton helicity flips (chiral odd).

In the past decades, GPDs have been extensively studied after their attention was brought up in the original papers [12, 16–18]. For major reviews on the topic one may refer to [14, 19–21].

The GPDs are functions of three kinematic variables (Fig. 2.1):

- the (average) longitudinal momentum fraction of the quark  $x$ ,
- the square of the four momentum transfer to the nucleon  $t = (p - p')^2$ ,
- the skewness parameter  $\xi = \frac{p^+ - p'^+}{p^+ + p'^+}$ .

Negative values of  $x$  correspond to an antiparticle. The GPDs are required to be real valued because of time reversal invariance [21].

With  $\xi > 0$  (analog for  $\xi < 0$ ), three distinct regions exist for the interval  $x \in [-1, 1]$  (Fig. 2.1).

1.  $x \in [\xi, 1]$ : GPDs describe emission and reabsorption of a quark.
2.  $x \in [-\xi, \xi]$ : GPDs describe emission of quark-antiquark pair.
3.  $x \in [-1, -\xi]$ : GPDs describe emission and reabsorption of antiquark.

In the regions 1 and 3, the GPDs evolve according to modified DGLAP equations [22–25], hence, the regions are referred to as “DGLAP region”. On the other hand, region 2 is comparable to the situation of the emission of meson. Here, the GPDs evolve according to modified ERBL equations [26, 27]. This

region is especially interesting since it does not exist in the description using PDFs and it allows to study the mesonic structure of the nucleon. Because gluons are their own antiparticles, the gluon GPDs are symmetric functions in  $x$ .

When arranging the quark and gluon operators  $\mathcal{O}_{S_{q'q}}$  in a particular way, the GPDs helicity structure is revealed and it is possible to form objects that are similar to helicity amplitudes

$$\begin{aligned} A_{S_{N'}S_{q'},S_N S_q}^q &= \int \frac{dz^-}{2\pi} e^{ixP^+z^-} \langle p', S_{N'} | \mathcal{O}_{S_{q'q}}^q(z) | p, S_N \rangle |_{z^+=z_\perp=0}, \\ A_{S_{N'}S_{q'},S_N S_q}^g &= \frac{1}{P^+} \int \frac{dz^-}{2\pi} e^{ixP^+z^-} \langle p', S_{N'} | \mathcal{O}_{S_{q'q}}^g(z) | p, S_N \rangle |_{z^+=z_\perp=0}. \end{aligned} \quad (2.1)$$

The indices  $S_q$  ( $S_{q'}$ ) denote the helicity of the parton before (after) the reaction. The amplitudes obey the following relation [15]

$$A_{-S_{N'}-S_{q'},-S_N-S_q} = (-1)^{S_{N'}-S_{q'}-S_N+S_q} (A_{S_{N'}S_{q'},S_N S_q})^*,$$

as a result of parity invariance. The GPDs  $H$  and  $E$  correspond to the sum of parton helicity and are therefore referred to as “unpolarized” while the GPDs  $\tilde{H}$  and  $\tilde{E}$  are called “polarized” since they correspond to the difference of parton helicity states. The helicity structure of the GPDs is also illustrated in Fig. 2.2.

Explicitly, the amplitudes for quarks and gluons in case of parton helicity conservation can be expressed as linear combinations of GPDs [15]

$$\begin{aligned} A_{+,+,+} &= \sqrt{1-\xi^2} \left( \frac{H + \tilde{H}}{2} - \frac{\xi^2}{1-\xi^2} \frac{E + \tilde{E}}{2} \right), \\ A_{-,-,+} &= \sqrt{1-\xi^2} \left( \frac{H - \tilde{H}}{2} - \frac{\xi^2}{1-\xi^2} \frac{E - \tilde{E}}{2} \right), \\ A_{+,-,+} &= -e^{-i\varphi} \frac{\sqrt{t_0-t} E - \xi \tilde{E}}{2m_p}, \\ A_{-,-,+} &= e^{i\varphi} \frac{\sqrt{t_0-t} E + \xi \tilde{E}}{2m_p}, \end{aligned} \quad (2.2)$$

where the helicities  $+\frac{1}{2}$  and  $-\frac{1}{2}$  are abbreviated by their sign. All other amplitudes follow from parity invariance. The quantity  $-t_0 = \frac{4\xi^2 m_p^2}{1-\xi^2}$  denotes the minimal value for  $-t$ . The angle  $\varphi$  denotes the azimuthal angle of the vector  $D = \frac{p'}{1-\xi} - \frac{p}{1+\xi}$ , i.e.  $e^{i\varphi} = (D^1 + iD^2)/|D|$  [21].

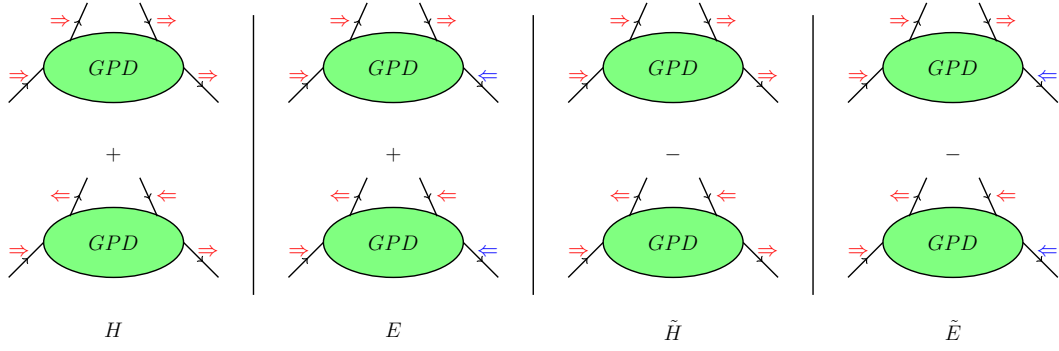


**FIGURE 2.2:** The different helicity states of the nucleon and parton with their corresponding GPDs. The arrows indicate the respective helicity state, while the blue arrows indicate a helicity flip of the nucleon. The same scheme applies for parton helicity flip GPDs, with the difference of the opposing direction of the parton helicities.

The amplitudes involving quark helicity flip read<sup>1</sup> [15]

$$\begin{aligned}
 A_{++,-}^q &= e^{i\varphi} \frac{\sqrt{t_0 - t}}{2m_p} \left( \tilde{H}_T^q + (1 - \xi) \frac{E_T^q + \tilde{E}_T^q}{2} \right), \\
 A_{-+,-}^q &= e^{i\varphi} \frac{\sqrt{t_0 - t}}{2m_p} \left( \tilde{H}_T^q + (1 + \xi) \frac{E_T^q - \tilde{E}_T^q}{2} \right), \\
 A_{++,-}^q &= \sqrt{1 - \xi^2} \left( H_T^q + \frac{t_0 - t}{4m_p^2} \tilde{H}_T^q - \frac{\xi^2}{1 - \xi^2} E_T^q + \frac{\xi^2}{1 - \xi^2} \tilde{E}_T^q \right), \\
 A_{-+,-}^q &= -e^{2i\varphi} \sqrt{1 - \xi^2} \frac{t_0 - t}{4m_p^2} \tilde{H}_T^q.
 \end{aligned} \tag{2.3}$$

The inversion of the amplitudes in Eq. 2.2 and Eq. 2.3 allows the extraction of the GPDs. An essential feature of the GPDs is that the mismatch between the initial and final helicity can be compensated by orbital angular momentum when  $t > t_0$ . This is visible in the prefactors of the above equation, which are in general given by  $\sqrt{t_0 - t} |S_{N'} - S_{q'} - S_N + S_q|$ .

The GPDs have various important properties that allow gaining a deeper understanding of their physical meaning. The relations also allow to restrict the number of possible functions applicable for the GPDs and lead to constraints for the modeling of GPDs.

### Forward Limit:

The forward limit is given with  $\xi = t = 0$ . In this case,  $x \rightarrow x_{Bj}$  where  $x_{Bj}$  denotes the Bjorken scaling variable. The GPDs then reduce to the parton

<sup>1</sup>The corresponding amplitudes for gluons receive an additional factor  $e^{i\varphi} \sqrt{1 - \xi^2} \sqrt{t_0 - t} / (2m_p)$ .

distribution functions [15]

$$\begin{aligned} H^q(x_{Bj}, 0, 0) &= q(x_{Bj}), & H^g(x_{Bj}, 0, 0) &= x_{Bj}g(x_{Bj}), \\ \tilde{H}^q(x_{Bj}, 0, 0) &= \Delta q(x_{Bj}), & \tilde{H}^g(x_{Bj}, 0, 0) &= x_{Bj}\Delta g(x_{Bj}). \\ H_T^q(x_{Bj}, 0, 0) &= \Delta_T q(x_{Bj}), \end{aligned}$$

The quantities  $q(x_{Bj})$ ,  $\Delta q(x_{Bj})$  and  $\Delta_T q(x_{Bj})$  are the unpolarized, helicity and transversity (anti)quark distribution functions, with the corresponding ones for gluons  $g(x_{Bj})$  and  $\Delta g(x_{Bj})$ . For the  $E$ ,  $\tilde{E}$ ,  $E_T$ ,  $\tilde{H}_T$  and  $H_T^g$  no such relation exists since they decouple from their defining equations [21, p. 10].

### Moments and polynomiality:

The polynomiality property of the GPDs states, that their  $n$ 'th Mellin moments are polynomials in  $\xi$  with the highest power  $n$ . For example, for even  $n$  and GPD  $H$  [12]

$$\int_{-1}^1 dx x^{n-1} H^q(x, \xi, t) = h_0^{(n)}(t)\xi^0 + h_2^{(n)}(t)\xi^2 + \dots + h_n^{(n)}(t)\xi^n.$$

The polynomiality property allows decomposing the  $n$ 'th Mellin moment of the GPDs as a set of form factors, here denoted by  $h$ . The case of  $n = 1$  is particular illustrative, since here the connection of the parton helicity conserving GPDs to the hadronic form factors is revealed [12]

$$\sum_q e_q \int_{-1}^1 dx H^q(x, \xi, t) = F_1(t), \quad \sum_q e_q \int_{-1}^1 dx H^q(x, \xi, t) = g_A(t), \quad (2.4)$$

$$\sum_q e_q \int_{-1}^1 dx E^q(x, \xi, t) = F_2(t), \quad \sum_q e_q \int_{-1}^1 dx E^q(x, \xi, t) = h_A(t), \quad (2.5)$$

where  $e_q$  denotes the charge of the quark. Here,  $F_1$  is the Dirac-,  $F_2$  the Pauli-,  $g_A$  the axial and  $h_A$  the pseudoscalar formfactor. The dependence on  $\xi$  is lost in the integration.

Another important property comes with the second Mellin moment of the sum of GPDs  $H$  and  $E$  which is connected to the total angular momentum  $J^q$  carried by the quark of flavor  $q$  [12]

$$\frac{1}{2} \lim_{t \rightarrow 0} \int_{-1}^1 dx x [H^q(x, \xi, t) + E^q(x, \xi, t)] = J^q. \quad (2.6)$$

A similar relation exists for gluons. The relations are also referred to as ‘‘Ji’s sum rule’’.

### Positivity:

The GPDs are found to obey a hierarchy of inequalities in relation to the three quark distributions. They were studied in several papers, while a summary

of the conditions can be found for instance in [20].

### Impact parameter space:

For  $\xi = 0$ , where no longitudinal momentum transfer occurs, a very descriptive picture of the GPDs exists. Now, the GPDs  $H(x, 0, t)$  may be interpreted as the probability density for the spatial distribution of partons. With  $V$  the center of momentum

$$V = \int_x \sum_q x \cdot q(x) dx \quad (2.7)$$

the Fourier transform of  $H(x, 0, t)$  results in the probability of finding a parton with longitudinal momentum fraction  $x$  at the position  $\vec{b}$  relative to  $V$  [28]. This is illustrated in Fig. 2.3 which shows the assumed spatial distribution of quarks at different values of the momentum fraction  $x$ . This feature is sometimes referred to as “nucleon tomography”.

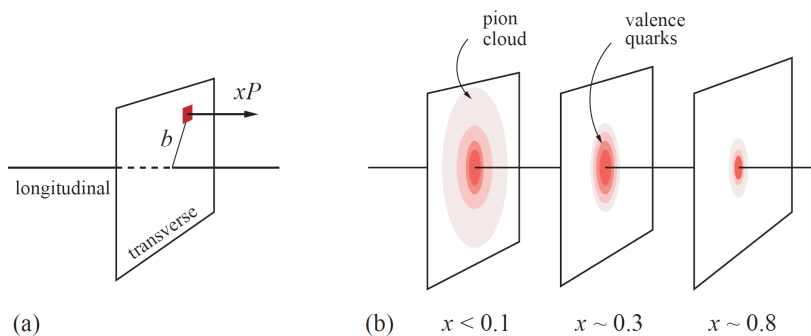


**FIGURE 2.3:** Tomography of the nucleon: (a) Spatial distribution of quarks with longitudinal momentum  $xP$  at a distance  $b$  from the center of momentum. (b) Tomographic pictures at different values of the momentum fraction  $x$ . ([29], based on [28, 30])

## 2.2 Hard Exclusive Meson Production

When probing GPDs, two processes are especially important. The cleanest channel is DVCS where in the scattering process, a virtual photon is absorbed by the nucleon and a real photon is produced. Comprehensive material for the DVCS process and the measurement at COMPASS can be found in [31, 32]. The other process is hard exclusive meson production (HEMP), where instead of a real photon, a meson is produced.

The hard exclusive production of a meson can be described in terms of the handbag model as depicted in Fig. 2.4. A lepton with initial (final) four-momentum  $k$  ( $k'$ ) scatters off a (anti-)quark of the target nucleon with initial (final) four-momentum  $p$  ( $p'$ ) by the exchange of a virtual photon  $\gamma^*$  with four-momentum  $q$ . The creation of the meson  $M$  with four-momentum  $q'$  is

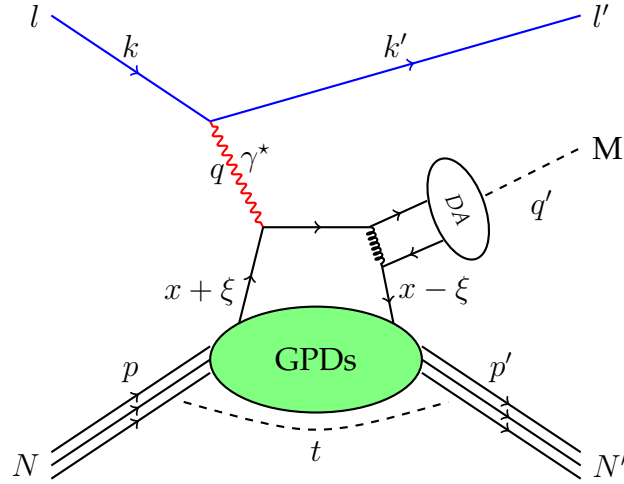


**FIGURE 2.4:** Schematic diagram for the hard exclusive meson production process  $lN \rightarrow l'N'M$  in the handbag model. The initial (final) state lepton is denoted by  $l$  ( $l'$ ) while the initial (final) state nucleon is denoted by  $N$  ( $N'$ ). The produced meson is denoted by  $M$ .

described by a distribution amplitude (DA). The GPDs describe the soft dynamics of the nucleon emitting and absorbing a (anti-)quark or gluon. The factorization into the partonic subprocess  $\gamma^*g \rightarrow Mg$ , where  $g$  denotes a parton of the nucleon, and the GPDs was proven strictly only for the case with longitudinally polarized virtual photons [17, 33]. In the case of transversely polarized virtual photons, infrared singularities appear in the collinear factorization that may be overcome only by phenomenological arguments in a model-dependent way [34].

The amplitudes for the production of a meson can be written in terms of helicity amplitudes  $\mathcal{M}_{S_{\gamma^*}S_N,S_M S_{N'}}$  with  $S_i$  the helicity of the particle  $i$ , while in case of the  $\pi^0$ ,  $S_M = 0$  in the following. In the picture of the factorization, the helicity amplitudes can be decomposed as [35]

$$\mathcal{M}_{S_{\gamma^*}S_N,0S_{N'}} = \sum_{S_q S_{q'}} \int_{-1}^1 dx g_{S_{\gamma^*}S_q,0S_{q'}}(x, \xi, t, Q^2) A_{S_{N'}S_{q'},S_N S_q}(x, \xi, t), \quad (2.8)$$

where the sum runs over the unobserved spins of the parton  $S_q$  ( $S_{q'}$ ) before (after) the reaction. Here,  $g_{S_{\gamma^*}S_q,S_M S_{q'}}$  describes the partonic subprocess while  $A_{S_{N'}S_{q'},S_N S_q}$  are the amplitudes containing the GPDs to describe the “soft” part given in Eq.2.2 and Eq.2.3. The separation into the two components and the involved spins are also illustrated in Fig.2.5. The integral and the sum over the parton spins in Eq.2.8 can be propagated down to the GPDs appearing in Eq.2.2 and Eq.2.3 and new items are defined [35]

$$\mathcal{F} = \sum_{S_q S_{q'}} \int_{-1}^1 dx g_{S_{\gamma^*}S_q,0S_{q'}}(x, \xi, t, Q^2) F(x, \xi, t), \quad (2.9)$$

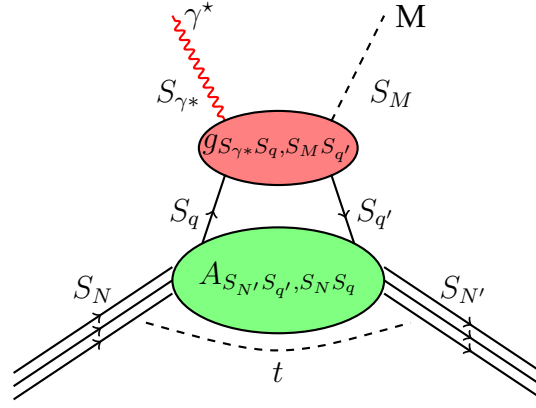


**FIGURE 2.5:** Schematic diagram of factorization and involved spins for the hard exclusive meson production process in the handbag model.

where  $F$  substitutes one of the GPDs. The items  $\mathcal{F}$  are called meson production form factors (MPFFs) which are the analog to the Compton form factors (CFFs) that appear in DVCS. The MPFFs involve the calculations of relevant Feynman graphs in conjunction with an appropriate meson waveform [34]. In the case of the  $\pi^0$  production, only the valence quarks contribute, so that the items replacing the GPDs in Eq. 2.2 and Eq. 2.3 read [36]

$$\mathcal{F}^{\pi^0} = \frac{1}{\sqrt{2}}(e_u \mathcal{F}^u - e_d \mathcal{F}^d).$$

The structure of the amplitudes in Eq. 2.2 and Eq. 2.3 persists, though. In case of other mesons, other flavor combinations enter and different (anti)quark or gluon GPDs can be probed.

The cross-section for exclusive  $\pi^0$  muoproduction,  $\mu N \rightarrow \mu' \pi^0 N'$ , on an unpolarized nucleon can be decomposed in terms of polarized photoabsorption cross-sections or interference terms  $\sigma_{S_N S_N}^{S_{\gamma^*} S_{\gamma^*}}$ . They are proportional to bi-linear combinations of helicity amplitudes [37]

$$\sigma_{S_N S_N}^{S_{\gamma^*} S_{\gamma^*}} \propto \sum_{S_{N'}} (\mathcal{M}_{S_{\gamma^*} S_N, 0 S_{N'}})^* \mathcal{M}_{S_{\gamma^*} S_N, 0 S_{N'}}. \quad (2.10)$$

The reduced cross-section, omitting terms depending on the target spin direction, reads [37, 38]

$$\begin{aligned} \frac{1}{\Gamma} \frac{d^4\sigma}{dQ^2 d\nu dt d\phi} = \frac{1}{2\pi} \left[ \frac{1}{2} (\sigma_{++}^{++} + \sigma_{++}^{--}) + \varepsilon \sigma_{00}^{++} - \varepsilon \cos(2\phi) \text{Re} \sigma_{+-}^{++} \right. \\ \left. - \sqrt{\varepsilon(1+\varepsilon)} \cos \phi \text{Re} (\sigma_{+0}^{++} + \sigma_{+0}^{--}) \right. \\ \left. - P_l \sqrt{\varepsilon(1-\varepsilon)} \sin \phi \text{Im} (\sigma_{+0}^{++} + \sigma_{+0}^{--}) \right]. \end{aligned} \quad (2.11)$$

The cross-section depends on the invariants  $Q^2 = -q^2$  and  $\nu = (p \cdot q)/m_p$ , the square of the four momentum transfer to the target nucleon  $t$  and the angle  $\phi$ , while  $m_p$  denotes the mass of the nucleon. The quantity  $P_l$  denotes

the polarization of the incident muon. The transverse virtual photon flux  $\Gamma$  reads when using Hand's convention<sup>2</sup> [40]

$$\Gamma(Q^2, \nu) = \frac{\alpha_{em}(1 - x_{Bj})}{2\pi Q^2 y E_\mu} \left[ y^2 \left( 1 - \frac{2m_\mu^2}{Q^2} \right) + \frac{2}{1 + Q^2/\nu^2} \left( 1 - y - \frac{Q^2}{4E_\mu^2} \right) \right], \quad (2.12)$$

where  $y$  is the fractional energy of the virtual photon. The virtual photon polarization parameter  $\varepsilon$  can be approximated by

$$\varepsilon = \frac{1 - y - \frac{1}{4}y^2\gamma^2}{1 - y + \frac{1}{2}y^2 + \frac{1}{4}y^2\gamma^2}. \quad (2.13)$$

in the considered kinematics where the mass of the incoming lepton  $m_\mu \ll Q^2$ . The angle  $\phi$  is defined in the target rest frame and denotes the angle between the leptonic and hadronic plane as illustrated in Fig. 2.6.

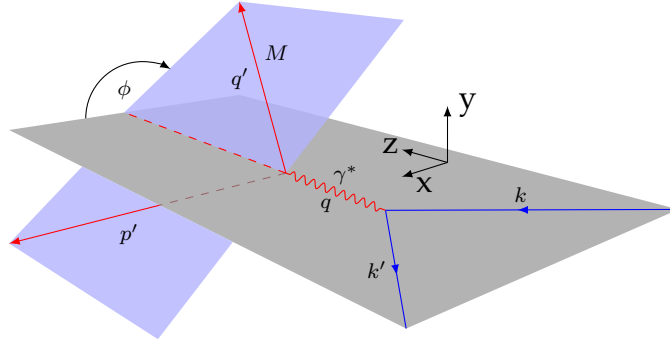


FIGURE 2.6: The angle  $\phi$  defined as the angle between the leptonic plane (grey) and the hadronic plane (blue).

The last term in Eq. 2.11, which represents the imaginary part of the interference term between amplitudes for longitudinal and transverse photons, is strongly suppressed by the factor  $\sqrt{\varepsilon(1-\varepsilon)}$ , which is very small for the data sample analyzed in Chapter 6. In any case, this term of the cross-section cancels when averaging cross-sections for  $\mu^+$  and  $\mu^-$  beams with opposite polarizations. Hence, the term is neglected in the following.

Usually, the explicit notation with the photoabsorption cross-sections and interference terms in Eq. 2.11 is omitted. Instead, an abbreviated notation is used that was introduced in [36]

$$\begin{aligned} \frac{d^2\sigma}{dt d\phi_{\pi^0}} &= \frac{1}{\Gamma} \frac{d^4\sigma}{dQ^2 d\nu dt d\phi_{\pi^0}} = \frac{1}{2\pi} \left[ \frac{d\sigma_T}{dt} + \varepsilon \frac{d\sigma_L}{dt} \right. \\ &\quad \left. + \varepsilon \cos(2\phi_{\pi^0}) \frac{d\sigma_{TT}}{dt} + \sqrt{2\varepsilon(1+\varepsilon)} \cos(\phi_{\pi^0}) \frac{d\sigma_{LT}}{dt} \right], \end{aligned} \quad (2.14)$$

<sup>2</sup> The formula results from [39] by replacing  $k = \nu(1 - x_{Bj})$  according to the Hand's convention.

where  $\sigma_T, \sigma_L, \sigma_{TT}, \sigma_{LT}$  are called structure functions. In this notation, the subscript T(L) denotes the contribution from transversely (longitudinally) polarized virtual photons, while the subscripts TT and LT denote the contributions from the interference between transversely-transversely and longitudinally-transversely polarized virtual photons. Also, in the analysis of exclusive  $\pi^0$  muoproduction, the angle  $\phi$  will be called  $\phi_{\pi^0}$ .

The goal of the analysis performed in Chapter 6 is to extract the virtual-photon proton cross-section for exclusive  $\pi^0$  muoproduction (Eq. 2.14) from the COMPASS 2012 DVCS data sample. To draw the connection to the GPDs, the result of the measurement is discussed in the context of a particular model for GPDs in Section 6.8.

## 2.3 Availability of data

The availability of measurements of exclusive production of pions is rather limited. There are two facilities with notable results. The HERMES collaboration measured exclusive production of  $\pi^+$  mesons, while experiments at JLab report measurements of  $\pi^+$  as well as  $\pi^0$  production. Both measurements were picked up wondrously by GPD phenomenologists, as current models were unable to describe the data. The following will shortly summarize the measurements at the two facilities. Note, that there exist also data in the domain  $Q^2 < 1 (\text{GeV}/c)^2$ , but since for the application of the factorization and the interpretation in terms of GPDs, at least  $Q^2 > 1 (\text{GeV}/c)^2$  is required, these measurements are not included here<sup>3</sup>.

The HERMES collaboration reports measurements of exclusive electroproduction of  $\pi^+$  mesons. First measurements in 1997 used a longitudinally polarized hydrogen gas target and 27.6 GeV positron beam. The HERMES spectrometer was used to reconstruct the scattered positron and the produced meson. Since the recoiling target nucleon was not detected, the exclusivity was ensured using the missing mass of the reaction. This setup allowed the first measurement of an azimuthal single-spin asymmetry in exclusive  $\pi^+$  electroproduction [42].

Subsequently, the HERMES collaboration conducted a similar measurement in 2002-2005, however using a transversely polarized target [43]. The extraction of Fourier amplitudes of single-spin azimuthal asymmetries allowed to draw first conclusions on the impact of certain GPDs.

Next to asymmetries, the HERMES collaboration also presented the measurement of the exclusive  $\pi^+$  electroproduction cross-section using a combined data set covering data taking periods from 1996 to 2005 [44]. The virtual-photon proton cross-section was extracted in bins of  $Q^2$ ,  $x_{Bj}$  and  $t' = t_0 - t$ , where  $t_0$  denotes the minimal possible transfer of the square of four-momentum to the proton. A result plot of HERMES is depicted in Fig. 2.7. It was found

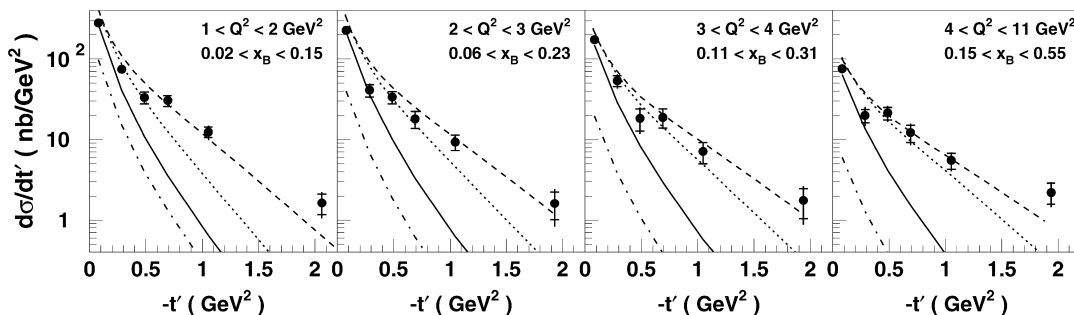


FIGURE 2.7: Result of HERMES for the differential virtual-photon proton cross-section for exclusive  $\pi^+$  electroproduction as a function of  $-t'$  for bins in  $Q^2$ . The markers represent the measurement while the lines are different theoretical computations. [44]

that theoretical GPD based calculations were lacking to describe the data.

<sup>3</sup>For example MAMI [41]

A first attempt to tackle this issue and forge a comprehensive description for  $\pi^+$  production was performed in the framework of the Goloskokov and Kroll (GK) model [36]. It was concluded, that the dominant part of the cross-section at small  $-t'$  comes from longitudinally polarized virtual photons while a major part originates from the pion pole exchange.

The absence of the pion pole contribution in the production of  $\pi^0$  mesons makes it appealing to study this channel as well. However, the detection of the two decay photons of the  $\pi^0$  makes this channel experimentally more challenging. In addition, the cross-section for  $\pi^0$  production is expected to be much smaller compared to  $\pi^+$  production.

The  $\pi^0$  production channel was first probed by the CLAS collaboration (JLab Hall B) in the measurement of beam-spin asymmetries [45]. In this experiment, a 5.77 GeV polarized electron beam and a liquid hydrogen target was used. The CLAS setup allowed the reconstruction of both decay photons of the  $\pi^0$  as well as the scattered target proton and the scattered electron. The measurement of asymmetries was later complemented by the measurement of the cross-section for exclusive  $\pi^0$  electroproduction [46, 47]. The vast amount of statistics allowed the CLAS collaboration to perform comprehensive studies in a variety of kinematic bins as well as to dissect the cross-section as a function of  $\phi_{\pi^0}$  in bins of  $t'$ ,  $Q^2$  and  $x_{Bj}$ . An excerpt of results from CLAS is depicted in Fig. 2.8. The results were found compatible with calculations from a more evolved GK model [48] which incorporates changes needed to fit the  $\pi^+$  data. Another approach to handle the  $\pi^+$  in the framework of GPDs was advocated by GL [49, 50]. Their ansatz results in a different behavior for the cross-section at small  $-t$ . However, the available data do not favor one approach over the other.

Complementary to the rather large kinematic coverage of CLAS, the JLab Hall A collaboration have presented measurements at small values of  $t'$ , ranging from  $0.01 (\text{GeV}/c)^2$  to  $0.206 (\text{GeV}/c)^2$ . For this, the JLab Hall A experiment used a 5.75 GeV electron beam impinging on a liquid hydrogen target. The kinematic was fixed at  $x_{Bj} = 0.37$  with two values for  $Q^2$ ,  $1.9 (\text{GeV}/c)^2$  and  $2.3 (\text{GeV}/c)^2$ . The experimental setup allows to detect the photons and the scattered beam electron, thus the exclusivity of the events is ensured using the missing mass technique [51].

The JLab Hall A experiment also conducted measurements using different beam energies. This allows for determining each individual structure function of the cross-section (*i.e.* separate  $d\sigma_T/dt$  and  $d\sigma_L/dt$ ) using Rosenbluth separation [52]. Their measurement is depicted in Fig. 2.9. While  $d\sigma_T/dt + \epsilon d\sigma_L/dt$  and  $d\sigma_{TT}/dt$  are compatible with the measurements at CLAS and well described by models, the result adds another issue to the picture, since the structure function  $d\sigma_{LT}/dt$  is found to be negative.

The JLab Hall C collaboration has results for the electroproduction of  $\pi^+$  [54] and  $\pi^0$  [55] mesons, too. However, with measurements performed

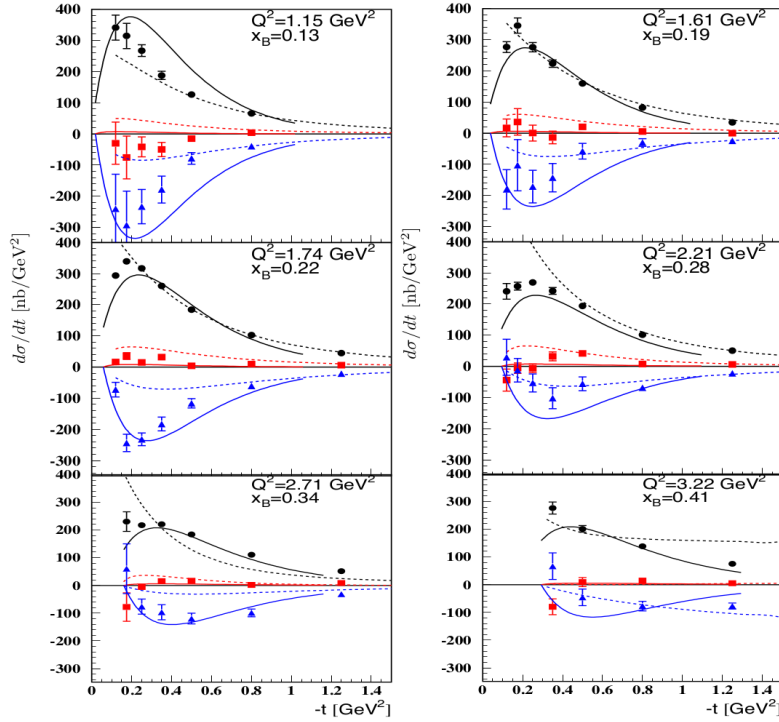


**FIGURE 2.8:** Excerpt of results for the structure functions as a function of  $-t$  at CLAS. The data and curves are as follows: black (filled circles) -  $d\sigma_U/dt = d\sigma_T/dt + \varepsilon d\sigma_L/dt$ , blue (triangles) -  $d\sigma_{TT}/dt$ , and red (squares) -  $d\sigma_{LT}/dt$ . The error bars are statistical only. The curves are theoretical predictions produced with the GK model [48] (solid) and the Goldstein and Liuti (GL) model [49, 50] (dashed). In particular: black (positive) -  $d\sigma_U/dt = d\sigma_T/dt + \varepsilon d\sigma_L/dt$ , blue (negative) -  $d\sigma_{TT}/dt$  and red (small) -  $d\sigma_{LT}/dt$ . [47]

close to the  $\Delta(1232)$  resonance, the physics topic of the experiment is not directly targeting GPDs.

Measurements of HEMP in order to access GPDs have been performed at the COMPASS experiment in the past already. By using polarized targets, the observables have been asymmetries for different configurations of target and beam polarization. That way, asymmetries have been measured for the  $\rho$  and  $\omega$  mesons [56, 57].

With the direct measurement of a meson production cross-section, here, a novel observable is studied at the COMPASS experiment. The measurements will add knowledge in an up to now uncharted kinematic domain. The specific setup of the experiment is detailed in the following chapter while the extraction of the cross-section is subject of Chapter 6.

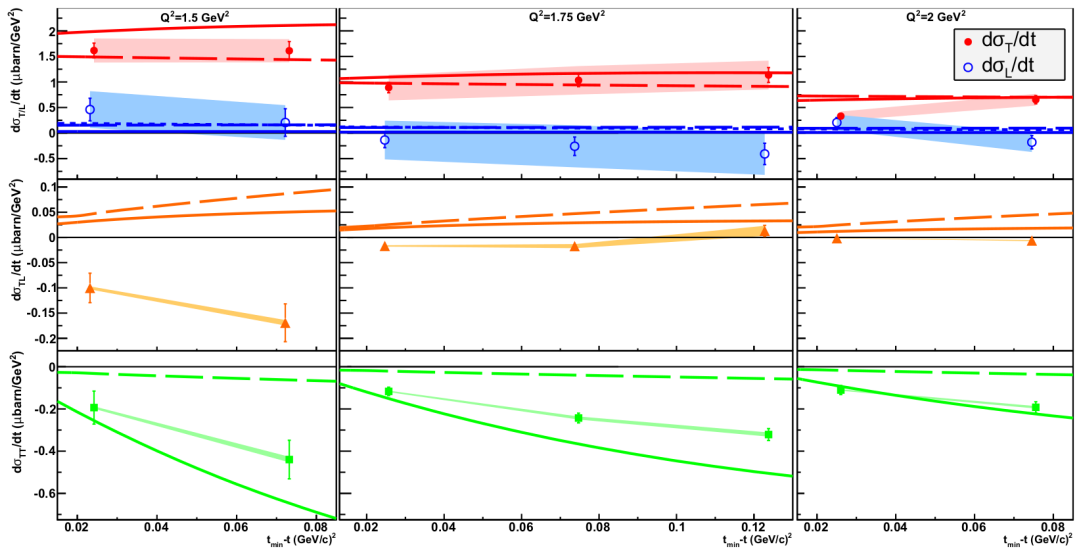


**FIGURE 2.9:** Result for the structure functions as a function of  $t_{min} - t$  measured at JLab Hall A for  $Q^2 = 1.5 \text{ (GeV/c)}^2$  (left),  $1.75 \text{ (GeV/c)}^2$  (center) and  $2 \text{ (GeV/c)}^2$  (right) at  $x_{Bj} = 0.36$ . In particular:  $d\sigma_T/dt$  (full circles),  $d\sigma_L/dt$  (open circles),  $d\sigma_{LT}/dt$  (triangles) and  $d\sigma_{TT}/dt$  (squares). The full lines are predictions from the GK model [48] while the long-dashed lines are from the GL model [49, 50]. The short-dashed line for  $d\sigma_L/dt$  are predictions from the VGG model [53]. Bands connecting the data points show normalized systematic uncertainties on the experimental data, which are strongly anti-correlated for  $d\sigma_L/dt$  and  $d\sigma_T/dt$ . [52]

---

## 3 COMPASS experiment

---

The COMPASS experiment continues the long history of high energy fixed-target experiments with muon beam conducted at CERN. It succeeds EMC, NMC and SMC and is set up in the same facilities, even still using the same strong bending magnet used in the experiments before. The COMPASS experiment, especially the target area and the spectrometer, are build in very modular fashion. The specific setup of the experiment highly depends on the physics program that is executed.

In the following section a description of the setup of the COMPASS experiment as it is used for the DVCS program will be given. For further reading and a more detailed description of the various detectors one may refer to [58].

### 3.1 Beam

Through the location at the end of the M2 beamline, the COMPASS experiment has different kinds of particle beams at its disposal. In the hadron program, pion and kaon beams are used for hadron spectroscopy and to investigate Drell-Yan or Primakov type processes. For tests and calibrations, a low-energy, low-intensity tertiary electron beam can be used. To study the spin structure of nucleons and in particular for the DVCS program, muon beams are used.

Initially, protons from the Super Proton Synchrotron (SPS) with a momentum of up to  $450 \text{ GeV}/c$  are collimated on a beryllium target (T6). Secondary particles, mainly pions with an admixture of about 3.6 % kaons, are produced. By varying the length of the T6 target, the intensity of the secondary particle beam can be adjusted. The beam is channeled into a decay tunnel with a length of about 600 m where a fraction of the particles decays via a weak interaction process into muons. The remaining hadrons are absorbed. The muon beam is then directed to the surface and shaped by various magnets before it arrives at the COMPASS target. About 23 % of the beam particles are found outside the center of the beam distribution with distances greater than 4 cm in the so-called halo.

Due to parity violation of the weak interaction, the muon beam is naturally polarized. The amount of polarization depends on the fraction of momentum of secondary to tertiary particles. For the COMPASS data taking, the beam parameters are optimized for beam intensity and an average polarization of 80 %. This is achieved with a pion momentum of  $172 \text{ GeV}/c$  and a

momentum for the positive muon beam of 160 GeV/c, still reaching the maximum allowed flux<sup>1</sup> of  $2 \cdot 10^8$  positive muons per SPS cycle [58].

## 3.2 Beam momentum and direction reconstruction

The beam optics allow a momentum spread of the muons by approximately 5%. As a consequence, for DIS like measurements, the momentum of each individual beam particle has to be known to determine the scattering kinematics and the beam polarization. For this, the beam momentum station (BMS) uses six measurement stations that are located in the beam line about 100 m upstream of the COMPASS target. The BMSs surround three dipole magnets

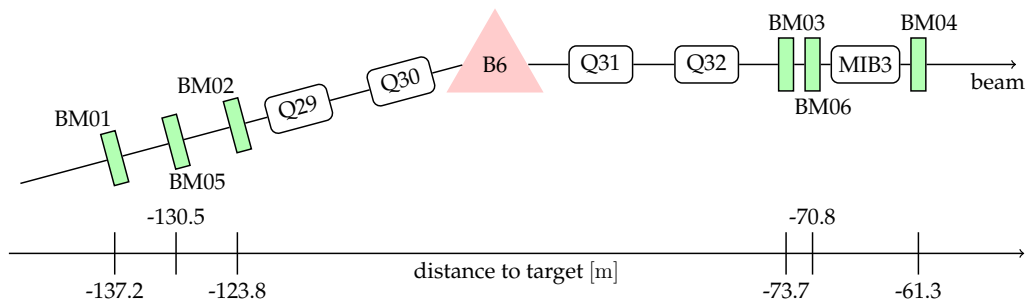


**FIGURE 3.1:** Beam momentum stations (BM01 to BM06) and beam magnets (Q29 to Q32) along the beamline. The beam momentum stations together with the bending magnet B6 are used for the beam momentum measurement. (adapted from [58])

(B6) that deflect the beam vertically as shown in Fig. 3.1. Each BMS is vertically segmented to measure the curvature and therefore the momentum of the particle.

In addition, to determine the interaction vertex in the space and time domain of the spatially extended COMPASS target, the direction and time of the beam particles are determined using the beam telescope (BT). The detectors used in the BT are built from scintillating fibers with planes in horizontal and vertical direction for good time and moderate space resolution. In addition, there are silicon detectors with planes in horizontal, vertical and two inclined directions ( $-45^\circ$  and  $45^\circ$ ), which feature excellent spatial and moderate time resolution.

## 3.3 Target area

### 3.3.1 Target

For the DVCS program, the COMPASS-II setup includes an unpolarized liquid hydrogen (LH<sub>2</sub>) target. This leaves enough room in the target surrounding to install a detector for the reconstruction of the recoiling target proton, see

<sup>1</sup>Due to radiation protection. The intensity of negative muon beam is approximately three times lower.



**TABLE 3.1:** Properties of the scintillators and photomultipliers of the inner (A) and outer (B) barrel of the CAMERA detector.

Property	A	B
length	275 cm	360 cm
depth	0.4 cm	5 cm
width	6.55 cm	29.65 cm
radius	25 cm	110 cm
material	BC408	
refraction index	1.58	
PMT	HR10533 [60]	ET9823B [61]
PMT window $\varnothing$	51 mm	130 mm

dynamic range. This is achieved by the application of the GANDALF-module equipped with analog-to-digital converters (ADCs). The readout electronics is described in more detail in Section 3.7. In particular, the description of the GANDALF-ADC firmware is subject of Chapter 4. The CAMERA detector was commissioned in a five weeks pilot run in 2012. Chapter 5 gives a detailed description of the modus operandi of the detector. Also, together with [31], the calibration and performance studies are carried out. First physics results using the detector are available in [31] and in Chapter 6.

## 3.4 Spectrometer

COMPASS uses a two-staged open field spectrometer. The Large Angle Spectrometer (LAS) covers angles of up to 180 mrad, while the acceptance of the Small Angle Spectrometer (SAS) amounts to  $\approx 30$  mrad. Strong bending magnets in each spectrometer stage, SM1 and SM2, allow momentum and charge measurements using the radius of curvature of charged particles. Their path is measured by tracking detectors, see Subsection 3.4.1. For particle identification and energy measurements, electromagnetic and hadronic calorimeters, a ring-imaging Cherenkov (RICH) and the muon system are used, see Subsection 3.4.2. Fig. 3.4 shows the setup of the COMPASS-II spectrometer for the DVCS program.

### 3.4.1 Tracking

The purpose of tracking detectors is to allow the reconstruction of the trajectory of a charged particle. Depending on the radial distance to the beam axis, different detector types are employed. In the very small area tracker (VSAT) section, close to the beam, detectors with very good timing or spatial resolution are used. Due to immediate proximity to the beam, these detectors need a high rate and radiation stability.

In the Small Area Tracker (SAT) area at distances of about 2.5 cm to 40 cm, a compromise between covered area and time respectively spatial resolution is made. For the very outer part, the Large Area Tracker (LAT) is equipped

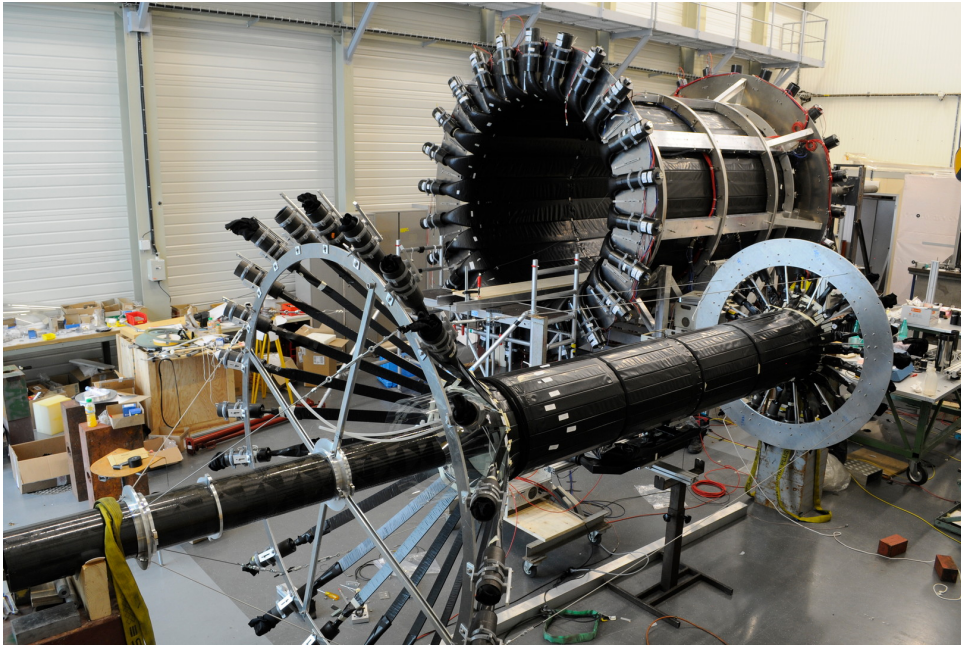


**FIGURE 3.3:** Photograph of the CAMERA detector during assembly. The inner barrel, here in the foreground build around a support structure, is inserted into the outer barrel. The support structure is then removed and the  $\text{LH}_2$  target is inserted. The long light guides allow for positioning the photomultipliers outside of the spectrometer acceptance. The light guides of the outer ring make a turn by  $90^\circ$  to minimize the space requirements. A picture of the fully assembled detector positioned in the COMPASS beamline is available in Appendix B.1.

with large-area detectors. The various detectors in the different stages together with their spatial coverage and resolutions are listed in Table 3.2.

### 3.4.2 Particle identification

To identify the particle species of a reconstructed track, the RICH detector, the muon filters and the calorimeters are used. The first stage of the spectrometer hosts the RICH detector. It is filled with  $\text{C}_4\text{F}_{10}$  gas, so that particles that pervade the detector emit Cherenkov radiation under a characteristic angle. The radii of the detected rings together with a separate momentum measurement allow for discrimination of pions, protons and kaons.

For the identification and energy measurement of photons a total of three electromagnetic calorimeters are installed. ECal0 is placed directly downstream of the target, before the SM1 magnet. This calorimeter is part of the COMPASS-II spectrometer update. A schematic picture of the calorimeter is depicted in Fig. 3.5. Its dimensions of about  $204 \times 206 \text{ cm}^2$  allow the detection of photons under very large angles. ECal1 and ECal2 are placed at the end of the two spectrometer stages, respectively. They are built mainly from lead glass, hence the absorbing and detecting material is the same. Photons are slowed down by the material and create an electron-positron shower. The shower emits Cherenkov radiation which is detected with photomultipliers. ECal0 and the central part of ECal1/ECal2 close to the beam use the sampling

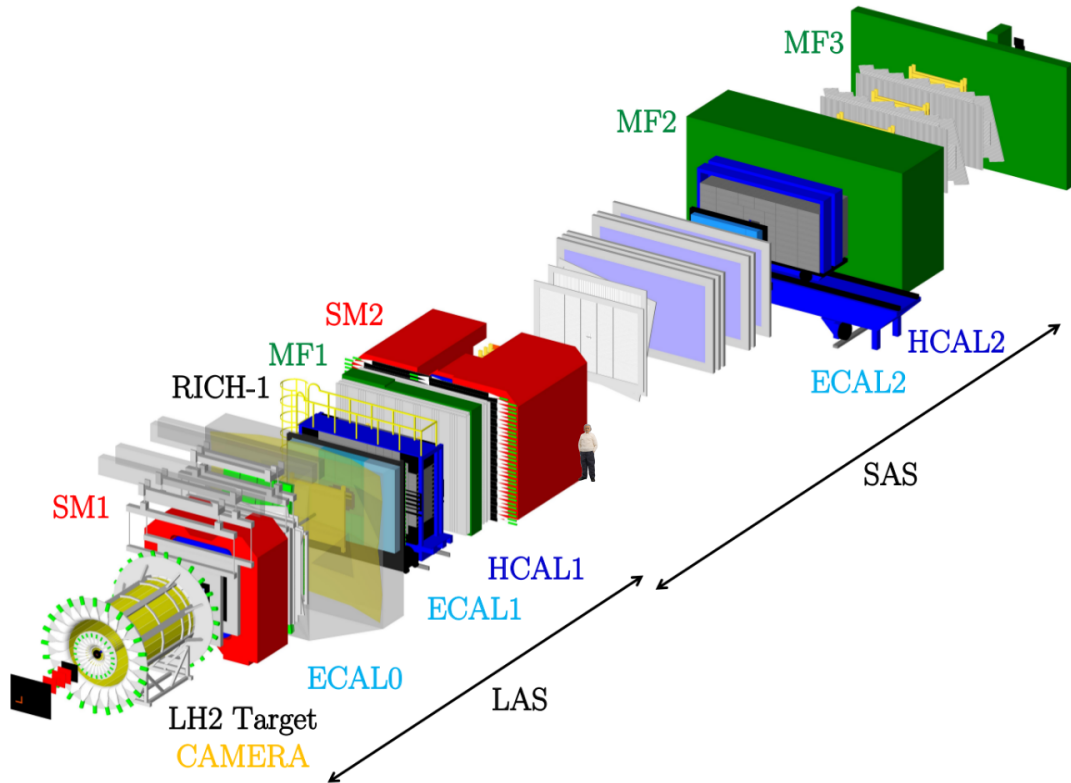


**FIGURE 3.4:** Overview of the COMPASS-II spectrometer [59]. The beam enters from the lower left and hits the  $\text{LH}_2$  target which is surrounded by the CAMERA detector (yellow barrel). The final state particles are detected by CAMERA and in the two spectrometer stages LAS and SAS. Each stage includes a bending magnet (SM1 and SM2), various tracking detectors (Subsection 3.4.1) and means for particle identification (Subsection 3.4.2). The construction is approximately 50 m long.

calorimeter principle. Here, absorbing lead layers are combined alternating with scintillating layers to enhance radiation stability.

ECal1 and ECal2 are accompanied by their hadronic counterparts HCal1 and HCal2. They are sampling calorimeters with iron as absorbing material.

The detection of muons by the muon system uses a combination of absorbers (MF1, MF2 and MF3) and trackers. Due to sufficient material in the absorbers, only muons are able to pass and create correlated hits in the trackers before and after the absorbers. The absorbers, called muon filters, are build from iron (MF1, MF3) or concrete (MF2).

### 3.5 Trigger

As a consequence of the high intensity of the beam crossing the active region of the spectrometer, a trigger system has to be set up for the selection of interesting physics events. The COMPASS trigger was initially installed for the measurement of DIS physics in a wide kinematic domain. Information from

TABLE 3.2: Listing of various detectors used to track the path of particles.  $\sigma_x$  denotes spatial,  $\sigma_t$  denotes time resolution.

Type	active area (cm <sup>2</sup> )	$\sigma_x$ ( $\mu$ m)	$\sigma_t$ (ps)	tracker stage
Scintillating Fibers	$(3, 9)^2 - (12, 3)^2$	130 – 210	0,4	VSAT
Silicon strips	$5 \times 7$	7 – 11	2,5	VSAT
Pixel-GEM	$10 \times 10$	95	9,9	VSAT
GEM	$31 \times 31$	70	12	SAT
MicroMeGas	$40 \times 40$	90	9	SAT
MWPC	$178 \times (90 - 120)$	1600		LAT
drift chambers (DCs)	$180 \times 127$	110 – 170		LAT
Straw Chambers	$280 \times 323$	190		LAT
Large Area DCs	$500 \times 250$	500		LAT

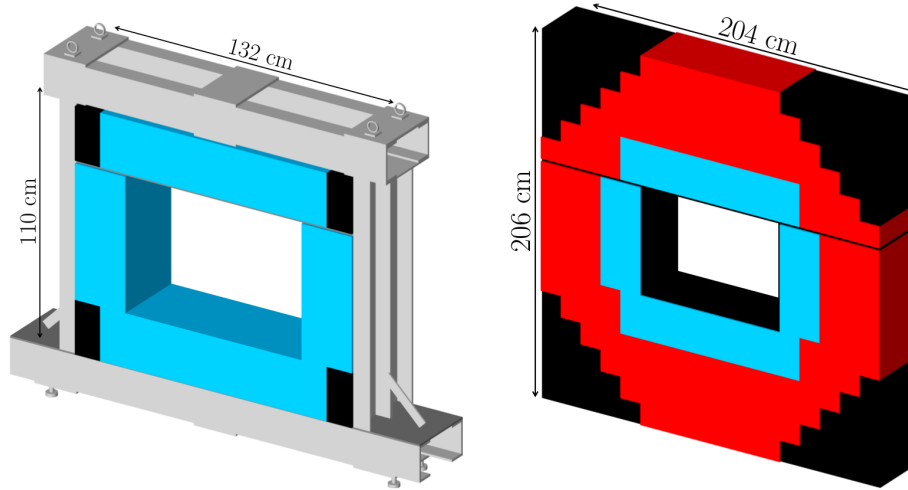


FIGURE 3.5: Visualization of the new electromagnetic calorimeter ECal0 [59]. The left picture shows the partially set up calorimeter as it was used in the 2012 DVCS pilot run while the right picture shows the fully assembled detector. The black color indicates inactive areas.

different detectors are combined to form a First Level Trigger (FLT). The trigger decision is then distributed to the readout and front-end electronics via the COMPASS Trigger Control System (TCS). Because of the finite memory of the readout and front-end electronics, the latency between initial muon interaction and the trigger decision has to be in the order of  $1 \mu$ s. At COMPASS, there exists no higher level trigger and there is even the plan to run the experiment in future with a trigger-less setup [62].

For the DVCS program, only a few changes had to be made to the existing setup. However, in addition to the muon triggers a new type of trigger was developed, which allows discriminating on the recoiling proton. Studies for this trigger and the principle considerations were already started when planning the electronics framework for CAMERA [63, 64]. For the concrete realization and a detailed description of the mode of operation refer to [65].

The COMPASS muon trigger uses two different techniques for the detection of

the scattered muon based on the energy loss or based on estimating the track origin. For both, two hodoscope stations with scintillating strips are put in coincidence while at least one of the hodoscopes is placed downstream of a muon filter. Additional triggers are the Veto Trigger and a true *random trigger*.

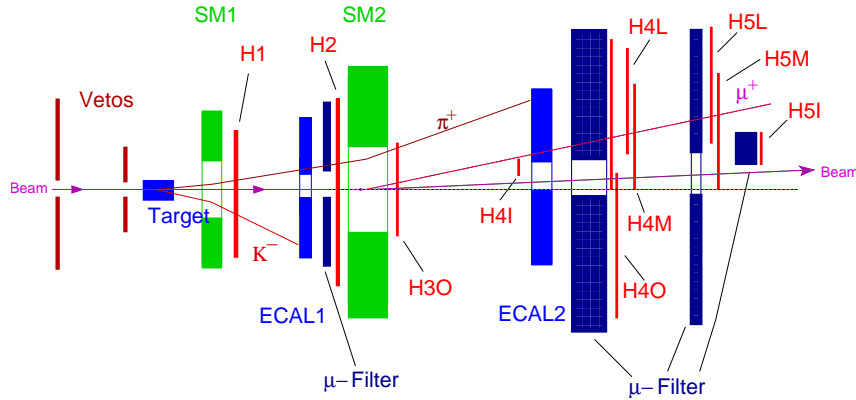


**FIGURE 3.6:** Illustration of the COMPASS trigger system. The hodoscopes (H\*) for the trigger on the scattered muons are placed upstream and downstream of the muon filters. The veto system is positioned upstream of the target. [66]

**Energy loss trigger:** The *energy loss trigger* uses the deflection of the muons in the dipole fields of the spectrometer magnets to determine the energy loss of the muon. For this, a coincidence matrix of vertically oriented strips in two hodoscope stations is used. This approach is realized in the Ladder Trigger (LT) system where both stations (H4L, H5L) are located behind muon filters close to the end of the spectrometer.

**Target pointing trigger:** The *target pointing trigger* uses coincidences in hodoscope stations with horizontally arranged strips to determine the scattering angle of the muon along the direction of the non-bending plane in the magnetic field. By extrapolating the track to  $z = 0$ , the compatibility with the target in vertical direction is tested. This approach is used for relatively large scattering angles (or  $Q^2$ ) by the Outer Trigger (OT) and the LAS Trigger (LAS). The Middle Trigger (MT) uses a combination of the *target pointing* and the *energy loss* approach.

**Veto Trigger:** As mentioned in Section 3.1, the beam is surrounded by a halo of particles. To reduce the trigger rate by muons that are not interacting with the target, the Veto Trigger (VT) upstream of the target is used. By combining two hodoscope stations, particles that are deflected from the beam axis can be detected. The VT is then put in anti-coincidence with the other triggers. However, using the VT system leads to a dead time for the whole spectrometer as discussed in [66]. For the determination of the effective muon flux, a precise knowledge of the veto dead time (VDT) is vital.

**Random trigger:** The *random trigger* is generated by the dominant  $\beta^+$  decay of a  $^{22}_{11}\text{Na}$  source. The decay positron annihilates with an electron and the two photons are detected by two scintillators. The coincidence of the scintillators is connected as a logical signal to the COMPASS trigger system.

## 3.6 Readout and DAQ

The acquisition, digitization and finally the recording of the detector data is a key task of a high energy experiment.

The raw detector information, mainly voltage or current pulses, are gathered by so-called front-end electronics. Their purpose is to convert the analog pulse into a digitized information containing its relevant properties. The different front-end types are

1. combination of discriminator and time-to-digital converter (TDC) to record timestamps,
2. combination of discriminator and scaler to record hit rates,
3. sampling and digitization of the analog pulse using analog-to-digital converters (ADCs).

Depending on the detector type, the front-end electronics is situated directly at the detector and the digital data is sent to a readout board. Alternatively, the front-end electronics is mounted to readout motherboards directly via mezzanine cards.

Taking the CAMERA readout as an example for a specific detector readout which has to satisfy a number of constraints. For digitizing the fast pulses of the plastic scintillators with rise-times in the order of nanoseconds, ADCs with very high sampling rate and sophisticated pulse shape analysis are required. No splitters should be used for distributing the signal to readout and trigger to not diminish the signal quality. Hence, the integration of readout and trigger into one homogeneous system is needed. Such system would also offer the possibility to use the amplitude in the trigger decision.

Finally, these considerations lead to the design and development of a well adapted, yet versatile framework for next-generation detector readout, see Section 3.7. It consists of two mainboards called GANDALF-module and TIGER-module, various mezzanine cards and the VXS-backplane switched serial fabric for fast communications.

All readout boards are connected to the COMPASS TCS. The TCS distributes triggers together with metadata (e.g. spill and event numbers) to identify the event. When the readout boards receive a trigger, they collect data from different front-end modules and form data packages containing the front-end data as well as the TCS metadata. The data packages are then transmitted via optical links to readout buffers. They package information of one event from different readout modules. The final event data containing all detector information is built by eventbuilders. They gather the event data

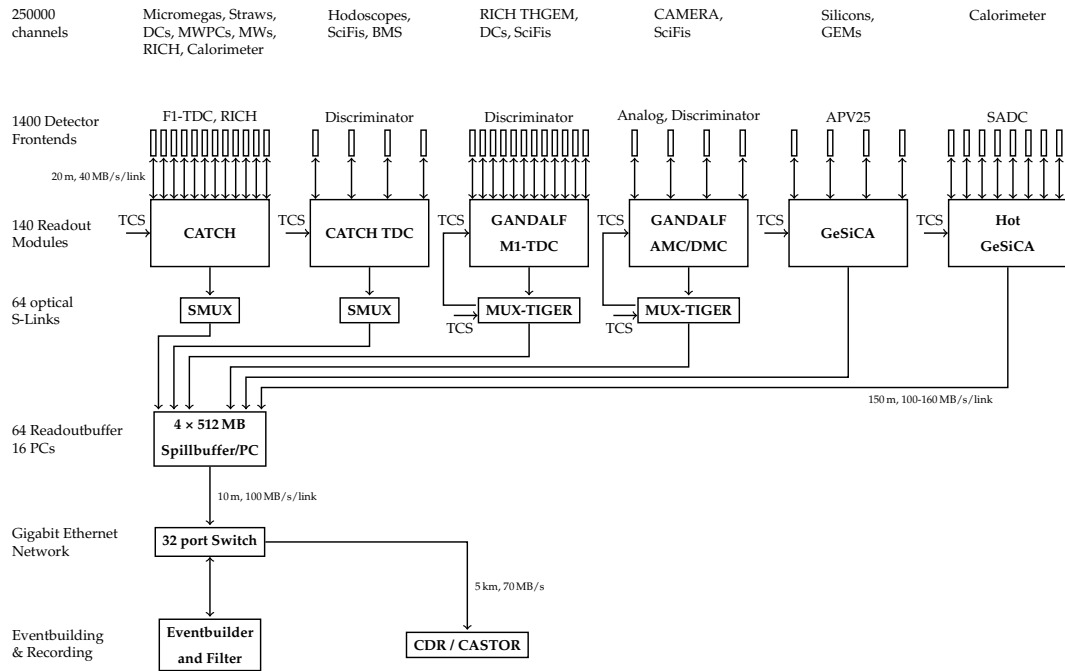


**FIGURE 3.7:** Overview of the components of the COMPASS data acquisition system (DAQ) used in the DVCS pilot run 2012 (adapted from [3] by [67]).

of different readout buffers and allow further filtering of the events. Finally, for long-term storage, the data is saved by the CERN advanced storage manager (CASTOR). The structure of the COMPASS readout is also illustrated in Fig. 3.7.

## 3.7 GANDALF framework

### 3.7.1 GANDALF-module

The GANDALF-module [63] is a versatile electronic device developed at the University Freiburg. For the motherboard, the 6U-VXS/VME64x formfactor was chosen. The board features two Virtex-5 FPGAs [68] complemented with large memory. Two mezzanine card slots and numerous interfaces allow the board to be adapted to a large number of applications. An overview of the GANDALF-module is given in Fig. 3.8. For more information and technical details one may refer to [63].

The GANDALF-modules are operated in the payload slots of the VXS-backplane. For configuration and monitoring, a CPLD is installed on the module. It allows for communication over the VME-backplane with the VME-CPU or with a PC using the front side USB interface.

As of now, mezzanine cards of three flavors are available. The optical mezzanine-card (OMC) offers data communication by means of four optical or copper transceivers. The digital mezzanine-card (DMC) provides 64 LVDS input or output connections for logic signals. The ADC mezzanine-card (AMC) hosts

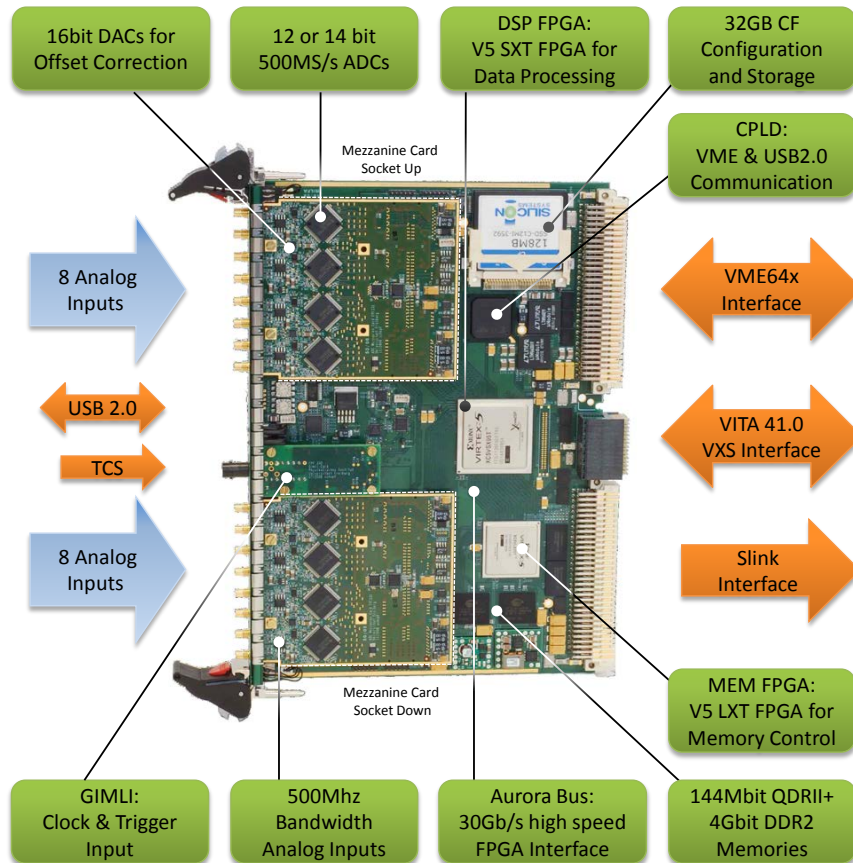


FIGURE 3.8: Overview of the GANDALF-module configured as transient recorder (without heat sinks). In this configuration, the two ADC mezzanine-cards (AMCs), marked by the white dashed lines, allow to readout 16 detector channels (light blue arrows). The available interfaces are depicted by orange arrows, hardware components by green boxes. [63]

eight ADC chips to digitize up to eight analog signals. The different mezzanine cards allow the GANDALF-module to be deployed as scaler [69], TDC [70] or as transient recorder [63, 71, 72]. The description of the firmware design for the transient recorder is subject of Chapter 4 of this thesis.

### 3.7.2 TIGER-module

The TIGER-module [64] is another electronic device recently developed at the University Freiburg. The module embodies a 6U-VXS switch board. Through the double-star routing of the VXS-bus, the two VXS switch-slots are connected to each GANDALF-module as well as to each other.

The main feature of the TIGER-module, apart from the VXS interface, is the very large dimensioned Virtex-6 FPGA [73]. It offers the possibility to implement sophisticated logic circuits to tackle complex tasks. Moreover, the computing power can be enhanced by using a GPU that can be mounted on the boards MXM socket. Since the TIGER-module cannot communicate with

the VME-CPU, it is equipped with a computer-on-module. This allows interfacing the FPGA via the PCIe bus. More details are available in Fig. 3.9, [64].

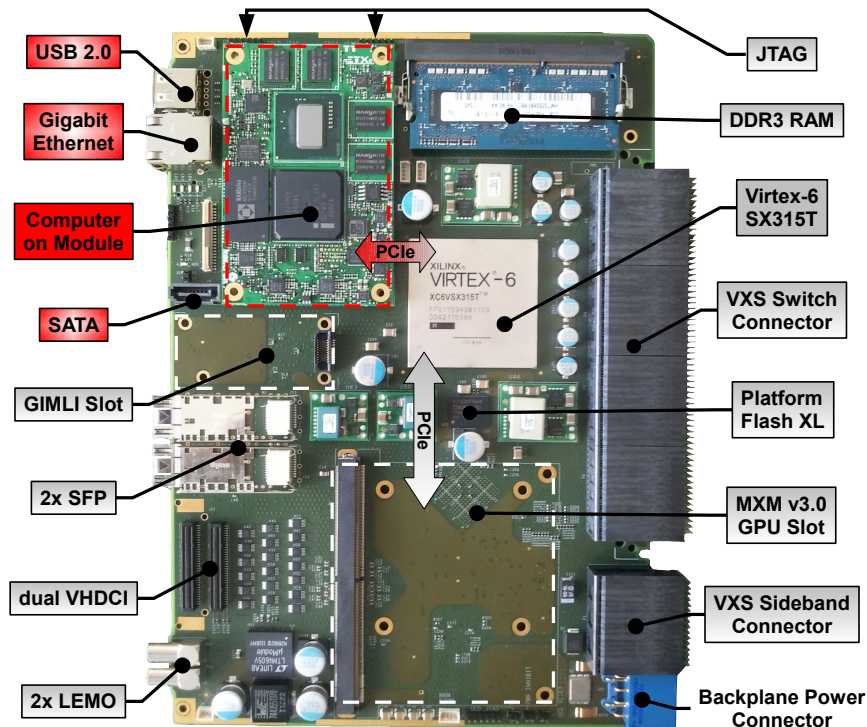


**FIGURE 3.9:** Overview of the TIGER-module and its most important components. The board may be divided into two subsystems. On the one hand, there is the FPGA with its related components (grey boxes), on the other hand, there is the computer-on-module with its related parts (red). The two systems communicate via the PCIe bus. The GPU, which can be used to assist the FPGA with heavy calculations, is not mounted in this picture. The GPU communicates also with the FPGA via PCIe bus. [67]

### 3.7.3 VXS-backplane

The VXS-backplane offers a double star bus fabric for interconnection between GANDALF and TIGER-modules. It offers space for 18 GANDALF and two TIGER-modules with the ability to implement high-speed connections between the modules, see also Fig. 3.10. The data-link developed in [67] allows sending data with  $1 \text{ GB s}^{-1}$  per GANDALF-module to each of the TIGER-modules.

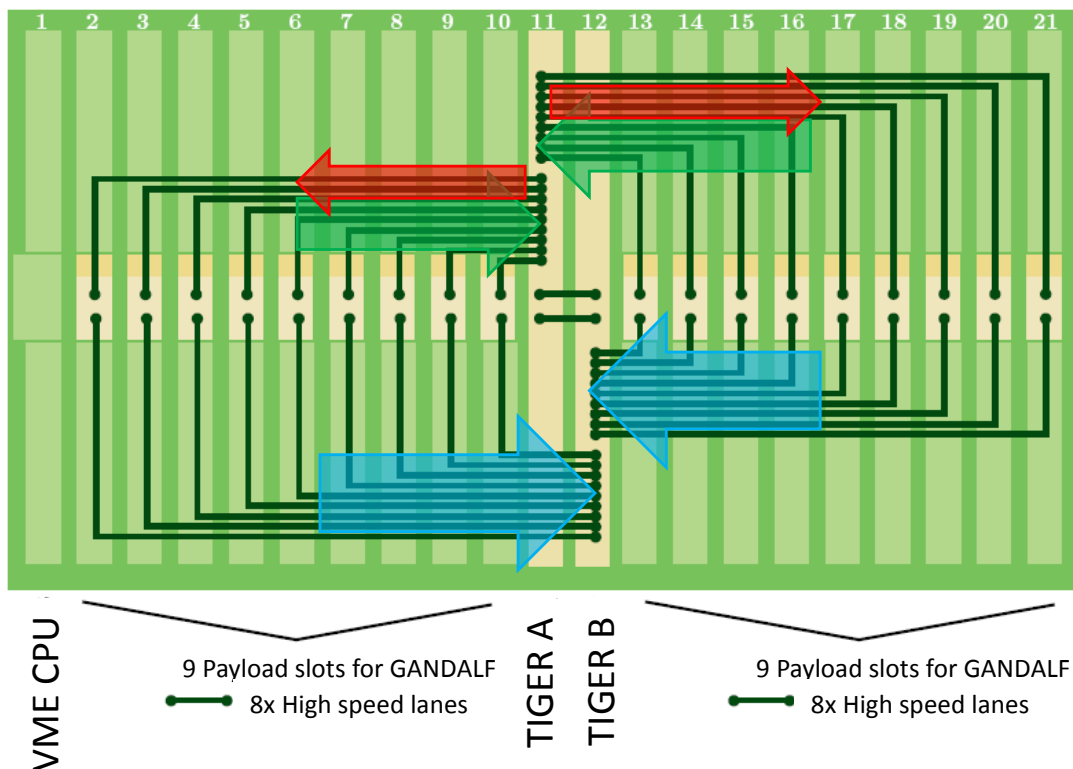


**FIGURE 3.10:** Structure of the double-star bus fabric of the VXS-backplane. The payload modules (GANDALF-modules) are placed in the slots 2 to 10 and 13 to 21. The switch modules (TIGER-modules) are placed in slots 11 and 12. Each payload slot has two buses with eight differential lanes. For TIGER A, the eight-bit wide bus is split into two RX and six TX lanes to allow bidirectional communication. The buses to TIGER B are operated unidirectional, hence are eight bit wide. The communication between the TIGER-modules is possible via the VXS sideband bus. It offers one differential RX- respectively TX-lane. [67, 74]



---

## 4 GANDALF-ADC firmware

---

The following chapter is devoted to the description of the firmware design for the GANDALF-module. As described in Subsection 3.7.1, the GANDALF-module was designed in a very flexible way. By mounting different mezzanine cards, it offers the possibility to fulfill many different purposes when it comes to the acquisition of detector data. One of the key applications of the GANDALF-module comes with its configuration with the ADC mezzanine-card (AMC), enabling the module to sample eight analog channels with 1 GHz and an amplitude resolution of 12 bit. Such GANDALF-ADCs were deployed for the readout of the CAMERA detector already for the 2012 DVCS pilot run. Studies of the readout and the CAMERA detector using this data are subject to the subsequent Chapter 5. The studies lead to important changes and improvements in the VHDL firmware design of the GANDALF-ADC. This chapter gives a comprehensive overview of the improvements and the general state of the design.

The challenging task to process the digitized data stream, extract pulse features and dispose them for further processing is performed in a specialized firmware for the GANDALF-module main FPGA, further referred to as the DSP-FPGA. The firmware design is arranged very flexible itself to adapt to the different operating environments and ways to distribute the gathered data. In the course of the development of the GANDALF-ADC firmware, the base design for the GANDALF-module ([63, p. 77]) was completed with interfaces to all relevant auxiliary components such as I<sup>2</sup>C, *configuration memory*, clock distribution, data input and output.

The chapter opens with a rough overview of the structure of the DSP-FPGA firmware design, where Section 4.1 gives a crude description of the general structure. Then, some key components are described in a more general way. First, Section 4.2 summarizes the most relevant hardware components of the AMC. Then, a description of the implementation of the I<sup>2</sup>C bus is given in Section 4.3 followed by an explanation of the treatment of the Si5326 clock multiplier chip (further referred to as “SI chip”) in Section 4.4. In Sections 4.5 to 4.8, detailed descriptions of important logic modules are given. The chapter closes with a description of the design verification using testbenches in Section 4.9.

The scope of the chapter is to give vital information for those who want to operate the GANDALF-ADC and give them also an idea of the effect of the settings they can or have to modify. On the other hand, the chapter shall also allow developers to understand where things are done so that they may

modify or revise the code. For this, specific parts of the firmware are described in greater detail.

The directory structure of the GANDALF-ADC project together with a description of important files is given in Appendix A.1.

## 4.1 DSP-FPGA firmware structure

The firmware design is composed of different logic modules that are responsible for specific tasks. These logic modules may contain further logic modules themselves. In the language of VHDL, the top-most logic modules are connected to each other in the so-called *toplevel*-module. The *toplevel*-module inputs and outputs correspond to the pins of the FPGA. A sketch of the *toplevel*-module for the DSP-FPGA is given in Fig. 4.1 together with a simplified summary of the inputs and outputs. The design of the *toplevel*-module con-

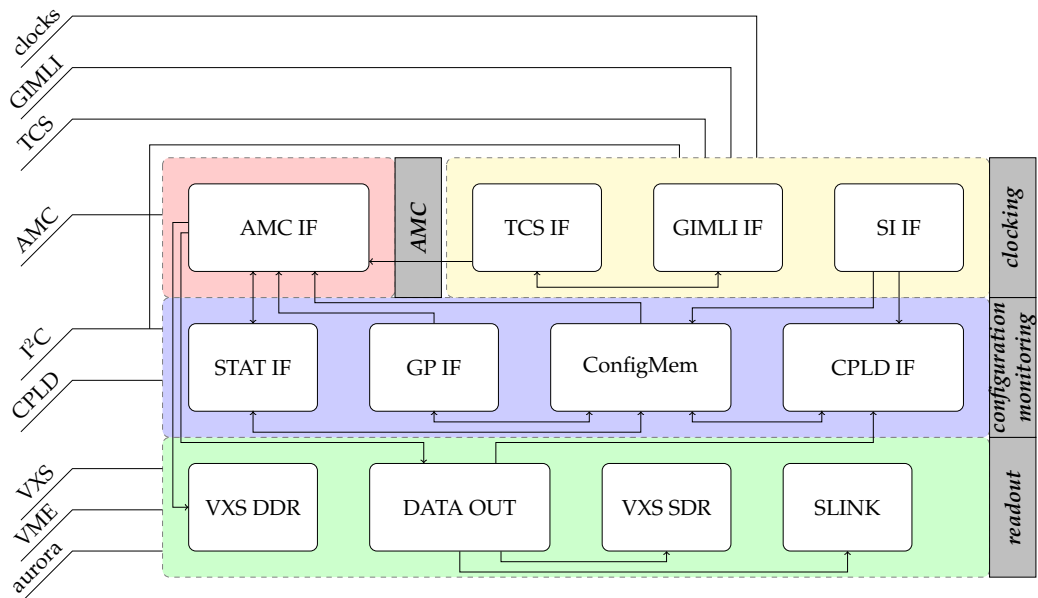


**FIGURE 4.1:** Overview of the DSP-FPGA firmware *toplevel*-module with associated logic modules. The logic modules can be grouped according to their purpose into four categories. The interconnections of the logic modules are indicated with arrows. The inputs to the DSP-FPGA (*i.e.* FPGA pins) are indicated on the left-hand side and are connected to the logic module group where they are needed.

sists of interconnected logic modules that can be classified by four different categories.

**Clocking** Involves handling the different possibilities to acquire the operating clock by means of different GIMLI cards, hence *GIMLI* interface, described in Section 4.5. It is also responsible of interfacing the *SI* chips mounted on the GANDALF-module as well as those mounted on the AMCs. This so-called *SI* interface is described in Section 4.4. Also, the *TCS* module is allocated to this category. It consumes the *TCS* clock and decodes the *TCS* data

which are modulated on the TCS clock. For a detailed description of the TCS decoding logic refer to [71].

**Configuration and Monitoring** The *configuration memory* is a block random access memory (BRAM) inside the DSP-FPGA where special registers are reserved for the run-time configuration of the firmware, described in Subsection 4.6.1. In addition, the DSP-FPGA uses so-called *fast-registers* for one-bit configuration settings and to trigger certain processes. The interface with the CPLD allows for access of the *configuration memory* and to issue *fast-registers*. For this, the command line tool *vme\_write* is used. The syntax to access the *configuration memory* register with address *addr* of a GANDALF-module with hex-id<sup>1</sup> *XY* is

```
$ vme_write e0XY2addr data
```

where *data* is the base 16 notation of a 32 bit number which will be written to the *configuration memory*. When *data* is omitted, the command returns the value stored in the *configuration memory*.

The syntax to access a *fast-register* with address *addr* of a GANDALF-module with hex-id *XY* is

```
$ vme_write e0XY7addr arg
```

where *arg* = 0 and *arg* = 1 set the register to the respective constant value and *arg* = 2 raises the register value to a logical one for a short time period.

The sections in this chapter that make use of the *configuration memory* or the *fast-registers* are prepended with blocks describing the registers relevant for the operation of the module described in the particular section. The template for blocks describing *configuration memory* registers looks like the following:

#### *configuration memory registers*

**identifier / addr\_vhdl / addr\_vme** short description or table with short description for bit(s)

The *identifier* is used to reference the register in the text. *addr\_vhdl* gives the register address in the BRAM from within the VHDL code, while *addr\_vme* gives the address of the register to be used in conjunction with the *vme\_write* command. In general, the two addresses are related by  $address\_vme\_write = 4 \cdot address\_vhdl$ . Both addresses are stated using base 16 notation.

The template for blocks describing *fast-registers* looks like the following:

#### *fast-registers*

**fr\_x / y / z** short description

<sup>1</sup>The hex-id of a GANDALF-module is set using two hardware switches, see also [63, p. 50].

where 'fr\_x' is used to reference the register in the text and also the name of the register in the VHDL code. Here,  $y$  is the position of the register in the VHDL *fast-registers* vector and  $z$  is the address to be used together with the *vme\_write* command. While  $y$  is given with base 10, the notation of  $z$  is in base 16. Their relation is  $z = \text{hex}(4 \cdot y)$ .

For monitoring, the *stat* interface and *general purpose (GP)* interface gather various status information about the DSP-FPGA and the AMC which is stored in the *configuration memory*, see Subsection 4.6.2.

**AMC** The handling of the ADC information is performed by a dedicated logic module, the *AMC* interface. It is responsible of interfacing the ADCs, sampling/reading the ADC bits, extracting pulse features and packing of event information for further processing. This task is described in detail in Section 4.7.

**Readout** The data can be sent by means of different output channels, such as the VXS interfaces to the TIGER-modules or through the VME-backplane with an S-LINK drain card. The different possibilities to distribute the data are managed by the *data out* module and described in Section 4.8. The CPLD interface is also related to the *data out* module since it offers a connection to a special FIFO, the so-called *spy\_fifo*, which can be used for readout via the VME-CPU or USB.

## 4.2 ADC mezzanine card (AMC)

The ADC mezzanine-card (AMC) was designed to establish a transient analyzer within the GANDALF-framework [71]. The card has eight SMC input connectors and eight ADS5463 ADCs [75]. The input voltage range covers either 0 V to  $-2$  V or 0 V to  $-4$  V. An offset voltage can be adjusted for each ADC input using digital-to-analog converters (DACs) [76] as illustrated in Fig. 4.2. The ADCs allows sampling their input with 500 MHz and 12 bit amplitude resolution. The sampling clock for the ADCs is provided by the SI chip mounted on the card. One output of the clock multiplier serves the even ADCs while the odd ADCs are connected to the other output. The two outputs of the SI chip can be configured to have a phase difference of  $\pi$ . This allows to operate two ADCs in the so-called interleaved mode where they read a common source<sup>2</sup> and a sampling of 1 GHz is achieved, see also Fig. 4.2. In this configuration, it is mandatory to adjust the DAC of both ADCs such that without a load, both ADCs yield the same value. The yield when there is no input signal from the detector is further referred to as baseline, sometimes also called pedestal.

The SI chip is controlled by an I<sup>2</sup>C bus. Connected to a second I<sup>2</sup>C bus, the card hosts an EEPROM to store configuration and calibration values and a

<sup>2</sup>In this configuration, only the even numbered front panel input connectors are operational.



firmware.

Yet being from the hardware perspective very simple, the usage of the I<sup>2</sup>C bus from within a hardware description language is not very comfortable and the implementation of the protocol offers numerous pitfalls. This is why a module from opencores ([78]) is used to implement the three I<sup>2</sup>C bus masters to guarantee a reliable communication with the I<sup>2</sup>C slaves. It handles the (de)serialization of the I<sup>2</sup>C traffic, the initialization and timing requirements of the bus. The module is operated as a wishbone slave, see [79] for a detailed description of the wishbone protocol.

Still, accessing the I<sup>2</sup>C bus consists of several steps. To further ease usage and maintenance of the I<sup>2</sup>C bus, the I<sup>2</sup>C wishbone interface is wrapped into more user-friendly modules to serve specific tasks. This results in hiding much of the boilerplate I<sup>2</sup>C operation commands, like the need of putting each access in between start/stop commands. Also, slave register selection is simplified. In case of the *SI* I<sup>2</sup>C bus, a bit vector is used for the selection of the target SI chip which reads '001', '010' and '100' for *SI<sub>G</sub>*, *SI<sub>A</sub>* and *SI<sub>B</sub>*.

In case of the *GP* I<sup>2</sup>C bus, the two I<sup>2</sup>C masters are merged and a single bit is used to switch between the two AMCs. Also, the read/write data port is extended to 32 bit<sup>3</sup>. Accessing the I<sup>2</sup>C is then possible using very simple state machines as depicted in Fig. 4.3.

---

<sup>3</sup>Internally, the I<sup>2</sup>C communication with the slave uses 8 bit, meaning the wrapper logic executes four read/write cycles in order to read/write a 32 bit word.

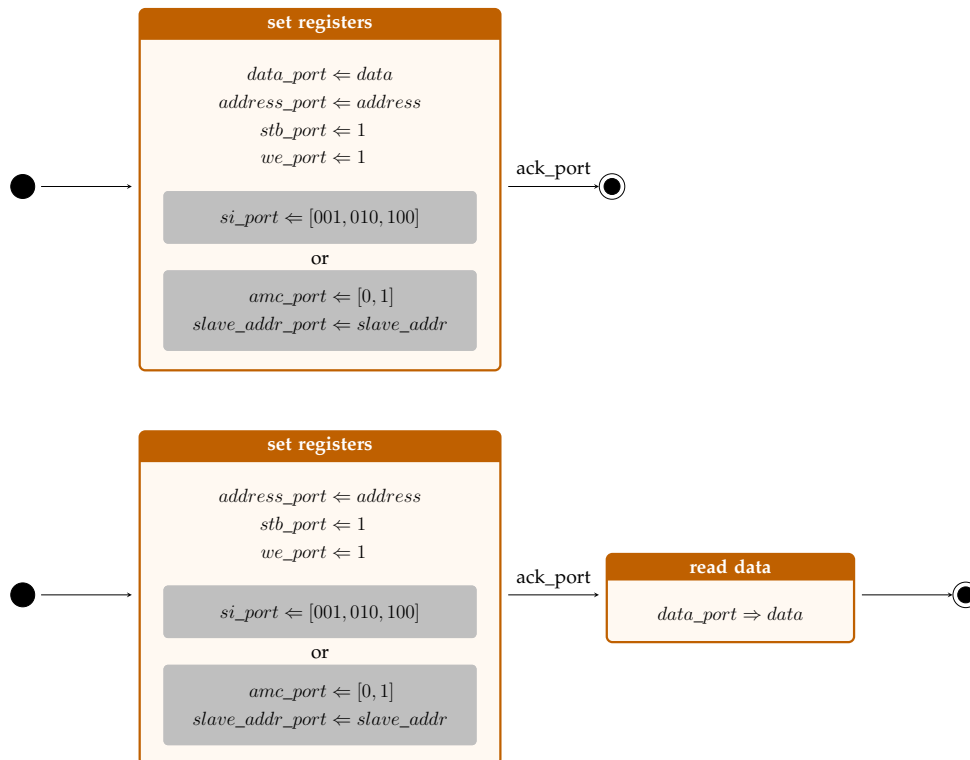


**FIGURE 4.3:** State machine for writing (top) and reading (bottom) from the *SI* respectively *GP* I<sup>2</sup>C bus. Input/Output signals of the I<sup>2</sup>C module are indicated by the suffix '*\_port*'. The *set registers* state is used to setup the input signals of the I<sup>2</sup>C master for the specific operation. The *stb\_port* signal is used to notify the module that the user wants to perform an operation. The *we\_port* signal determines if the operation is a read or a write operation to (from) the address *addr\_port*. In case of the *SI* I<sup>2</sup>C bus, the target *SI* chip is determined by the *si\_port* register. In case of the *GP* I<sup>2</sup>C bus, the target *AMC* is chosen with the *amc\_port* signal where the logical '0' ('1') selects the lower (upper) *AMC*. The I<sup>2</sup>C slave on the *AMC* is selected using the *slave\_addr\_port* register. For the possible slave addresses refer to [71], Appendix C. The I<sup>2</sup>C module acknowledges that the operation succeeded with the signal *ack\_port*. When reading, the requested data is then available at the *data\_port*.

## 4.4 SI chips

### *configuration memory registers*

**SI configuration / 0x000 .. 0x00b / 0x000 .. 0x02c** 45 1 B register, each *configuration memory* word contains 4 register. Refer to [80] for a description of the individual registers.

#### **SI phase configuration / 0x00c / 0x030**

bit(s)	ident	description
31	apply_phase	whether to apply the phase settings
30	lop_val	set loss-of-phase bit active low
29	mon_val	expected value for monitoring process
15 .. 8	n_coarse	coarse-steps
7 .. 0	n_fine	fine-steps

#### **SI sweep configuration / 0x00d / 0x034**

bit(s)	ident	description
31 .. 16	n_samples_sweep	number of samples to take at each step
15 .. 8	n_coarse_sweep	number of coarse-steps to process
0	no_wait_tcs	whether to skip waiting for TCS channel discovery (see also GANDALF-module status word 'tcs sync', Subsection 4.6.2). Needed when GANDALF-ADC is operated in an environment where no TCS information is encoded on the TCS clock.

Note: the GANDALF-ADC hosts three SI chips. To allow their individual configuration, each has its own space in the *configuration memory* using the following address offsets to be added to the above-stated addresses:

**0x080 / 0x200** for SI chip on upper mezzanine-card (SI<sub>A</sub>),

**0x180 / 0x600** for SI chip on upper mezzanine-card (SI<sub>B</sub>),

**0x280 / 0xA00** for SI chip on GANDALF-module (SI<sub>G</sub>).

However, the sweep configuration commonly stored in the GANDALF-module SI chip configuration block for all SI chips.

*fast-registers*

`fr_conf_si / 10 / 0x028` Trigger the SI configuration process.

`fr_sweep_si / 60 / 0x0F0` Trigger the SI sweep process.

`fr_phase_align_si / 61 / 0x0F4` Trigger the SI phase alignment process.

In this section, the mode of operation of the SI chip is described in a general way. The objective is to configure the SI chip and to have a deterministic phase between the clock outputs and the reference clock input. To interface the SI chips, the *SI* I<sup>2</sup>C bus is used as described in Section 4.3.

#### 4.4.1 Configuration

The SI chips are configured by sending a stream of configuration values via I<sup>2</sup>C when *fast-register* `fr_conf_si` is toggled. The configuration values are read from the *configuration memory*, where each SI chip has its own space. In the default configuration<sup>4</sup> a reference clock of  $f_{tcs} = 155.52$  MHz is assumed. The SI chip outputs can then be configured by means of a division and multiplication factor that is applied to the reference clock. The outputs of the GANDALF-module SI chip are configured as

$$\begin{aligned} f_{vxs} &= 466.56 \text{ MHz} = 3/1 \cdot f_{tcs} \quad \text{and} \\ f_{aurora} &= 77.76 \text{ MHz} = 1/2 \cdot f_{tcs} \end{aligned}$$

while the SI chips on the AMCs are configured to output

$$f_{adc} = 466.56 \text{ MHz} = 3/1 \cdot f_{tcs}$$

with a phase of  $\pi$  between the outputs. Appropriate values for the configuration registers for different clock setups can be obtained by using the SI chip configuration tool provided by the manufacturer [81].

#### 4.4.2 Phase alignment

Due to the fact that after loading the SI chip, the phase of the synthesized clock is at a random position with respect to the reference clock, a special phase alignment procedure is needed. It uses the possibility of the SI chip to move the phase by using coarse-steps with  $\sim 220$  ps and fine-steps with  $\sim 5$  ps, dividing the space between two coarse-steps into 44 segments<sup>5</sup>. The idea is to determine the phase of the synthesized clock to the reference clock as a function of SI chip steps. With the knowledge of this function, the phase can be set to a predefined value.

<sup>4</sup>The default configuration is stored in the *G\_PARAMETERS.vhd*, see project directory structure Appendix A.1

<sup>5</sup>The size of the fine-steps and the number of segments depends on the SI chip configuration and are reported by the SI chip configuration tool.

### Why is a deterministic phase important ?

**Clock domain crossing:** In the implementation step of hardware design, the router program is able to safely route signals from one clock domain into another only if the clocks are related. The relation exists if the one clock is replicated from the other one or if the designer specifies the relation<sup>6</sup>. The router is then able to consider these paths in the timing analysis and reports possible timing violations. In the *Xilinx* tools default configuration, signals crossing unrelated clock domains are not reported at all and are in many cases source for weird behavior of the logic. It is the designers own responsibility to take care of such clock domain crossings properly and best practice is to avoid them as far as possible, for instance by synchronizing the clocks and defining their relation.

**Sampling of source-synchronous signals:** Usually, when sampling a source-synchronous signal at the FPGA input, the phase between clock and signal has to be accounted for by using a calibration procedure. This calibration procedure either shifts the signal or (and) the clock. If the phase between clock and signal does not change after re-initialization of the electronics, the calibration values are static and have to be obtained only once.

**Time measurement:** Comparing the measured point in time of two devices that use a clock generated from a common reference clock is only meaningful when the phase of the generated clocks to each other is constant, *i.e.* the phase to the reference clock is constant. This phase has to be restored after re-initialization. The uncertainty of the method to restore the phase directly affects the accuracy of the time measurement.

The alignment of the synthesized clock to the reference clock can be measured with a flip-flop. The flip-flop is driven by the reference clock while the flip-flop data-in port is connected to the synthesized clock. Thus, the flip-flop can sweep the synthesized clock using the reference clock. The flip-flop data-out port represents the value of the synthesized clock sensed at the flip-flop input at the time of the clock transition of the reference clock. Depending on the current phase of the clocks, there are different outcomes for the flip-flop data-out value where in the extreme case the clock transition of the synthesized clock coincides with the flip-flop readout. The flip-flop, however, being a binary device, will only yield either one or zero. This means, that in this scenario, the flip-flop value is unstable when monitored over time. The window in which the flip-flop value is unstable is enhanced even more due to jitter of either clock. Moving away from this extreme position, the flip-flop value gets more stable. By monitoring the flip-flop value over a period of time for a specific phase setting, it is possible to discriminate stable areas from unstable areas.

---

<sup>6</sup>In particular, for two clocks that enter the FPGA, the designer has to specify the possible relation.

The procedure can be improved by using two flip-flops both wired similarly like above, as illustrated in Fig. 4.4. All in all, three outcomes for the values

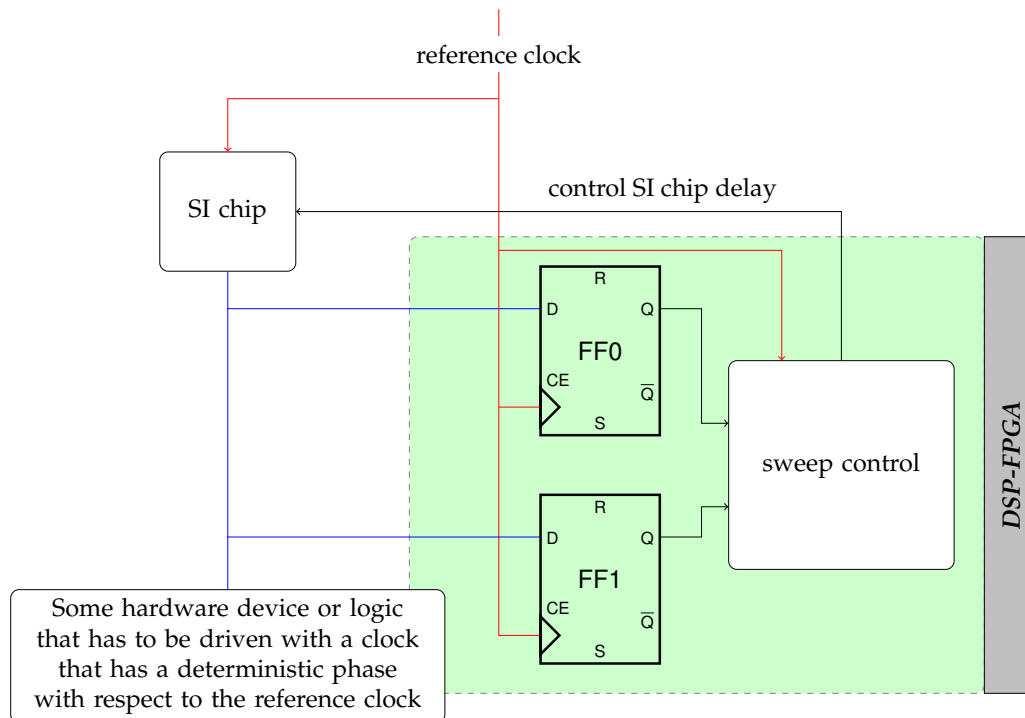


**FIGURE 4.4:** Schematic circuit used to sweep the synthesized clock of a SI chip. The SI chip generates the synthesized clock (blue lines) using the reference clock (red lines). The synthesized clock is routed in the FPGA to the data-in ports of two flip-flops. The flip-flops are driven by the reference clock. The sweep-control module monitors the flip-flop yields with respect to the reference clock and adjusts the phase of the SI chip. After the phase alignment procedure, the synthesized clock has a deterministic phase with respect to the reference clock.

sensed by the two flip-flops are now possible:

- both flip-flops read a logical zero ('00'),
- both flip-flops read a logical one ('11'),
- flip-flop values differ.

Even though the two flip-flops receive the same input, due to jitter and different clock and data paths inside the FPGA, the flip-flops tend to sense different values especially in the area where the transition of the synthesized clock coincides with the sampling of the flip-flops<sup>7</sup>. Counting the different outcomes over time as a function of the phase setting leads to a pattern such as shown in Fig. 4.5. The figure displays the data received on the CPU reading the *spy\_fifo*. For each SI chip fine-step, the phase alignment logic writes a header to identify the step followed by three words that contain the counts for the three outcomes, as illustrated in Table 4.1. The process is toggled using the *fast-register fr\_sweep\_si*.

<sup>7</sup>One flip-flop already sees the 'new' value, while the other still senses the 'previous' value.

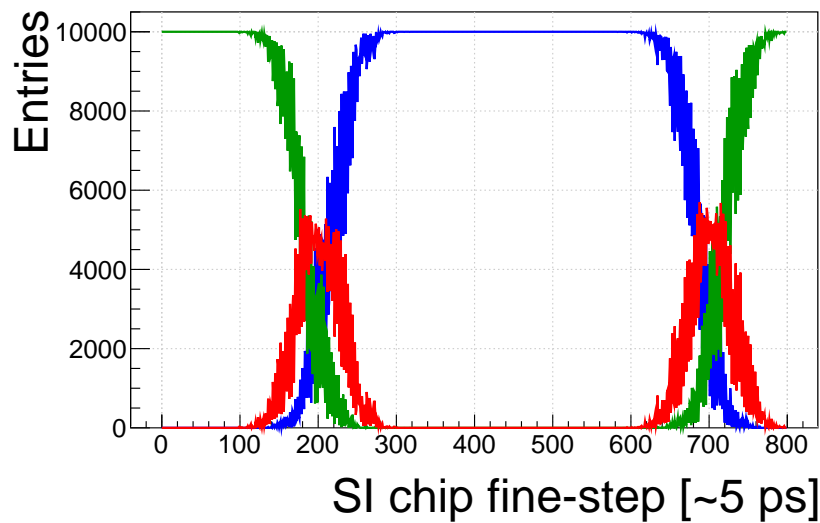


**FIGURE 4.5:** The yield of the flip-flops was monitored for ten thousand clock cycles of the reference clock for each phase setting before incrementing the phase setting by one fine-step. The blue (green) line represents the number of counts for '00' ('11'). The red line represents the number of counts where the flip-flop values differed. A clock transition from '0' -> '1' ('1' -> '0') is visible at a delay setting of 200 (700). Note, that even though the logic illustrated in Fig. 4.4 is fixed in the FPGA, the manifestation of this picture varies when building a new firmware. A build-by-build check of the sweep performance is therefore required.

With a program analyzing the measurement on a CPU, the precise delay setting of the clock transition of the synthesized clock can be determined and with this the mapping between delay setting to phase is found. The phase of the SI chip output can now be set by programming a specific delay setting in the *configuration register* 'SI phase configuration'. The settings are applied by using *fast-register fr\_phase\_align\_si*.

The position of an edge can be determined with an accuracy of  $\sim 3$  ps as also illustrated in Fig. 4.6. As stated earlier, the uncertainty of the phase alignment procedure directly affects the time measurement. With the presented method, an accuracy better than 9 ps is achieved for a single phase alignment. For most applications, such as the readout of scintillators with an inherent time resolution in the order of hundreds of picoseconds, this precision is well enough. A detailed description of the analyses, as well as comprehensive stability tests, are given in [31, p. 163].

TABLE 4.1: Data format used in the phase alignment procedure.

	bit(s)	ident	description
word0	31	mark	marks a header word
	30 .. 29	si_no	SI chip identification
	15 .. 8	i_coarse	current coarse-step
	7 .. 0	i_fine	current fine-step
word1	31 .. 16	-	-
	15 .. 0	n_differ	counts where flip-flops read different values
word2	31 .. 16	-	-
	15 .. 0	n_zero	counts where both flip-flops read a logical zero
word3	31 .. 16	-	-
	15 .. 0	n_one	counts where both flip-flops read a logical one

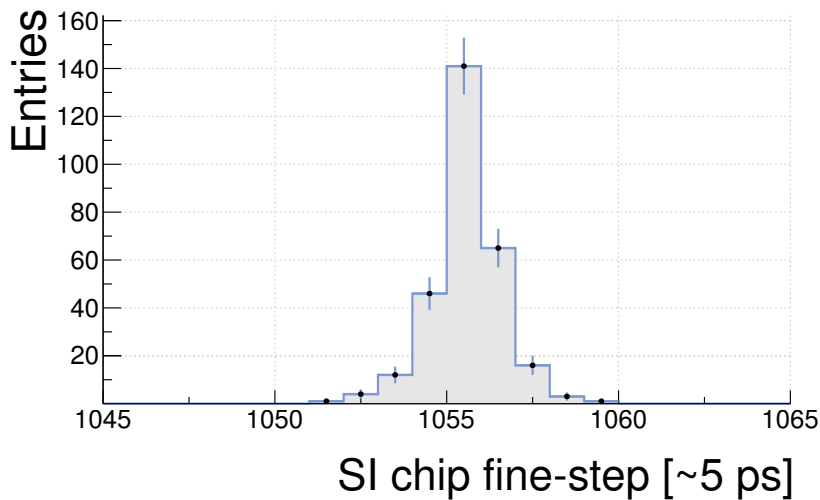


FIGURE 4.6: Resolution of the phase alignment procedure. For a few 100 phase alignment attempts, the difference of the positions for two succeeding rising edges is determined. The resolution is at the order of one SI chip fine-step. (adapted from [31, p. 168])

## 4.5 Clocking and clock distribution

For the operation of the GANDALF-ADC, different clocks are needed to drive specific components. The main clock of the DSP-FPGA is generated by an oscillator that is mounted on the GANDALF-module with  $f_{osc} = 40$  MHz. This clock is available without further configuration and is used for the start-up routine of the system and for the communication with the CPLD.

In addition, the GANDALF-module hosts a Si5326 clock multiplier chip ( $SI_G$ ) whose two outputs are connected to the DSP-FPGA. In the firmware, the outputs are used to generate the reference clock for the VXS DDR link<sup>8</sup> and to generate the clock for the aurora primitive. The reference clock for  $SI_G$  as well as for the clock multipliers on the AMCs is provided by a GIMLI mezzanine card. The GIMLI mezzanine socket is connected to a clock buffer which distributes the reference clock to the SI chips. The socket is also connected to the DSP-FPGA with two differential lanes. The reference clock, further referred to as  $tcs\_clk$ , is usually generated by an external source, such as the Trigger Control System (TCS). Using this clock ensures that all devices in the experiment are synchronous to each other and the comparison of timestamps between different modules is made possible. For this, derived clocks have to have a deterministic phase with respect to the  $tcs\_clk$ . In case of the SI chips this is achieved by a sweep procedure as described in the preceding Section 4.4.

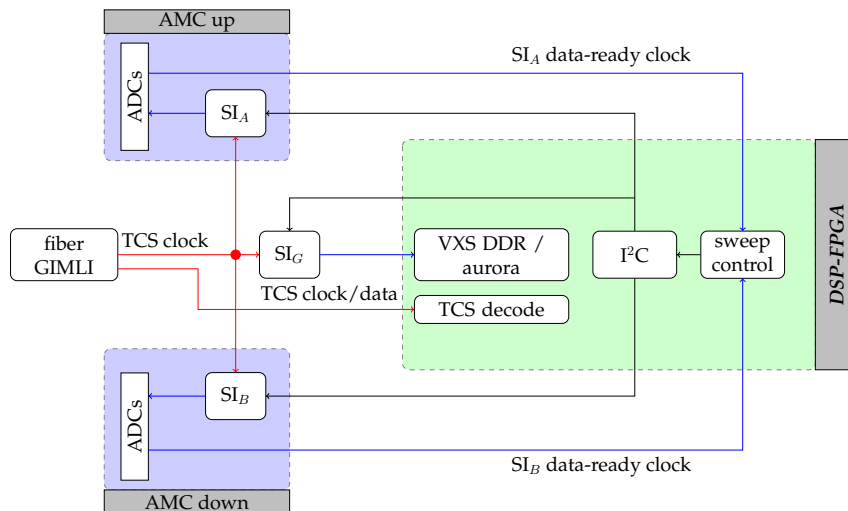
The  $tcs\_clk$  can enter the GANDALF-module through different routes and different GIMLI cards (Fig. 4.7) are used to deliver the reference clock to the SI chips. The DSP-FPGA firmware design has to adjust accordingly. From



FIGURE 4.7: GIMLI mezzanine cards used with the GANDALF-ADC. From left to right: Fiber GIMLI, copper GIMLI, VXS GIMLI.

FPGA view, *i.e.* electrical circuits, the different setups are not compatible with each other. Therefore, a generic switch allows executing the different design builds. The different clock circuits with different GIMLI cards are illustrated in Figures 4.8 to 4.10.

<sup>8</sup>For the operation of the VXS DDR link it is important that the operating clocks on both sides (GANDALF-module and TIGER-module) react very similar to jitter. It was found, that the most stable result is achieved when at the GANDALF-module end, the VXS DDR clock ( $f_{vxs}$ ) is generated directly by the SI chip as opposed to using a PLL inside the FPGA.



**FIGURE 4.8:** The fiber GIMLI offers an optical connection to the TCS fiber. A microprocessor is used to recover clock and data, which are then passed to the DSP-FPGA directly. Also, the recovered clock is sent to the clock buffer to serve as the reference clock for the clock multipliers.

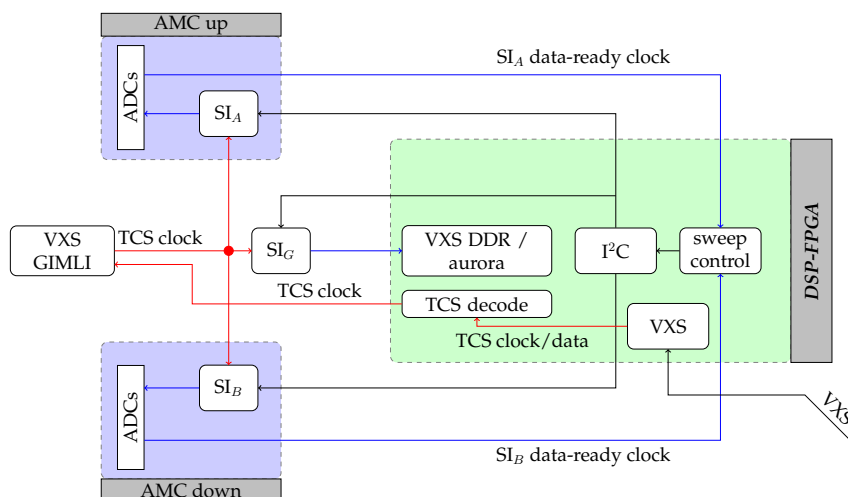


**FIGURE 4.9:** The VXs GIMLI is used together with a TIGER-module. The TIGER-module uses a fiber GIMLI to receive data and clock from the TCS and distributes the signal via the VXs-backplane directly to the DSP-FPGA. To deliver the reference clock to the SI chips, the VXs GIMLI receives the *tcs\_clk* from the DSP-FPGA and reroutes it to the clock buffer.

The usage of this technique simplifies the setup of the readout with multiple GANDALF-modules dramatically, since only one TCS fiber is needed.

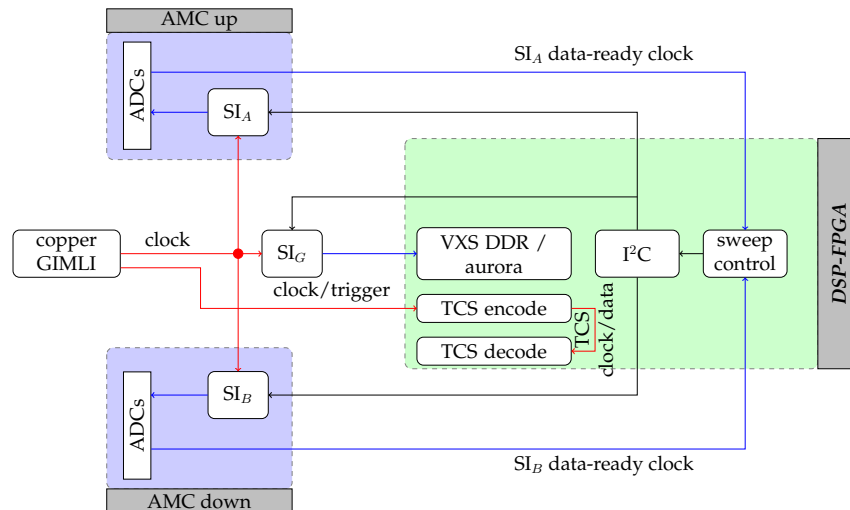


**FIGURE 4.10:** The copper GIMLI is used when the GANDALF-module is operated as an autonomous measuring device. The GIMLI hosts an oven controlled oscillator to generate a high quality, highly stable and low jitter clock with a frequency of  $f_{ocxo} = 20$  MHz. Again, the clock is distributed to the SI chips. A trigger may be connected to the second LEMO connector of the GIMLI and both trigger and data are routed to the DSP-FPGA.

Since in this setup no TCS information is available, the design uses a TCS encoder to generate valid TCS information from the trigger input. This information is then served to the TCS decoder so that most of the logic modules can remain unchanged. The TCS encoder is controlled using *fast-registers* to generate TCS commands such as Begin of Spill (BoS) or End of Spill (EoS), see Subsection 4.8.3.

A different clock may be used through a LEMO connector. In this case, the configuration of the SI chips has to be adapted to adjust for the changed reference clock frequency.

## 4.6 GANDALF-module configuration and monitoring

The CPLD mounted on the GANDALF-module is used to interface the FPGA. The CPLD itself can be interfaced via the VME-backplane or using the USB interface. A set of standard tools exist for seamless communication using either option. The tools allow to transmit the firmware to the FPGA, gain read/write access to the *configuration memory* (see Subsection 4.6.1) and to issue *fast-registers*.

In addition, the CPLD can read values off a special FIFO instantiated in the FPGA, the so-called *spy\_fifo*. This *spy\_fifo* can be used for data readout as described in Subsection 4.8.3 and is also used in the phase alignment procedure (Subsection 4.4.2).

### 4.6.1 Configuration memory

The *configuration memory* is a dedicated BRAM block in the DSP-FPGA. It is used to store run-time configuration settings. One of its two ports is connected to the CPLD logic to allow the CPLD priority access to the *configuration memory*.

In the FPGA, different modules need access to the *configuration memory*. In order to grant access to the BRAM in an ordered and controlled way and to omit problems due to concurrent access, the modules are connected to the second port of the *configuration memory* as wishbone slaves. The implementation is based on a logic module published on opencores [82]. The access to the *configuration memory* from within a particular module is then possible using very simple state machines, see Fig. 4.11. Note the similarity to operating the I<sup>2</sup>C bus illustrated in Fig. 4.3. A great portion of the GANDALF-ADC logic consists of a concatenation of these two kinds of state machines.

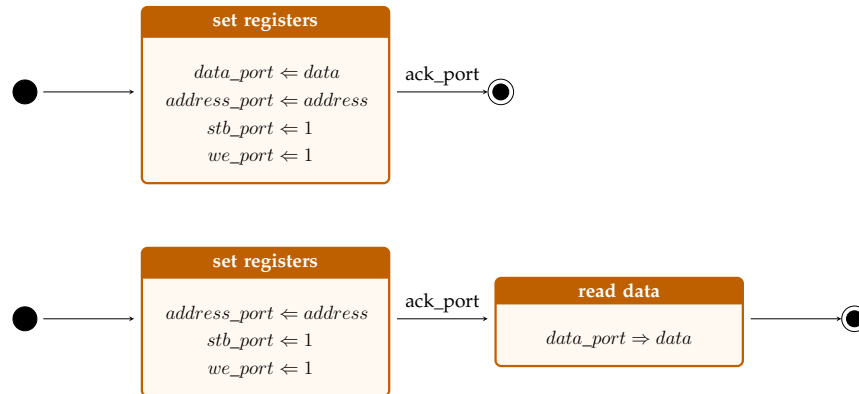


**FIGURE 4.11:** State machine for writing (top) and reading (bottom) from the *configuration memory*. Input/Output signals of the *configuration memory* module are indicated by the suffix '*\_port*'. The *set registers* state is used to setup the input signals of the *configuration memory* module for the specific operation. The *stb\_port* signal is used to notify the module that the user wants to perform an operation. The *we\_port* signal determines if the operation is a read or a write operation to (from) the address *addr\_port*. The I<sup>2</sup>C module acknowledges that the operation succeeded with the signal *ack\_port*. When reading, the requested data is then available at the *data\_port*.

### 4.6.2 Status and general purpose (GP) interface

#### configuration memory registers

##### GANDALF-module status word / 0x203 / 0x80c

bit(s)	ident	description
31 .. 24	header	fixed to 0xdf
22	vccaux alarm	$V_{CCAUX}$ - sensor alarm output
21	vccint alarm	$V_{CCINT}$ - sensor alarm output
20	temp alarm	SysMon temperature - sensor alarm output
18	bit_err	alert on <i>bit-error</i> in the sampling of ADC bits
17	flt_err	alert on unexpected FLT
16	ev_num_err	alert on unexpected event number
15	readout not ready	no endpoint for processed data set
14	link full flag	overfull buffers in readout
13	tcs sync	synchronized TCS channels, signaled by TCS interface
12	tcs lock	lock to TCS system acquired, signaled by the GIMLI
10	SI <sub>A</sub> lop	phase to TCS clock not set
9	SI <sub>A</sub> lol	SI chip loss-of-lock
8	SI <sub>A</sub> los	SI chip loss-of-signal
6 .. 4	SI <sub>B</sub> status	analog to SI <sub>A</sub>
2 .. 0	SI <sub>G</sub> status	analog to SI <sub>A</sub>

##### AMC up info / 0x000 / 0x000

bit(s)	ident	description
15 .. 12	type	AMC type
11 .. 0	sn	AMC serial number

**AMC up temperature / 0x010 / 0x040** temperature reading of TMP175 sensor

**AMC down info / 0x100 / 0x400** see AMC up info

**AMC down temperature / 0x110 / 0x440** see AMC up temperature

**DSP-FPGA info / 0x200 / 0x800** see [63, p. 181]

**DSP-FPGA temperature / 0x210 / 0x840** temperature reading of the System Monitor

**DSP-FPGA  $V_{CCAUX}$  / 0x218 / 0x860** reading of the System Monitor

**DSP-FPGA  $V_{CCINT}$  / 0x220 / 0x880** reading of the System Monitor

*fast-registers*

**fr\_update\_temps / 4 / 0x010** Read temperature information and write to *configuration memory*.

**fr\_write\_status / 22 / 0x058** Read status information and write to *configuration memory*.

**fr\_init\_gp / 44 / 0x0B0** initialize the *GP* interface

The status interface offers a simple way to retrieve general information about the state of the GANDALF-module. The FPGA System Monitor ([83]) is instantiated here as well. Its status registers are readout on using the *fast-register* *fr\_write\_status* and the values are stored in the *configuration memory*. In addition, the *GP* interface offers an ADC specific status word that can be requested using *fast-register* *fr\_update\_temps*. The *GP* interface also handles the communication between DACs and *configuration memory* for the AMC baseline configuration (Subsection 4.7.3).

For information on the interpretation of the temperature and voltage readings refer to [63, p. 64].

## 4.7 Treatment of ADC

Each ADC of an AMC is connected to the FPGA via 14 differential data lanes and one data-ready lane<sup>9</sup>. For a time measurement, it is crucial that the phase of the SI chip with respect to the input clock is constant. Therefore, the technique described in Subsection 4.4.2 is applied for the SI chip on each mezzanine card. The particularities are described in the following section.

### 4.7.1 ADC clock distribution

The ADCs sampling clock is generated by the SI chip located on the AMC. As outlined in Subsection 4.4.2, the phase of the clock generated by the SI chip can be measured using two flip-flops and the reference clock. In case of the AMC cards, however, the generated clocks of the SI chip are not directly accessible by the DSP-FPGA and the data-ready signal of the ADCs is used as a substitute. The data-ready signal indicates, that the ADC has finished the digitization of the input in the current clock cycle and that the data bits are valid. Since the ADCs sends the data with DDR, the data-ready clock frequency amounts to half the clock frequency generated by the SI chip, *i.e.*

$$f_{amc} = f_{adc}/2 = 233.28 \text{ MHz.}$$

The next subsection describes the processing of the ADC data bits and the data-ready signals in the DSP-FPGA.

<sup>9</sup>The ADS5463 ADCs only use 12 data lanes. However, it is foreseen to solder different yet pin compatible ADCs which use all data lanes.

## 4.7.2 ADC bit sampling and bit error monitoring

### *configuration memory registers*

**AMC delay setting / 0x0c0 .. 0x0ce / 0x300 .. 0x338** Forms a table of ADC bits, whose IODelays are incremented when `fr_read_gta_delay` is toggled. The IODelay is selected by ADC number and *bit* number. The memory address selects the *bit* number while the data word selects the ADC number. The upper (lower) 16 bit of the data word control the *CE (INC)* port of the IODelay. Multiple bits can be enabled at once.

For example, to activate bit2 of ADC5 and ADC8 the following address and data word is used: *vhdl\_address* = 0x0c2, *data* = 0x01200120.

**AMC edge status / 0x264 .. 0x274 / 0x990 .. 0x9d0** 16 words with *bit-error* status for ADCs starting from ADC0; the lower 12 bit of the word contains the *bit-error* status for the 12 ADC bits where a high bit indicates a *bit-error*.

### *fast-registers*

**fr\_clear\_biterr\_flag / 31 / 0x07C** Reset edge status of ADC bits.

**fr\_read\_gta\_delay / 51 / 0x0CC** Increment the IODelays as specified in *configuration register* 'AMC delay setting'.

**fr\_read\_adc\_edge\_info / 52 / 0x0D0** Write the *configuration register* AMC edge status.

Each differential data lane of the ADC enters the FPGA through a DDR input buffer. The current value of the signal is evaluated by a clock that drives the DDR input buffer. This clock has to be in phase to the clock that generates the data. Therefore, the data-ready signal is used to drive the buffers and the forthcoming logic, where the signal yields are processed. Since the phase of  $SI_A$  and  $SI_B$  has been adjusted (Subsection 4.7.1), both data-ready signals are also in phase with respect to each other. Thus, one may decide to use the one or the other to sample all ADC bits.

Due to differences in the lane length of the data signals, the timing of the data signals has to be adjusted. For this, each input buffer is appended with an IODelay component, as illustrated in Fig. 4.12. With this, the data signal can be moved in time such that the signal is aligned correctly with respect to the sampling clock. The delay setting has to be found for each IODelay component of each data lane individually. Again, the values of two flip-flops sampling the data signal are used to find the correct position as depicted in Fig. 4.12. However, since the phases of the data signals with respect to the data-ready signal are fixed, this procedure has to be performed only once in order to find the constant delay settings. In first order, the delay constants also do not depend on GANDALF-module or AMC.

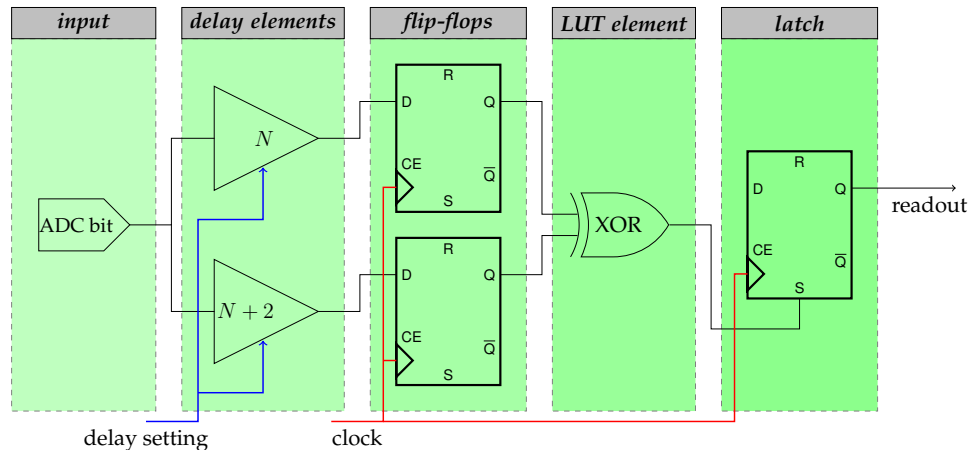


**FIGURE 4.12:** Circuitry for the edge detection. The setting for the delay elements differs by two steps, which results in a delay of the signal by 148 ps between the outputs of the delay elements. This window can be moved by incrementing  $N$ . When the edge of the ADC bit falls into the window, the inputs of the two flip-flops differ and the XOR-gate switches to logic one. The following RS-flip-flop is set to logic one and keeps the value until it is reset. In normal operation,  $N$  is determined such that the edge of the ADC bit never falls into the window. If the RS-flip-flop ever yields logic one, a bit error occurred and an error signal is issued. (adapted from [84])

It is also worth noting that opposed to the phase alignment of the SI chip, these delay settings have no influence on the time measurement. The only consequence of a bad delay setting is a possible wrong sampling of the bit leading to *bit-errors* on the specific channel. At first order, the quality of the sampling can be monitored with the circuit illustrated in Fig. 4.12. After calibration, the two flip-flops should always read the same value. In case they do not, the 'bit\_err' flag in the GANDALF-module status word is raised. The calibration procedure of the IODelay values for the ADC bits is described in detail in [84]<sup>10</sup>.

The ADC data bits are grouped according to their channel source to form the digitized voltage bit vectors. Since the input buffers are DDR and the AMC input of one channel is stripped to two ADCs, at each clock cycle, four digitized voltage values are present. They are stored in shift registers for immediate processing and stored additionally into a ring buffer for later processing, see Subsection 4.7.4.

<sup>10</sup> The proposed implementation in [84] uses  $SI_G$  for the sampling of the ADC bits. This is a valid option when the phase alignment procedure for this SI chip is performed, *i.e.* it is synchronous to the SI chips on the AMCs respectively synchronous to the ADC sampling clock. The clock output of  $SI_G$ , however, has to be connected to the VXS DDR link logic directly and is not available anymore. Despite the concerns in [84], the data-ready signal is used for the sampling of the ADC bits as described in the text, so far without any issues.

### 4.7.3 Baseline adjustment

#### *configuration memory registers*

**AMC up baseline / 0x030 .. 0x033 / 0x0c0 .. 0x0cc** Eight 16 bit words representing the DAC offset values for ADC0 to ADC7.

**AMC down baseline / 0x130 .. 0x133 / 0x4c0 .. 0x4cc** See 'AMC up baseline'.

#### *fast-registers*

**fr\_read\_eeprom / 8 / 0x020** Mirror data from EEPROM to *configuration memory*.

**fr\_write\_eeprom / 9 / 0x024** Mirror data from *configuration memory* to EEPROM.

**fr\_set\_dacs / 11 / 0x02C** Read values from *configuration memory* and program DACs.

An offset voltage  $V_{off}$  can be added to each ADC input. It is used to move the input signal into an optimal window for the ADC operation or to equalize the baseline between different ADC channels, respectively. The voltage can be controlled by a DAC that is connected to the I<sup>2</sup>C bus, see also Fig. 4.2. Using *fast-register fr\_set\_dacs*, the GP interface reads the offset values from the *configuration memory* and sends them to the corresponding DAC. Since the DAC values are bound to an AMC and the values are constant over long periods, the baseline values are stored in the AMCs EEPROM. Thus, the DAC values are persistent without powering the module and it is also easy to mount the card on another GANDALF-module without the need of reevaluating the DAC values. The GP interface can be instructed to transmit the values from the EEPROM to the *configuration memory* and vice versa using *fast-register fr\_read\_eeprom* and *fast-register fr\_write\_eeprom*.

#### 4.7.4 Signal processing and event packaging

##### *configuration memory registers*

###### **src\_id / 0x201 / 0x804**

bit(s)	ident	description
9 .. 0	src_id	source ID inserted into S-LINK header [85]

###### **data processing configuration 1 / 0x234 / 0x8d0**

bit(s)	ident	description
19 .. 12	prescaler	scaling factor for the output of debug events
10 .. 0	baseline	online subtraction of baseline

###### **data processing configuration 2 / 0x2c0 / 0xb00**

bit(s)	ident	description
31 .. 16	framewidth	number of samples to process
15 .. 0	latency	latency (in number of samples) for processing of stored samples

###### **CFD configuration / 0x2c5 / 0xb14**

bit(s)	ident	description
23 .. 16	threshold	threshold
12 .. 8	delay	delay
5 .. 0	frac	fraction factor

###### **streaming CFD configuration / 0x340 / 0xd00**

bit(s)	ident	description
28 .. 16	t_threshold	threshold
12 .. 8	t_delay	delay (not used)
5 .. 0	t_frac	fraction factor (not used)

##### *fast-registers*

**fr\_read\_gta\_conf / 13 / 0x034** Read configuration values from *configuration memory* and write into registers.

**fr\_ct\_bos\_reset / 23 / 0x05C** Reset coarse time on next begin-of-spill.

After the ADC bits have been sampled in the FPGA, the AMC interface is in charge of further processing the ADC values. For this, the AMC interface features two implementations of the constant fraction discriminator (CFD) algorithm for the extraction of pulse features from the sampled data. They were designed and described by [72]. One version of the CFD algorithm is

applied in a streaming manner on the samples. It offers a fixed latency and hands over the extracted pulse features to the VXS DDR link communication interface, see also Subsection 4.8.2 and [67, 72] for details on the implementation and data format definition. The second version of the CFD algorithm operates on the samples stored in the BRAM ring buffer. It is only executed when a trigger from the TCS is received and extracts pulse features from a window with specified length and latency. The parameters for both algorithms are stored in the *configuration memory* and applied by using *fast-register fr\_read\_gta\_conf*. A detailed description of the data processing is given in [72, p. 96].

The extracted pulse features are then further processed in the event packaging logic, see Fig. 4.13. The process starts when the TCS module has decoded the event info, which is then read from the TCS FIFO. If the event number from TCS is not equal to the increment of the last event number, the 'ev\_num\_err' flag in the GANDALF-module status word is raised. The process reads the information of each channel and merges the data into a S-LINK formatted package. For begin/end of spill/run events, the package consists only of headers<sup>11</sup>. The logic can only process one event at a time. If yet another FLT arrives and the process is still active, the 'flt\_err' flag in the GANDALF-module status word is raised. When the process is finished, the packaged event data are further processed by the readout logic. The operation of the process is blocked, when 'flt\_err' or 'ev\_num\_err' are raised or when no endpoint for the data is set in the readout logic. In the latter case, 'flt\_err' and 'ev\_num\_err' are cleared.

## 4.8 Readout

### *fast-registers*

**fr\_out\_vme / 70 / 0x118** Send data via VME.

**fr\_out\_vxs / 71 / 0x11C** Send data via VXS SDR.

**fr\_out\_cpld / 72 / 0x120** Send data via CPLD.

The GANDALF-ADC firmware offers different ways to dispose of the data. These are using a drain card plugged into the VME-backplane (Subsection 4.8.1), utilizing the connection to the switch ports by the VXS-backplane (Subsection 4.8.2) and finally using the GANDALF-modules CPLD (Subsection 4.8.3). While currently not used, in future applications the MEM-FPGA can be included in the data path to be able to buffer a significant amount of data (Subsection 4.8.4).

<sup>11</sup> These events are not physics events anyways. Also, sending large end of spill events triggered a DAQ bug where a reset signal sent from the TCS controller after each spill did not respect the DAQ timeouts. It may happen, that the DAQ is still busy processing the last event of the spill and the reset is received. The DAQ truncates the event and ends up in a broken state from which it does not recover. Only sending headers for the end of spill events is an effective workaround.

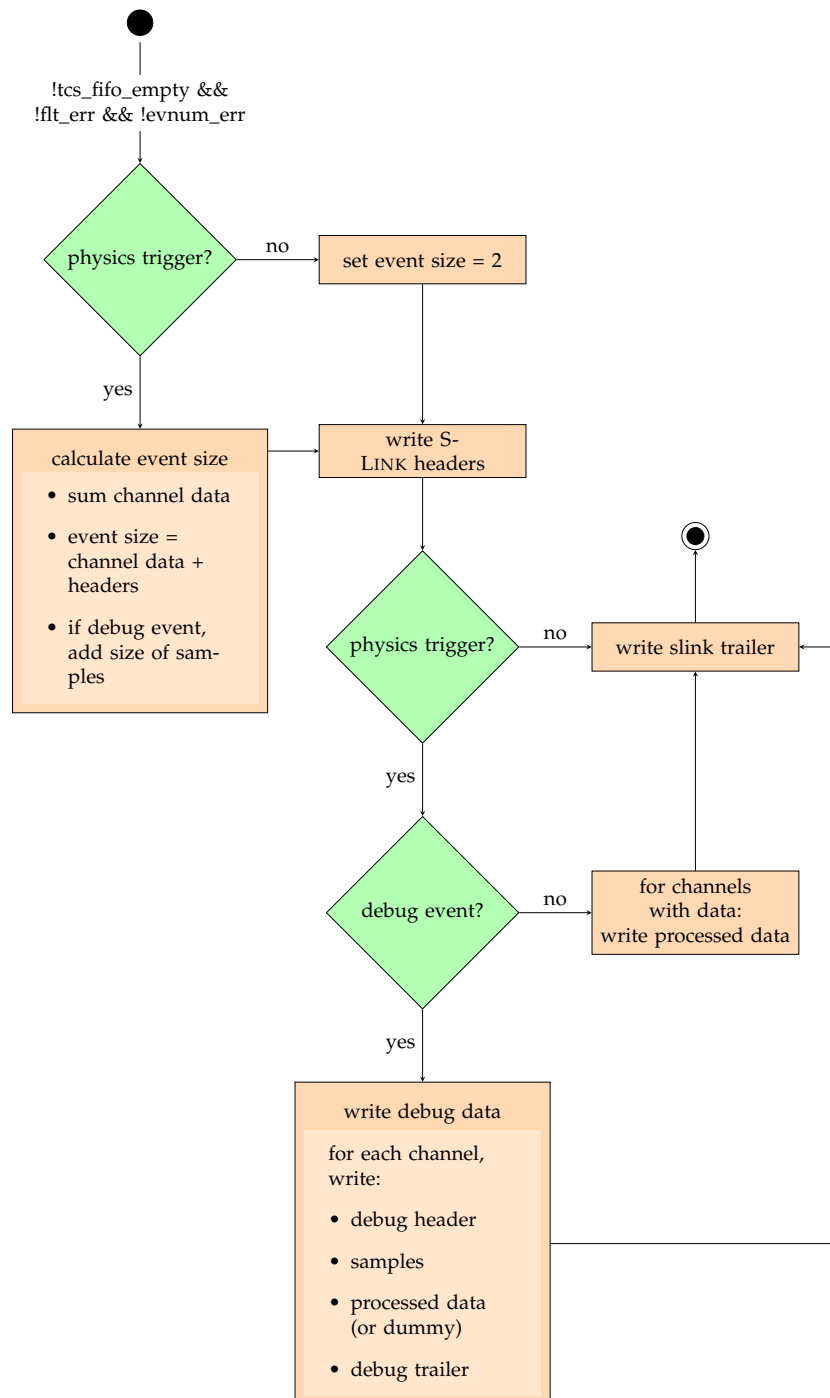


**FIGURE 4.13:** State machine used to collect the pulse features extracted for each channel and pack them into an S-LINK event. The destination for the data is a FIFO in the *data out* module. The *data out* module then directs the data to a specific endpoint, see also Section 4.8.

While the pulse features extracted with the streaming CFD are currently only transmitted via the VXS connection, the destination for the packaged event data can be selected by using *fast-register* *fr\_out\_vme*, *fr\_out\_vxs* and *fr\_out\_cpld*. The option to send the data to the CPLD can be enabled in conjunction with the other destinations. With this, it is possible to spy into the data stream while the flow control remains by the primary data path.

#### 4.8.1 Readout via VME-backplane using S-LINK source card

By using a S-LINK drain card plugged into the VME-backplane, the processed event data can be send to a DAQ via optical fiber. The S-LINK protocol offers a technical data rate of  $1280 \text{ Mbit s}^{-1}$ , the effective data rate is approximately  $700 \text{ Mbit s}^{-1}$ .

#### 4.8.2 Readout via VXS-backplane

##### *fast-registers*

**fr\_readouttigerready / 41 / 0x0 A4** Report module active to TIGER in readout slot

**fr\_triggertigerready / 42 / 0x0 A8** Report module active to TIGER in trigger slot

**fr\_startvxslinkcal / 43 / 0x0 AC** Trigger the calibration process for the VXS DDR link

The VXS connectors offer eight bidirectional differential lanes to each TIGER-module. Two data link implementations exist to transmit data. A simple single data rate link is used to send the packaged event data to the readout TIGER-module. It uses one lane to transmit a clock, one lane as a data enable, and three lanes for data. A data rate of  $466.56 \text{ Mbit s}^{-1}$  is available [86].

To send data to the trigger TIGER-module, a DDR data link was developed by [67]. Each VXS lane is used to transmit the extracted pulse features of one GANDALF-ADC readout channel with a data rate of  $1 \text{ Gbit s}^{-1}$ .

For both links, the GANDALF-modules need to report to the TIGER-module that they are alive by raising *fast-register* *fr\_readouttigerready* respectively *fast-register* *fr\_triggertigerready*. In addition, the VXS DDR link requires a calibration procedure to be executed by toggling *fast-register* *fr\_startvxslinkcal*.

### 4.8.3 Readout via VME-CPU or USB

#### *fast-registers*

- fr\_self\_triggered / 15 / 0x03C** Whether the GANDALF-ADC should trigger itself (not implemented).
- fr\_bor / 16 / 0x040** Signal TCS controller to create a new run.
- fr\_bos / 17 / 0x044** Signal TCS controller to create a new spill.
- fr\_eos / 18 / 0x048** Signal TCS controller to stop the current spill.
- fr\_trg / 19 / 0x04C** Signal TCS controller to create an artificial trigger.

The CPLD can be instructed to read data out of a special FIFO, called *spy\_fifo*, instantiated in the DSP-FPGA firmware. Depending on application of the board, the CPLD can direct the data either to the USB chip or to the VME-backplane. This enables the acquisition of data using the VME-CPU or a PC connected to the USB port of the GANDALF-module. The achievable effective data rate is limited to approx  $160 \text{ Mbit s}^{-1}$ . During the setup procedure of the module, the *spy\_fifo* is used to set the baseline and to store the sweep measurement. After the setup procedure, the *spy\_fifo* can be used to either readout all packaged event data or spy into the data stream of the VXS or VME readout.

Using the readout via CPLD together with the copper GIMLI, the GANDALF-ADC can be used as a standalone data acquisition tool. Since in this configuration no TCS is present, a TCS controller module is used in the firmware. It can be controlled via the *fast-registers* listed above. The processed event data are then stored in the *spy\_fifo* and therefore available for readout via USB or VME-CPU.

### 4.8.4 Including the MEM-FPGA

The GANDALF-module hosts a second FPGA called MEM-FPGA, which can be used to interface 144 Mbit of QDR memory and 4 Gbit of DDR memory. In future applications of the GANDALF-module, the speed of the data links or the processing at the receiving end may be too slow. For example, scenarios exist, where large amounts of data is collected in a short time frame, but the time between triggers is large. The data may then be stored on the GANDALF-module and slowly disposed to the DAQ in between triggers. A recent development will allow to implement such scenarios by utilizing the aurora link to send data with up to  $25 \text{ Gbit s}^{-1}$  from the DSP-FPGA to the MEM-FPGA, store the data in the QDR- and DDR-RAM modules, and send the data back to the DSP-FPGA to dispose of the data via the before mentioned data paths [87].

## 4.9 Testbench

In contrast to software programming, the development and debugging process using a hardware description language renders more difficult, since it is not possible to quickly compile and run the code. Creating the firmware usually takes in the order of hours and there is no debugger and no stacktrace available to pin down errors in the “deployed” code. The firmware behaves more like a black box. Only by probing the device with specific input and monitoring the reaction of the output one may infer the location of an error. A more straightforward way for debugging and testing is to simulate the logic using a testbench. The testbench itself is realized as a VHDL logic module. Its purpose is to serve as an environment, where the logic module under test is placed and stimulated with inputs. For the simulation, some extensions to the VHDL vocabulary exist which are not synthesizable into logic but help to create stimuli, for instance random number generators. To execute the simulation of the design, *ModelSim*<sup>12</sup> is used. Prior to the simulation, *ModelSim* compiles the VHDL code and reports syntactical errors.

The simulation evaluates the logical circuit for a certain amount of time and the evolution of the signals can be examined. It is possible to stop and resume the simulation and to interact with the design in order to force the state of a specific logic element.

In VHDL programming, it is best practice to write a testbench for each logic module to ensure its functionality. It is also easier to generate and verify meaningful stimuli when penetrating an isolated module directly.

Still, to verify the design start-up and the overall functionality of the design, the *oplevel*-module needs to be simulated. Also, to test the behavior of the logic with different hardware configurations and to test the communication between the hardware entities of a GANDALF-module, a GANDALF-module *oplevel*-simulation-module is used. The GANDALF-ADC *oplevel*-simulation-

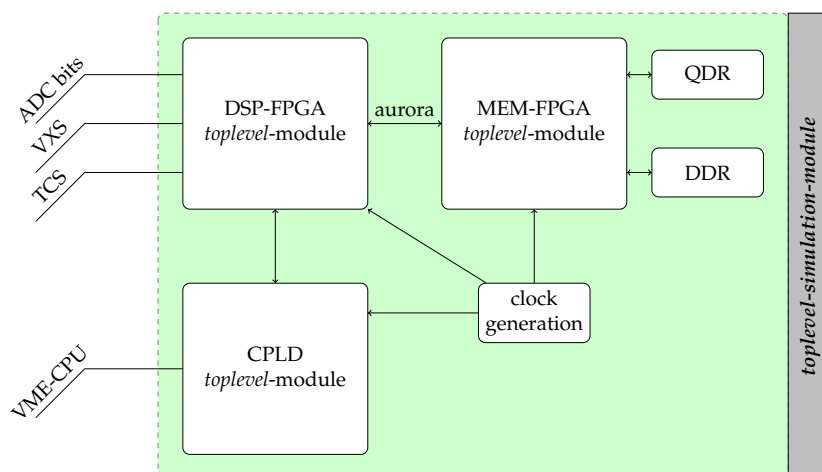


FIGURE 4.14: Overview of the *oplevel*-simulation-module.

module, illustrated in Fig. 4.14, embeds the two GANDALF-module FPGA

<sup>12</sup>Mentor *ModelSim* SE 10.1c

firmware designs as well as the CPLD firmware design and their interconnections. It also includes simulation models for the QDR and DDR memory. The *toplevel-simulation-module* therefore is able to entirely mimic a GANDALF-ADC so that it can be stimulated in the same way as it would be stimulated in reality. Like the inputs/outputs of the *toplevel-module* correspond to the pins of the DSP-FPGA, the inputs/outputs of the *toplevel-simulation-module* correspond to the inputs/outputs of the GANDALF-module, such as the VME and VXS pins or the pins of the mezzanine sockets.

Currently, a testbench is utilized which simulates the application of the GANDALF-module in the COMPASS environment, *i.e.* the module is “put into a VME crate” and has TCS available. The testbench uses a TCS encoder module to generate the TCS clock including the modulated TCS data which is served to the input of the *toplevel-simulation-module*. For the interaction with the simulated GANDALF-module, the usual *vme\_write* command is available from the *ModelSim* console. The testbench allows for instance to verify the start-up behavior, the communication with the VME-CPU and the processing and decoding of the TCS signal.

Using *ModelSim*, the testbench for the GANDALF-ADC is controlled by a few files, where the starting point is the *testbench.fdo*, see Appendix A.2. It can be called in the *ModelSim* console with the command *do*, which processes the file line-by-line.

For the verification of the CAMERA readout, a very sophisticated simulation of the GANDALF-framework exists. It includes two GANDALF-ADC *toplevel-simulation-modules* and two TIGER *toplevel-simulation-modules*<sup>13</sup>, connected by a simulation of the VXS bus fabric. The GANDALF-ADCs read the simulated signals of four scintillators of the inner respectively outer ring. For this, the testbench creates random pulses. They are discretized in time and amplitude and used to drive the GANDALF-ADC mezzanine signals. The TIGER-modules are configured as trigger respectively readout concentrator. Thereby, it is possible to monitor and verify the entire data processing path:

1. Starting from the streaming pulse feature extraction logic implemented in the GANDALF-module,
2. the transmission of the pulse features to the TIGER trigger module using the VXS DDR link,
3. the processing of the pulse features in the trigger coincidence logic,
4. the generation and release of a trigger by the TIGER trigger module,
5. the receiving of the trigger by the GANDALF-module and initiating the processing of the buffered data,

---

<sup>13</sup>For the TIGER-module, there exists as well a simulation module containing its relevant hardware entities. The TIGER-module *toplevel-module* is described in [64, p. 105] while information on the *toplevel-simulation-module* can be obtained from [65, 67].

6. the packaging of the event according to the COMPASS data format specifications, ([85])
7. the transmission of the event to the DAQ.



## 5 CAMERA calibration and commissioning

The Apparatus for Measurement of Exclusive ReActions (CAMERA) was already introduced in Subsection 3.3.2. It consists of two nested barrels with a diameter of  $r_A = 25$  cm and  $r_B = 110$  cm respectively, see also Fig. 5.1. Each barrel is built from 24 scintillators that are  $w_A = 6.55$  cm and  $w_B = 29.65$  cm wide. The scintillators are readout on the up- and downstream side using

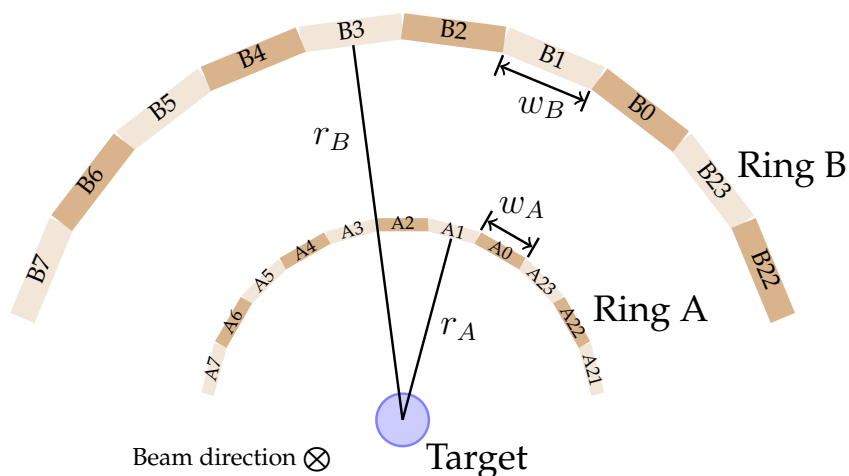


**FIGURE 5.1:** Schematic front view of a segment of the CAMERA detector. The full detector continues in a circular shape.

photomultipliers. The construction is placed alongside surrounding the target allowing for full azimuthal angular coverage. The azimuthal resolution is enhanced by rotating the inner barrel by half a segment with respect to the outer barrel. To enhance the polar angular acceptance, the detector covers more than the full length of the target, with a length of 275 cm (360 cm) for the inner (outer) scintillators. The diameter of the barrels is chosen with regards on the requirements for the particle time-of-flight measurement. The track of particles can be reconstructed by combining hits in segments of the barrels so that the track direction points to the target. The scintillators of the inner barrel are very thin (4 mm) to optimize proton acceptance with kinetic energies down to 35 MeV/c. Particle identification can be achieved through the characteristic energy loss of the particles when they pierce through the scintillators. For this, the light output produced by the particles is determined by employing GANDALF-ADCs.

A laser system, inducing light in the middle of each scintillator, is used to calibrate and monitor the voltage settings of the photomultipliers.

## 5.1 Concepts

Denoting  $t_{up}$  ( $t_{dn}$ ) the time of the pulse at the upstream (downstream) photomultiplier, the longitudinal position  $z$  and the timestamp  $t$  of a hit are given by

$$\begin{aligned} z &= \frac{1}{2} \cdot c_{eff} \cdot (t_{up} - t_{dn}) + k_z, \\ t &= \frac{t_{up} + t_{dn}}{2}, \end{aligned} \quad (5.1)$$

with  $c_{eff}$  the effective speed-of-light in the scintillator. The calibration constant  $k_z$  ensures the correct longitudinal position of the scintillator with respect to the COMPASS coordinate system. Together with  $c_{eff}$ ,  $k_z$  has to be determined for each counter individually.

When a charged particle traverses the inner and the outer counters, Eq. 5.1 can be calculated for both scintillators, yielding the longitudinal positions and timestamps in the inner (outer) scintillator  $z_A$  ( $z_B$ ) and  $t_A$  ( $t_B$ ). Hence, the time-of-flight (ToF),  $t_{ToF}$ , the corresponding distance-of-flight (DoF),  $s_{DoF}$ , and the scattering angle  $\theta$  (see Fig. 5.2) are given as:

$$\begin{aligned} t_{ToF} &= t_A - t_B + k_t, \\ s_{DoF} &= \sqrt{(z_B^2 - z_A^2) + d^2}, \\ \theta &= \arccos\left(\frac{z_A + z_B}{s_{DoF}}\right). \end{aligned} \quad (5.2)$$

The quantity  $d$  denotes the difference between the radii of the inner and outer ring and  $k_t$  a calibration constant. With the assumption that the charged particle was a proton, the raw fractional velocity  $\beta_{raw}$  and the raw momentum  $p_{raw}$  are given by

$$\begin{aligned} \beta_{raw} &= \frac{s_{DoF}}{c \cdot t_{ToF}}, \\ p_{raw} &= \frac{m_p \cdot \beta_{raw}}{\sqrt{1 - \beta_{raw}^2}}, \end{aligned} \quad (5.3)$$

using the speed-of-light in vacuum  $c$  and the mass of the proton  $m_p$ . The particle energy loss along the track due to the material is added to the raw quantities to end up with quantities at the interaction vertex. For this, the calculations from [88] are used. The azimuthal angle results from the mean of the azimuthal position of the involved counters. Hence, the theoretical azimuthal resolution of the detector results to  $7.5^\circ$ .

The procedure to obtain the calibration constants  $c_{eff}$ ,  $k_z$  and  $k_t$  for the 2012 DVCS pilot run is outlined in Section 5.2. There, a precise calibration of the detector using physics events is performed. For commissioning and monitoring however, less precise but faster calibration methods are needed. For the first adjustment of the gain factors of the photomultipliers, a pion beam

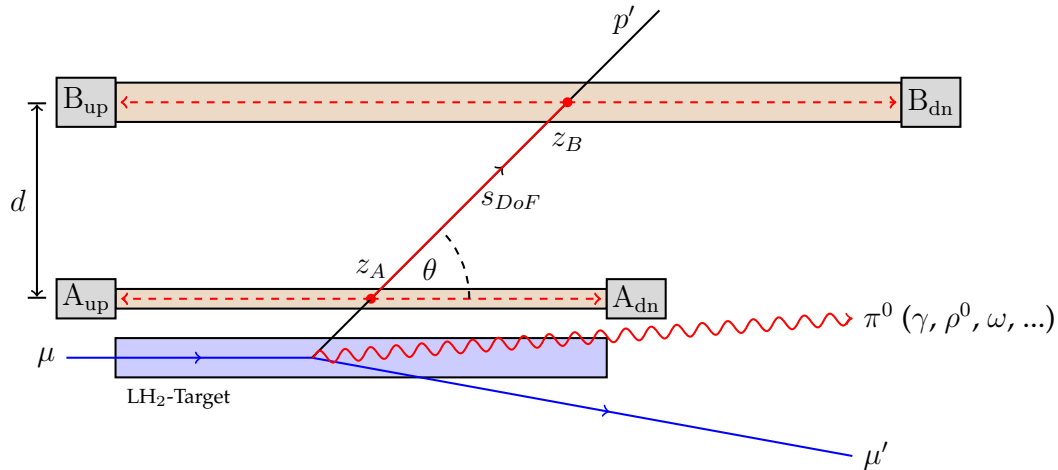


**FIGURE 5.2:** Schematic side view of the CAMERA detector and the target displaying the principle of the ToF measurement of recoiling protons in exclusive reactions. The incoming muon  $\mu$  scatters off a target proton. The light in the scintillators produced by the recoiled proton  $p'$  is detected by the photomultipliers  $A_{up}$ ,  $A_{dn}$  and  $B_{up}$ ,  $B_{dn}$ . The scattered lepton  $\mu'$  and in this case the  $\pi^0$  are detected in the COMPASS spectrometer.

is used. The advantage of the pion beam is a very high rate of elastically scattered protons visible in CAMERA. After that, the stability of the amplification can be monitored with a laser system which connects each scintillator to a pulsed laser. Both calibration methods require a trigger which is provided by the GANDALF-framework.

In the DVCS data taking period 2016/2017, an additional calibration method with a trigger on cosmic muons was used [89].

## 5.2 Calibration

The calibration procedure for CAMERA is based on physics events and composed of different steps. Three different types of particles are used.

**Delta electrons:** Delta electrons are emitted when the beam pierces through the target. They travel at the speed-of-light and are the dominant source for signals in the scintillators.

**Protons from elastic pion-proton scattering:** Using a pion beam, events where the beam particle elastically scattered off a target proton are selected. The elastic process allows the prediction of the proton trajectory by measuring the incident and the scattered pion. The predicted proton trajectory can then be correlated with measurements in the scintillators. The selection criteria for the process read:

- one vertex labeled as the best primary vertex<sup>1</sup>,

<sup>1</sup>Function provided by COMPASS reconstruction software CORAL.

- vertex longitudinal position  $z_v$  inside target:  
 $-314.19 \text{ cm} < z_v < -68.19 \text{ cm}$ ,
- vertex transverse position  $r_v$  inside target:  $r_v < 1.6 \text{ cm}$ ,
- momentum of beam particle  $188 \text{ GeV}/c < p_{\pi,in} < 194 \text{ GeV}/c$
- vertex has exactly one outgoing particle,
- the outgoing particle passed less than 10 radiation lengths,
- same charge for outgoing particle and beam particle,
- scatter angle of outgoing particle  $\theta_{\pi,out} > 0.5 \text{ mrad}$ ,
- exactly one track in CAMERA.

**Protons from exclusive  $\rho^0$  muoproduction:** In exclusive muoproduction processes at COMPASS, the kinematics of the event is fully determined already without making use of CAMERA. For the purpose of the calibration, an exclusive production channel with a large cross-section such as the  $\rho^0$  channel can be utilized. Here, the trajectory of the proton is predicted from the measurements of the beam, the scattered muon and the decay products of the  $\rho^0$ . A kinematic fit is performed to achieve the best resolution for the scattering angle of the predicted proton trajectory. More details on the exclusive  $\rho^0$  muoproduction sample and the kinematic fit can be found in [31].

### 5.2.1 Radial position calibration

For the calibration of the radial position, elastic pion-proton scattering events are used. The predicted radial position  $\varphi_{pred}$ , given by the proton trajectory is assigned to hits in the scintillator. The resulting histogram for each scintillator shows a signal at the  $\varphi_{pred}$  segment that is actually covered by the scintillator, *i.e.* where the hits indeed originated from the proton, see Fig. 5.3. The

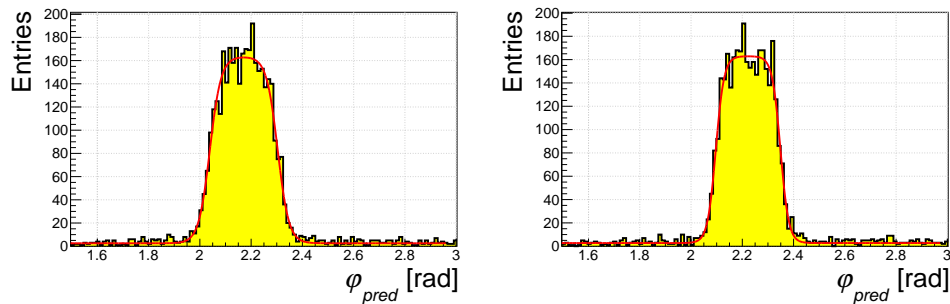


**FIGURE 5.3:** The predicted radial position  $\varphi_{pred}$  for hits in A0 (left) and B0 (right), respective. A fit using two sigmoid functions for the edges (indicated in red) is applied in order to extract the center of the distribution, which gives the radial position of the scintillator.

signal is fitted with two sigmoid functions, where the center parameter of the

fit function gives the radial position  $\varphi$  of the scintillator. When comparing the calibrated radial position with the nominal radial position  $\varphi_{nominal}$  of the scintillators, an oscillation is found for both rings as seen in Fig. 5.4. The nominal radial position  $\varphi_{nominal}$  is given by

$$\varphi_{nominal} = (8 - i) \cdot 15^\circ + \varphi_{offset} \quad (5.4)$$

with  $i$  the number of the counter and  $\varphi_{offset} = 0^\circ$  for the inner scintillators and  $\varphi_{offset} = 7.5^\circ$  for the outer scintillators. The oscillation implies that the

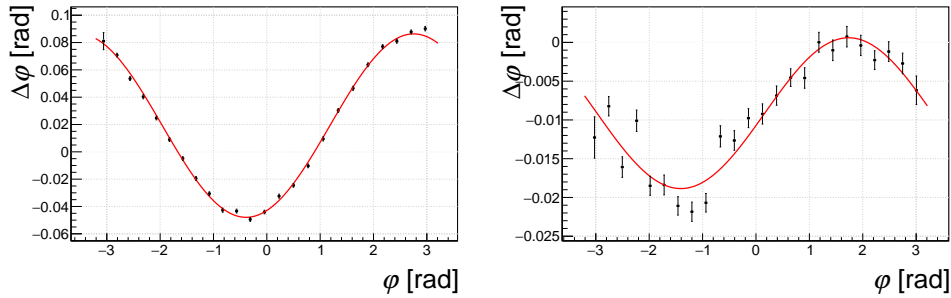


**FIGURE 5.4:** Difference of nominal and calibrated radial position  $\Delta\varphi = \varphi - \varphi_{nominal}$  as a function of the calibrated radial position for the inner ring (left) and the outer ring (right). The fit  $F_\varphi$  is indicated by the red line.

rings are not located concentrically around the target, but slightly *out-of-focus*. The actual center (or focus)  $f_{oc}$  can be calculated in polar coordinates using a fit  $F_\varphi$  to the data

$$\begin{aligned} F_\varphi(x) &= p_0 + p_1 \cdot \sin(p_2 \cdot x + p_3), \\ r_{foc} &= \tan(|p_1|) \cdot r_{nominal}, \\ f_{oc} &= \begin{pmatrix} r_{foc} \\ -p_3 \end{pmatrix}, \end{aligned} \quad (5.5)$$

with fit parameters  $p_0$  to  $p_3$  and  $r_{nominal}$ , the radius of the inner respectively outer scintillator. Using the following definitions

$$\begin{aligned} v &:= \begin{pmatrix} 1 \\ \varphi \end{pmatrix}, \\ p &:= -2 \cdot (v \cdot f_{oc}), \\ q &:= f_{oc}^2 - r_{nominal}^2, \end{aligned}$$

the radii of the scintillators with respect to  $f_{oc}$  are then given by

$$r = -p/2 + \sqrt{p^2/4 - q}. \quad (5.6)$$

Alternatively, since the width of the signal in Fig. 5.3 corresponds to the angular slice that is actually covered by the scintillator, the radial distance of

the scintillator to the target can be calculated with

$$r_w = \frac{w_{A/B}/2}{\tan(w_{fit})}, \quad (5.7)$$

with  $w_{A/B}$  the nominal width of the inner/outer scintillators and  $w_{fit}$  the width of the signal distribution given by the fit. This method has the advantage, that a deformation of the rings from a perfect circle is taken into account. However, the width extracted by the fit includes a bias towards a larger width. This is due to the blurred edges of the box that are modeled by sigmoid functions (cf. Fig. 5.3), where the extracted width is given by the distance between the two inflection points.

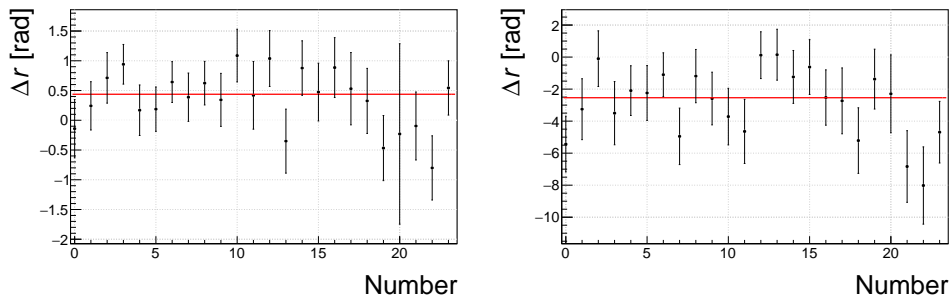


**FIGURE 5.5:** Difference of radii obtained with Eq. 5.6 and Eq. 5.7  $\Delta r = r - r_w$  as a function of scintillator number for inner ring (left) and outer ring (right). The compatibility with the constant fit indicates that within the accuracy of the methods, a perfect circle for the CAMERA rings can be assumed.

When comparing the two methods to obtain the radii of the scintillators, an offset between the methods by  $(4 \pm 1)$  mm for the inner ring and  $(-26 \pm 4)$  mm for the outer ring is visible. For both rings, the comparison is compatible with a straight line fit, which suggests that there is no measurable deviation of the rings from a perfect circle.

Because of the possible bias in the method with the sigmoid functions, the calibration values are taken using Eq. 5.6. Though, these values are only preliminary and will be refined in the next calibration step.

## 5.2.2 Longitudinal position calibration

The positioning of the detector in the COMPASS coordinate system by finding  $c_{eff}$ ,  $k_z$  and refining the radial position  $\varphi$  of the scintillators is done by using the exclusive  $\rho^0$  muoproduction sample.

The calibration of the longitudinal position uses the correlation between the time difference of the hits in the scintillator and the position predicted by the proton trajectory, see Fig. 5.6. To predict the longitudinal position of the proton in the outer (inner) scintillator  $z_{B,pred}$  ( $z_{A,pred}$ ), the vertex  $\vec{r}_{vtx} =$

$(x_{vtx}, y_{vtx}, z_{vtx})$  and the predicted scattering angle of the proton  $\theta_{p,pred}$  are used

$$\begin{aligned} z_{B,pred} &= z_{vtx} + \left( r_B - \sqrt{x_{vtx}^2 + y_{vtx}^2} \right) / \tan(\theta_{p,pred}), \\ z_{A,pred} &= z_{vtx} + \frac{\left( r_A - \sqrt{x_{vtx}^2 + y_{vtx}^2} \right)}{\left( r_B - \sqrt{x_{vtx}^2 + y_{vtx}^2} \right)} z_{B,pred}. \end{aligned} \quad (5.8)$$

For the inner ring, one can take advantage of hits in the already calibrated outer ring to determine  $z_{A,pred}$  more precisely. To obtain the calibration values  $c_{eff}$  and  $k_z$ , Eq. 5.1 can be used as shown in Fig. 5.6. However, the stability

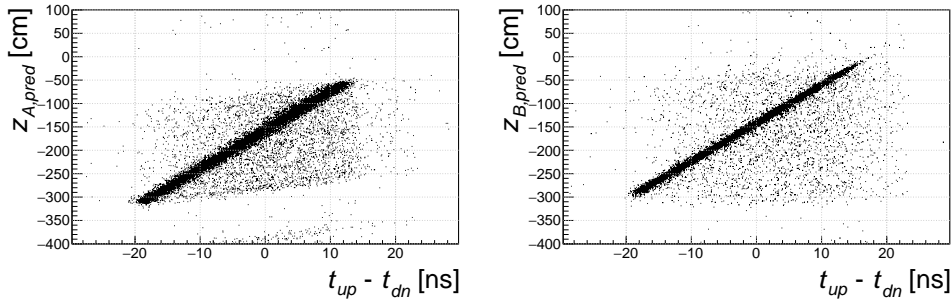


FIGURE 5.6: Predicted longitudinal position as a function of the measured time difference of the up and downstream timestamps for A0 (left) and B0 (right). By fitting Eq. 5.1, the calibration constants  $c_{eff}$  and  $k_z$  can be obtained.

and accuracy of the calibration can be improved by solving Eq. 5.1 for  $k_z$

$$k_z = z - \frac{1}{2} \cdot c_{eff} \cdot (t_{up} - t_{dn}), \quad (5.9)$$

and plotting it as a function of  $c_{eff}$  while substituting  $z$  for the predicted longitudinal position  $z_{A,pred}$  respectively  $z_{B,pred}$ . The resulting two dimensional plots are illustrated in Fig. 5.7. The calibration constants  $c_{eff}$  and  $k_z$  are then

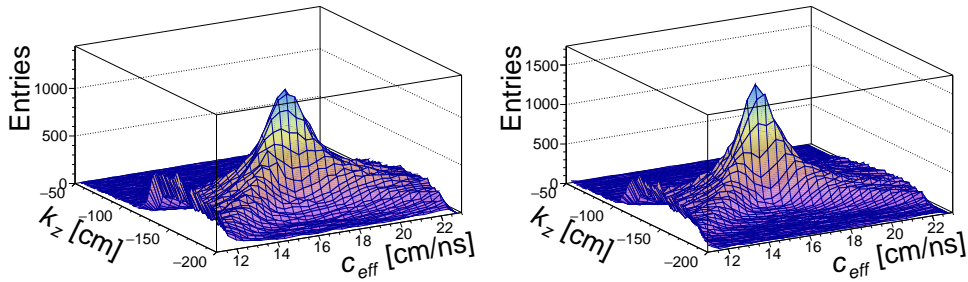
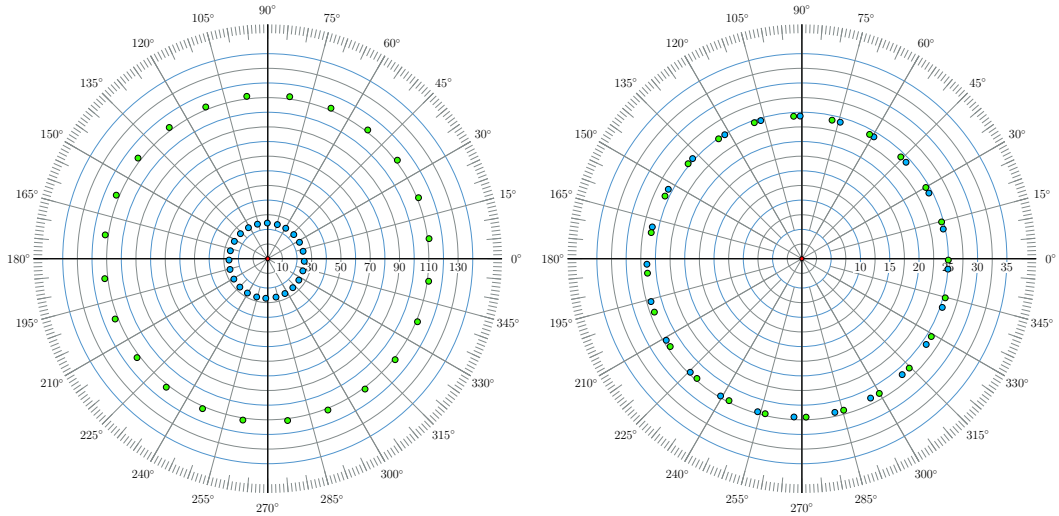


FIGURE 5.7: The calibration constant  $k_z$  as a function of the calibration constant  $c_{eff}$  for A0 (left) and B0 (right) using Eq. 5.9 and the predicted longitudinal position. The effective speed-of-light  $c_{eff}$  is chosen at the value, where the distribution has the smallest width. The central value of the distribution then yields  $k_z$ .

obtained using the value for  $c_{eff}$  where the distribution for  $k_z$  has the minimum width.

To have a consistent set of calibration constants, the calibration of the radial position is performed as described in Subsection 5.2.1, this time using the exclusive  $\rho^0$  muoproduction sample. Also, the calibration of the radial position can now be refined. By plotting the predicted  $\varphi$  angle as a function of the longitudinal position of the hits, a twist of the inner ring along the z-axis is revealed. The final radial positions for the scintillators of the inner and outer ring are visualized in Fig. 5.8.



**FIGURE 5.8:** Extracted radial position of scintillators. Left: Position of scintillators of the inner ring (blue dots) and outer ring (green dots). Right: Visualization of the twist of the inner ring scintillators. Green dots give the position at the upstream end and blue dots the position at the downstream end.

### 5.2.3 Time-of-Flight and momentum calibration

To compensate time jumps of the readout, the extraction of the time-of-flight (ToF) calibration constant  $k_t$  is performed on a run-by-run basis. When plotting the distance-of-flight  $s_{DoF}$  versus the time-of-flight  $t_{ToF}$ , a strong correlation in form of a straight line can be observed, see Fig. 5.9. It can be assumed, that the line manifests because of delta electrons traveling at the speed-of-light from the target through the inner and outer ring. Instead of fitting the straight line,  $k_t$  is obtained by projecting along the line,

$$k_t = t_A - t_B + \frac{s_{DoF}}{c}, \quad (5.10)$$

as shown on the right-hand side of Fig. 5.9.

In the last calibration step, the momentum yields given by CAMERA are compared to the momentum yields of the predicted protons using the exclusive  $\rho^0$  muoproduction sample. The comparison suggests subtracting 330 ps from

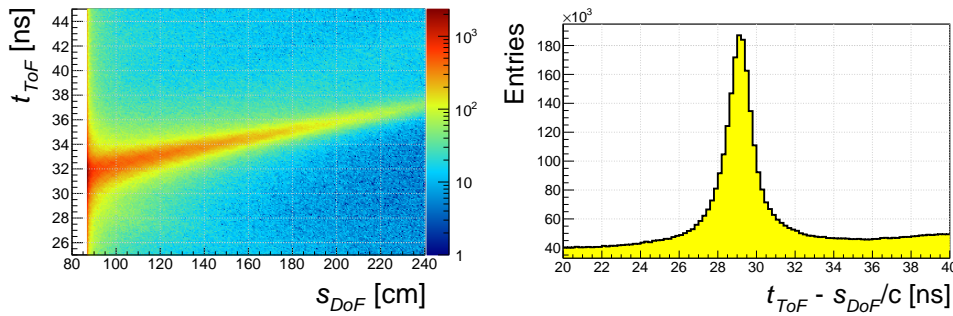


FIGURE 5.9: Left:  $t_{ToF}$  as a function of  $s_{DoF}$  for tracks in the CAMERA segment A0/B0. The strong correlation in form of a straight line originates from delta electrons. Right: Projection of the left histogram using the speed-of-light for the slope. The central value leads to the calibration constant  $k_t$ .

$k_t$ . This global shift appears most likely due to a bias in the determination of the time-of-flight  $k_t$ . As it is also visible in Fig. 5.9, the target histogram for the calibration is slightly asymmetric and the background features a slope. It is therefore understandable, that the fit used to extract the calibration constant can be biased (which is fine, as long as the bias is common in all fits).

### 5.3 Data quality and stability

By extracting the calibration constants for each run individually, the stability of the CAMERA readout can be studied. Different issues of the readout appeared which triggered further development on the readout. The revised firmware of the GANDALF-ADC was already outlined in Chapter 4.

The following list summarizes the issues that have arisen:

- After reloading, the **system synchronization** problem lead to GANDALF-modules that were not synchronous to the GANDALF master-time module, which rendered their measured timestamps to be useless.
- Also after reloading, the **clock ambiguity** problem lead to possible time jumps between the GANDALF-modules with 2 ns size.
- The **phase alignment** procedure developed in [84] did not work reliably. This lead to time jumps between the GANDALF-modules in the order of 200 ps.
- Another consequence of the bad phase alignment were **sampling errors of the ADC bits** leading to a distortion of the pulses and efficiency/accuracy loss of the pulse feature extraction method.

The issues given in boldface are explained in the following sections in greater detail.

### 5.3.1 System synchronization

A timestamp in an event of the COMPASS experiment is always given relative to the time of the First Level Trigger (FLT), which triggered the event. To measure the time of the FLT, each equipment type uses a master-time module<sup>2</sup>. The time measured by a GANDALF-module therefore reads  $t_{meas} = t - t_{MT}$ , where  $t$  is the time of a hit measured by the GANDALF-module and  $t_{MT}$  is the time of the FLT determined by the GANDALF master-time module. To end-up with a meaningful time, the counters in the GANDALF master-time module and in the GANDALF-modules need to be synchronized. In terms of the GANDALF-module firmware, this means, that the main counters representing the *current time* of the modules have to be reset synchronously at a specific moment in time. For this, the time of the Begin of Spill (BoS) signal is used. In contrast to other equipment in the experiment, the GANDALF-module does not reset its counters at each BoS but only when the request for synchronization is sent to the GANDALF-modules via a *fast-register*. It arms the module to reset its main counter on account of the next BoS.

The command has to be issued after reloading one or more GANDALF-modules so that all of them are synchronous. During the 2012 pilot run, this synchronization was not consequently applied since the logic that consumes the *fast-register* did not work reliably.

The issue leads to asynchronous GANDALF-modules and it is not possible to put their timestamps into context with each other. The part of the CAMERA detector readout by the asynchronous GANDALF-modules is lost. The periods with asynchronous GANDALF-modules are disregarded by a quality flag (see also Subsection 5.3.5 paragraph 'unsync\_cam.list and sync\_in\_run.list').

### 5.3.2 Clock ambiguity

In Fig. 5.10, the stability of the calibration constant  $k_t$  is depicted as a function of the run number for an exemplary segment of the CAMERA detector. It is striking, that three populations of  $k_t$  values emerge, each separated by  $\sim 2$  ns. The reason for this behavior is explained by a design flaw in the 2012 GANDALF-ADC firmware. At that time, the GANDALF-ADC operating clock (see also Subsection 4.4.1) was chosen as an odd multiple of the TCS data clock,

$$f_{amc,2012} = 13/2 \cdot f_{tcs,data} = 252.72 \text{ MHz, with } f_{tcs,data} = 38.88 \text{ MHz.} \quad (5.11)$$

As a consequence, the GANDALF-ADC operating clock is synchronous to every second edge of the TCS data clock, as illustrated in Fig. 5.11. The edge is chosen by chance on every reload of the module. Two modules can therefore have a phase between each other with the size of half the GANDALF-ADC operating clock latency, which amounts to  $\sim 2$  ns. The three populations in Fig. 5.10 are explained by

<sup>2</sup> Equipment type in this context refers to the timeunit of the device. The timeunit is used to translate from the internal time unit of the device into natural units. Equipment with the same timeunit may share a master-time module.

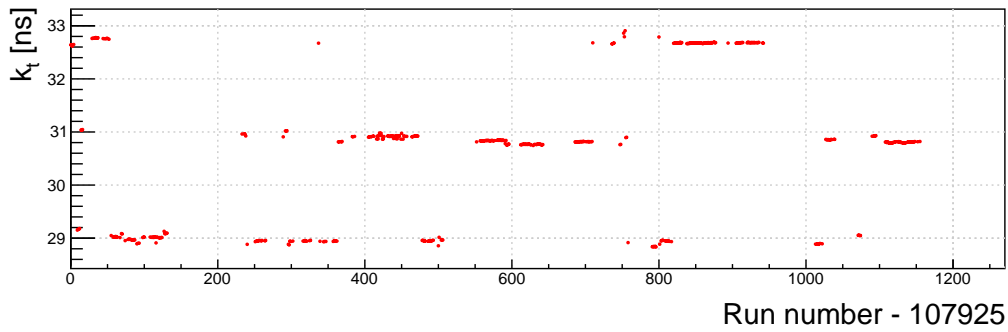


**FIGURE 5.10:**  $k_t$  as a function of run number for CAMERA segment A3/B4. Three populations of values are visible, separated by  $\sim 2$  ns. It was found, that the positions of the jumps correlate with a reload of the involved GANDALF-modules.

**population at  $\sim 31$  ns:** both GANDALF-modules chose the same edge,

**population at  $\sim 33$  ns:** B GANDALF-module chose the later edge,

**population at  $\sim 29$  ns:** A GANDALF-module chose the later edge.

The stability of the calibration constant  $k_t$  can be assessed by joining the three populations using a discrete shift equal to the clock latency. As shown in the histogram on the left-hand side of Fig. 5.12, the value spread amounts to  $\sim 100$  ps. The reason for this broad spectrum is explained in the following Subsection 5.3.3. The histogram on the right-hand side of Fig. 5.12 shows the stability for the calibration constant  $k_t$  for a period where the detector readout was stable, *i.e.* the electronics was not reloaded. One can conclude that the method used for the extraction of  $k_t$  is rather stable.

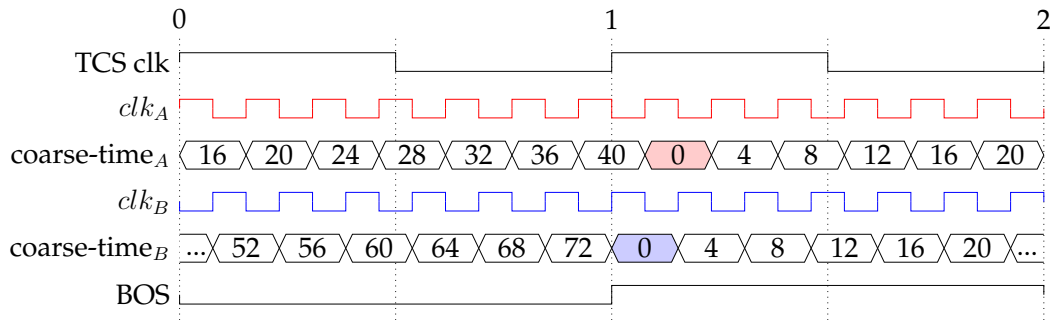


**FIGURE 5.11:** Illustration of the clock ambiguity of two GANDALF-ADC modules (A and B). The rising edge of  $clk_A$ , the operating clock of module A, is synchronous to the even rising edges of the TCS clk. The rising edge of  $clk_B$ , the operating clock of module B, is synchronous to the odd rising edges of the TCS clk. The modules choose the edge after reloading by chance. In the depicted scenario, the modules are not synchronized in the beginning, *i.e.* the values of the internal time counters ( $coarse-time_A$  and  $coarse-time_B$ ) do not match. The rising edge of the BoS signal, used to reset the internal time counters, coincides with the rising edge of the TCS clk and coincides therefore as well with the rising edge of  $clk_B$ . The module A reads the BoS signal one half operating clock cycle later, which results in an offset of the time measurement between the modules of one half operating clock cycle ( $\sim 2$  ns).

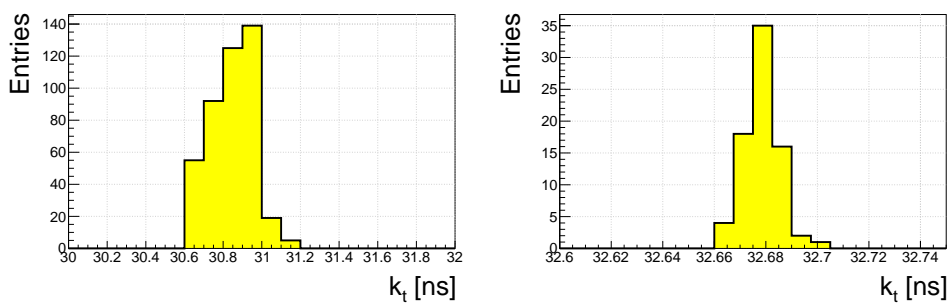


**FIGURE 5.12:** Left: Histogram of  $k_t$  values obtained for CAMERA segment A3/B4 after joining the three populations by shifting with the clock latency, *cf.* Fig. 5.10. The width of the distribution of  $RMS = 105$  ps can be attributed to the inaccuracy of the phase alignment, see also Subsection 5.3.3. Right: Histogram of  $k_t$  values for a subset runs 108 746 to 108 867 in which the readout was stable. The width of the distribution of  $RMS = 6$  ps shows the principle reliability of the calibration method.

### 5.3.3 Phase alignment

In Subsection 4.4.2, the importance of the phase alignment for the SI chip was discussed. In the 2012 data set some indications were found leading to the conclusion, that the phase alignment method used at that time did not work accurately enough, where an accuracy in the order of a few pico seconds is required. It was finally pinned down by thoroughly analyzing the ADC delay settings using the tools developed by [84]. It was found, that when re-aligning the phase, the sampling window for all ADC bits may jump by some IODelay steps as seen in Fig. 5.13. A jump that affects all ADC bits can

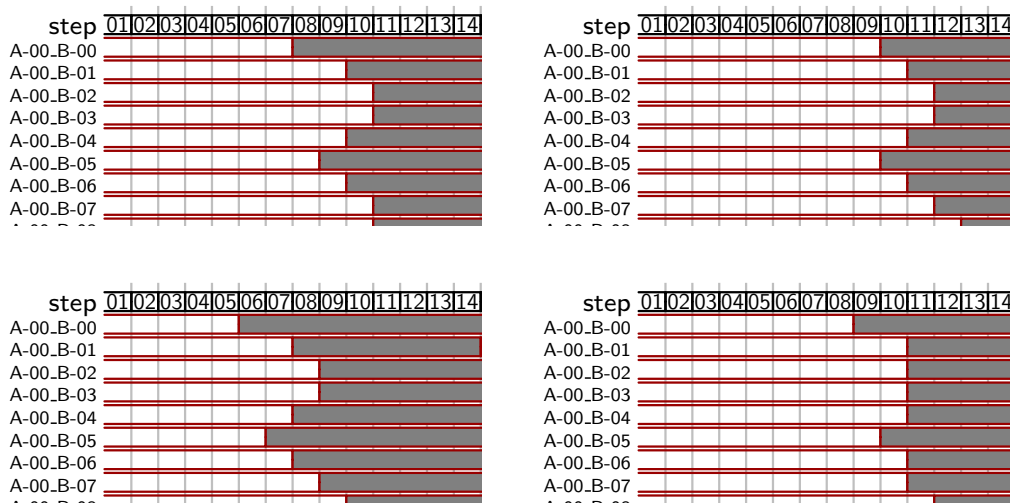


**FIGURE 5.13:** Excerpt of the ADC delay graphs, each after an attempt to re-align the SI chip phase. Unstable areas for the sampling of the particular ADC bit are indicated in grey. The 'step' gives the delay setting for the IODelay, one 'step' amounts (on average) to 78 ps [90]. For each 'step', the circuit illustrated in Fig. 4.12 was used to determine whether the bit sampling is valid. One can observe that the position of the unstable areas is shifted between the different pictures, which is attributed to the inaccurate phase alignment procedure.

only be explained by a change in the phase of the ADC clock with respect to the IODelay clock, *i.e.* the ADC bit sampling clock. The final conclusion is that the phase alignment procedure used is only working within an accuracy of five IODelay steps (approximately two SI chip coarse steps), meaning the accuracy only amounts to  $\sim 400$  ps. For a measurement of time deltas in the order of pico seconds, this is not satisfying, which is why the phase alignment procedure was revised.

### 5.3.4 Sampling errors of the ADC bits

As a consequence of Subsection 5.3.3 the timing of the sampling of the ADC bits can be displaced by up to  $\sim 400$  ps. Assuming a save sampling window for an ADC bit of  $\sim 600$  ps and also taking into account clock jitter and the fact that the delay values for the IODelays were not perfectly centered in the

first place, the wrong sampling of ADC bits is understandable. In addition, the wrong sampling of ADC bits was enhanced by a wrong reset logic which results in malfunctioning IODelay components and as a consequence ADC bits that appeared constant (or inactive). Both issues are further referred to as *bit-errors*.

The impact is clearly visible by spikes in the pulse shapes depending on the ADC bit which was sampled incorrectly, *cf.* Fig. 5.14. Because of the

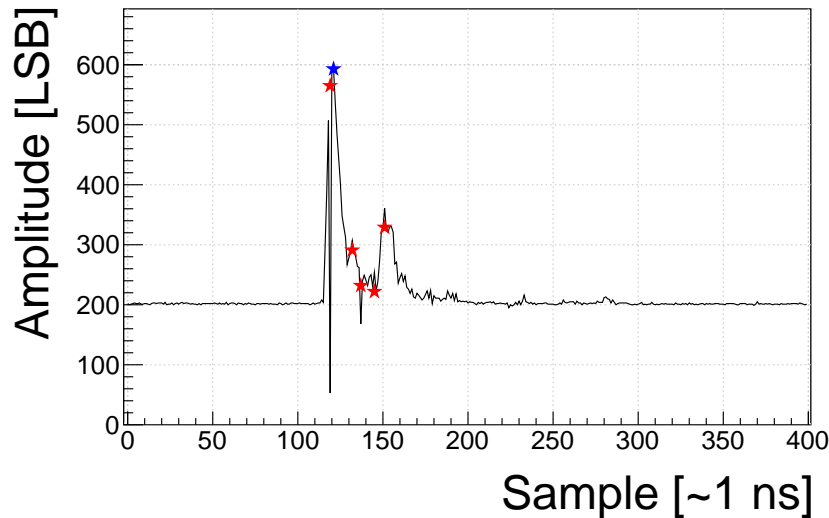


**FIGURE 5.14:** Frame recorded with the GANDALF-ADC. The unit of the ordinate *Least Significant Bit* (LSB) denotes the smallest quantity the ADC can resolve (here, corresponding to  $\sim 1$  mV). *Bit-errors* are visible as spikes in the pulse shape. The hit detected by the online pulse shape analysis is marked with a blue star. The red stars indicate the position of *bit-errors* found with an offline algorithm.

link to Subsection 5.3.3, the re-adjustment of the phase after reloading the GANDALF-module influences the rate of *bit-errors* on a particular channel. Hence, phases exist, where a channel experiences severe problems whereas in another phase the channel is working fine.

Attempts to recover the data by correcting the impact of the *bit-errors* on the time measurement ended up without success. Hence, a method was developed to identify and exclude phases in which a channel suffered from *bit-errors* as described in Subsection 5.3.5, paragraph “Treatment of *bit-errors*”.

### 5.3.5 Bad spill list and quality flags

To use the CAMERA detector in physics analysis, deficiencies of the detector have to be taken into account. For measurements where the CAMERA detector is vital, periods where CAMERA or parts of CAMERA were unavailable have to be identified and excluded. In COMPASS analyses, this is usually done by means of bad spill lists. For CAMERA, the following bad spill lists are created mostly on account of the issues described in Section 5.3. In total, 8247 out of 35386 spills are excluded due to instabilities related to CAMERA.

In the following list of bad spill list, the number in brackets gives the number of spills excluded by the particular list.

**'unsync\_cam.list' (7787) and 'sync\_in\_run.list' (140):** Spills where one or more GANDALF-modules were not synchronized to the GANDALF master-time module are easily identified by plotting the target histogram for the  $k_t$  calibration (Subsection 5.2.3) for each spill and looking for empty bins. Also, as of Subsection 5.3.1, attempts to synchronize the modules were issued during runs. Therefore, an already synchronized module may experience a time jump within a run because of the clock ambiguity problem (Subsection 5.3.2). These time jumps are identified during the calibration procedure by extracting  $k_t$  for each spill. If a jump is detected, only those spills are kept where  $k_t$  is constant for the most number of spills.

**'out\_of\_phase\_cam.list' (337):** A software tool was used to record the status words (see also Subsection 4.6.2) of the GANDALF-modules during large periods of the pilot run. The information was stored in a database and includes information on the status of the SI chips. This allows querying for periods where the connection to the TCS was completely lost by one or more GANDALF-modules. The corresponding spills are collected in this list.

**'jumpy\_cam.list' (418):** The list removes spills with a large variance in the number of hits in a CAMERA channel normalized to the muon flux [31].

**Treatment of *bit-errors*:** As described in Subsection 5.3.4, *bit-errors* can appear on readout channels of CAMERA with varying strength. To cope with the issue, first, a method to identify problematic runs and channels is needed. The method is based on the distribution of the time difference of the up and downstream timestamps of a scintillator, where in some cases a comb-like structure is observed as shown in Fig. 5.15. The strength of the comb-like

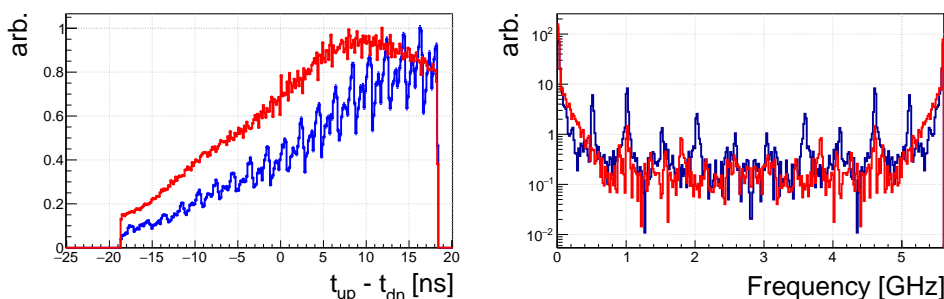


**FIGURE 5.15:** Left: Comparison of time difference distribution of scintillator B12 for runs 108718 (blue) and 108953 (red), normalized to their integral. A strong comb-like structure is visible for in run 108718. Right: Magnitude of the fast Fourier transform (FFT) of the left distributions. The integral in the interval  $(1010 \pm 200)$  MHz can be used as a measure of the strength of the comb-like structure.

structure varies from scintillator to scintillator and from run to run. It can also disappear as shown in Fig. 5.15 as well. The frequency of the comb is found to match exactly (multiples of) the sampling frequency of the GANDALF-ADC, *i.e.*  $1010.88 \text{ MHz}^3$ . This again is an indication for the source of the comb-like structure. *Bit-errors* are likely to affect the CFD algorithm such that it picks up a spike from a *bit-error* as a regular hit. Because of the large amplitude difference between the spike and the preceding sample, the extracted time-stamps fine-time is most likely close to 0.

By using a FFT, the strength of the comb-like structure can be measured using the integral of the FFT magnitude in the interval  $(1010 \pm 200) \text{ MHz}$ . For each ring, a cut-off value is chosen to classify bad channels as illustrated in Fig. 5.16. In contrast to the bad spill lists, here, only the affected CAM-

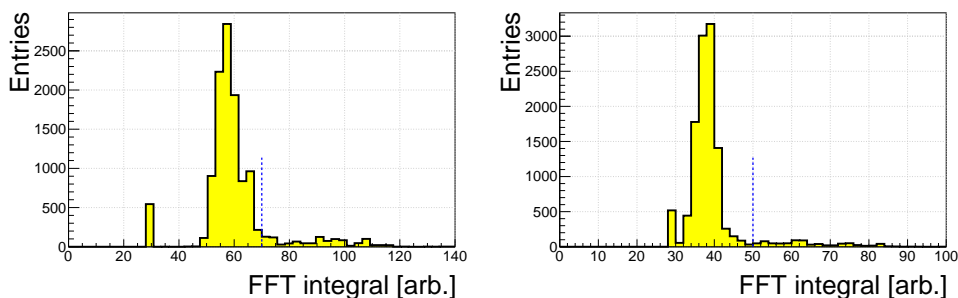


**FIGURE 5.16:** Histogram of the integral between  $(1020 \pm 200) \text{ MHz}$  of the time difference distribution FFT for A (left) and B (right). A cut is used for the inner (outer) ring at 70 (50) to disable the affected scintillator for the respective run.

ERA scintillator is excluded on a run-by-run basis. This efficiency loss is accounted for by calculating an effective efficiency for each CAMERA segment, taking into account only the *seen* flux. The total loss of flux on account of the *bit-error* issue is  $\sim 11\%$ . For a detailed description of the efficiency calculation and the inclusion of the inefficiency introduced by the *bit-errors*, refer to [31]. At the time of writing the thesis, new possibilities to study the *bit-errors* became available. An algorithm was developed that is able to find spikes in a frame, as demonstrated in Fig. 5.14. The spikes originate from errors on single or multiple bits in a sample leading to a discontinuity to the previous and succeeding sample. As a measure of the severity of *bit-errors*, the algorithm is used to count the number of spikes in a frame normalized to the number of hits in the frame. This rate of *bit-errors* per hit is extracted for each frame of a specific ADC channel and run. The comparison to the FFT method is shown in Fig. 5.17. A clear correlation between the two methods is visible, while the *bit-error* rate method seems to be more restrictive. Still, the FFT method is favored since the *bit-error* rate method is oversensitive for *bit-errors* on small bits that actually do not affect the time measurement.

<sup>3</sup>In interleaved mode, the sampling frequency amounts to  $2 \cdot f_{adc,2012} = 1010.88 \text{ MHz}$ , see also Subsection 5.3.2.

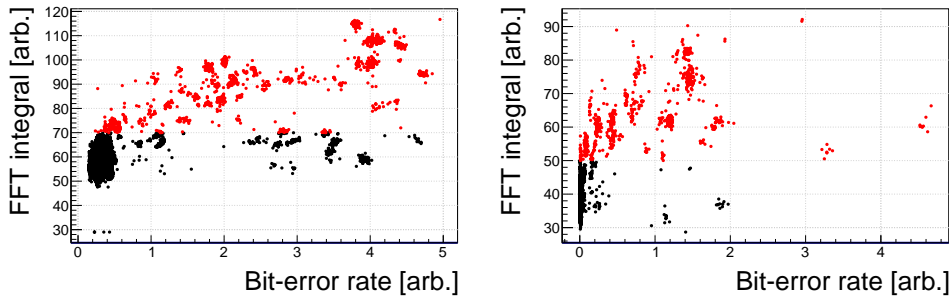


FIGURE 5.17: FFT integral value versus the *bit-error* rate for A (left) and B (right). The values in red are above the threshold posed by the FFT method, as explained in Fig. 5.16. The bulk of the entries are concentrated in the lower left blobs. In general, a good correlation between the methods is observable.

## 5.4 Start counter

In the 2012 DVCS pilot run, an additional fiber station was positioned in front of the target. The purpose of the station was to precisely measure the timing of beam particles. Hence, it is built with regards for best timing resolution. Using this detector, the momentum vector of the recoiling proton can be reconstructed with the vertex and the hit in the outer ring of the CAMERA detector as illustrated in Fig. 5.18. For this, an inter-calibration between the start counter and the outer ring is needed. The proton time-of-flight is then

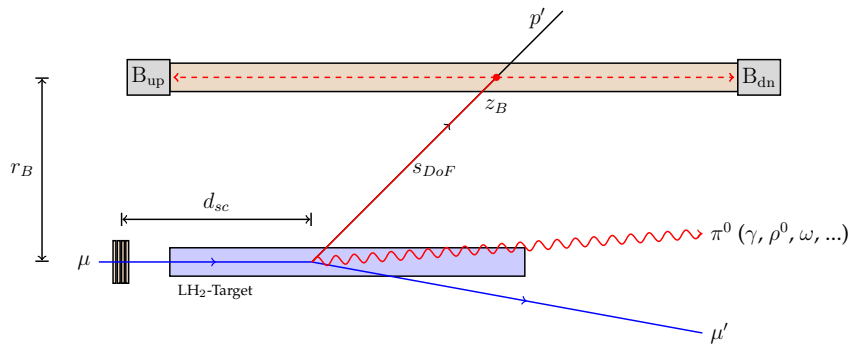


FIGURE 5.18: Schematic side view of the CAMERA outer ring, the target and the start counter, illustrating the principle of the ToF measurement of recoiling protons in exclusive reactions. The incoming muon  $\mu$  is detected in the start counter and scatters off a target proton. The light in the scintillator produced by the recoiled proton  $p'$  is detected by the photomultipliers  $B_{up}$  and  $B_{dn}$ . The scattered lepton  $\mu'$  and in this case the  $\pi^0$  are detected in the COMPASS spectrometer.

determined by measuring the time difference between the muon hit in the start counter and the time  $t$  of the proton hit in the CAMERA scintillator and subtracting the time the muon needs to cover the distance “start counter to vertex”. With  $\vec{r}_B$ , the position of the hit in the out ring of CAMERA, and  $d_{sc}$  the distance between start counter and vertex  $\vec{r}_{vtx}$ , the time-of-flight  $t_{ToF}$  and

distance-of-flight  $s_{DoF}$  are given as

$$\begin{aligned} t &= \frac{t_{up} + t_{dn}}{2}, \\ t_{ToF} &= \sum (t + k_{t,sc,i} - t_{sc,i}) / n_{hits} - d_{sc}/c, \\ s_{DoF} &= |\vec{r}_B - \vec{r}_{vtx}|. \end{aligned} \quad (5.12)$$

The number of hits  $n_{hits}$  associated with the muon in the start counter is given by a clusterization algorithm [91]. The quantity  $t_{sc,i}$  corresponds to the time of the  $i$ 'th hit of the cluster. The calibration constant  $k_{t,sc}$  has to be found for each combination of CAMERA scintillator and start counter fiber. The calibration procedure is described in the following Subsection 5.4.1.

To calculate the proton momentum at the vertex, the energy loss along the track of the proton has to be taken into account. For this, the calculation from [88] is revised. The speed of the proton at the vertex does not correspond to  $\beta = \frac{t_{ToF}}{s_{DoF}}$  since  $t_{ToF}$  includes the deceleration due to the material along the proton track. Therefore, the true  $\beta$  at the vertex is obtained numerically by emitting a proton with a certain momentum  $p_p$  at the vertex  $\vec{r}_{vtx}$  and measuring the effective time  $t_{ToF,eff}$  it needs to travel to the position of the hit in the CAMERA scintillator  $\vec{r}_B$ , whilst taking into account the successive deceleration due to the material. The final proton momentum is then obtained by minimizing

$$(t_{ToF} - t_{ToF,eff}(p_p; \vec{r}_{vtx}, \vec{r}_B))^2 \quad (5.13)$$

as a function of  $p_p$ .

### 5.4.1 Calibration

The first attempt to calibrate the detector used the exclusive  $\rho^0$  muoproduction sample mentioned in Section 5.2. To combine runs in order to enhance statistics, stability periods had to be defined due to the instabilities of the CAMERA readout. It turned out, that this task is not feasible and that the calibration had to be performed run-by-run which is not possible with the limited statistics of the exclusive  $\rho^0$  muoproduction sample.

Thus, the calibration uses tracks originating from delta electrons. To estimate the delta electrons distance of flight  $s_{DoF}$ , its vertex  $\vec{r}_{vtx,\delta}$  is assumed at the target center  $(x_{t,center}, y_{t,center})$  with the longitudinal position given by the hit in the inner scintillator  $z_A$ ,

$$\vec{r}_{vtx,\delta} = (x_{t,center}(z_A), y_{t,center}(z_A), z_A).$$

A parametrization for the target provided by [92] is used to obtain the target center as a function of the longitudinal position. With the delta electron traveling at the speed-of-light and  $s_{DoF} = |\vec{r}_B - \vec{r}_{vtx,\delta}|$ , the calibration constant is

obtained by

$$\begin{aligned} t_{ToF} &= s_{DoF}/c = t + k_{t,sc,i} - t_{sc,i} - d_{sc}/c, \\ \Rightarrow k_{t,sc,i} &= t_{sc,i} + (d_{sc} + s_{DoF})/c - t. \end{aligned} \quad (5.14)$$

An example of the time peak for the calibration is shown in Fig. 5.19. The

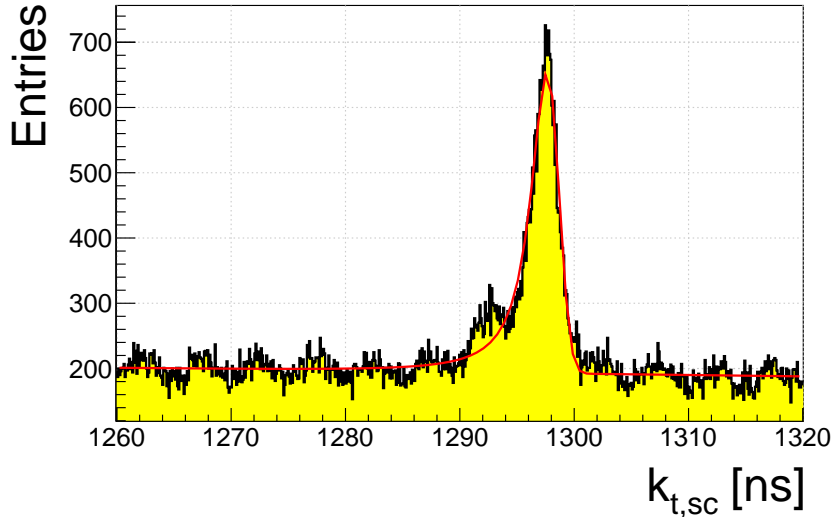


**FIGURE 5.19:** Time peak for the inter-calibration of the start counter 13U1-j plane wire 0 and CAMERA scintillator B0. A mirrored Landau distribution convoluted with a Gaussian is used to fit the signal with a polynomial of second order for the background. The origin for the background modulation is unknown.

calibration constant is extracted with a fit constructed from a convolution of a mirrored Landau distribution with a Gaussian and a second order polynomial for the background. As visible in Fig. 5.19, the fit function does not fully describe the signal. However, the thereby introduced bias should be constant and common for all combinations of scintillator and fiber. The fit is merely used to give a fixed time reference. Hence, in the final calibration step, the momentum yields for the start counter/CAMERA combination are compared to the momentum yields obtained by the spectrometer using the exclusive  $\rho^0$  muoproduction sample. It results in the additional global offset of  $-500$  ps for the time-of-flight measurement with the inter-calibration of start counter and CAMERA.

## 5.5 Results

Using a sample of reconstructed exclusive  $\rho^0$  muoproduction data, one can compare the yields for the proton predicted by the spectrometer and measured by the calibrated CAMERA detector. One should note that the displayed resolutions are not the bare detector resolutions but the resolutions with respect to the resolution of beam and spectrometer measurements.

In Fig. 5.20, the obtained resolution for the radial and longitudinal position calibration is depicted. The Fig. 5.21 shows the mean (bias) and the sigma

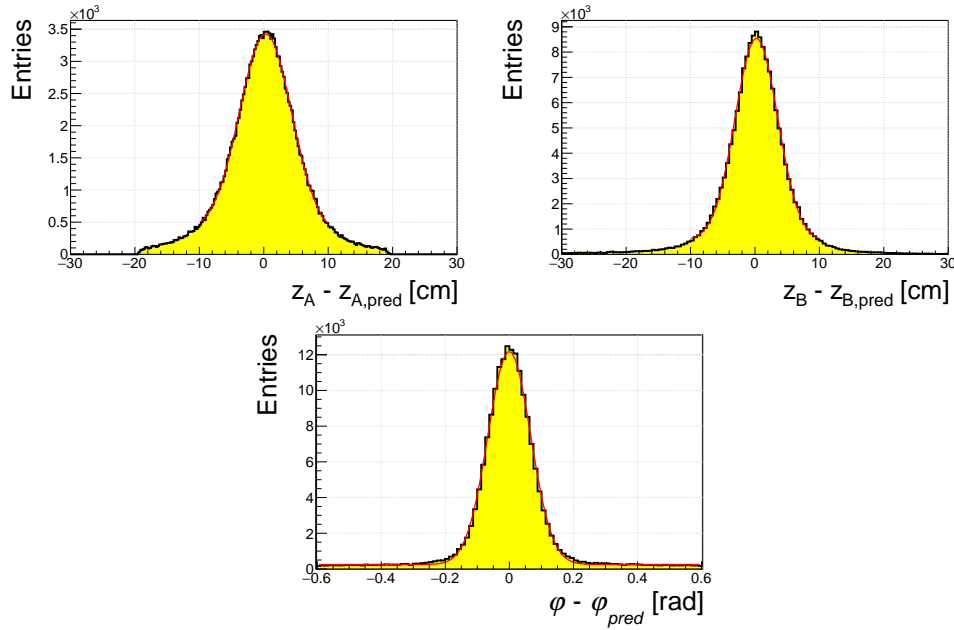


**FIGURE 5.20:** Top: Resolution for the longitudinal position reconstruction of the inner (left) and outer (right) CAMERA ring. The achieved resolution for the inner (outer) ring is  $\sigma = 4.1$  cm ( $\sigma = 3.3$  cm). Bottom: Resolution for the radial position reconstruction, where  $\varphi$  is given as the mean azimuthal angle in the CAMERA segment. The full width half maximum value is given with  $\sigma_{FWHM} = 8.9^\circ$ .

(resolution) for slices of the distribution for  $\Delta p/p_{p,pred}$  as a function of  $p_{p,pred}$ . The quantity  $\Delta p = p_p - p_{p,pred}$  denotes the difference of  $p_p$ , the proton momentum measured with CAMERA, and  $p_{p,pred}$ , the proton momentum predicted using only spectrometer quantities. While the left-hand side of the figure shows the measurement with both CAMERA rings, on the right-hand side the inter-calibration of start counter and CAMERA outer ring is shown. For momenta smaller than  $0.28 \text{ GeV}/c$ , a bias in the momentum determination is observed. However, the bias is located beneath the lower bound for the analysis, which is given by the four-momentum transfer squared of  $|t| > 0.08 (\text{GeV}/c)^2$ , which corresponds to proton momenta larger than  $0.28 \text{ GeV}/c$ .

The momentum resolution can be separated into two domains. For small momenta, the beam and spectrometer uncertainties dominate. This is demonstrated by comparing the yields for the predicted proton momentum with the generated proton momentum in an exclusive  $\rho^0$  muoproduction Monte Carlo sample. For intermediate and large momenta, the CAMERA resolution dominates. This is due to the fact that for large velocities, the impact of the uncertainty on the time-of-flight measurement becomes relevant.

The performance of the reconstruction of protons with the start counter shows to be comparable with the pure CAMERA reconstruction. However, since the start counter was only partially available during the 2012 DVCS pilot run, it does not enter in the physics analysis but it serves as an additional measure

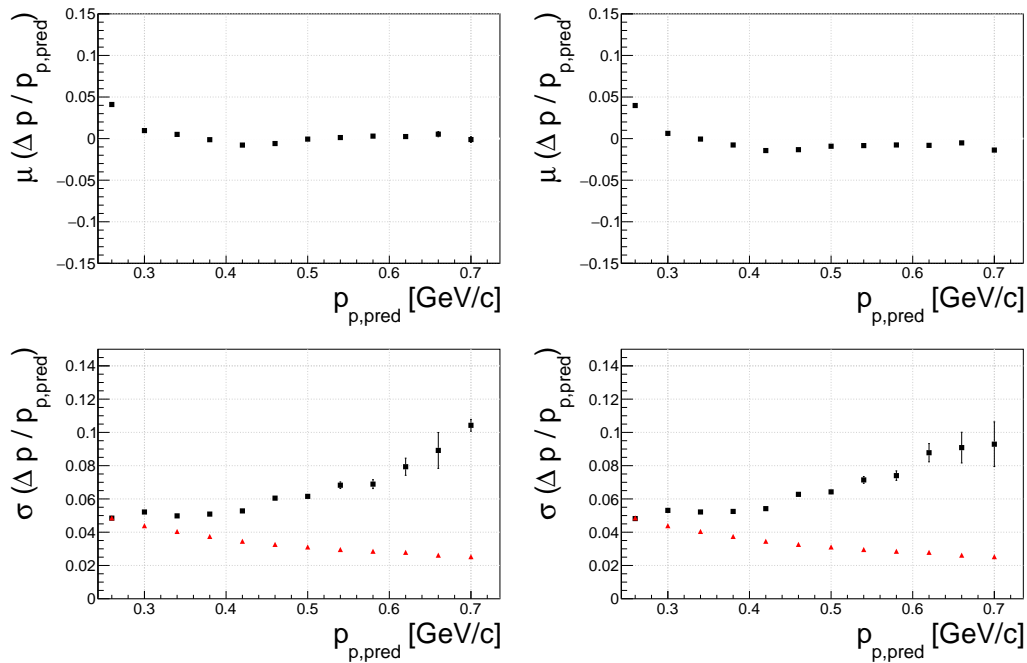


**FIGURE 5.21:** Left: Normalized momentum bias (top) and resolution (bottom) for protons measured with CAMERA as a function of the proton momentum predicted with spectrometer quantities  $p_{p,pred}$ . Right: The same for protons reconstructed using the inter-calibration of start counter and CAMERA outer ring. The red triangles give the resolution for the predicted proton momentum using only beam and spectrometer. For this, the predicted proton momentum is compared to the generated proton momentum in an exclusive  $\rho^0$  muoproduction Monte Carlo sample.

to clean up the data sample for the CAMERA efficiency determination, see [31, p. 82].



---

## 6 Extraction of the exclusive $\pi^0$ muoproduction cross-section

---

Next to the exclusive *one-photon production*, which is considered as the «golden channel» to study GPDs, *meson production* channels provide supplementary data to constrain GPDs, as outlined in Section 2.2.

At COMPASS, the data recorded in the 2012 DVCS pilot run allow for examining different *meson production* channels, like the  $\rho^0$  production that was used for the calibration of CAMERA in Chapter 5. In the course of this chapter, a pioneering measurement of the exclusive  $\pi^0$  muoproduction cross-section at COMPASS kinematics will be presented.

The knowledge of the cross-section is not only relevant for the understanding of GPDs but also serves as vital input to the background studies in measurements of the DVCS cross-section since a major background for exclusive *one-photon production* originates from exclusive *two-photon production* (the decay products of the  $\pi^0$ ), when one of the photons remains undetected.

Before the extraction of the cross-section can be performed, various requirements have to be established, starting with a review of the data quality and the determination of the luminosity in Section 6.1. In the event selection for exclusive  $\pi^0$  muoproduction, a kinematic fit is used which allows for the best determination of the event kinematics as well as an enhancement of the signal purity. The kinematic fit is discussed in Section 6.2 while the details of the event selection follow in Section 6.3. The measurement of the cross-section requires a detailed knowledge of the detector and the detector response for the particular physics channel, as well as an estimate of the contribution from background processes. These aspects are addressed in Section 6.4 and Section 6.5. The extraction of the exclusive  $\pi^0$  muoproduction cross-section is then accomplished in Section 6.6 followed by the study of systematic uncertainties in Section 6.7. The chapter closes with a discussion of the results in the context of GPDs in Section 6.8.

### 6.1 Data

The data analyzed herein were recorded in fall of 2012 during a pilot run for the dedicated DVCS data taking period (2016 and 2017). The data taking period of the pilot run covered five weeks, while the beam charge and polarization was switched multiple times. The magnetic fields of the spectrometer magnets were inverted when switching beam charge and polarization. The

muon beam was served by the SPS in a spill cycle of 48 s, with a 9.6 s on-spill period for COMPASS. In total, 35386 spills enter into the analysis.

During the data taking period, the beam quality, as well as the quality of the particle detection, can vary. Therefore, the quality of the data is assessed by different methods that operate on the level of spills. The most established method to quantify the quality of the spills at COMPASS is a nearest neighbor method, where different quantities are used to construct a metric which allows removing outliers. The quantities include for example the number of vertices or the number of tracks per event. The procedure is detailed in [93] while its application for the 2012 DVCS pilot run was performed by [94]. The provided list excludes 1695 spills.

For the usage of CAMERA within the analysis, special bad spill lists have to be used, excluding 8247 spills as discussed in Subsection 5.3.5. Because the GANDALF-TDC was also affected by problems related to the TCS phase alignment procedure, spill-by-spill time jumps were observed for detectors readout by GANDALF-TDCs. The affected spills are collected in a list that excludes 1334 spills [95].

All in all, 9029 of 35386 spills are excluded by bad spill lists (some lists have an overlap).

### 6.1.1 Luminosity determination

For the determination of a cross-section, a precise knowledge of the total flux of beam particles  $\Phi$  and the target properties are required. The quantities form the integrated luminosity  $\mathcal{L}$  which is given by

$$\mathcal{L} = \frac{\Phi \cdot l \cdot N_a \cdot \rho_{\text{LH}_2}}{m_p},$$

with  $m_p$  the mass of the proton, the effective length of the target  $l = 240$  cm, Avogadro's constant  $N_a$  and the density of liquid hydrogen  $\rho_{\text{LH}_2}$ . The flux of beam particles is determined by two methods that are explained in the following paragraphs. Both methods use similar conditions for the selection of eligible beam tracks:

**Beam through target:** The track of the beam particle has to point through the full length of the target, *i.e.* the transverse distance from the target center must be smaller than 1.9 cm over the full target length. For this, a parametrization of the target cell provided by [92] was used (Fig. 6.1).

**Beam track momentum:**  $140 \text{ GeV}/c < p_\mu < 180 \text{ GeV}/c$ .

**Beam reconstruction:** For a decent reconstruction of the beam track, at least hits in two Scintillating Fiber detectors, hits in three Silicon Strips detectors and hits in three beam momentum stations are required.

**Time in spill:** Only events with a time in spill  $t_{spill}$  between 1 s and 10.4 s are used<sup>1</sup>. The effective duration of a spill is therefore  $T_{spill} = 9.4$  s.

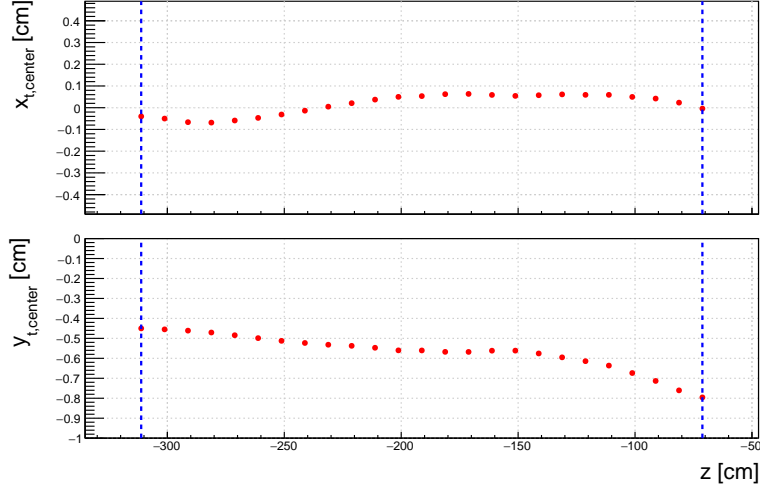


**FIGURE 6.1:** Transverse position of the target cell center as a function of the longitudinal position. The target cell center is almost straight in vertical direction, while in the horizontal direction it is slightly inclined. The blue lines indicate the part of the target used in the analysis. The parametrization for the target cell is provided by [92].

The very same conditions will be used accordingly in the event selection for the process studied in Section 6.3.

### Random trigger method

The method is based on counting the number of beam tracks  $N_{beam}$  for randomly triggered events. Beam particles, where the time determined by the beam telescope are within a certain time frame  $\Delta t$  are counted. With the number of random trigger attempts  $N_{rnd}$ , the observed time period of the spill results in  $N_{rnd} \cdot \Delta t$ . The total number of beam particles  $\Phi$  results from extrapolating to  $T_{spill}$ , the duration of a spill

$$\Phi = T_{spill} \cdot \frac{\sum_{i=1}^{N_{rnd}} N_{beam,i}}{N_{rnd} \cdot \Delta t}. \quad (6.1)$$

When using physics triggers, this number has to be corrected for the veto dead time (VDT) since the random trigger is not connected to the beam veto system. The quantity  $c_{VDT}$  accounts for the time period, where the veto system blocked physics triggers. The effective number of beam particles  $\Phi_{eff}$  available in the analysis is therefore given as

$$\Phi_{eff} = (1 - c_{VDT})\Phi. \quad (6.2)$$

<sup>1</sup>The time in spill  $t_{spill}$  is measured with respect to the BoS signal which is issued 1 s in advance of the beam.

The method was carried out by [96] for the 2012 DVCS pilot run. The resulting list provides the number of beam particles and the corresponding VDT for each spill.

### Via structure function $F_2^p$

The idea is to reverse the measurement of the structure function  $F_2^p$  and to use world data as an input for  $F_2^p$ . The luminosity is then calculated according to

$$\begin{aligned}\mathcal{L} &= \frac{1}{\sigma_{\Delta\Omega}} \sum_{i=1}^N \frac{\eta(Q_i^2, x_{Bj,i})}{a(Q_i^2, x_{Bj,i})}, \\ \sigma_{\Delta\Omega} &= \int_{\Delta\Omega} \frac{4\pi\alpha^2}{Q^4} \frac{F_2^p(Q^2, x_{Bj})}{x_{Bj}} \left( 1 - y - \frac{Q^2}{E_l^2} + \right. \\ &\quad \left. \left( 1 - \frac{2m_l^2}{Q^2} \right) \frac{y^2 + Q^2}{2E_l^2(1 + R(Q^2, x_{Bj}))} \right) dx_{Bj} dQ^2, \quad (6.3)\end{aligned}$$

with  $\sigma_{\Delta\Omega}$  the integrated differential cross-section in the phase space  $\Delta\Omega$  according to [97] and  $N$  the number of events measured in the phase space  $\Delta\Omega$ . Radiative corrections  $\eta(Q^2, x_{Bj})$  and acceptance corrections  $a(Q^2, x_{Bj})$  are applied event-by-event. The Tulay's fit [98] is used for the parametrization of  $F_2^p$ . For the cross-section ratio of longitudinal to transverse virtual-photons  $R$ , the fit provided by [99] is used. Besides the above-mentioned requirements for the beam track, additional conditions have to be formulated for the scattered muon. The peculiarities of the event selection and the detailed results can be found in [100].

The results of both methods correlate strongly. However, a systematic offset of about 3% is observed which will be considered in the systematic studies for the cross-section measurement (Subsection 6.7.1). Because of the smaller statistical error, finally, the random trigger method is used. Table 6.1 summarizes the flux of beam particles and the corresponding luminosity for the accepted spills of the 2012 DVCS pilot run.

TABLE 6.1: Integrated number of beam particles and integrated luminosity for the 2012 DVCS pilot run.

	$\mu^+$	$\mu^-$	$\mu^+ + \mu^-$
$\Phi/10^{-12}$	2.582	2.622	5.203
$\Phi_{eff}/10^{-12}$	1.871	2.330	4.201
$\mathcal{L}/\text{pb}^{-1}$	18.887	23.526	42.413

## 6.2 The kinematic fit for exclusive $\pi^0$ muoproduction

For the measurement of exclusive processes, the determination of the event kinematics can be greatly improved by combining all available information and using energy and momentum conservation conditions by means of kinematic fitting. The kinematic fit for exclusive measurements at COMPASS was originally developed by [31]. The concept, a general description and the implementation of the kinematic fit is illustrated in [31, p. 50]. Based on the notation developed there, the following section describes the modifications for the exclusive  $\pi^0$  muoproduction process. The formalism is to a large extent analogous to the specific descriptions of the application of the kinematic fit for DVCS and exclusive  $\rho^0$  muoproduction outlined in [31, p. 65 and p. 108].

The measured quantities for the process  $\mu p \rightarrow \mu' p' \pi^0 \rightarrow \mu' p' \gamma_h \gamma_l$ , where  $\gamma_h$  ( $\gamma_l$ ) indicates the higher (lower) energetic photon, are denoted by the vector  $\vec{k}$

$$\vec{k} = \begin{pmatrix} k_1 \\ \cdot \\ \cdot \\ \cdot \\ k_{27} \end{pmatrix} := \begin{pmatrix} \vec{p}_p \\ \vec{p}_\mu \\ \vec{a}_\mu \\ \vec{0}_{18} \end{pmatrix} + \begin{pmatrix} \vec{0}_8 \\ \vec{p}_{\mu'} \\ \vec{a}_{\mu'} \\ \vec{0}_{13} \end{pmatrix} + \begin{pmatrix} \vec{0}_{13} \\ r_A \\ \varphi_A \\ z_A \\ r_B \\ \varphi_B \\ z_B \\ p_{p'} \\ \vec{0}_6 \end{pmatrix} + \begin{pmatrix} \vec{0}_{20} \\ p_{\gamma_h} \\ \vec{a}_{\gamma_h} \\ p_{\gamma_l} \\ \vec{a}_{\gamma_l} \end{pmatrix}, \quad (6.4)$$

while the unmeasured quantities are denoted by the vector  $\vec{h}$

$$\vec{h} = \begin{pmatrix} h_1 \\ \cdot \\ \cdot \\ \cdot \\ h_9 \end{pmatrix} := \begin{pmatrix} \theta_{p'} \\ \varphi_{p'} \\ \theta_{\gamma_h} \\ \varphi_{\gamma_h} \\ \theta_{\gamma_l} \\ \varphi_{\gamma_l} \\ \vec{r}_v \end{pmatrix}. \quad (6.5)$$

The used abbreviations are described in the following:

- $\vec{0}_N$  denotes the neutral element of  $\mathbb{R}^N$ ,
- the target proton is assumed at rest,  $\vec{p}_p = \vec{0}$ ,
- $\vec{p}_\mu$  ( $\vec{p}_{\mu'}$ ) and  $\vec{a}_\mu$  ( $\vec{a}_{\mu'}$ ) denote the momentum three-vector and the transverse position of the incident (final) muon,
- $p_{p'}$  denotes the momentum of the final proton with the measured quantities  $r_A$ ,  $\varphi_A$  and  $z_A$  ( $r_B$ ,  $\varphi_B$  and  $z_B$ ) denoting the radius, azimuth angle

and longitudinal position of the hit in the inner (outer) ring, which are treated together with the unmeasured quantities  $\theta_{p'}$  and  $\varphi_{p'}$  denoting the scattering and azimuthal angle of the final proton,

- $p_{\gamma_h}$  ( $p_{\gamma_l}$ ) and  $\vec{a}_{\gamma_h}$  ( $\vec{a}_{\gamma_l}$ ) denote the momentum and the transverse position of the higher (lower) energetic photon cluster, which are determined together with the unmeasured quantities  $\theta_{\gamma_h}$  ( $\theta_{\gamma_l}$ ) and  $\varphi_{\gamma_h}$  ( $\varphi_{\gamma_l}$ ) denoting the scatter and azimuth angle of the higher (lower) energetic photon,
- $\vec{r}_v$  denotes the vertex position.

Note, that the position of the muons is parameterized as transverse coordinates at a certain longitudinal position. The COMPASS analysis software allows propagating the muon through the magnetic field using Runge–Kutta methods. Hereby, the transverse position of the muons at the longitudinal position of the vertex is used as the input to the kinematic fit. As for the transverse position of the photon clusters, they are given at the longitudinal position of the respective ECal with coordinates estimated using the cluster's center of gravity.

The kinematic fitter then calculates corrections  $\Delta\vec{k}$  to the measured quantities  $\vec{k}$  such that the corrected measurements:

$$\vec{k}_{fit} = \vec{k} + \Delta\vec{k}, \quad (6.6)$$

together with the unmeasured quantities  $\vec{h}$  minimize the least squares function ([31, p. 109])

$$\chi^2(\vec{k}) := \Delta\vec{k}^T \hat{C}^{-1} \Delta\vec{k}. \quad (6.7)$$

Here,  $\hat{C}$  denotes the covariance matrix corresponding to the measured quantities  $\vec{k}$ . The minimization of  $\chi^2(\vec{k})$  under fulfillment of the constraints  $g(\vec{k}, \vec{h})$  is performed by minimizing

$$L(\vec{k}, \vec{\lambda}) = \chi^2(\vec{k}) + 2 \sum_{i=1}^N \lambda_i g_i(\vec{k}, \vec{h}), \quad (6.8)$$

using the Lagrange multiplier method. The  $N$  constraints are described in the following.

### Momentum and energy conservation

$$\begin{aligned} g_i &= p_{\mu,i}^{fit} - p_{\mu',i}^{fit} - p_{p',i}^{fit} - p_{\gamma_h,i}^{fit} - p_{\gamma_l,i}^{fit} = 0, \\ g_4 &= E_{\mu}^{fit} + m_p c^2 - E_{\mu'}^{fit} - E_{p'}^{fit} - E_{\gamma_h}^{fit} - E_{\gamma_l}^{fit} = 0, \end{aligned} \quad (6.9)$$

$\forall i \in \{1, 2, 3\}$  denoting the component of the three-vectors. The superscript "fit" denotes quantities that are corrected by the kinematic fit.

**Common vertex for all tracks (except initial and final state proton)**

$$\begin{aligned}
g_{5+i} &= p_{j,3}^{fit} (x_v - x_j^{fit}) - p_{j,1}^{fit} (z_v - z_j^{fit}) = 0, \\
g_{6+i} &= p_{j,3}^{fit} (y_v - y_j^{fit}) - p_{j,2}^{fit} (z_v - z_j^{fit}) = 0,
\end{aligned} \tag{6.10}$$

$\forall (i,j) \in \{(0, \mu), (2, \mu'), (4, \gamma_h), (6, \gamma_l)\}$  denoting the tracks of the initial and final state muons and the photons. All tracks are constrained to the common vertex denoted by  $\vec{r}_v = (x_v, y_v, z_v)$ .

The structure of the constraints arises through the parametrization of a track of a particle by a straight line

$$\vec{r}(\beta) = \vec{r}' + \beta \vec{p}, \tag{6.11}$$

with  $\vec{r}'$  a known point on the track,  $\vec{p}$  the momentum of the particle and  $\beta$  a free parameter. For the z- and x-component, one finds

$$\begin{aligned}
z &= z' + \beta p_3 \Rightarrow \beta p_3 = z - z', \\
x &= x' + \beta p_1 \Rightarrow x p_3 = x' p_3 + \beta p_1 p_3, \\
&\Rightarrow x p_3 = x' p_3 + p_1 (z - z'), \\
&\Rightarrow p_3 (x - x') + p_1 (z - z') = 0.
\end{aligned} \tag{6.12}$$

Analogous for the y-component

$$\Rightarrow p_3 (y - y') + p_2 (z - z') = 0. \tag{6.13}$$

**Constraints for final state proton**

$$\begin{aligned}
g_{13+i} &= p_{p',3}^{fit} (x_j^{fit} - x_v) - p_{p',1} (z_j^{fit} - z_v) = 0, \\
g_{14+i} &= p_{p',3}^{fit} (y_j^{fit} - y_v) - p_{p',2} (z_j^{fit} - z_v) = 0,
\end{aligned} \tag{6.14}$$

$\forall (i,j) \in \{(0, A), (2, B)\}$  denoting the measured points in the inner respectively outer ring of CAMERA<sup>2</sup>. These so-called extrapolation constraints are very similar to the vertex constraints. Here, it is assumed that the particle originates from the vertex  $\vec{r}_v$  and a point on the track  $\vec{r}$  is given by (cf. Eq. 6.11)

$$\vec{r}(\beta) = \vec{r}_v + \beta \vec{p}. \tag{6.15}$$

Through transformations analogous to Eq. 6.12 one arrives at the given constraints.

---

<sup>2</sup>Note that in case of CAMERA, the measured quantities are actually given in a cylindrical coordinates so that a coordinate system transition to Cartesian coordinates is required.

**Mass constraint**

$$g_{17} = (E_{\gamma_h}^{fit} + E_{\gamma_l}^{fit})^2 - (\vec{p}_{\gamma_h}^{fit} + \vec{p}_{\gamma_l}^{fit})^2 - m_{\pi^0}^2 = 0, \quad (6.16)$$

the invariant mass of the photon system is constrained to the  $\pi^0$  PDG [2] mass  $m_{\pi^0}$ .

The kinematic fit is used to arrive at the best determination for the kinematic variables in the analysis of the exclusive  $\pi^0$  muoproduction. The fit is important in the determination of  $t$ , the square of the four-momentum transfer. Here, the fit performs the transition between the low  $|t|$  region, where the determination using CAMERA is superior,

$$t_{cam} = (p - p')^2,$$

and the high  $|t|$  region where the spectrometer determination is superior<sup>3</sup>,

$$k := \nu - \sqrt{\nu^2 + Q^2} \cdot \cos \theta_{\gamma^* \pi^0},$$

$$t_{spec} = \frac{-Q^2 - 2\nu k}{1 + k/m_p},$$

with  $\theta_{\gamma^* \pi^0}$  being the polar angle between the virtual-photon and the  $\pi^0$ . This matter is also illustrated in (Fig. 6.2). Furthermore, the kinematic fit is used to

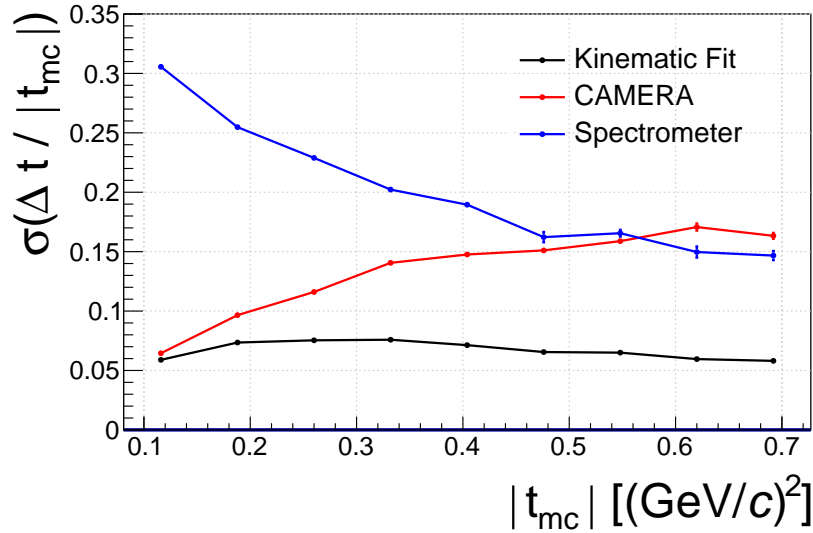


**FIGURE 6.2:** Relative resolution for different methods to calculate the square of the four-momentum transfer to the target proton  $t$ , evaluated using an exclusive  $\pi^0$  muoproduction Monte Carlo. The quantity  $\Delta t$  is determined using the kinematic fit ( $\Delta t = t_{fit} - t_{mc}$ ), CAMERA ( $\Delta t = t_{cam} - t_{mc}$ ) and spectrometer ( $\Delta t = t_{spec} - t_{mc}$ ) as a function of the generated square of four-momentum transfer  $t_{mc}$ .

<sup>3</sup>This determination is called «constraint  $t$ » in literature, see *e.g.* Ref. [31] for derivation.

improve the signal to background ratio in the event selection of the analysis, Subsection 6.3.7.

### 6.3 Event selection

This section outlines the event selection for the process  $\mu p \rightarrow \mu' p' \pi^0 \rightarrow \mu' p' \gamma_h \gamma_l$ . The two photons are ordered by their energy, where  $\gamma_h$  ( $\gamma_l$ ) represents the higher (lower) energetic photon. The notation of the four-momenta is depicted in Fig. 6.3. They read  $k, k', q, q', p, p'$  for the incident muon, outgoing

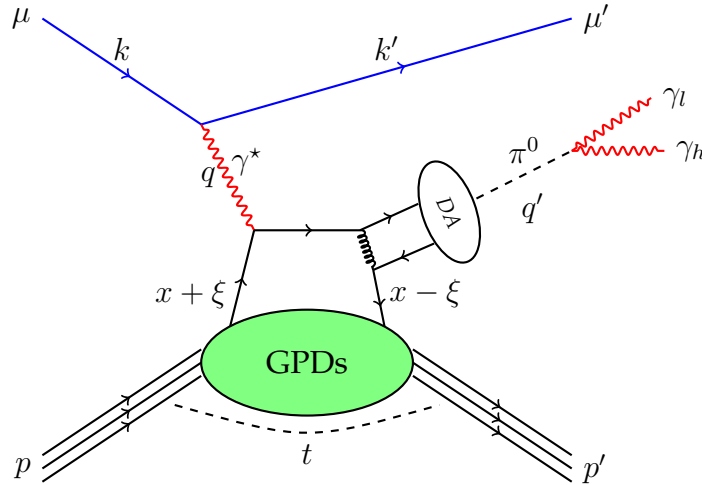


FIGURE 6.3: Schematic diagram for the hard exclusive meson production process in the handbag model.

muon, virtual-photon,  $\pi^0$  meson, target proton and outgoing proton. The event selection for the process involves a number of steps that are outlined in detail in the following sections and shortly summarized in the following list:

1. Filter vertices with constraints on the quality of the incoming and outgoing muons and on the vertex properties.
2. Create pairs of neutral clusters in the electromagnetic calorimeters to reconstruct the decayed  $\pi^0$ . Combine the cluster pairs with the vertices of step 1 to obtain the  $\pi^0$  four-momentum. At this point, a prediction for the recoil proton can be made using only spectrometer quantities.
3. Reconstruct tracks of recoil protons in CAMERA.
4. Compare the recoil proton tracks to the predicted recoil proton tracks of step 2 by means of so-called exclusivity variables. Apply cuts on the exclusivity variables.
5. Accept the event, if exactly one combination survives step 4.
6. Accept the event, if the mass of the two photon system  $M_{\gamma\gamma}$  is compatible with the  $\pi^0$  mass.
7. Apply kinematic fit and accept events based on conditions established by the fit.

As general selection criteria, only events associated with a physics trigger (MT, LT or OT, *cf.* Section 3.5) are considered.

### 6.3.1 Selection of beam particles and vertices

The demands on the beam track are specified in accordance with the luminosity determination in Subsection 6.1.1. In addition, the following requirements are used to select vertex candidates, also taking into account the identification of the scattered particle.

**Only primary vertices:** Vertices are reconstructed and tagged as *primary* by the COMPASS reconstruction software CORAL when the vertex originates from a beam particle.

**Vertex inside target:** In addition to the «Beam through target» requirement posed in the luminosity determination, the vertex transverse distance from the target center is required to be smaller than 1.9 cm. The Fig. 6.4 shows the transverse position of the selected vertices for data and Monte Carlo with and without the «Beam through target» respectively the condition for the transverse distance. In addition, the longitudinal position of the vertex has to be within  $-311.2 \text{ cm} < z_v < -71.2 \text{ cm}$  (*cf.* Fig. 6.1), resulting in the effective target length of 240 cm. The distribution of the longitudinal vertex position is given in Fig. 6.5.

**One outgoing particle, correct charge:** The vertex must have only one outgoing particle which must have the same charge as the beam track.

**Outgoing particle passed muon filter:** The outgoing particle must traverse at least 15 radiation lengths to qualify as a muon candidate.

**Outgoing particle track longitudinal lever:** The track of the outgoing particle must be measured over a long range, where the first (last) measured point is located before (after) the first spectrometer magnet:  $Z_{first} < 350 \text{ cm}$  and  $Z_{last} > 350 \text{ cm}$ .

**DIS cuts:** The DIS cuts of  $1 (\text{GeV}/c)^2 < Q^2 < 5 (\text{GeV}/c)^2$  and  $8.5 \text{ GeV} < \nu < 28 \text{ GeV}$  select an area in the phase space where the COMPASS acceptance is valid, see Section 6.5. Also, the lower  $Q^2$  cut is required to be in the domain of perturbative QCD.

Different properties of the selected muons are depicted in Fig. 6.6. The distributions for the photon virtuality  $Q^2$  and the Lorentz invariant quantity  $\nu$  are given in Fig. 6.7 together with the distribution of the Bjorken scaling variable  $x_{Bj}$  and the photon polarization factor  $\varepsilon$ .

Events may contain multiple vertices fulfilling the above conditions. The list of selected vertices is further referred to as *vertex candidates*.

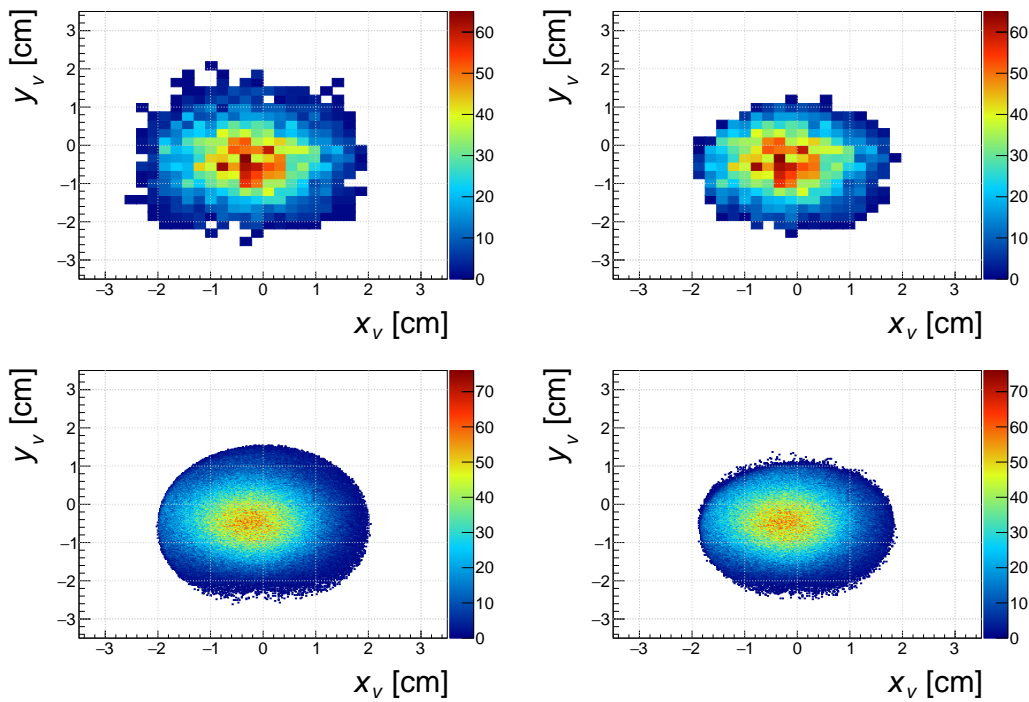


FIGURE 6.4: Transverse position of the vertex for data (top) and Monte Carlo (bottom) before (right) and after (left) demanding that the transverse distance of the vertex is smaller than 1.9 cm and that the incident muon track points through the full length of the target.

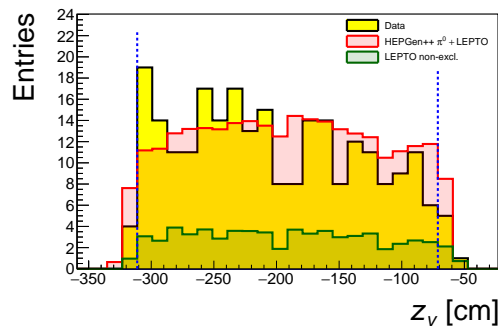


FIGURE 6.5: Distribution of the longitudinal vertex position. The distributions are shown for the full event selection while disabling the cut on the respective variable if applicable. Note, that other selection cuts, most notably the selection cuts for the proton tracks (Subsection 6.3.3), already constrain this quantity.

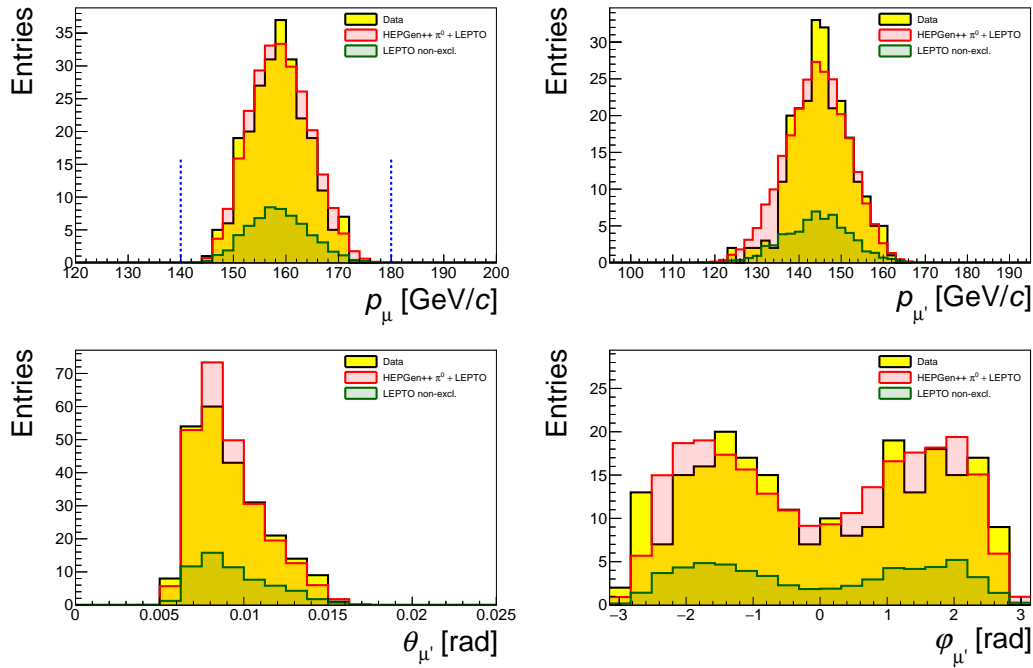


FIGURE 6.6: Top left (right): magnitude of the momentum of the initial (final) state muon. Bottom left (right): scattering (azimuthal) angle of the final state muon in the laboratory system. The distributions are shown for the full event selection while disabling the cut on the respective variable if applicable.

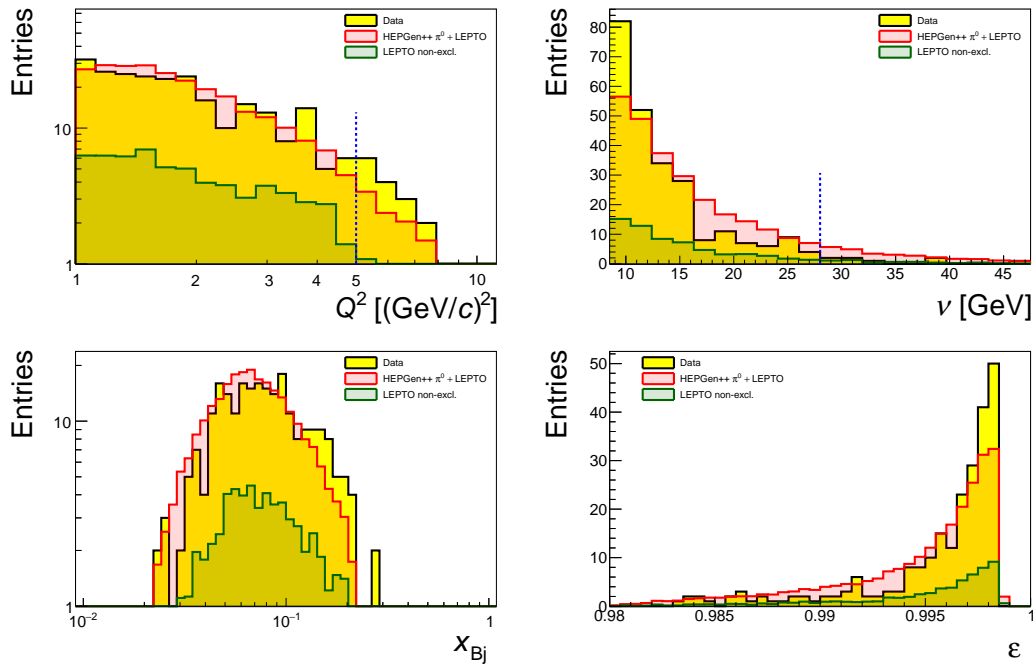


FIGURE 6.7: Distribution of kinematic variables. The distributions are shown for the full event selection while disabling the cut on the respective variable if applicable.

### 6.3.2 Selection of neutral cluster pairs

Only clusters in ECal0 and ECal1 are considered for this analysis. Because of the kinematic coverage, the signal in ECal2 is expected to be very weak and drowned by noise. In ECal1, clusters that are associated to a charged track are ignored. Since ECal0 is placed straight after the target, there is no tracking and no track can be associated to a cluster. Therefore, all clusters are treated as neutral clusters.

A cut on the cluster timing as a function of the cluster energy is applied as illustrated in Fig. 6.8. Clusters are combined in pairs when the higher energetic

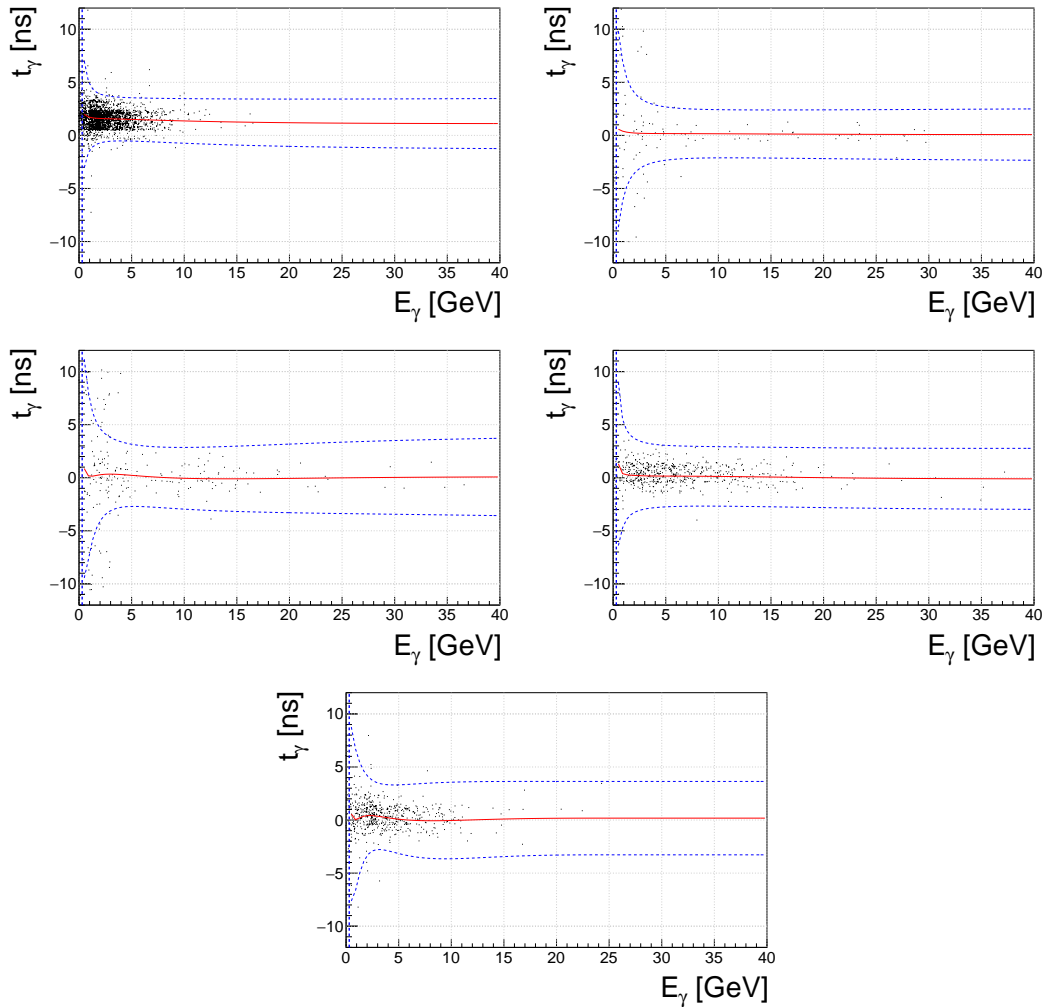


FIGURE 6.8: Cluster time as a function of the cluster energy. The mean cluster energy (red line) was extracted by [101]. A two sigma cut is applied (blue hatched lines).

cluster exceeds the thresholds

$$\begin{aligned} E_{\gamma_h, ECal0} &> 1 \text{ GeV}, \\ E_{\gamma_h, ECal1} &> 2 \text{ GeV}, \end{aligned}$$

and the lower energetic cluster exceeds the hardware threshold of the read-out electronics

$$E_{\gamma_i} > 0.3 \text{ GeV.}$$

The hereby created list of cluster pairs is further referred to as  $\pi^0$  candidates.

### 6.3.3 Selection of proton tracks

Proton tracks inside CAMERA are selected if

- the hits belong to scintillators that face each other,
- the velocity of the particle fulfills  $0.1 < \beta := \frac{v}{c} < 1$ ,
- the longitudinal positions of the hits in the inner and outer ring are inside the domain of the scintillators

$$\begin{aligned} -366.19 \text{ cm} &< z_A < 8.81 \text{ cm}, \\ -338.94 \text{ cm} &< z_B < 71.06 \text{ cm}. \end{aligned}$$

The resulting list of proton tracks measured by CAMERA is further referred to as *proton candidates*.

### 6.3.4 Exclusivity conditions

The track of the recoiled proton can be calculated from pure spectrometer quantities. For this, *vertex candidates* and  $\pi^0$  candidates are combined. For each *vertex candidate* and  $\pi^0$  candidate,  $q'$  is calculated from the positions and energies of the clusters, assuming that they are associated with photons originating from the vertex. The so-called predicted proton four-momentum  $p'_{pred}$  can now be calculated by

$$p'_{pred} = k + p - k' - q'.$$

By matching the predicted proton four-momentum with the *proton candidates*, cuts that are sensitive on the exclusivity of the event are possible. In the following, quantities derived from the predicted proton four-momentum are denoted with the subscript *pred* while the quantities measured by CAMERA have no additional subscript. The investigated variables to check the exclusivity are

- the azimuthal angle  $\varphi$ ,
- the transverse momentum  $p_{\perp}$ ,
- the comparison of inner ring hit position  $z_A$  to the predicted hit position  $z_{A,pred}$ , which is obtained by interpolation between the vertex and the hit in the outer ring  $z_B$  (*cf.* longitudinal position calibration Eq. 5.8),

- the missing mass (or undetected mass) squared  $M_X^2$ .

The exclusivity variables are then defined as follows:

$$\begin{aligned}\Delta\varphi &= \varphi_{pred} - \varphi, \\ \Delta p_{\perp} &= p_{\perp,pred} - p_{\perp}, \\ \Delta z &= z_{A,pred} - z_A, \\ M_X^2 &= (k + p - k' - q' - p')^2,\end{aligned}$$

The cuts applied to the exclusivity variables read

$$\begin{aligned}|\Delta\varphi| &< 0.4 \text{ rad}, \\ |\Delta p_{\perp}| &< 0.3 \text{ GeV}/c, \\ |\Delta z| &< 16 \text{ cm}, \\ |M_X^2| &< 0.3 (\text{GeV}/c^2)^2.\end{aligned}$$

Fig. 6.9 shows the distributions for the exclusivity variables.

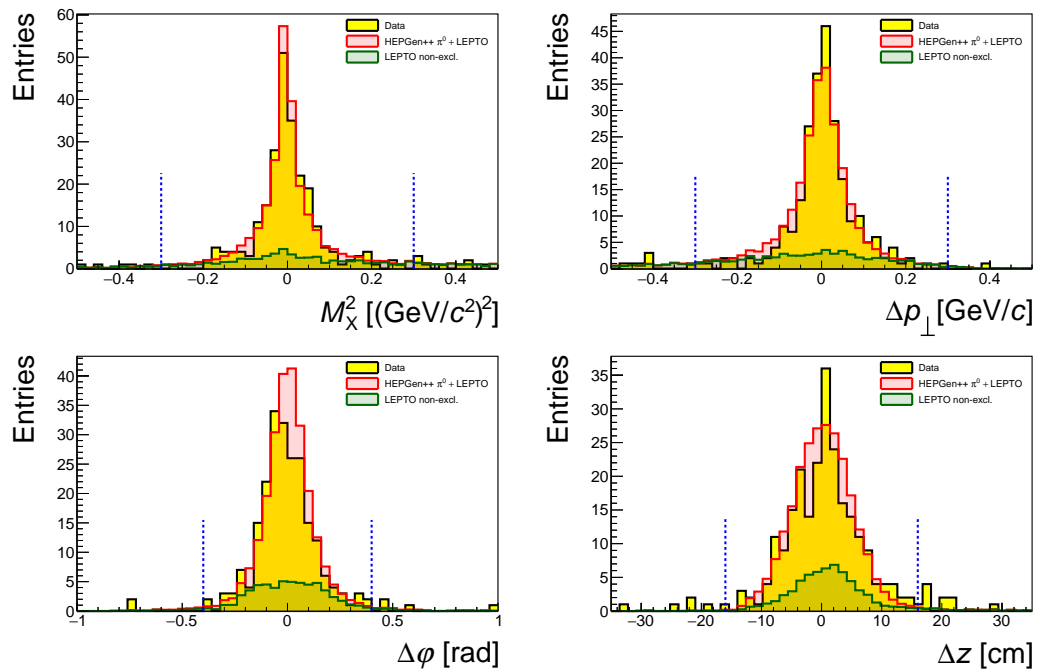


**FIGURE 6.9:** Distribution of exclusivity variables. The distributions are shown for the full event selection while disabling the cut on the respective variable if applicable.

The imposed cuts are not optimized for the event selection at hand but are kept similar to the cuts used in the DVCS event selection ([31, p. 105]). In a future analysis, these cuts may be put more restrictively to suppress background at an earlier stage.

### 6.3.5 Multiplicity condition

The multiplicity  $K$  of an event is given as the number of combinations of *vertex candidates*,  $\pi^0$  candidates and *proton candidates* that fulfill the exclusivity conditions. By definition, an exclusive event must be unambiguous in the association of measured quantities to particles. Hence, in general, only events where  $K = 1$  are selected. As an exception in section 6.4.3, events with higher multiplicity are allowed in order to perform background studies.

### 6.3.6 Cut on $\pi^0$ signal

Fig. 6.10 shows the distribution of the invariant mass of the two photon system  $M_{\gamma\gamma}$ . Here, not the full event selection is used but the conditions imposed by the kinematic fit (see Subsection 6.3.7) are disabled to make the full  $M_{\gamma\gamma}$  spectrum visible. The  $\pi^0$  signal is clearly visible at the nominal  $\pi^0$  mass

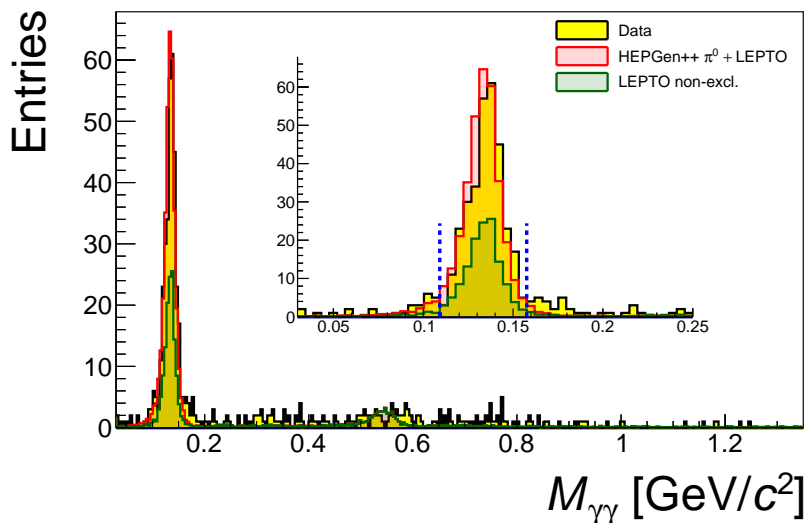


**FIGURE 6.10:** Distribution of the invariant mass of the two photon system  $M_{\gamma\gamma}$ . The distributions are shown for the full event selection while the cuts imposed by the kinematic fit and the cut on the  $\pi^0$  mass are disabled.

( $m_{\pi^0} = \sim 0.135 \text{ GeV}/c^2$ ). In addition, a small peak at the nominal mass of the  $\eta$  meson ( $m_{\eta} = \sim 0.547 \text{ GeV}/c^2$ ) is visible, indicating the possibility of a future measurement of exclusive  $\eta$  muoproduction.

To select exclusive  $\pi^0$  candidate events, a Gaussian is applied to the  $\pi^0$  mass signal which defines a  $2.5\sigma$  cut for the signal selection that reads

$$0.1092 \text{ GeV}/c^2 < M_{\gamma\gamma} < 0.1576 \text{ GeV}/c^2.$$

Fig. 6.11 displays the distribution of the  $\pi^0$  mass signal for the full event selection.

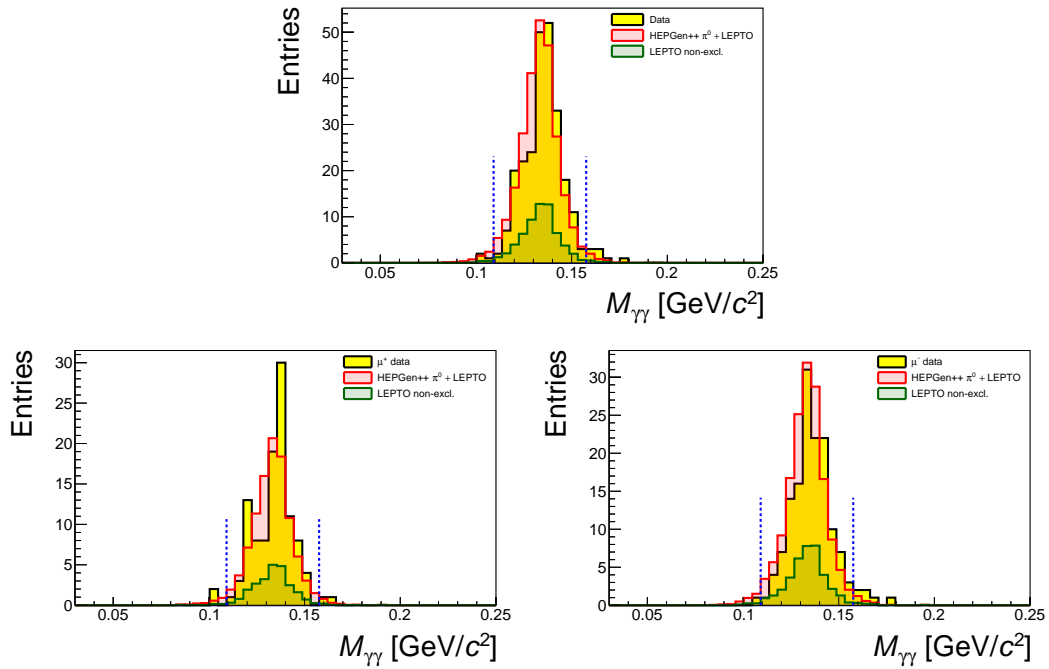


FIGURE 6.11: Distributions for the mass of the two photon system  $M_{\gamma\gamma}$  for  $\mu^+$  (bottom left) and  $\mu^-$  (bottom right) beam and the sum (top). The distributions are shown for the full event selection while disabling the cut on the  $\pi^0$  mass.

### 6.3.7 Kinematic fit

The kinematic fit for the exclusive  $\pi^0$  muoproduction was introduced in Section 6.2. At this stage of the event selection, all quantities for the input to the fit have been gathered and the fit can be executed. The fit performs corrections to the measured quantities and all derived quantities are recalculated. The fit also offers the possibility to sort of rank the events using the  $\chi^2$ . A large  $\chi^2$  indicates that the kinematics of the event doesn't add up which supports the assumption that an event is a background event. Hence, it is possible to improve the signal to background ratio by naively cutting the tail of the  $\chi^2$  distribution. For this, however, one has to be certain that the  $\chi^2$  for data events is comparable to the  $\chi^2$  for Monte Carlo events. This is only true when all resolutions/uncertainties of the measured quantities agree for data and Monte Carlo. If this is not fulfilled, a bias will be introduced in the acceptance calculation and in the background subtraction.

For this analysis, a more conservative approach was chosen. Instead of the  $\chi^2$  distribution, individual pull distributions of specific quantities are used, where the Monte Carlo description and data agree evidently well. This offers a better control over each individual cut. Figures 6.12 to 6.18 show the pulls of the measured quantities that enter the kinematic fit. The pulls are normalized to the difference of the error before and after the fit. Figures B.4 to B.10 in the appendix show the corresponding distributions without normalization.

In general, data and Monte Carlo behave very similar in the fit. However, a shift in the pulls in the longitudinal component of the momentum  $p_{\mu,3}$  and

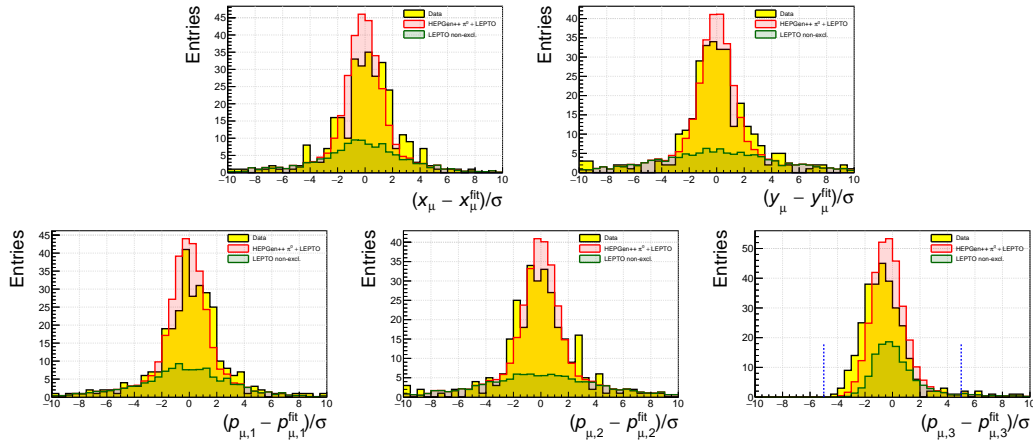


**FIGURE 6.12:** Pull distributions for the incoming  $\mu$ . The quantities  $x$  and  $y$  denote the track position at the  $z$ -position measured at the point closest to the vertex. Here,  $p_{1,2,3}$  denote the components of the momentum vector. The normalization factor  $\sigma$  denotes the difference of the error on the quantity before and after the fit. The distributions are shown for the full event selection while disabling all cuts imposed by the kinematic fit.

$p_{\mu',3}$  is visible for the muons. This discrepancy between the measurement of the beam and scattered muon was also found in [31, p. 110], yet its origin remains unknown. The issue is treated as a systematic uncertainty in Subsection 6.7.5. Also, the widths of the pulls for data and Monte Carlo do not always agree perfectly, which supports the decision to not blindly cut on the  $\chi^2$  distribution. The following pull distributions are identified to be eligible for a cut:

- $\varphi$  angle of the hit in the A ring of CAMERA:  $\left| (\varphi_A - \varphi_A^{fit}) / \sigma \right| < 2.5$ ,
- $\varphi$  angle of the hit in the B ring of CAMERA:  $\left| (\varphi_B - \varphi_B^{fit}) / \sigma \right| < 2.5$ ,
- $z$  momentum of incoming  $\mu$ :  $\left| (p_{\mu,3} - p_{\mu,3}^{fit}) / \sigma \right| < 5$ ,
- $z$  momentum of outgoing  $\mu'$ :  $\left| (p_{\mu',3} - p_{\mu',3}^{fit}) / \sigma \right| < 5$ ,
- $x$  position of the higher energetic cluster:  $\left| (x_{\gamma_h} - x_{\gamma_h}^{fit}) / \sigma \right| < 5$ ,
- $y$  position of the higher energetic cluster:  $\left| (y_{\gamma_h} - y_{\gamma_h}^{fit}) / \sigma \right| < 5$ ,
- $x$  position of the lower energetic cluster:  $\left| (x_{\gamma_l} - x_{\gamma_l}^{fit}) / \sigma \right| < 5$ ,
- $y$  position of the lower energetic cluster:  $\left| (y_{\gamma_l} - y_{\gamma_l}^{fit}) / \sigma \right| < 5$ .

The cuts are also shown in the respective figures. In addition, Figures B.2 to B.3 in the appendix show the kinematic variables and the exclusivity variables without the cuts on the pull distributions.

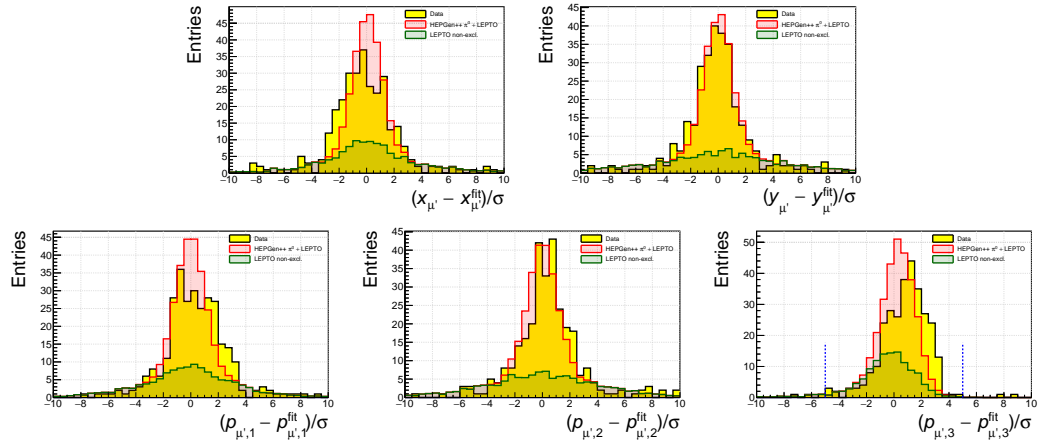


**FIGURE 6.13:** Pull distributions for the outgoing  $\mu$ . The quantities  $x$  and  $y$  denote the track position at the  $z$ -position measured at the point closest to the vertex. Here,  $p_{1,2,3}$  denote the components of the momentum vector. The normalization factor  $\sigma$  denotes the difference of the error on the quantity before and after the fit. The distributions are shown for the full event selection while disabling all cuts imposed by the kinematic fit.

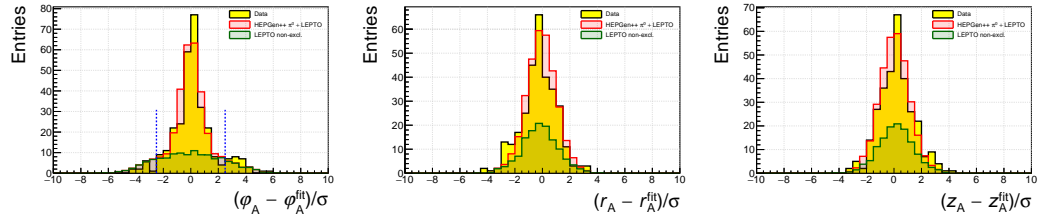


**FIGURE 6.14:** Pull distributions for the position in ring A of CAMERA. The measured quantities are the azimuth angle  $\varphi$ , the radius  $r$  and the longitudinal position  $z$  of the hit. The normalization factor  $\sigma$  denotes the difference of the error on the quantity before and after the fit. The distributions are shown for the full event selection while disabling all cuts imposed by the kinematic fit.

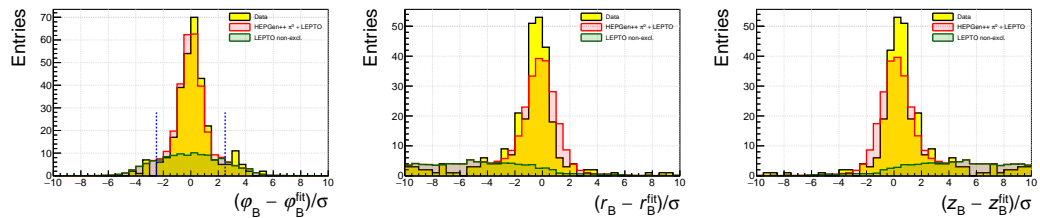


**FIGURE 6.15:** Pull distributions for the position in ring B of CAMERA. The measured quantities are the azimuth angle  $\varphi$ , the radius  $r$  and the longitudinal position  $z$  of the hit. The normalization factor  $\sigma$  denotes the difference of the error on the quantity before and after the fit. The distributions are shown for the full event selection while disabling all cuts imposed by the kinematic fit.

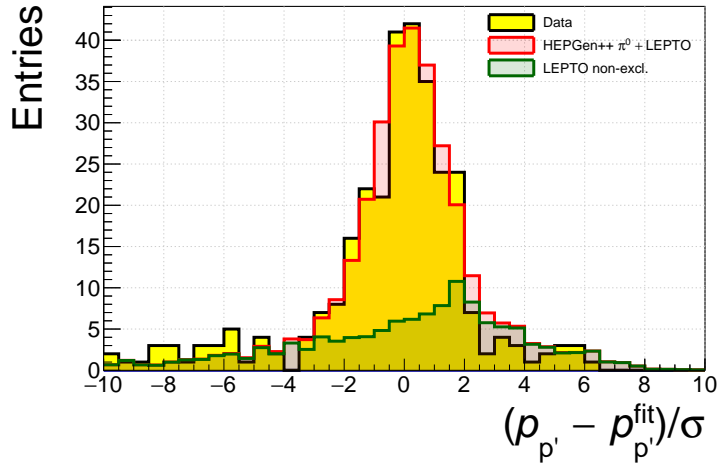


**FIGURE 6.16:** Pull distribution for the magnitude of the momentum of the recoil proton. The normalization factor  $\sigma$  denotes the difference of the error on the quantity before and after the fit. The distributions are shown for the full event selection while disabling all cuts imposed by the kinematic fit.

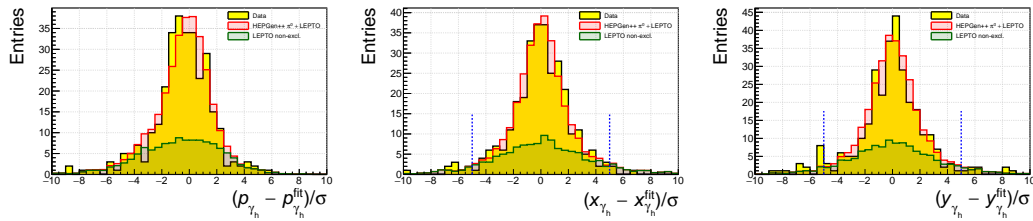


**FIGURE 6.17:** Pull distributions for the higher energetic  $\gamma$ .  $x$  and  $y$  denote the track position at the  $z$ -position measured at the respective ECal,  $p$  denotes the magnitude of the momentum of the  $\gamma$ . The normalization factor  $\sigma$  denotes the difference of the error on the quantity before and after the fit. The distributions are shown for the full event selection while disabling all cuts imposed by the kinematic fit.

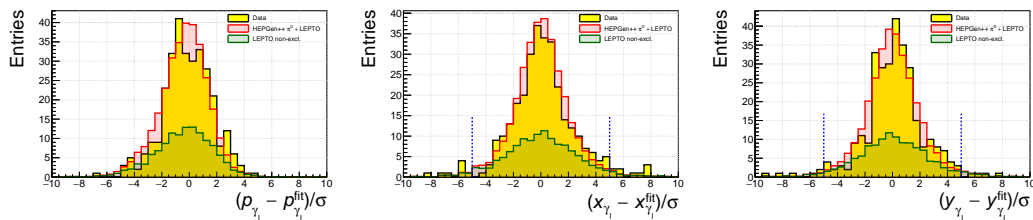


**FIGURE 6.18:** Pull distributions for the lower energetic  $\gamma$ .  $x$  and  $y$  denote the track position at the  $z$ -position measured at the respective ECal,  $p$  denotes the magnitude of the momentum of the  $\gamma$ . The normalization factor  $\sigma$  denotes the difference of the error on the quantity before and after the fit. The distributions are shown for the full event selection while disabling all cuts imposed by the kinematic fit.

## 6.4 Simulations

After the application of the event selection, the signal still includes background that can not be easily separated. The majority of the background in the measurement of the exclusive  $\pi^0$  muoproduction at COMPASS is originating from events where the target proton was destroyed. The detected recoil particle in CAMERA may then be a result of the fragmentation process instead of the scattered target proton. Likewise, the detected clusters may be a result of a  $\pi^0$  produced in the fragmentation process. In the events where the proton was destroyed the  $\pi^0$  is not produced exclusively but it is accompanied by other particles. These events are further referred to as non-exclusive background.

The kinematic and topological properties of non-exclusive background processes can be quite well simulated by Monte Carlo generators which allows studying the detector response for these events. In particular, the simulation of the non-exclusive background will be used to estimate the irreducible background in the presented analysis. For this, the LEPTO generator is used whose parameters were tuned to fit COMPASS best. A detailed description of LEPTO is given in [102] while the adjustments for COMPASS are outlined in [103]. As it will be demonstrated in Subsection 6.4.2, the Monte Carlo yield has to be normalized to the data which is the subject of Subsection 6.4.3.

For a pure simulation of signal events, HEPGEN++, a generator not only for the exclusive  $\pi^0$  muoproduction process, is used. It completes the model of the data in conjunction with LEPTO. Also, the generator is used for the evaluation of the acceptance correction in Section 6.5. Details about the generator and the implemented processes can be found in [104, 105].

The simulation of the detector response is provided by TGEANT [106] which is built on top of the GEANT4 [107] framework. Starting from upstream of the liquid hydrogen target, it includes all relevant active and inactive materials of the COMPASS experiment which are in the acceptance of the interesting final state particles. Among others, it also provides simulations for pile-up and the beam halo, electronic noise in the calorimeters and a parametrization for the calorimeter particle cluster shape tuned to data. The output of TGEANT is then further processed by the same production chain as used for the data<sup>4</sup>. The event selection of Monte Carlo events differs then only marginally from the one described in Section 6.3. Most notably, since the beam momentum stations are not included in the simulation, the respective cuts have to be disabled. Further, in following subsections the DIS cuts mentioned in Section 6.3 are replaced by the following cuts

- $y > 0.05$ ,
- $Q^2 > 1 \text{ (GeV/c)}^2$ ,
- $|t_{cam}| > 0.08 \text{ (GeV/c)}^2$ ,

<sup>4</sup> The Monte Carlo samples used are the productions identified with "Production\_16-02-v2", see [108].

to enhance the statistics and therefore the stability of the normalization procedure. Here,  $t_{cam}$  denotes the square of the four-momentum transfer to the target nucleon using the four-momentum of the recoiled proton  $p'$  as determined by the CAMERA detector.

### 6.4.1 HEPGEN++

The HEPGEN++ generator is a weighted Monte Carlo generator. Each event generated at a specific point in the phase space  $\Delta\Omega$  is weighted by the cross-section evaluated at that point. Still, the generator does not distribute the events flatly in the phase space. The number of generated events is distributed over the phase space approximately like the expected number of real data events.

Fig. 6.19 shows the mass of the two photon system  $M_{\gamma\gamma}$  after the event selection for data and the HEPGEN++ Monte Carlo sample. Here, the HEPGEN++ Monte Carlo sample is normalized to the Monte Carlo luminosity  $\mathcal{L}_{hep}$

$$\mathcal{L}_{hep} = \frac{\sum_{i=1}^{N_{hep}^{\Delta\Omega}} w_i}{\sigma_{tot}}, \quad (6.17)$$

$$\sigma_{tot} = \int_{\Delta\Omega} \frac{d\sigma_{HEPGEN++}^{\pi^0}}{d\Omega} d\Omega, \quad (6.18)$$

with  $w$  the event weight,  $N_{hep}^{\Delta\Omega}$  the total number of events generated in the phase space  $\Delta\Omega$  and  $\sigma_{tot}$  the integrated cross-section in the phase space  $\Delta\Omega$ . The integrated cross-section  $\sigma_{tot}$  is calculated by integrating the differential cross-section function  $\frac{d\sigma_{HEPGEN++}^{\pi^0}}{d\Omega}$  in the phase space  $\Delta\Omega$ . The corresponding function from the HEPGEN++ package was used to obtain the differential cross-section in accordance with how the events  $N_{hep}^{\Delta\Omega}$  were generated. As

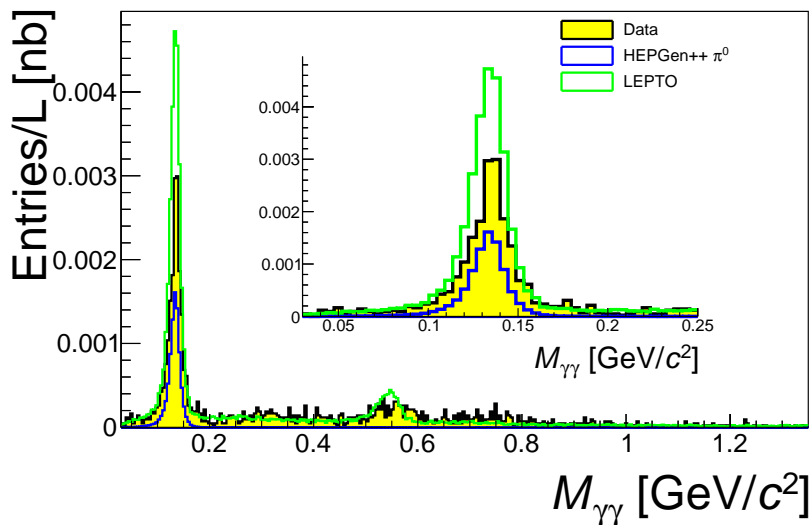


FIGURE 6.19: Distribution of the invariant mass of the two-photon system  $M_{\gamma\gamma}$  for data, HEPGEN++ and LEPTO, normalized to their respective luminosities.

expected, the events generated by HEPGEN++ are only located around the nominal  $\pi^0$  mass. It is worth noting, that the model implemented in HEPGEN++ for the exclusive  $\pi^0$  muoproduction process seems to predict a reasonable cross-section for COMPASS kinematics.

### 6.4.2 LEPTO

The LEPTO generator is a well-accepted tool for generating SIDIS events. Again, Fig. 6.19 shows the mass of the two photon system  $M_{\gamma\gamma}$  after the event selection for data and the LEPTO Monte Carlo sample. The Monte Carlo luminosity  $\mathcal{L}_{lep}$ , used for the normalization of the LEPTO Monte Carlo, is given by

$$\mathcal{L}_{lep} = \frac{N_{lep}^{\Delta\Omega}}{\sigma_{tot}}, \quad (6.19)$$

with  $N_{lep}^{\Delta\Omega}$  the total number of events generated in the phase space  $\Delta\Omega$  and  $\sigma_{tot}$  the integrated cross-section in the phase space, which is provided by LEPTO<sup>5</sup>.

It is striking, that the distribution for LEPTO in Fig. 6.19 shows a strong signal at the nominal  $\pi^0$  mass. Further investigations show, that LEPTO itself produces events that feature an exclusive  $\pi^0$  event topology, *i.e.* four final state particles - the scattered muon, a proton and two photons. Hence, the LEPTO Monte Carlo can be split into three contributions:

1. Events with exclusive  $\pi^0$  topology and a recoiling proton.
2. Events with exclusive  $\pi^0$  topology and a proton from hadronization.
3. other events.

Both events of type 1 and type 2 have to be considered as signal events since they feature an exclusive  $\pi^0$  muoproduction topology in the sense that they are indistinguishable from events generated by HEPGEN++.

To further understand the origin of these events on the level of the generator, a typical JETSET output for the events of type 1 is given in listing B.11 and one for the events of type 2 is given in listing B.12. In case of the type 1 events, the struck proton seems to immediately recombine with the active quark while in the case of type 2 events, the active quark forms a cluster from which by chance a single proton is created.

The similarity of the events of type 1 and 2 to HEPGEN++ is demonstrated best when studying the behavior of the different event types when the kinematic fit is applied as shown in Fig. 6.20. The full set of pull distributions is shown in Figures B.13 to B.19 in the appendix. It can be observed, that the entries in the pull for event type 1, type 2 and HEPGEN++ are very similar distributed. On the other hand, the pull distribution for events of type 3 very well describes the background of the data, which is especially visible in the

<sup>5</sup>See «PARL[23]» in [102, p. 25].

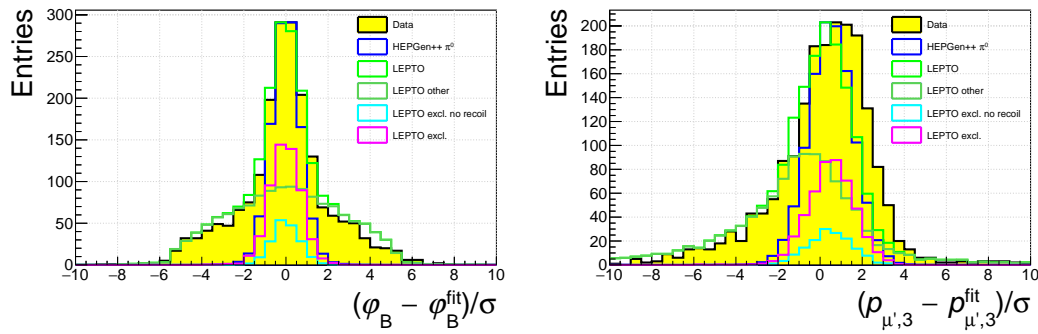


**FIGURE 6.20:** Pull distributions for data, HEPGEN++ and LEPTO respectively different event types produced by LEPTO. Events of type 1 are labeled by “LEPTO excl.”, events of type 2 by “LEPTO excl. no recoil” and events of type 3 by “LEPTO other”. The left pull distribution shows the azimuth angle in the outer scintillator  $\varphi_B$  while the right pull distribution shows the  $z$  component of the momentum of the scattered muon  $p_{\mu',3}$ . Here, HEPGEN++ and the full contribution of LEPTO are normalized to the data using the integral.

pull distribution for the azimuth angle in the outer scintillator  $\varphi_B$ .

Since LEPTO shall be used to only describe the background in the measurement of the exclusive  $\pi^0$  muoproduction, event types 1 and 2 are unwanted. Only the event types 3 of LEPTO are further used and labeled as “LEPTO background”. The full description of the data is then a combination of LEPTO type 3 events to account for the non-exclusive background and HEPGEN++ to model the signal. The mixture of the two, respectively the amount of “LEPTO background” needed to describe the background in data, is subject of Subsection 6.4.3.

### 6.4.3 Normalization

The objective is to find the correct normalization for “LEPTO background” to describe the non-exclusive background in the data. The procedure is applied for  $\mu^+$  and  $\mu^-$  separately, to be exemplary, in the following only  $\mu^-$  is considered.

As a starting point, both “LEPTO background” and HEPGEN++ are independently normalized to the region of the  $M_{\gamma\gamma}$  distribution as shown on the left-hand side in Fig. 6.21. At that point, each Monte Carlo describes the full signal. Proceeding from this normalization, the procedure in principle scales and sums up the two Monte Carlo contributions such that a good description for the data is achieved. For this, the distributions of the exclusivity variables (cf. Subsection 6.3.3) are examined. By removing the respective exclusivity condition in the so-called *signal like* selection, the distributions are both sensitive to the signal at their central value and also to background in their tails. While in the *signal like* selection the signal dominates, in the so-called *background like* selection the background dominates. For this, the event selection is modified to select events with an ambiguous number of exclusive candidates by requiring  $K > 1$  (cf. Subsection 6.3.5). The right-hand side of

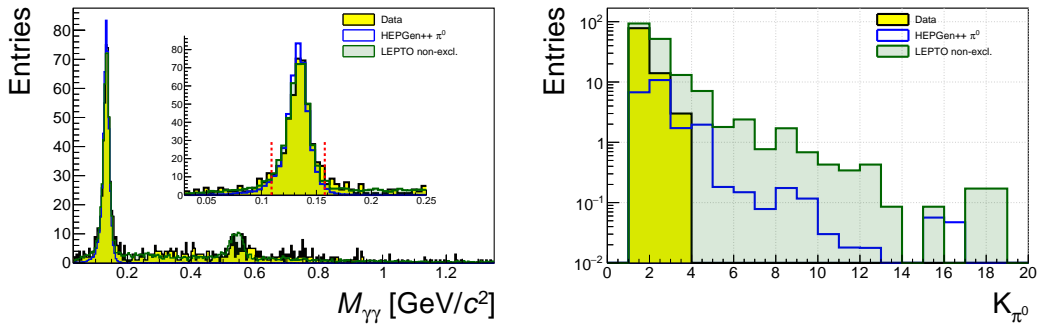


FIGURE 6.21: Left: Spectrum for the mass of the two photon system  $M_{\gamma\gamma}$  for data, HEPGEN++ and LEPTO, normalized to the integral of data events inside the  $M_{\gamma\gamma}$  cut range (cf. Subsection 6.3.6). Right: Distribution of multiplicity for the *background like* selection (same normalization as in the left plot). Although in the event selection  $K > 1$  is required, one can see entries for  $K_{\pi^0} = 1$ . This is because the cut on the  $\pi^0$  mass is applied after the multiplicity condition. In comparison to data, LEPTO tends to produce higher multiplicities.

Fig. 6.21 shows the distribution of multiplicity  $K_{\pi^0}$  for the *background like* selection. The quantity  $K_{\pi^0}$  denotes the number of exclusive candidates within the  $\pi^0$  mass range. The discrimination between  $K$  and  $K_{\pi^0}$  is due to the  $\pi^0$  signal cut (Subsection 6.3.6) being applied after the multiplicity condition (Subsection 6.3.5).

It can be observed, that the statistics in the data for higher multiplicities ( $K_{\pi^0} > 3$ ) is not sufficient (mind the logarithmic scale in Fig. 6.21). Therefore, a cut is introduced, limiting the multiplicity  $K_{\pi^0} < 3$ . The evolution of the  $M_X^2$  distribution as a function of the upper limit of  $K_{\pi^0}$  is displayed in Fig. 6.22. The dependency of the method on the upper limit of  $K_{\pi^0}$  is studied at the end of the subsection.

As one can observe in Fig. 6.22, events originating from HEPGEN++ create a narrow peak centered around  $M_X^2 = 0$  where the width is the result of detector resolutions. Even though HEPGEN++ only creates exclusive events, due to the admixture of background in the Monte Carlo simulation (e.g. noise in ECals), events with multiplicity  $K > 1$  exist.

“LEPTO background” events are almost equally distributed over the full range of the histogram with a small peak at  $M_X^2 = 0$ . Positive  $M_X^2$  values are enhanced as a consequence of not detecting all final state particles in non-exclusive events. Negative  $M_X^2$  values are the result of misidentifying final state particles.

The objective is now to scale LEPTO and HEPGEN++ such that the best description of the data is achieved. For this, a least squares fit is used minimizing the sum  $S$  running over the  $N$  bins of the histogram:

$$S(\vec{r}) = \sum_{i=1}^N (w_i r_i)^2. \quad (6.20)$$

Different residuals  $r_i$  are investigated to find a convincing agreement between data and model. For the weight of the residual  $w_i = 1/\sigma_i$ , the statistical

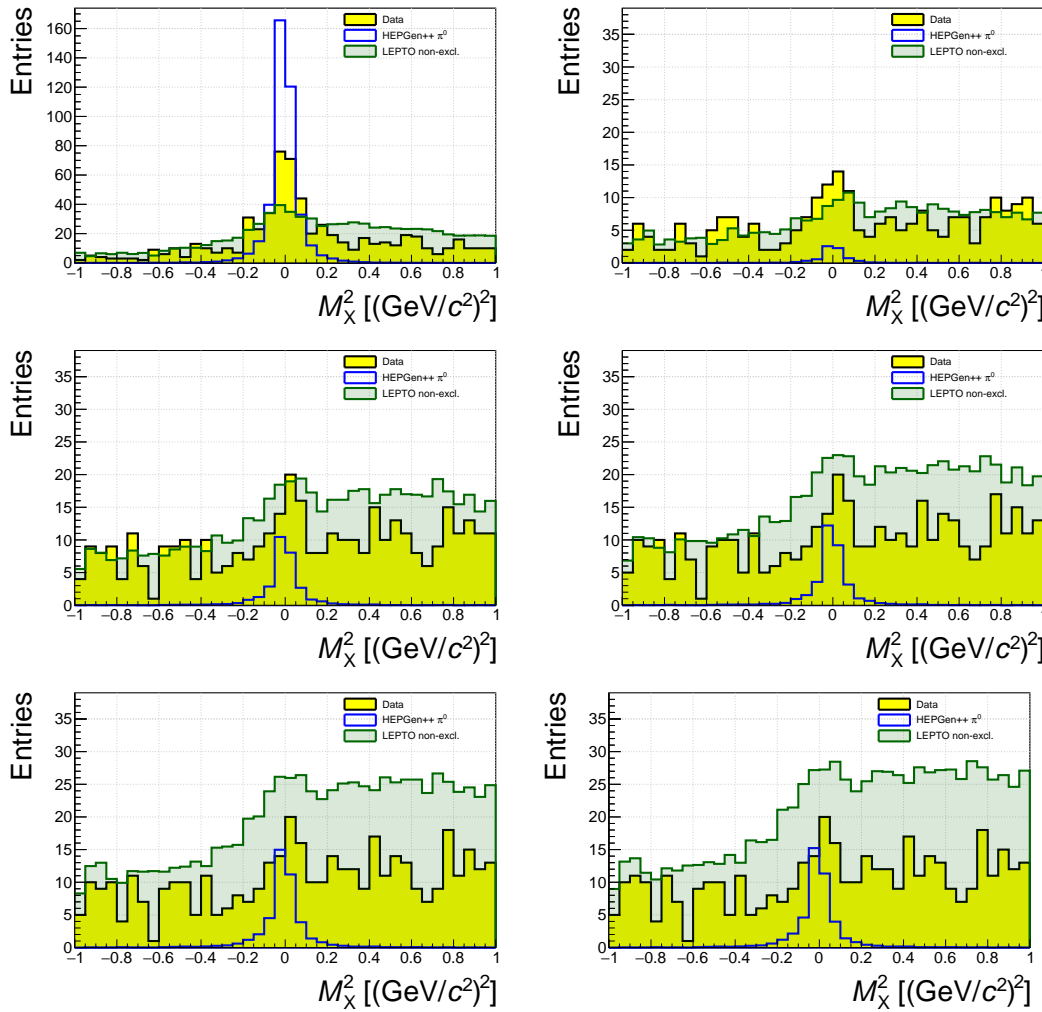


**FIGURE 6.22:** Evolution of the  $M_X^2$  distribution for different multiplicities. Top left: *signal like* selection, where a  $K = 1$  is demanded. The other plots show the *background like* selection ( $K > 1$ ) for different upper limits  $K_{\pi^0}$ . Top right:  $K_{\pi^0} < 2$ . Middle left (right):  $K_{\pi^0} < 3$  (4). Bottom left (right):  $K_{\pi^0} < 5$  (6). The normalization is given by the  $M_{\gamma\gamma}$  distribution (Fig. 6.21) for all distributions.

error of the respective data bin  $\sigma_i$  is used.

**Method 1** only uses the *signal like* selection. The residual is defined as

$$r_i = y_i^s - f(\beta_0; y_{i,L}^s, y_{i,H}^s),$$

$$f(a; L, H) := aL + (1 - a)H, \quad (6.21)$$

where  $y_i^s$ ,  $y_{i,H}^s$  and  $y_{i,L}^s$  denote the content of the  $i$ 'th bin of the *signal like* selection for data, HEPGEN++ and LEPTO. The free parameter  $\beta_0$  describes the share between “LEPTO background” and HEPGEN++ needed to describe the data. Applying the method to the  $M_X^2$  signal distribution, the scaling is obtained as displayed on the left-hand side of Fig. 6.23. The obtained scaling can also be allied to the  $M_X^2$  background distribution, which is depicted on the right-hand side of the figure.

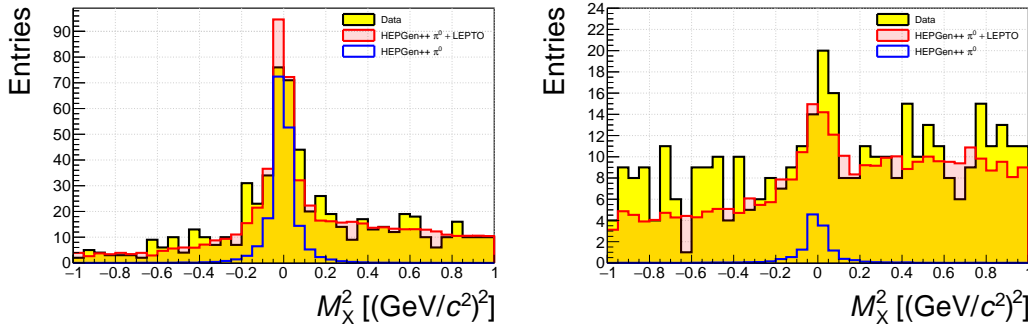


FIGURE 6.23: Left: Distribution of the quantity  $M_X^2$  for the *signal like* selection for data, HEPGEN++ and the combined Monte Carlo, with the ratio of HEPGEN++ determined by method 1. Right: Distribution of the quantity  $M_X^2$  for the *background like* selection for data, HEPGEN++ and the combined Monte Carlo, with the ratio of HEPGEN++ determined by method 1.

One can observe, that even though the background in the distribution for the *signal like* selection already fits the data quite well, in the *background like* selection, the model slightly underestimates the data. This shows again, that the multiplicity is not perfectly described by LEPTO.

**Method 2** gives the fit information on the background by simultaneously fitting the *signal like* selection and the *background like* selection. Here, the residual is defined as

$$r_i = y_i^s - f(\beta_0; y_{i,L}^s, y_{i,H}^s) + \quad (6.22)$$

$$y_i^b - f(\beta_0; y_{i,L}^b, y_{i,H}^b),$$

$$f(a; L, H) := aL + (1 - a)H, \quad (6.23)$$

with the superscripts  $s$  ( $b$ ) selecting the distribution for the *signal like* selection (*background like* selection). Again, the free parameter  $\beta_0$  describes the share between “LEPTO background” and HEPGEN++ needed to describe the data. The result of this method is displayed in Fig. 6.24. The agreement in the *background like* selection is slightly improved, but it is not possible to find one common share between “LEPTO background” and HEPGEN++ for both the *signal like* selection and *background like* selection at the same time.

**Method 3** disentangles the ratio between LEPTO and HEPGEN++ by introducing the additional free parameters  $\beta_1$  and  $\beta_2$  in the residual,

$$r_i = y_i^s - f(\beta_0, \beta_1; y_{i,L}^s, y_{i,H}^s) + \quad (6.24)$$

$$y_i^b - f(\beta_0, \beta_2; y_{i,L}^b, y_{i,H}^b),$$

$$f(a, b; L, H) := bL + aH, \quad (6.25)$$

The parameters  $\beta_1$  and  $\beta_2$  describe the share of “LEPTO background” in the *signal like* selection respectively the *background like* selection while the share

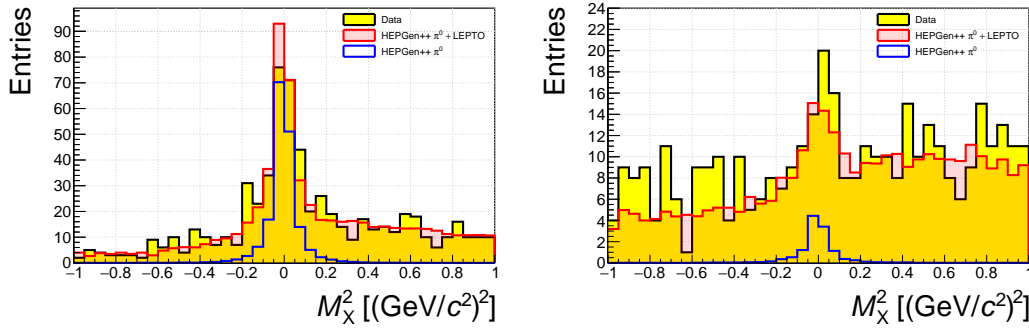


FIGURE 6.24: Left: Distribution of the quantity  $M_X^2$  for the *signal like* selection for data, HEPGEN++ and the combined Monte Carlo, with the ratio of HEPGEN++ determined by method 2. Right: Distribution of the quantity  $M_X^2$  for the *background like* selection for data, HEPGEN++ and the combined Monte Carlo, with the ratio of HEPGEN++ determined by method 2.

of HEPGEN++ is still fixed in both selections by the parameter  $\beta_0$ . The agreement of data and model for both the signal and background is now very well achieved as depicted in Fig. 6.25.

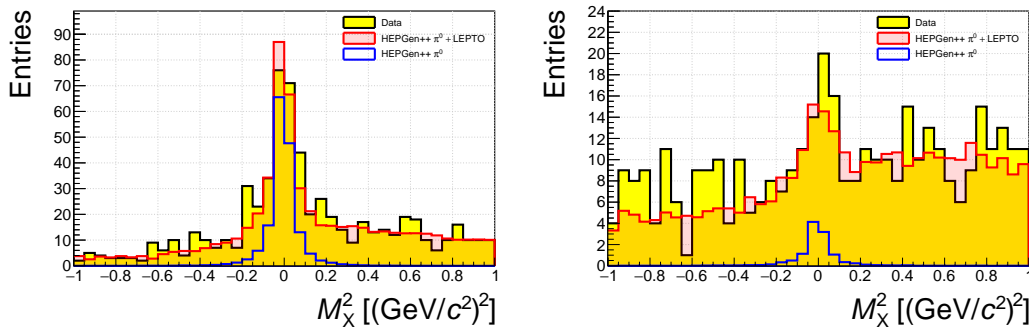


FIGURE 6.25: Left: Distribution of the quantity  $M_X^2$  for the *signal like* selection for data, HEPGEN++ and the combined Monte Carlo, with the ratio of HEPGEN++ determined by method 3. Right: Distribution of the quantity  $M_X^2$  for the *background like* selection for data, HEPGEN++ and the combined Monte Carlo, with the ratio of HEPGEN++ determined by method 3.

To compare the different methods, the share for “LEPTO background” can be assessed for each method. In method 1 and method 2, the share is given by the parameter  $\beta_0$

$$r_{lepto} = \beta_0,$$

while for method 3, it is given by the weighted average for the calculated share in the *signal like* selection and *background like* selection

$$r_{lepto} = \frac{\beta_1/s_{\beta_1}^2 + \beta_2/s_{\beta_2}^2}{1/s_{\beta_1}^2 + 1/s_{\beta_2}^2},$$

where  $s_{\beta_1}$  and  $s_{\beta_2}$  denote the standard deviations reported by the minimizer. In Fig. 6.26 (Fig. 6.27), the results for  $r_{lepto}$  for the methods is summarized for

$\mu^-$  ( $\mu^+$ ) data. Next to the exclusivity variables  $M_X^2$ ,  $\Delta p_\perp$  and  $\Delta\varphi$ , in addition, the pure spectrometer quantity  $E_{miss}$  is investigated as well. The figures also show the influence of the variation due to a different upper limit for the multiplicity  $K_{\pi^0}$ .

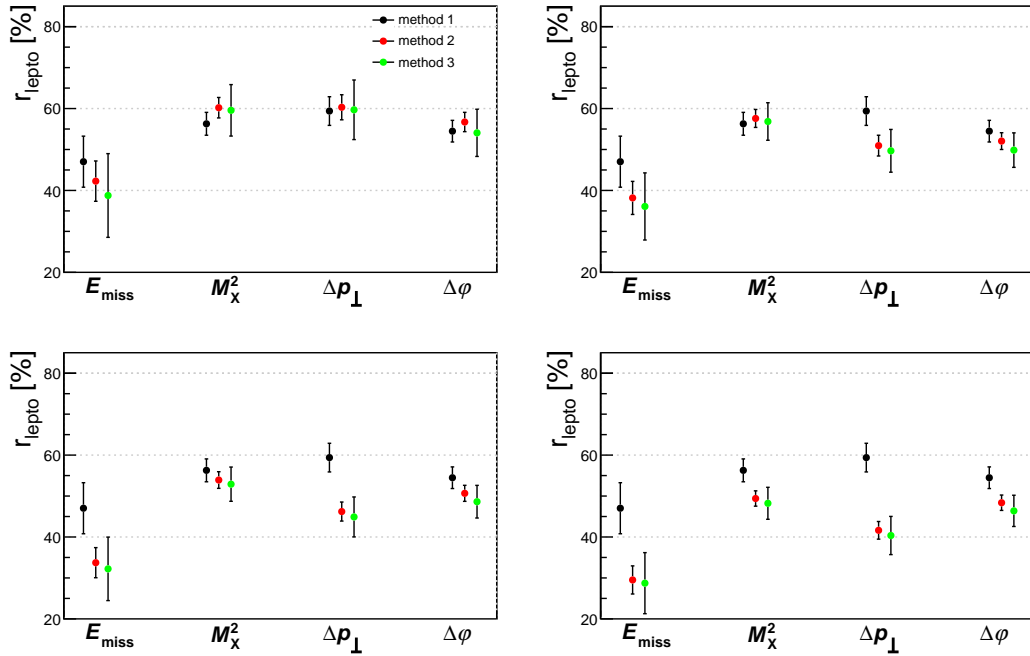


**FIGURE 6.26:** Values for the fraction of “LEPTO background” in the data obtained with the different methods for  $E_{miss}$ ,  $M_X^2$ ,  $\Delta p_\perp$  and  $\Delta\varphi$  for  $\mu^-$  data. The different plots show the variation of the result when modifying the upper limit on the multiplicity. Top left (right):  $K_{\pi^0} < 2(3)$ ; Bottom left (right):  $K_{\pi^0} < 4(5)$

Since in method 2, the share between “LEPTO background” and HEPGEN++ is constrained to the same value for the *background* and *signal like* selection and in method 3, the share of “LEPTO background” is disentangled in the *background* and *signal like* selection, both methods are sensitive to the upper limit of the multiplicity  $K_{\pi^0}$ . As method 1 only uses the *signal like* selection, it is not affected by a variation of the upper limit.

From Fig. 6.26 and Fig. 6.27 the fraction of “LEPTO background”  $r_{lepto}$  with respect to the normalization to the  $M_{\gamma\gamma}$  data distribution is estimated as well as upper and lower limits, as summarized in Table 6.2, while a nominal value of  $r_{lepto} = 60\%$  for both beam charges is chosen. The limits stated in Table 6.2 will enter into systematic studies, Subsection 6.7.4.

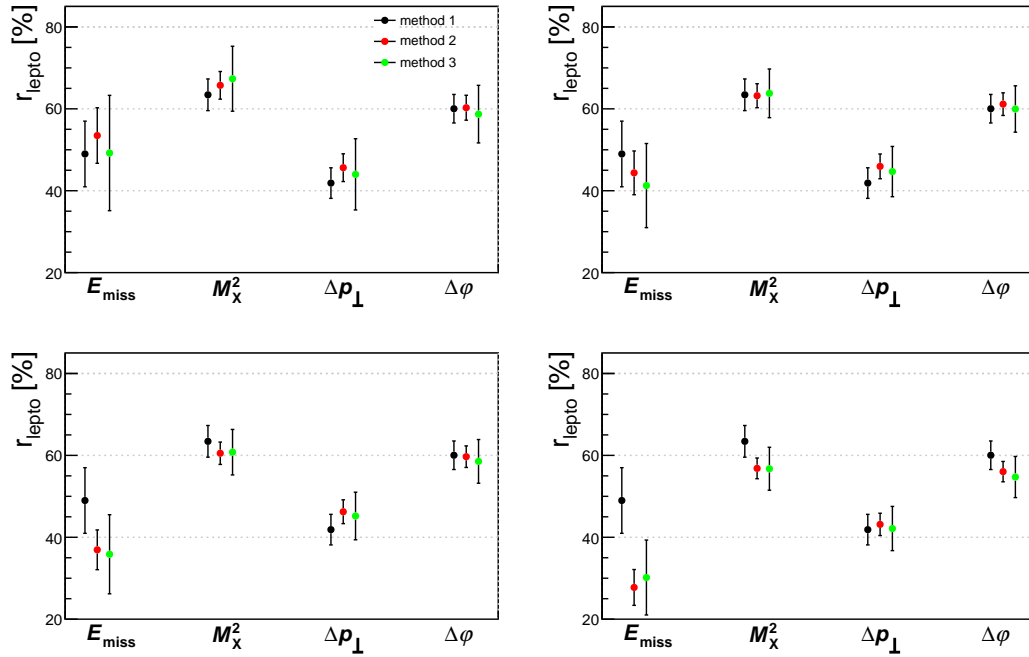


FIGURE 6.27: Values for the fraction of “LEPTO background” in the data obtained with the different methods for  $E_{miss}$ ,  $M_X^2$ ,  $\Delta p_\perp$  and  $\Delta\varphi$  for  $\mu^+$  data. The different plots show the variation of the result when modifying the upper limit on the multiplicity. Top left (right):  $K_{\pi^0} < 2(3)$ ; Bottom left (right):  $K_{\pi^0} < 4(5)$

TABLE 6.2: Values for the estimated fraction of “LEPTO background”  $r_{lepto}$  in the data. The values are determined by using Fig. 6.26 and Fig. 6.27.

	nominal	max. BG	min. BG
$r_{lepto}^{\mu^-}/\%$	60	65	50
$r_{lepto}^{\mu^+}/\%$	60	65	45

## 6.5 Acceptance

The acceptance was calculated by using the HEPGEN++ exclusive  $\pi^0$  Monte Carlo sample, *cf.* Section 6.4. The spectrometer acceptance  $a_{\Delta\Omega}$  for the phase space segment  $\Delta\Omega$  is defined as

$$a_{\Delta\Omega} = \frac{\sum_{i=1}^{N_{reco}^{\Delta\Omega}} w_i}{\sum_{i=1}^{N_{gen}^{\Delta\Omega}} w_i} \equiv \frac{N_{data}^{\Delta\Omega}}{N_{real}^{\Delta\Omega}}, \quad (6.26)$$

where  $N_{gen}^{\Delta\Omega}$  denotes the generated events in the phase space segment  $\Delta\Omega$  with boundaries given by the generated kinematic. The quantity  $N_{reco}^{\Delta\Omega}$  denotes the events reconstructed in the phase space segment  $\Delta\Omega$  with boundaries given by the reconstructed, fitted kinematic. Thus, the acceptance also accounts for smearing effects (at first order). In the measurement, the acceptance gives the ratio of the number of reconstructed events  $N_{data}^{\Delta\Omega}$  to the number of actual events  $N_{real}^{\Delta\Omega}$ .

The acceptance was calculated for  $\mu^+$  and  $\mu^-$  separately in bins of

- the photon virtuality  $Q^2$ ,
- the Lorentz invariant quantity  $\nu$ , which, in the laboratory frame, corresponds to the energy difference between incident and final muon,
- the square of the four-momentum transfer to the proton  $t$ ,
- the angle between the leptonic and hadronic plane  $\phi_{\pi^0}$  (see also Fig. 2.6).

In each four-dimensional bin, the acceptance is given according to Eq. 6.26.

Fig. 6.28 shows the acceptance in bins of  $Q^2$  and  $\nu$  as a function of  $\phi_{\pi^0}$ , averaged over  $t$ . The Figures B.20 to B.24 in Appendix B.3.3 display the acceptance for each  $t$  bin.

For  $Q^2 > 5 (\text{GeV}/c)^2$  and small  $\nu$ , the acceptance for large  $\phi_{\pi^0}$  drops to zero. On the other hand, for  $\nu > 28 \text{ GeV}$  and small  $Q^2$ , the acceptance in the center of  $\phi_{\pi^0}$  drops to zero. This leads to the  $Q^2$  and  $\nu$  range of the analysis:

$$1 (\text{GeV}/c)^2 < Q^2 < 5 (\text{GeV}/c)^2,$$

$$8.5 \text{ GeV} < \nu < 28 \text{ GeV}.$$

The acceptance averaged over the quantity  $\phi_{\pi^0}$  as a function of  $t$  in bins of  $Q^2$  and  $\nu$  is displayed in Fig. 6.29.

Here, the acceptance appears to be rather flat. Again, the acceptance approaches zero for the bin at large  $Q^2$  and small  $\nu$ . The corresponding figures for each  $\phi_{\pi^0}$  bin are available in Appendix B.3.3, Figures B.25 to B.32.

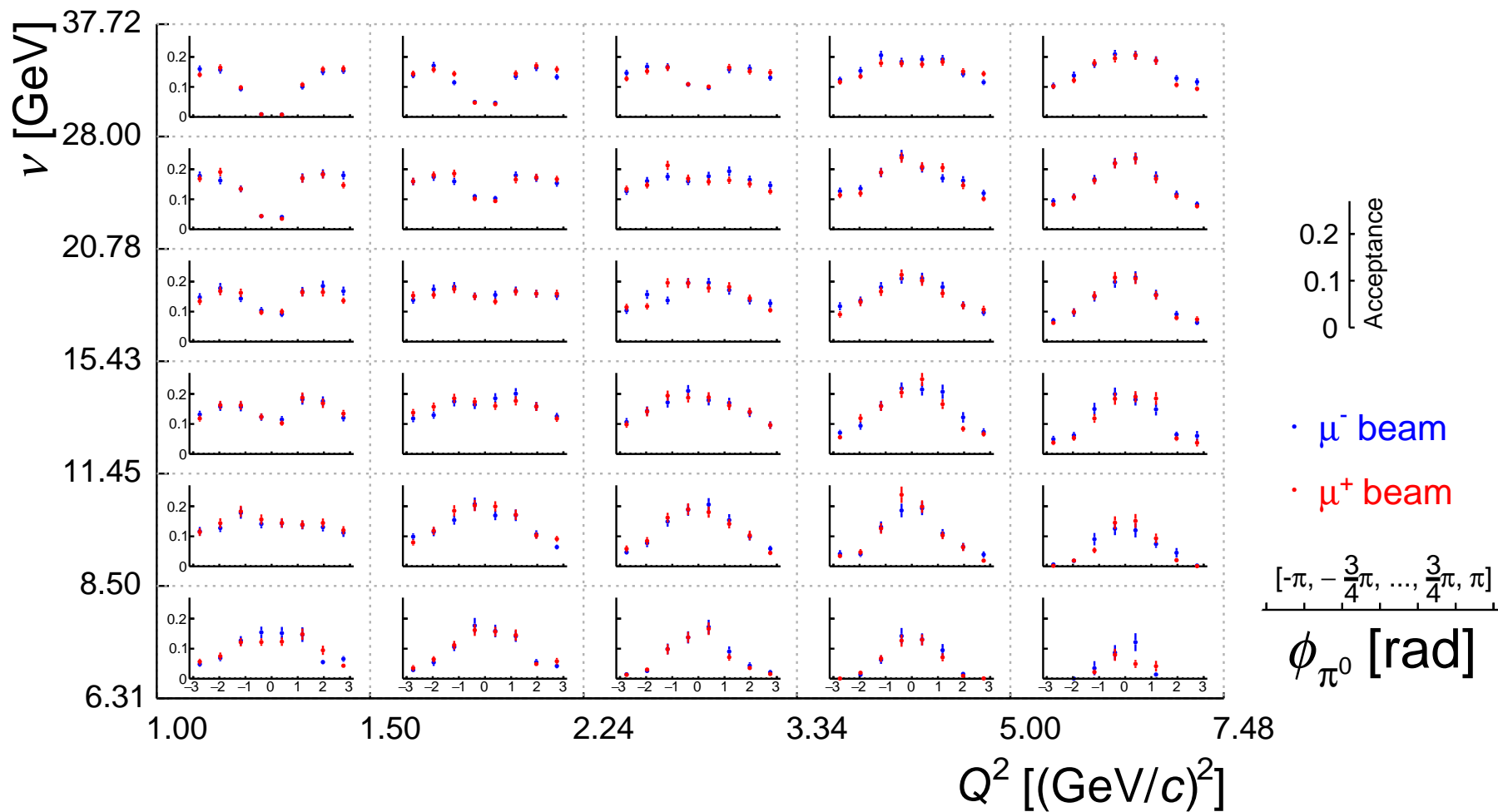


FIGURE 6.28: Acceptance as function of  $\phi_{\pi^0}$  for bins in  $\nu$  and  $Q^2$ , averaged over  $t$ .

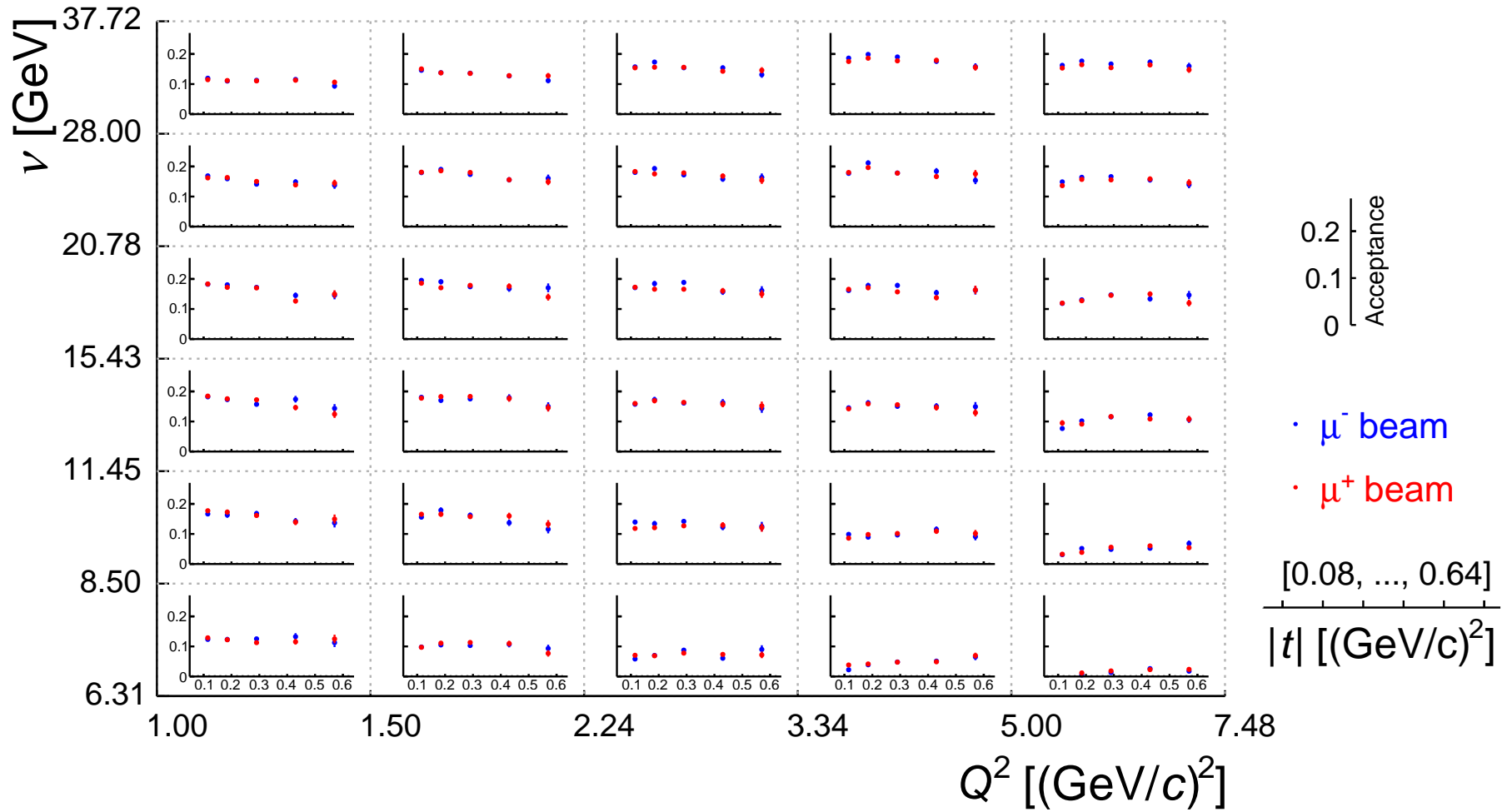


FIGURE 6.29: Acceptance as function of  $t$  for bins in  $\nu$  and  $Q^2$ , averaged over  $\phi_{\pi^0}$ .

## 6.6 Cross-section extraction

This section outlines the extraction of the cross-section for the process

$$\gamma^* p \rightarrow \pi^0 p$$

in the kinematic range

$$\begin{aligned} 0.08 (\text{GeV}/c)^2 &< |t| < 0.64 (\text{GeV}/c)^2, \\ 1 (\text{GeV}/c)^2 &< Q^2 < 5 (\text{GeV}/c)^2, \\ 8.5 \text{ GeV} &< \nu < 28 \text{ GeV}, \end{aligned}$$

as a function of the square of the four-momentum transfer to the proton  $t$  and as a function of the angle between the leptonic and hadronic plane  $\phi_{\pi^0}$ . After introducing the extraction method in general, Subsection 6.6.1, the steps to extract the cross-section as a function of  $t$  and  $\phi_{\pi^0}$  are explained in Subsection 6.6.3 and Subsection 6.6.4. Throughout the section, the kinematic variables determined by the kinematic fit are used.

### 6.6.1 Extraction method

In an ideal experiment with 100% acceptance, efficiency and purity, a given luminosity  $\mathcal{L}$  and integrated cross-section  $\sigma$  for a particular process  $\mu p \rightarrow \mu p \pi^0$  results in a number of measured events  $N_{data}$

$$\mathcal{L}\sigma = N_{data}.$$

In case of a differential cross-section in  $\Omega$ , where  $\Omega$  denotes a kinematic dependence of the cross-section, the measurement is made in a certain interval  $\Delta\Omega$  of the differential variable

$$\mathcal{L} \int_{\Delta\Omega} \frac{d\sigma}{d\Omega} d\Omega = N_{data}^{\Delta\Omega}, \quad (6.27)$$

with  $N_{data}^{\Delta\Omega}$  the number of events in the bin. The differential cross-section  $\frac{d\sigma}{d\Omega}$  is not directly accessible by the experiment, one can only measure the mean differential cross-section in the bin

$$\left\langle \frac{d\sigma}{d\Omega} \right\rangle_{\Delta\Omega} := \frac{\int_{\Delta\Omega} \frac{d\sigma}{d\Omega} d\Omega}{\Delta\Omega} = \frac{N_{data}^{\Delta\Omega}}{\mathcal{L}\Delta\Omega}.$$

Using the virtual-photon flux  $\Gamma$  (Eq. 2.12), the mean differential virtual-photon proton cross-section for the process  $\gamma^* p \rightarrow p\pi^0$  is given by

$$\left\langle \frac{d\sigma}{d\kappa} \right\rangle_{\Delta\Omega} := \frac{\int_{\Delta\Omega} \frac{1}{\Gamma} \frac{d\sigma}{d\Omega} d\Omega}{\Delta\Omega}, \quad (6.28)$$

Explicitly, here  $d\Omega = d\kappa dQ^2 d\nu$  respectively  $\Delta\Omega = \Delta\kappa \Delta Q^2 \Delta\nu$ , where  $\kappa$  is a substitute for either  $t$  or the angle  $\phi_{\pi^0}$ . In case of the extraction as a function of  $t$ , the  $\phi_{\pi^0}$  dimension is integrated over from  $-\pi$  to  $\pi$ . The determination of the integral in Eq. 6.28 follows as

$$\begin{aligned}
\int_{\Delta\Omega} \frac{d\sigma}{d\Omega} \frac{1}{\Gamma} d\Omega &= N_{data}^{\Delta\Omega} \frac{\int_{\Delta\Omega} \frac{d\sigma}{d\Omega} \frac{1}{\Gamma} d\Omega}{N_{data}^{\Delta\Omega}}, \\
&= N_{data}^{\Delta\Omega} \int_{\Delta\Omega} \left( \frac{d\sigma}{d\Omega} / N_{data}^{\Delta\Omega} \right) \frac{1}{\Gamma} d\Omega, \\
&= \frac{N_{data}^{\Delta\Omega}}{\mathcal{L}} \int_{\Delta\Omega} \left( \frac{d\sigma}{d\Omega} / \int_{\Delta\Omega} \frac{d\sigma}{d\Omega} d\Omega \right) \frac{1}{\Gamma} d\Omega, \quad (\text{using Eq. 6.27}) \\
&= \frac{N_{data}^{\Delta\Omega}}{\mathcal{L}} \int_{\Delta\Omega} \frac{1}{\Gamma} P(\Omega) d\Omega, \quad \text{with} \tag{6.29} \\
P(\Omega) &= \frac{d\sigma}{d\Omega} / \int_{\Delta\Omega} \frac{d\sigma}{d\Omega} d\Omega \quad \text{and} \quad \int_{\Delta\Omega} P(\Omega) = 1.
\end{aligned}$$

From Eq. 6.29 one can see that solving the integral comes down to calculating the expectation value  $E_{\frac{1}{\Gamma}} = \int_{\Delta\Omega} \frac{1}{\Gamma} P(\Omega) d\Omega$  with probability density function  $P(\Omega)$ . However, the function  $P(\Omega)$  is unknown, since it essentially consists of the cross-section that is to be determined. Hence, the expectation value  $E_{\frac{1}{\Gamma}}$  is estimated using data (which are naturally distributed according to the probability density function),

$$E_{\frac{1}{\Gamma}} \approx \frac{1}{N_{data}^{\Delta\Omega}} \sum_{i=1}^{N_{data}^{\Delta\Omega}} \frac{1}{\Gamma(\Omega_i)}, \tag{6.30}$$

by effectively calculating the mean value of  $\frac{1}{\Gamma(\Omega_i)}$  within the phase space segment  $\Delta\Omega$ , where  $\Omega_i$  denotes the kinematics of the  $i$ 'th event. Resolution effects when evaluating  $\Gamma(\Omega_i)$  are at the percent level and are therefore neglected, see also Fig. B.33 in the appendix.

An alternative approach uses the model prediction for  $P(\Omega)$  with the cost of a model dependent result. Since model predictions are very weak for the studied process in the particular kinematic range, this approach is assessed in a systematic study in Appendix B.5.

Inserting Eq. 6.30 into Eq. 6.29, the measurement of the mean differential virtual-photon proton cross-section defined in Eq. 6.28 can be performed by evaluating

$$\left\langle \frac{d\sigma^{data}}{d\kappa} \right\rangle_{\Delta\Omega} = \frac{1}{\mathcal{L} \Delta\Omega} \sum_{i=1}^{N_{data}^{\Delta\Omega}} \frac{1}{\Gamma(\Omega_i)}. \tag{6.31}$$

Since the experiment is not perfect, the acceptance introduced in Section 6.5 is used to account for the “lost” events by weighting the events with their

probability of detection. Using Eq. 6.26

$$a_{\Delta\Omega} = \frac{N_{data}^{\Delta\Omega}}{N_{real}^{\Delta\Omega}} \Rightarrow N_{real}^{\Delta\Omega} = a_{\Delta\Omega}^{-1} N_{data}^{\Delta\Omega},$$

and Eq. 6.31 is adapted

$$\left\langle \frac{d\sigma^{data}}{d\kappa} \right\rangle_{\Delta\Omega} = \frac{1}{\mathcal{L}\Delta\Omega} \sum_{i=1}^{N_{data}^{\Delta\Omega}} \frac{a(\Omega_i)^{-1}}{\Gamma(\Omega_i)}. \quad (6.32)$$

In this equation, the acceptance is used as it would be a smooth function and is evaluated for the kinematics of the  $i$ 'th event  $\Omega_i$ . The bin sizes of the acceptance are considered to be sufficiently small, hence the acceptance can be considered constant within an acceptance bin. Effects due to the binning of the acceptance are absorbed into the systematic uncertainties, see Subsection 6.7.3.

The background originating from non-exclusive processes is subtracted from Eq. 6.32 on the level of cross-sections

$$\begin{aligned} \left\langle \frac{d\sigma}{d\kappa} \right\rangle_{\Delta\Omega} &= \left\langle \frac{d\sigma^{data}}{d\kappa} \right\rangle_{\Delta\Omega} - \left\langle \frac{d\sigma^{BG}}{d\kappa} \right\rangle_{\Delta\Omega}, \\ &= \frac{1}{\mathcal{L}\Delta\Omega} \cdot \left( \sum_{i=1}^{N_{data}^{\Delta\Omega}} \frac{a(\Omega_i)^{-1}}{\Gamma(\Omega_i)} - \sum_{i=1}^{N_{BG}^{\Delta\Omega}} \frac{a(\Omega_i)^{-1}}{\Gamma(\Omega_i)} \right). \end{aligned} \quad (6.33)$$

where the cross-section for the non-exclusive background  $d\sigma^{BG}$  is estimated using the number of events  $N_{BG}^{\Delta\Omega}$  of the "LEPTO background" that was normalized to the data according to Subsection 6.4.3.

As one can see from Eq. 6.33, the cross-section is a result of summing up weights for data respectively "LEPTO background" events, where  $w_i$ , the weight of the  $i$ 'th event, is given by

$$w_i = \frac{1}{\mathcal{L}\Delta\Omega} \frac{a(\Omega_i)^{-1}}{\Gamma(\Omega_i)}. \quad (6.34)$$

Rewriting Eq. 6.33, the cross-section can be expressed as

$$\left\langle \frac{d\sigma}{d\kappa} \right\rangle_{\Delta\Omega} = \left( \sum_{i=1}^{N_{data}^{\Delta\Omega}} w_i - \sum_{i=1}^{N_{BG}^{\Delta\Omega}} w_i \right),$$

$$\left( \sum w_i \right)_{\Delta\Omega}^{\pm} := \left( \sum_{i=1}^{N_{data}^{\Delta\Omega}} w_i - \sum_{i=1}^{N_{BG}^{\Delta\Omega}} w_i \right), \quad (6.35)$$

$$(6.36)$$

where the signs  $\pm$  denote the selection of  $\mu^+$  respectively  $\mu^-$  data. The associated variance is given by the sum of squares of weights

$$V \left[ \left\langle \frac{d\sigma}{d\kappa} \right\rangle_{\Delta\Omega} \right] = \left( \sum_{i=1}^{N_{data}^{\Delta\Omega}} w_i^2 + \sum_{i=1}^{N_{BG}^{\Delta\Omega}} w_i^2 \right) \approx \sum_{i=1}^{N_{data}^{\Delta\Omega}} w_i^2,$$

$$\left( \sum w_i^2 \right)_{\Delta\Omega}^{\pm} := \sum_{i=1}^{N_{data}^{\Delta\Omega}^{\pm}} w_i^2.$$

while the low statistical uncertainty of the Monte Carlo allows for dropping the term introduced by the “LEPTO background”.

The acceptance and the estimation of the non-exclusive background depend on the beam charge. Therefore, Eq. 6.35 is evaluated separately for  $\mu^+$  and  $\mu^-$  and the average finally leads to the value of the cross-section in the bin  $\Delta\Omega$

$$\left( \sum w_i \right)_{\Delta\Omega} := \frac{1}{2} \left[ \left( \sum w_i \right)_{\Delta\Omega}^+ + \left( \sum w_i \right)_{\Delta\Omega}^- \right], \quad (6.37)$$

with variance

$$\left( \sum w_i^2 \right)_{\Delta\Omega} := \frac{1}{4} \left[ \left( \sum w_i^2 \right)_{\Delta\Omega}^+ + \left( \sum w_i^2 \right)_{\Delta\Omega}^- \right]. \quad (6.38)$$

## 6.6.2 Extraction of unseparated cross-section

Here, the extraction of the unseparated cross-section in a single bin  $\Delta\Omega$  is performed. The bin spans over the full  $Q^2$ ,  $\nu$  and  $|t|$  range of the analysis. Hence, the width of the bin is given by  $\Delta\Omega = \Delta Q^2 \Delta\nu \Delta t$  with  $\Delta Q^2 = 4 (\text{GeV}/c)^2$ ,  $\Delta\nu = 19.5 \text{ GeV}$  and  $\Delta t = 0.56 (\text{GeV}/c)^2$  and the event weight (Eq. 6.34) reads

$$w_i = \frac{1}{\mathcal{L} \Delta Q^2 \Delta\nu \Delta t} \frac{a(\Omega_i)^{-1}}{\Gamma(\Omega_i)}.$$

Using Eq. 6.37, the unseparated cross-section results in

$$\left\langle \frac{d\sigma_T}{d|t|} + \varepsilon \frac{d\sigma_L}{d|t|} \right\rangle = \left\langle \frac{d\sigma^{\gamma^* p \rightarrow \pi^0 p}}{d|t|} \right\rangle = \left( \sum w_i \right)_{\Delta\Omega} = 6.02 \frac{\text{nb}}{(\text{GeV}/c)^2}.$$

The standard deviation follows from the variance (Eq. 6.38) as

$$\sqrt{V \left[ \left\langle \frac{d\sigma^{\gamma^* p \rightarrow \pi^0 p}}{d|t|} \right\rangle \right]} = \sqrt{\left( \sum w_i^2 \right)_{\Delta\Omega}} = 1.44 \frac{\text{nb}}{(\text{GeV}/c)^2}.$$

The numbers that enter into these calculations are collected in Table 6.6 at the end of the section.

### 6.6.3 Extraction of the cross-section as a function of $t$

The following section will guide through the steps to obtain the cross-section as a function of  $t$ . The common notation for this dependence is by using the absolute value  $|t|$  which is used from here on. The principle is equivalent to the preceding extraction of the unseparated cross-section while restricting to a certain range in  $|t|$ . Now, the event weight (*cf.* Eq. 6.34) reads

$$w_i = \frac{1}{\mathcal{L}\Delta Q^2\Delta\nu\Delta t_n} \frac{a(\Omega_i)^{-1}}{\Gamma(\Omega_i)},$$

where the width of the  $n$ 'th  $|t|$ -bin is denoted by  $\Delta t_n$  while  $\Delta Q^2 = 4(\text{GeV}/c)^2$  and  $\Delta\nu = 19.5\text{ GeV}$  are given by the kinematic range of the analysis. The extraction bins and their widths are listed in table Table 6.3. Using Eq. 6.37, the cross-section in the  $n$ 'th extraction bin reads

$$\left\langle \frac{d\sigma^{\gamma^*p \rightarrow \pi^0 p}}{d|t|} \right\rangle_{\Delta\Omega_n} = \left( \sum w_i \right)_{\Delta\Omega_n}. \quad (6.39)$$

TABLE 6.3: Ranges and widths of the cross-section extraction bins in  $|t|$ .

bin	$t_1$	$t_2$	$t_3$	$t_4$	$t_5$
$\frac{\text{range}}{(\text{GeV}/c)^2}$	[0.08,0.15[	[0.15,0.22[	[0.22,0.36[	[0.36,0.5[	[0.5,0.64[
$\frac{\Delta t}{(\text{GeV}/c)^2}$	0.07	0.07	0.14	0.14	0.14

The numbers that enter are visualized in Fig. 6.30 where the number of events as function of  $|t|$  after the event selection is displayed together with the properly normalized “LEPTO background” contribution, separated for  $\mu^-$  and  $\mu^+$  beam.

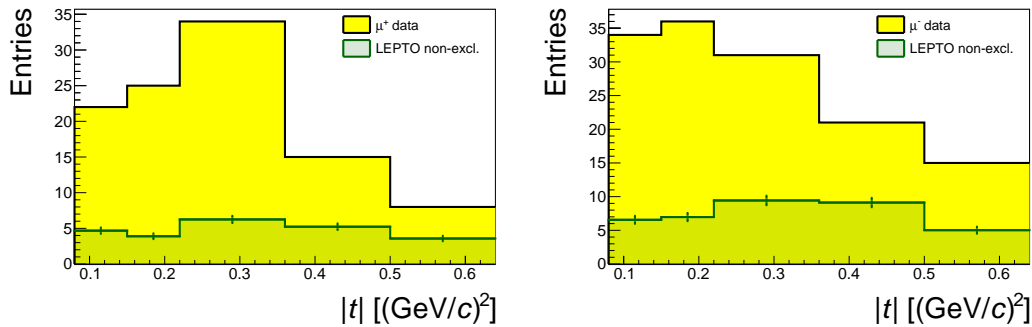
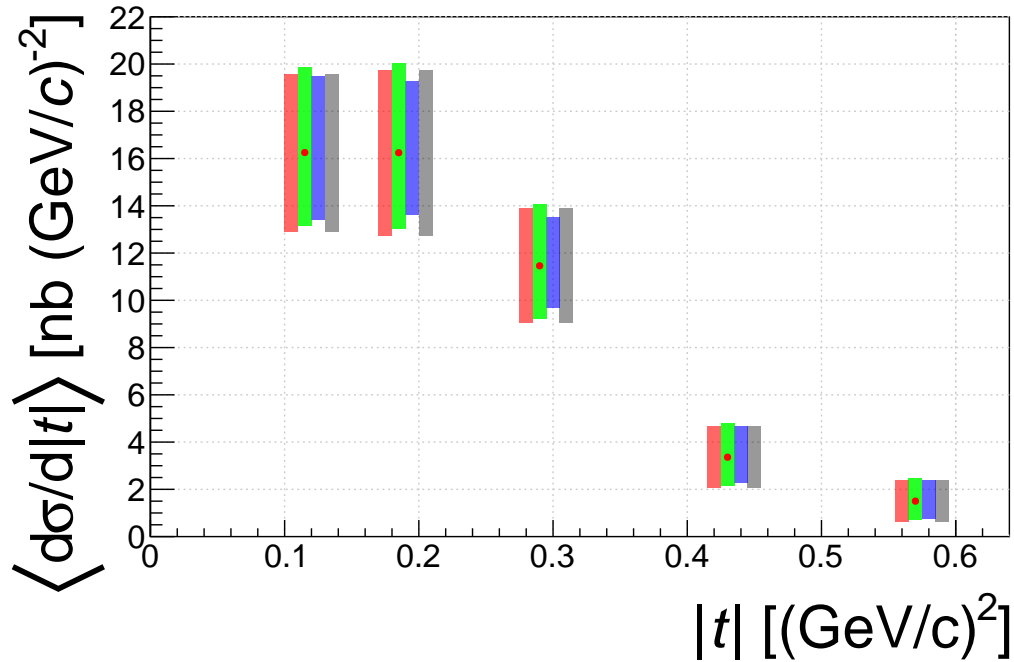


FIGURE 6.30: Number of events as a function of  $|t|$  for  $\mu^+$  (left) and  $\mu^-$  (right) after the full event selection.

By evaluating Eq. 6.39 for each extraction bin, the final result is obtained as depicted in Fig. 6.31. Since the number of events that enter into the cross-



**FIGURE 6.31:** Differential virtual-photon proton cross-section for the process  $\gamma^*p \rightarrow \pi^0p$  as function of  $|t|$ . The red points represent the mean differential cross-section in the bins defined in Table 6.3. The points are plotted at the center of the respective bin. The red and green bars represent confidence intervals obtained using the bootstrap where the green bars illustrate the confidence intervals with exact coverage, see following Subsection 6.6.5. Just for comparison, the blue bar represents the relative Poisson confidence interval using the number of data events in the bin. The gray bar represents the square root of the variance, *cf.* Eq. 6.38.

section is quite small, the estimation of the respective confidence intervals using the variance is not accurate. A method to obtain appropriate confidence intervals is outlined in Subsection 6.6.5. For comparison, different confidence intervals are compared in Fig. 6.31. All numbers are collected in Table 6.6 at the end of the section.

#### 6.6.4 Extraction of the cross-section as a function of $\phi_{\pi^0}$

The extraction of the cross-section as a function of  $\phi_{\pi^0}$  is performed in eight equidistant  $\phi_{\pi^0}$ -bins listed in Table 6.4 that cover the range  $-\pi < \phi_{\pi^0} < \pi$  and one  $|t|$  bin covering the full range of the analysis  $0.08 (\text{GeV}/c)^2 < |t| < 0.64 (\text{GeV}/c)^2$ .

In an analogous fashion to the extraction as a function of  $|t|$  in the preceding section, here, the event weight reads

$$w_i = \frac{1}{\mathcal{L}\Delta Q^2\Delta\nu\Delta t\Delta\phi_{\pi^0,n}} \frac{a(\Omega_i)^{-1}}{\Gamma(\Omega_i)}.$$

TABLE 6.4: Ranges and widths of the cross-section extraction bins in  $\phi_{\pi^0}$ .

bin	$\phi_{\pi^0,1}$	$\phi_{\pi^0,2}$	$\phi_{\pi^0,3}$	...	$\phi_{\pi^0,8}$
$\frac{range}{rad}$	$[-\frac{4\pi}{4}, -\frac{3\pi}{4}[$	$[-\frac{3\pi}{4}, -\frac{2\pi}{4}[$	$[-\frac{2\pi}{4}, -\frac{\pi}{4}[$	...	$[\frac{3\pi}{4}, \frac{4\pi}{4}[$
$\Delta\phi_{\pi^0}$	$\frac{\pi}{4}$	$\frac{\pi}{4}$	$\frac{\pi}{4}$	...	$\frac{\pi}{4}$

The width of the  $n$ 'th  $\phi_{\pi^0}$  bin is denoted by  $\Delta\phi_{\pi^0,n}$  while  $\Delta Q^2 = 4 (\text{GeV}/c)^2$ ,  $\Delta\nu = 19.5 \text{ GeV}$  and  $\Delta t = 0.56 (\text{GeV}/c)^2$  are given by the kinematic range of the analysis. The mean differential cross-section extracted in the  $n$ 'th bin of  $\phi_{\pi^0}$  reads

$$\left\langle \frac{d^2\sigma^{\gamma^*p \rightarrow \pi^0 p}}{d|t|d\phi_{\pi^0}} \right\rangle_{\Delta\Omega_n} = \left( \sum w_i \right)_{\Delta\Omega_n}. \quad (6.40)$$

In Fig. 6.32, the number of events as a function of  $\phi_{\pi^0}$  after the event selection is displayed together with the properly normalized "LEPTO background" contribution separated for  $\mu^-$  and  $\mu^+$  beam. By evaluating Eq. 6.40 for each

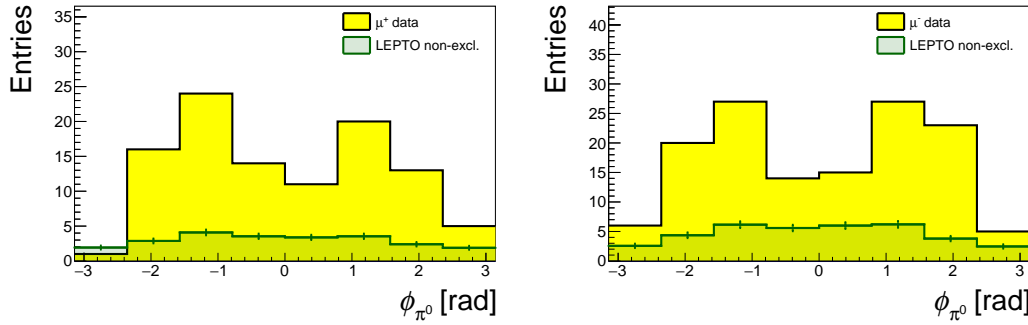


FIGURE 6.32: Number of events as a function of  $\phi_{\pi^0}$  for  $\mu^+$  (left) and  $\mu^-$  (right) after the full event selection.

extraction bin, the final result is obtained as depicted in Fig. 6.33. Here, the number of events that enter into the extraction is even smaller compared to the extraction as a function of  $|t|$ . Especially the bins at the edges suffer from low statistics. Again, different confidence intervals are compared in Fig. 6.33 while the method to obtain appropriate confidence intervals is outlined in Subsection 6.6.5. All numbers are collected in Table 6.6 at the end of the section.

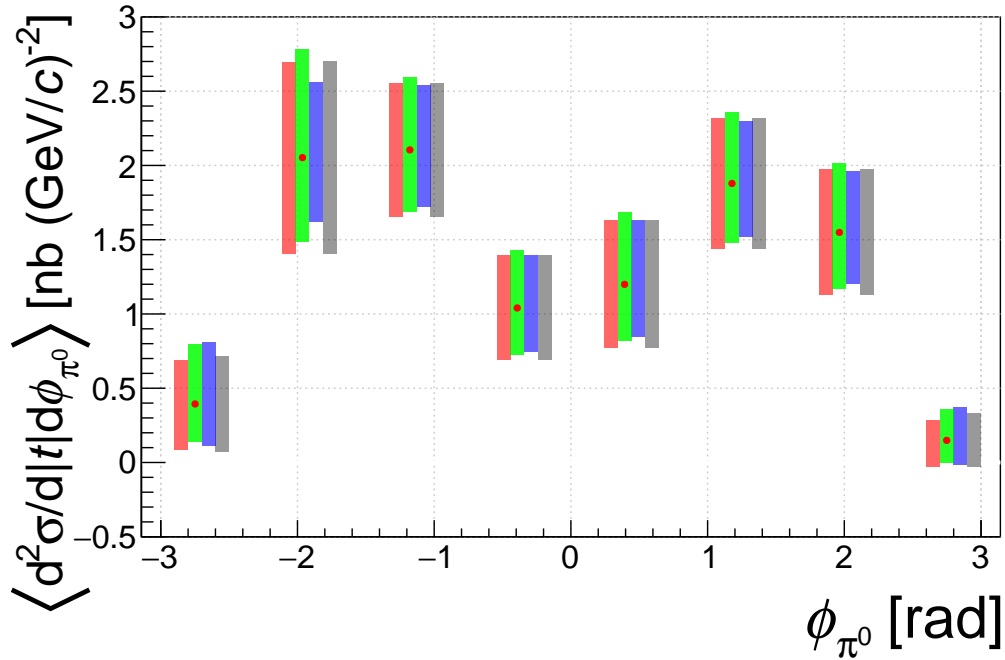


FIGURE 6.33: Differential virtual-photon proton cross-section for the process  $\gamma^*p \rightarrow \pi^0p$  as function of  $\phi_{\pi^0}$ . The red points represent the mean differential cross-section in the bins defined in Table 6.4. The points are plotted at the center of the respective bin. The red and green bars represent confidence intervals obtained using the bootstrap where the green bars illustrate the confidence intervals with exact coverage, see following Subsection 6.6.5. Just for comparison, the blue bar represents the relative Poisson confidence interval using the number of data events in the bin. The gray bar represents the square root of the variance, *cf.* Eq. 6.38.

### 6.6.5 Estimation of uncertainties

In this section, the technique for the estimation of the confidence intervals in Fig. 6.31 and Fig. 6.33 is outlined. The value in each bin corresponds to a sum of Poisson distributed weights. Hence, the underlying probability density function (PDF) can be described by a compound Poisson distribution. The mean and the variance of the distribution follow as quoted in Eq. 6.37 and Eq. 6.38. However, since the number of events is small and the PDF of the weights is unknown, the confidence interval can not be inferred from the variance of the measurement.

Here, the technique to estimate the PDF from data using the Poisson bootstrap is used as proposed in [109]. A bootstrap sample  $w_{boot}$  is created from data by modifying the sum of observed weights  $w_{obs}$  (*cf.* Eq. 6.35) as

$$w_{obs} := \sum_{i=1}^{N_{data}^{\Delta\Omega}} w_i \rightarrow \sum_{i=1}^{N_{data}^{\Delta\Omega}} n_i w_i =: w_{boot}, \quad (6.41)$$

where  $n_i$  is a randomly chosen Poisson distributed number with mean  $\lambda = 1$ .

The resulting Poisson bootstrap distribution can be treated as an estimation of the PDF. The plots in Fig. 6.34 (Fig. 6.35) show the Poisson bootstrap distributions for each extraction bin in  $t$  ( $\phi_{\pi^0}$ ).

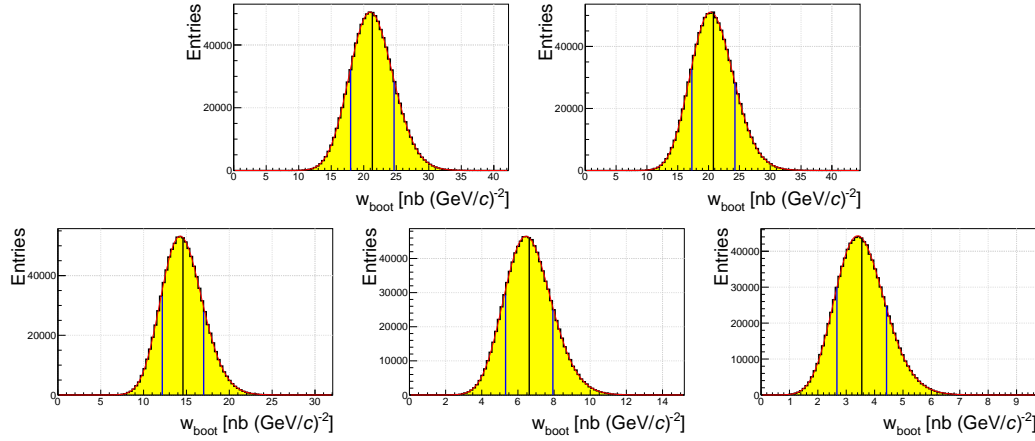


**FIGURE 6.34:** Poisson bootstrap distributions for values in bins of  $t$  (in ascending order from left to right, top to bottom). The black line indicates the measured value while the blue lines indicate the confidence interval with  $1 - \alpha = 68.27\%$  confidence level obtained by integrating the respective distribution. The red curve is a fit to the distribution.

The black lines indicates  $w_{obs}$  in the respective bin. The red curves in Fig. 6.34 and Fig. 6.35 correspond to fits to the distributions using  $P_{Gamma}$ , the PDF of the *Gamma* distribution. The fitted function reads

$$Gamma(x; \vec{p}) = p_0 \cdot P_{Gamma}\left(p_3 + \frac{x - p_1}{p_2}, p_3, 1\right),$$

where  $\vec{p} = (p_0, p_1, p_3, p_3)$  denotes the fitted parameters while  $P_{Gamma}$  is taken from the ROOT package [110].

The respective confidence intervals  $[C_l, C_u]$  with  $1 - \alpha = 68.27\%$  significance level are inferred from the fitted functions by calculating

$$\begin{aligned} \frac{\alpha}{2} &= \int_{-\infty}^{C_l} Gamma_{\lambda=1}(x; \vec{p}) dx / F, \\ 1 - \frac{\alpha}{2} &= \int_{C_h}^{\infty} Gamma_{\lambda=1}(x; \vec{p}) dx / F, \\ \text{with } F &= \int_{-\infty}^{\infty} Gamma_{\lambda=1}(x; \vec{p}) dx. \end{aligned} \quad (6.42)$$

The subscript  $\lambda = 1$  emphasizes that the *Gamma* functions correspond to the Poisson bootstrap distributions in Fig. 6.34 and Fig. 6.35. The hereby obtained confidence intervals are illustrated in Fig. 6.31 and Fig. 6.33 by the red bars. A summary of the corresponding numbers is available at the end of the section in Table 6.6.

**Confidence interval with exact coverage:** Following [109], the calculation of the upper limit of the confidence interval with exact coverage  $C_u^*$  can be performed by creating a bootstrap sample for which the mean of the Poisson  $\lambda_u$  is chosen such that portion of the distribution below the observed value  $w_{obs}$  amounts to  $\alpha/2$ :

$$\frac{\alpha}{2} = \int_{-\infty}^{w_{obs}} \text{Gamma}_{\lambda_u}(x; \vec{p}) dx, \quad (6.43)$$

$$C_u^* = \lambda_u \cdot w_{obs}.$$

Here,  $\text{Gamma}_{\lambda_u}(x; \vec{p})$  denotes the function corresponding to the Poisson bootstrap distribution where the bootstrap samples are created by using  $\lambda_u$  as the mean of the Poisson distribution.

Similarly, the lower limit of the confidence interval  $C_l^*$  follows with

$$\frac{\alpha}{2} = \int_{w_{obs}}^{\infty} \text{Gamma}_{\lambda_l}(x; \vec{p}) dx, \quad (6.44)$$

$$C_l^* = \lambda_l \cdot w_{obs}.$$

Technically, the distributions that correspond to  $\lambda_l$  and  $\lambda_u$  are obtained using a parametrization of the Poisson bootstrap distributions as a function of  $\lambda$ , outlined in the following Subsection 6.6.6.

The confidence intervals obtained by the Poisson bootstrap with exact coverage are displayed in Fig. 6.34 and Fig. 6.35 with green bars and summarized in Table 6.6.

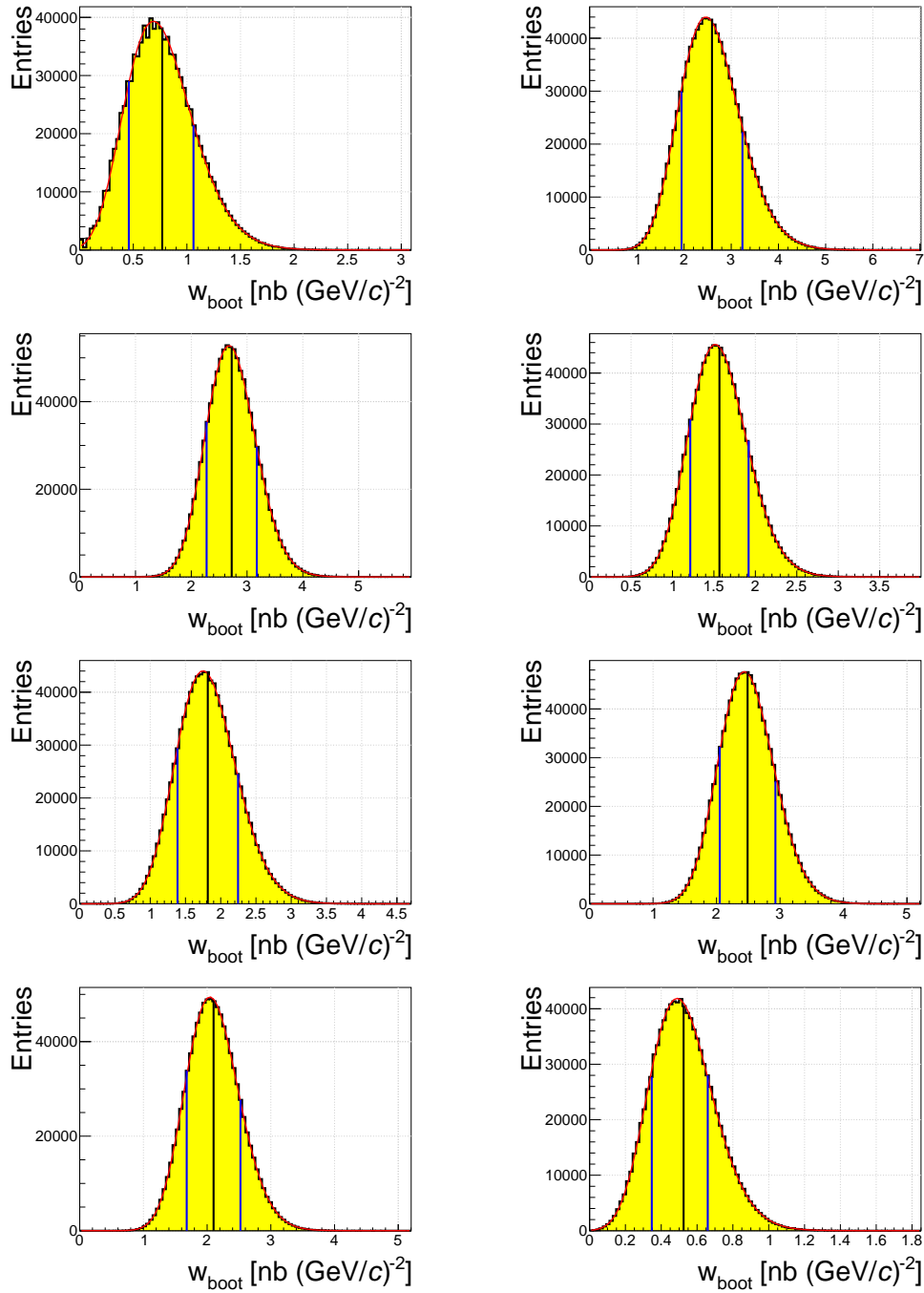


**FIGURE 6.35:** Poisson bootstrap distributions for values in bins of  $\phi_{\pi^0}$  (in ascending order from left to right, top to bottom). The black line indicates the measured value while the blue lines indicate the confidence interval with  $1 - \alpha = 68.27\%$  confidence level obtained by integrating the respective distribution. The red curve is a fit to the distribution.

### 6.6.6 Parameterization of compound Poisson distribution evolution

The Poisson bootstrap allows obtaining the PDF in an extraction bin represented by the Poisson bootstrap distribution. By extracting the Poisson bootstrap distribution for multiple values of the Poisson mean  $\lambda$ , it is possible to extract the evolution of these distributions.

As an example Fig. 6.36 shows some of the Poisson bootstrap distributions obtained in the extraction bin  $\phi_{\pi^0,2}$  while the evolution of the fitted parameters as a function of  $\lambda$  is depicted in Fig. 6.37.

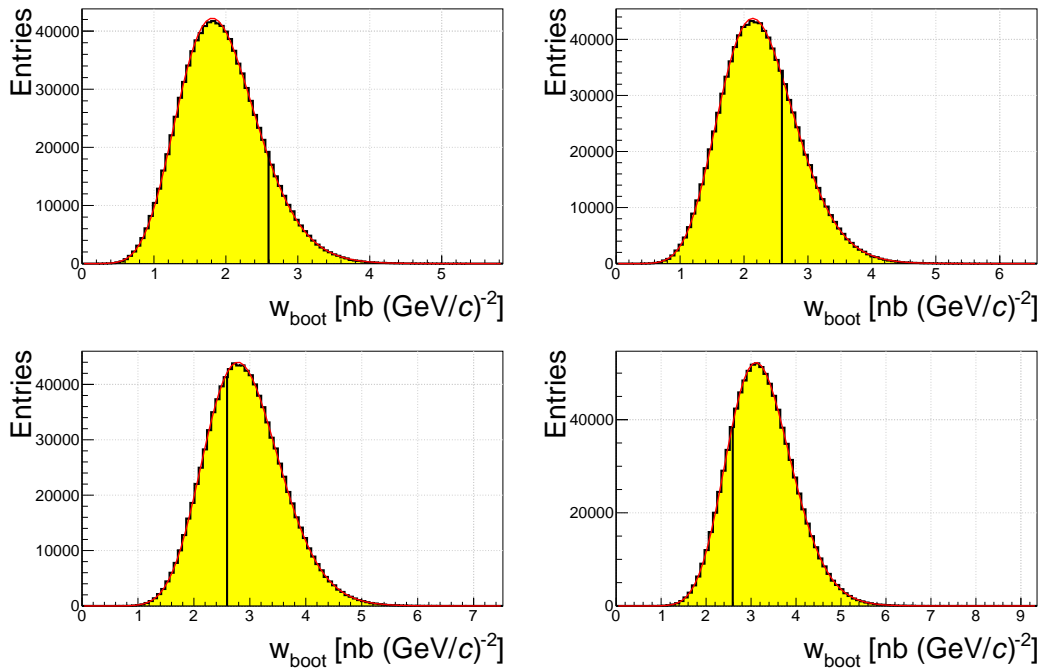


**FIGURE 6.36:** Poisson bootstrap distributions for different values of  $\lambda$  in the extraction bin  $\phi_{\pi^0,2}$ . The values of  $\lambda$  read from left to right and top to bottom  $\lambda = \{0.75, 0.875, 1.125, 1.25\}$ . Additionally, the distribution for  $\lambda = 1$  is depicted in Fig. 6.34. The red curve corresponds to the fitted *Gamma* functions while the black line indicates the measured value  $w_{obs}$  in the bin.

Note that in Fig. 6.37, the scale parameter  $p_0$  obtained by the fit is re-scaled such that

$$\int_{-\infty}^{\infty} Gamma_{\lambda}(x; \vec{p}) dx = 1.$$

The dependence of the parameters is fitted using linear functions. The slope and intersect parameters are then used to create a model of the PDF in the respective bin

$$f_{\Gamma}(k; v = \lambda \cdot w_{obs}) = Gamma(k; \vec{p}(v)),$$

which gives the probability  $f_{\Gamma}(k; v)$  to measure  $k$  for a given expectation value  $v$ . The corresponding parameter set for the *Gamma* function  $\vec{p}(v)$  is

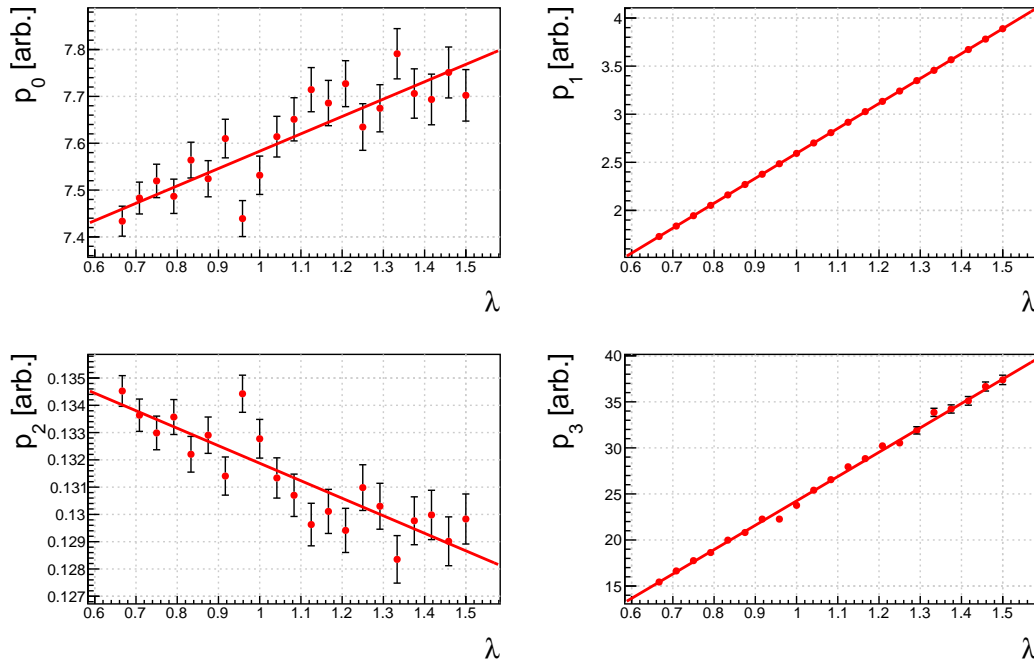


**FIGURE 6.37:** Fit parameters of  $\text{Gamma}_\lambda(x; \vec{p})$  as a function of  $\lambda$  in the extraction bin  $\phi_{\pi^0,2}$ . The red line indicates a linear fit that is used to parameterize the dependence of the respective parameter on  $\lambda$ . See Fig. 6.36 for examples of Poisson bootstrap distributions with  $\lambda = \{0.75, 0.875, 1.125, 1.25\}$ .

obtained with

$$p_i(v) = a_i + b_i \cdot (v/w_{obs}),$$

where  $a_i$  and  $b_i$  denote the intersect and slope parameter of the linear fit for the  $i$ 'th parameter of the  $\text{Gamma}$  function.

### 6.6.7 Binned maximum likelihood fit

As mentioned in the introduction, a modulation in  $\phi_{\pi^0}$  is expected which is clearly visible in Fig. 6.33. To extract the amplitudes of the modulations, a binned maximum likelihood fit is used.

In accordance to Eq. 2.14, the objective is to fit the function

$$\frac{d^2\sigma}{d|t|d\phi_{\pi^0}} = \frac{1}{2\pi} \left[ p_0 + \varepsilon \cdot \cos(2\phi_{\pi^0}) \cdot p_1 + \sqrt{2\varepsilon(1+\varepsilon)} \cdot \cos(\phi_{\pi^0}) \cdot p_2 \right], \quad (6.45)$$

$$p_0 = \left\langle \frac{d\sigma_T}{d|t|} + \varepsilon \frac{d\sigma_L}{d|t|} \right\rangle, \quad p_1 = \left\langle \frac{d\sigma_{TT}}{d|t|} \right\rangle, \quad p_2 = \left\langle \frac{d\sigma_{LT}}{d|t|} \right\rangle, \quad \varepsilon = 0.996,$$

and extract the parameters  $p_0$ ,  $p_1$  and  $p_2$ . For the value of the polarization factor  $\varepsilon$ , the mean value of the background corrected data is used.

The parameter  $p_0$ , which corresponds to the unpolarized cross-section, is independent of  $\phi_{\pi^0}$  and was already determined in Subsection 6.6.2.

To apply the binned maximum likelihood fit, Eq. 6.45 has to be normalized

and the actual fit function follows as

$$\sigma(\phi_{\pi^0}; \vec{\beta}) = \frac{1}{2\pi} \left[ 1 + \varepsilon \cdot \cos(2\phi_{\pi^0}) \cdot \beta_1 + \sqrt{2\varepsilon(1+\varepsilon)} \cdot \cos(\phi_{\pi^0}) \cdot \beta_2 \right], \quad (6.46)$$

with  $\vec{\beta} = (\beta_1, \beta_2)$  and  $\beta_1 = \frac{p_1}{p_0}$ , respectively  $\beta_2 = \frac{p_2}{p_0}$ .

The likelihood function for binned data can be derived from the joint PDF

$$L(\vec{\beta}) = f_{joint}(\vec{k}; \vec{\beta}) = \prod_{n=1}^8 f_n(k_n; \vec{\beta}), \quad (6.47)$$

where  $\vec{k} = (k_1, \dots, k_8)$  denotes the measured values while  $k_n = (\sum w_i)_n \cdot \Delta\phi_{\pi^0, n}$  represents the value in the  $n$ 'th extraction bin. The quantity  $f_n$  denotes the probability to find  $k_n$  entries in the  $n$ 'th extraction bin for given model parameters  $\vec{\beta}$ . The expected number of events in the bin  $v_n(\vec{\beta})$  for given model parameters  $\vec{\beta}$  is computed with

$$v_n(\vec{\beta}) = \left( \sum_{j=1}^8 k_j \right) \cdot [\mathbf{S}(\phi_{\pi^0}; \vec{\beta})]_{a_n}^{b_n}, \quad (6.48)$$

where the function  $\mathbf{S}$  is the antiderivative of the function  $\sigma(\phi_{\pi^0}; \vec{\beta})$  which is evaluated at  $a_n$  ( $b_n$ ) denoting the left (right) edge of the  $n$ 'th extraction bin. Explicitly, the function  $\mathbf{S}$  reads

$$\begin{aligned} \mathbf{S}(\phi_{\pi^0}; \vec{\beta}) &= \frac{1}{2\pi} [\phi_{\pi^0} + \mathbf{S}_{TT}(\phi_{\pi^0}; \beta_1) + \mathbf{S}_{LT}(\phi_{\pi^0}; \beta_2)], \\ \mathbf{S}_{TT}(x; \beta_1) &= \frac{1}{2} \cdot \varepsilon \sin(2x) \beta_1, \\ \mathbf{S}_{LT}(x; \beta_2) &= \sqrt{2\varepsilon(1+\varepsilon)} \sin(x) \beta_2. \end{aligned} \quad (6.49)$$

Here, the number of events in each bin is assumed to follow the Poisson distribution, where the mean value of the Poisson is fixed by the number of expected entries in the bin  $v_n(\beta)$ . Thus, the PDF reads

$$f_{Poisson}(k_n; \vec{\beta}) = \frac{v_n^{k_n}(\vec{\beta})}{k_n!} e^{-v_n(\vec{\beta})}. \quad (6.50)$$

The log-likelihood function is derived by inserting  $f_{Poisson}$  in the joint PDF (Eq. 6.47) and keeping only terms that depend on the model parameters

$$\log L(\vec{\beta}) = \sum_n \left[ k_n \cdot \log v_n(\vec{\beta}) \right]. \quad (6.51)$$

The negative log-likelihood function is minimized for the parameters  $\beta_1$  and  $\beta_2$  and to obtain the parameters  $p_1$  and  $p_2$

$$\begin{aligned}\left\langle \frac{d\sigma_{TT}}{d|t|} \right\rangle &= p_1 = \beta_1 \cdot p_0 = 6.02 \frac{\text{nb}}{(\text{GeV}/c)^2}, \\ \left\langle \frac{d\sigma_{LT}}{d|t|} \right\rangle &= p_2 = \beta_2 \cdot p_0 = 1.44 \frac{\text{nb}}{(\text{GeV}/c)^2}\end{aligned}\quad (6.52)$$

**Uncertainties from minimizer:** The calculation of uncertainties associated to  $p_1$  and  $p_2$  involves a correction since the log-likelihood function is expressed for Poisson distributed random numbers in the bin, Eq. 6.50. The corrected covariance matrix  $C$  is obtained by evaluating

$$\begin{aligned}C &= C_w \cdot C_{w^2}^{-1} \cdot C_w, \\ &= \begin{pmatrix} 1.73 & 0.49 \\ 0.49 & 0.24 \end{pmatrix},\end{aligned}\quad (6.53)$$

where  $C_w$  is the covariance matrix retrieved by minimizing the log-likelihood function for the sum of weights as given in Eq. 6.51. The covariance matrix  $C_{w^2}$  is the result of minimizing the log-likelihood function for the sum of square of weights through substituting  $k_n \rightarrow k_n^2$ .

The validity of this correction was checked in a toy Monte Carlo. Additionally, in Appendix B.4.2 a replication method, inspired by the Poisson bootstrap, was used to further study the uncertainties and the stability of the fit, including a correlation plot for the parameters. Finally, using the parametrization of the PDF (Subsection 6.6.6), a modified likelihood is used in Appendix B.4.3 that does not need the covariance matrix correction.

Conclusively, the numbers for the parameters together with their standard deviations read

$$\begin{aligned}\left\langle \frac{d\sigma_{TT}}{d|t|} \right\rangle &= -6.02 \pm 1.31 \frac{\text{nb}}{(\text{GeV}/c)^2}, \\ \left\langle \frac{d\sigma_{LT}}{d|t|} \right\rangle &= 1.44 \pm 0.49 \frac{\text{nb}}{(\text{GeV}/c)^2}.\end{aligned}\quad (6.54)$$

With the fitted parameters, the fit function can be drawn together with the cross-section values as shown in Fig. 6.38. Additionally, the parameters can be varied within their standard deviations to form the uncertainty band visible in Fig. 6.38. It can be observed that the parameter set corresponding to the best fit leads to a function that goes below zero in the regions where  $\phi_{\pi^0}$  approaches  $\pi$  or  $-\pi$ . One may therefore argue, that this parameter set is unphysical or that the model does not fit the data. However, the uncertainty band shows, that the parameters together with their uncertainties are very well physical. Complementary to this interpretation of the result in the picture of frequentist probabilities, in the following section, the interpretation of the result in the Bayesian picture is outlined.

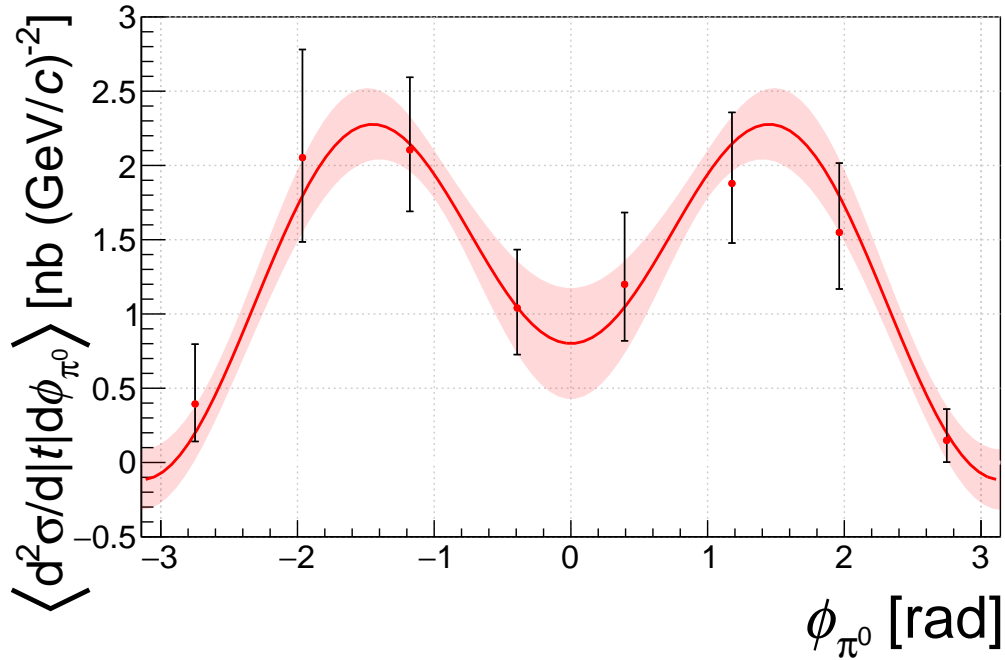


FIGURE 6.38: Differential virtual-photon proton cross-section for the process  $\gamma^*p \rightarrow \pi^0p$  as function of  $\phi_{\pi^0}$ . Each point represents the mean differential cross-section in the bins defined in Table 6.4. The points are plotted at the center of the respective bin. The error bars represent the confidence interval with exact coverage as discussed in Subsection 6.6.5. The red curve together with the red uncertainty band is the result of a binned maximum likelihood fit to the data using Eq. 6.45. The red band visualizes the effect of varying the fitted parameters within one standard deviation.

### 6.6.8 Bayesian interpretation

Minimizing the likelihood Eq. 6.51 results in a parameter set that results in negative cross-section values near  $\phi_{\pi^0} = \pm\pi$ . This motivates to consider the Bayesian interpretation of the result. In the Bayesian approach, the goal is to quote the best guess for the parameters and express the probability that this statement is true. This allows for incorporating prior information  $\pi(\vec{\beta})$  into the posterior  $P(\vec{\beta}|\vec{k})$  through Bayes' Theorem

$$P(\vec{\beta}|\vec{k}) = \frac{P(\vec{k}|\vec{\beta})\pi(\vec{\beta})}{\int P(\vec{k}|\vec{\beta})\pi(\vec{\beta}) d\vec{\beta}}$$

where  $\vec{\beta}$  denotes the model parameters and  $\vec{k}$  denotes the measured values in analogy to the previous section. Here, the likelihood  $P(\vec{k}|\vec{\beta})$  is proportional to  $L(\vec{\beta})$  stated in Eq. 6.47.

The goal is now to maximize the log-posterior for a set of parameters. However, minimizers like the one used before, in general, do not behave well with discontinuities that are introduced by the prior. Also, since in the

Bayesian interpretation model parameters are random variables as well, the result is not necessarily a single number, but the PDF for the respective parameter. This is why different techniques are established that are more suited to the task.

One common approach is the Markov chain Monte Carlo (MCMC) sampling method. Here, an implementation of the method [111] is used to draw samples from the log-posterior probability distribution

$$\begin{aligned}\log P(\vec{\beta}|\vec{k}) &= \log P(\vec{k}|\vec{\beta}) + \log \pi(\vec{\beta}), \\ &= \log L(\vec{\beta}) + \log \pi(\vec{\beta}).\end{aligned}\quad (6.55)$$

The prior  $\pi(\vec{\beta})$  is defined to be equal to 1 if the chosen parameters result in a strictly positive cross-section or else 0. Compared to the previous formulation of the likelihood, the normalization parameter  $p_0$  can not anymore be treated independently since the prior can introduce a dependence of the normalization on the model parameters. The normalization enters as an additional model parameter  $\beta_0 = p_0$  in the likelihood and  $p_1$  and  $p_2$  are obtained by (cf. Eq. 6.45 and Eq. 6.46)

$$\begin{aligned}p_1 &= \beta_1 \cdot \beta_0, \\ p_2 &= \beta_2 \cdot \beta_0.\end{aligned}\quad (6.56)$$

The quantity  $v_n(\vec{\beta})$ , denoting the expected number of events in the  $n$ 'th bin, now depends on the normalization parameter

$$v_n(\vec{\beta}) = \beta_0 \cdot [\mathbf{S}(\phi_{\pi^0}; \vec{\beta})]_{a_n}^{b_n}. \quad (6.57)$$

The likelihood  $L(\vec{\beta})$  is formulated based on the extended maximum likelihood approach

$$L(\vec{\beta}) = f(\vec{k}; \beta_0) \cdot f_{joint}(\vec{k}; \vec{\beta}) = f(\vec{k}; \beta_0) \cdot \prod_{n=1}^8 f_n(k_n | \nu_n(\vec{\beta})), \quad (6.58)$$

where  $f(\vec{k}; \beta_0)$  denotes the probability to measure the unseparated cross-section. The probability density in the bins is given by the parameterizations of the PDFs obtained in Subsection 6.6.6, therefore  $f_n(k_n | \nu_n(\vec{\beta}))$  is substituted by  $f_{\Gamma_n}(k_n | \nu_n(\vec{\beta}))$ . In an analogous way,  $f(\vec{k}; \beta_0)$  is expressed using a parameterization of the PDF of the combined measurement.

The MCMC sampler is then used to draw samples from the log-posterior<sup>6</sup>. The density of the samples in the three-dimensional parameter space corresponds to the probability of the respective parameter set. The density already represents the Bayesian result. However, in order to quantify the result, the

<sup>6</sup> In the Appendix B.4.4, the MCMC is applied to a log-posterior with a flat prior.

most probable parameter set can be extracted as

$$\begin{aligned} \left\langle \frac{d\sigma_T}{d|t|} + \varepsilon \frac{d\sigma_L}{d|t|} \right\rangle &= \left\langle \frac{d\sigma_U}{d|t|} \right\rangle = 8.11 \frac{\text{nb}}{(\text{GeV}/c)^2}, \\ \left\langle \frac{d\sigma_{TT}}{d|t|} \right\rangle &= -5.32 \frac{\text{nb}}{(\text{GeV}/c)^2}, \\ \left\langle \frac{d\sigma_{LT}}{d|t|} \right\rangle &= 1.37 \frac{\text{nb}}{(\text{GeV}/c)^2}. \end{aligned} \quad (6.59)$$

In order to visualize the surroundings around the most probable parameter set, Fig. 6.39 shows slices of each parameter and parameter combination<sup>7</sup>. In

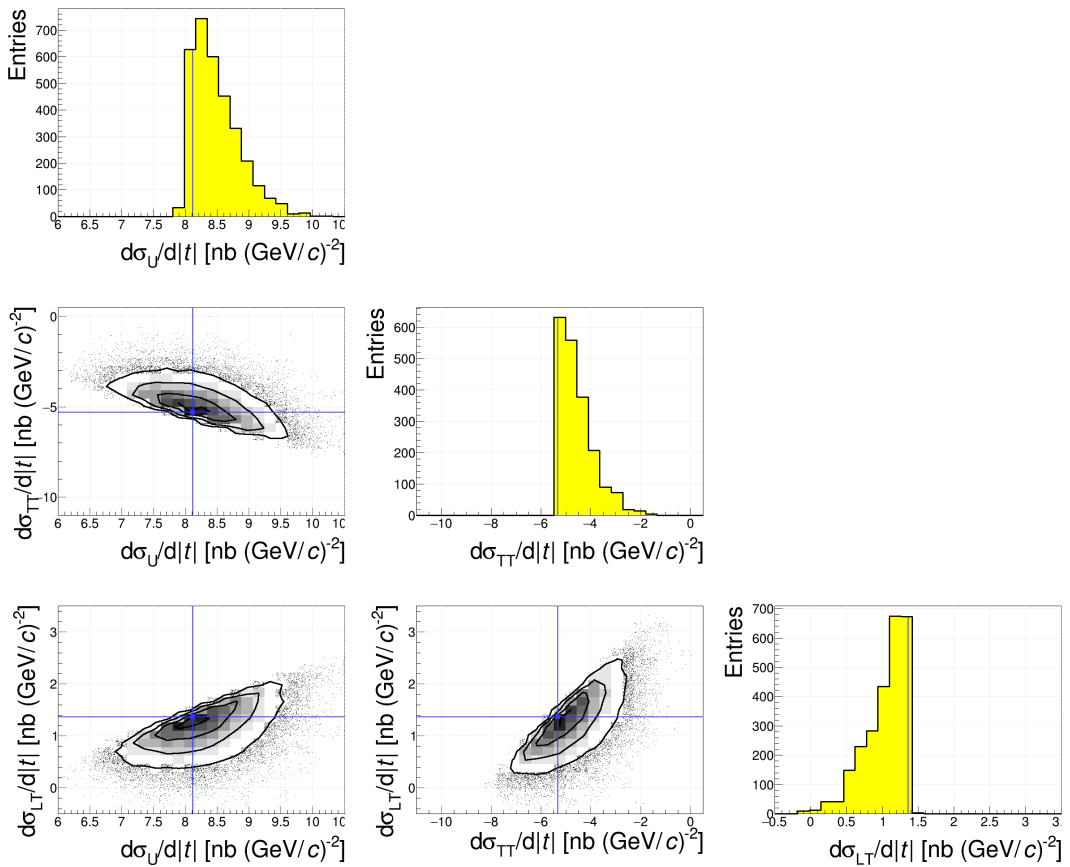


**FIGURE 6.39:** Visualization of the most probable parameter set obtained using the MCMC sampling method. The histograms show the values for the respective parameter or parameter combination when slicing the other parameters. For instance, the lower left shows the samples for  $\langle \frac{d\sigma_{LT}}{d|t|} \rangle$  and  $\langle \frac{d\sigma_U}{d|t|} \rangle$  for a slice in  $\langle \frac{d\sigma_{TT}}{d|t|} \rangle$ . The blue lines and marker indicate the position of the most probable parameter set. The contours contain from dark to light  $\{10, 40, 70, 90\}$ % of the most probable parameters.

all histograms in Fig. 6.39, a diagonal cut in the parameter space, respectively a steep edge, can be observed as a result of the choice of the prior. One can

<sup>7</sup>The widths of the slice amounts to  $\sim 1\%$  of the respective parameter value.

observe, that the most probable parameter set is located very close at the edge of the allowed parameter space.

It is not clear how to assign statistical errors on the most probable parameter set. Another possible way to present and quantify the MCMC result is by integrating the parameters as depicted in Fig. 6.40. The mean and RMS of the

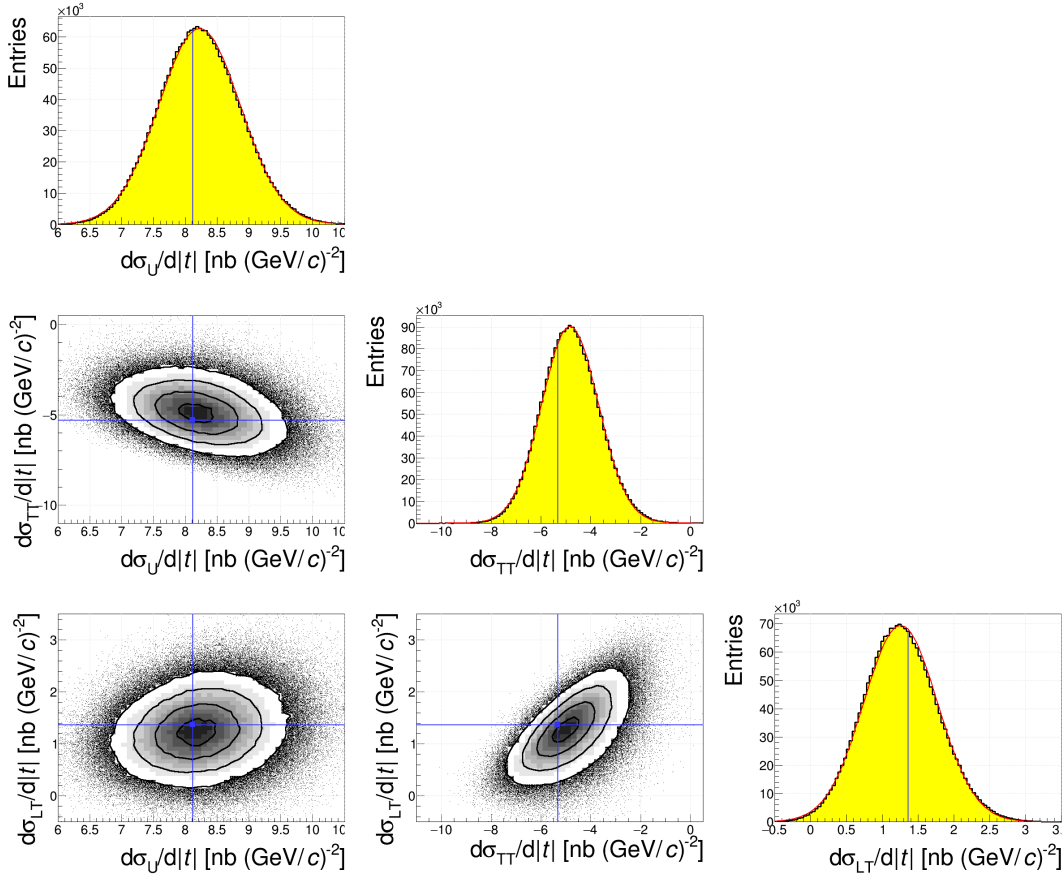


**FIGURE 6.40:** Visualization of the distribution of parameters obtained with the MCMC. The histograms show the values for the respective parameter or parameter combination when integrating the other parameters. For instance, the lower left shows the values for  $\langle \frac{d\sigma_{LT}}{d|t|} \rangle$  and  $\langle \frac{d\sigma_U}{d|t|} \rangle$  when integrating over  $\langle \frac{d\sigma_{TT}}{d|t|} \rangle$ . The blue lines and marker indicate the position of the most probable parameter set. The contours contain from dark to light  $\{10, 40, 70, 90\}\%$  of the most probable parameters.

resulting one dimensional PDF for the respective parameter can then be used to extract the following values

$$\begin{aligned}
 \left\langle \frac{d\sigma_T}{d|t|} + \varepsilon \frac{d\sigma_L}{d|t|} \right\rangle &= \left\langle \frac{d\sigma_U}{d|t|} \right\rangle = 8.22 \pm 0.65 \frac{\text{nb}}{(\text{GeV}/c)^2}, \\
 \left\langle \frac{d\sigma_{TT}}{d|t|} \right\rangle &= -4.82 \pm 1.15 \frac{\text{nb}}{(\text{GeV}/c)^2}, \\
 \left\langle \frac{d\sigma_{LT}}{d|t|} \right\rangle &= 1.26 \pm 0.52 \frac{\text{nb}}{(\text{GeV}/c)^2}. \tag{6.60}
 \end{aligned}$$

It is also possible to state the corresponding covariance matrix

$$C = \begin{pmatrix} 0.42 & -0.25 & 0.06 \\ -0.25 & 1.32 & 0.36 \\ 0.06 & 0.36 & 0.27 \end{pmatrix}.$$

It shall be noted that this quantification of the result obscures the fact, that parts of the parameter space is not allowed by the choice of the prior as shown in Fig. 6.39. Still, the numbers obtained by the projections (Eq. 6.60) are the ones that will be used in the forthcoming sections.

A comparison of the resulting curves for the two parameter sets (Eq. 6.59 and Eq. 6.60) is depicted in Fig. 6.41. The uncertainty band is created by drawing

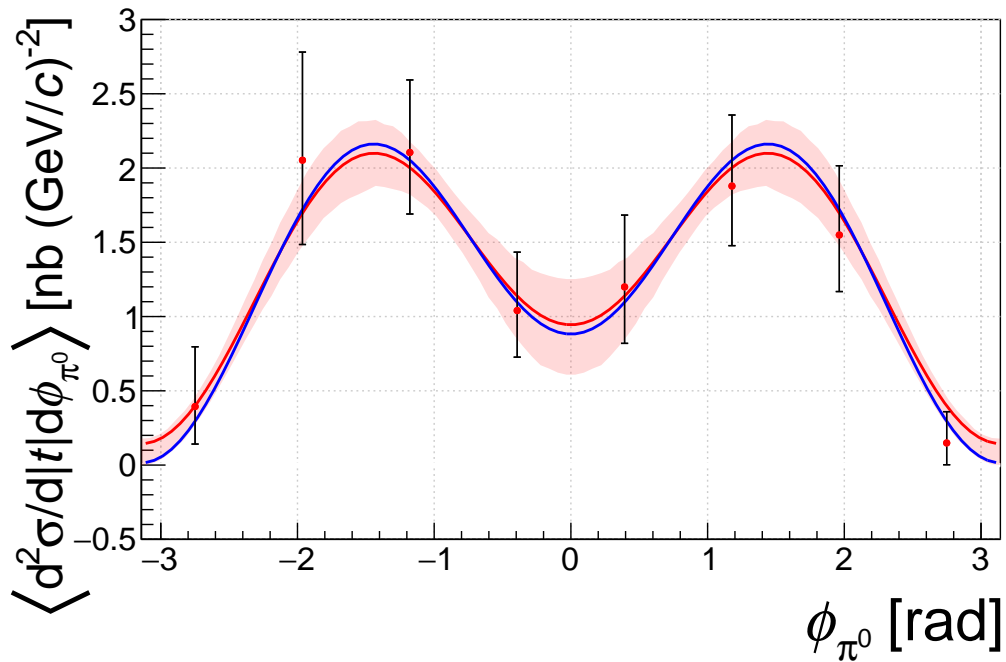


**FIGURE 6.41:** Differential virtual-photon proton cross-section for the process  $\gamma^*p \rightarrow \pi^0p$  as a function of  $\phi_{\pi^0}$ . Each point represents the mean differential cross-section in the bins defined in Table 6.4. The points are plotted at the center of the respective bin. The error bars represent the confidence interval with exact coverage as discussed in Subsection 6.6.5. The red and blue curve together with the red uncertainty band are the result of sampling the log-posterior Eq. 6.58 using an MCMC sampler. The red curve represents the parameter set obtained by projecting the MCMC sample distribution to the respective parameter (Eq. 6.60) while the blue curve represents the parameters corresponding to the most probable value (Eq. 6.59). The red band visualizes the spread of the curves when drawing 68% of the most probable values of the MCMC sample.

the parameter sets of the MCMC sample and taking spread of the 68% most probable values at every  $\phi_{\pi^0}$  position. As expected, the model curve does not cross into the negative region.

### 6.6.9 Summary

Throughout the section, the extraction of the cross-section was performed as a function of  $\phi_{\pi^0}$  and as a function of  $|t|$ . On account of the low statistics, the confidence intervals associated with the measurement were computed using the Poisson bootstrap technique. A collection of relevant involved numbers and the final cross-section values in each bin, as well as the value for the unseparated cross-section, is presented in Table 6.6. In Table 6.5, the final result of the measurement with statistical and systematical uncertainties is summarized. The systematic uncertainties are discussed in the following Section 6.7. The results are also visualized in Fig. 6.42 and Fig. 6.43.

**TABLE 6.5:** Summary of the measurements with statistical and systematical uncertainties. The systematic uncertainties are determined in the following Section 6.7. In case of the unseparated cross-section, the statistical uncertainty follows from the variance while the statistical uncertainty in the individual bins is given by the confidence intervals with exact coverage.

	$\left\langle \frac{d\sigma\gamma^*p \rightarrow \pi^0 p}{d t } \right\rangle_{t_1}$	=	(16.3	$\begin{array}{l} +3.6 \\ -3.1 \end{array}$	<sub>stat</sub>	$\begin{array}{l} +2.0 \\ -2.0 \end{array}$	<sub>sys</sub> )	$\frac{\text{nb}}{(\text{GeV}/c)^2}$
	$\left\langle \frac{d\sigma\gamma^*p \rightarrow \pi^0 p}{d t } \right\rangle_{t_2}$	=	(16.2	$\begin{array}{l} +3.8 \\ -3.2 \end{array}$	<sub>stat</sub>	$\begin{array}{l} +2.1 \\ -1.9 \end{array}$	<sub>sys</sub> )	$\frac{\text{nb}}{(\text{GeV}/c)^2}$
	$\left\langle \frac{d\sigma\gamma^*p \rightarrow \pi^0 p}{d t } \right\rangle_{t_3}$	=	(11.5	$\begin{array}{l} +2.6 \\ -2.2 \end{array}$	<sub>stat</sub>	$\begin{array}{l} +1.5 \\ -1.4 \end{array}$	<sub>sys</sub> )	$\frac{\text{nb}}{(\text{GeV}/c)^2}$
	$\left\langle \frac{d\sigma\gamma^*p \rightarrow \pi^0 p}{d t } \right\rangle_{t_4}$	=	(3.4	$\begin{array}{l} +1.4 \\ -1.2 \end{array}$	<sub>stat</sub>	$\begin{array}{l} +0.8 \\ -0.5 \end{array}$	<sub>sys</sub> )	$\frac{\text{nb}}{(\text{GeV}/c)^2}$
	$\left\langle \frac{d\sigma\gamma^*p \rightarrow \pi^0 p}{d t } \right\rangle_{t_5}$	=	(1.5	$\begin{array}{l} +1.0 \\ -0.8 \end{array}$	<sub>stat</sub>	$\begin{array}{l} +0.4 \\ -0.2 \end{array}$	<sub>sys</sub> )	$\frac{\text{nb}}{(\text{GeV}/c)^2}$
	$\left\langle \frac{d^2\sigma\gamma^*p \rightarrow \pi^0 p}{d t d\phi_{\pi^0}} \right\rangle_{\phi_{\pi^0,1}}$	=	(0.4	$\begin{array}{l} +0.4 \\ -0.3 \end{array}$	<sub>stat</sub>	$\begin{array}{l} +0.1 \\ -0.1 \end{array}$	<sub>sys</sub> )	$\frac{\text{nb}}{(\text{GeV}/c)^2}$
	$\left\langle \frac{d^2\sigma\gamma^*p \rightarrow \pi^0 p}{d t d\phi_{\pi^0}} \right\rangle_{\phi_{\pi^0,2}}$	=	(2.1	$\begin{array}{l} +0.7 \\ -0.6 \end{array}$	<sub>stat</sub>	$\begin{array}{l} +0.3 \\ -0.2 \end{array}$	<sub>sys</sub> )	$\frac{\text{nb}}{(\text{GeV}/c)^2}$
	$\left\langle \frac{d^2\sigma\gamma^*p \rightarrow \pi^0 p}{d t d\phi_{\pi^0}} \right\rangle_{\phi_{\pi^0,3}}$	=	(2.1	$\begin{array}{l} +0.5 \\ -0.4 \end{array}$	<sub>stat</sub>	$\begin{array}{l} +0.3 \\ -0.3 \end{array}$	<sub>sys</sub> )	$\frac{\text{nb}}{(\text{GeV}/c)^2}$
	$\left\langle \frac{d^2\sigma\gamma^*p \rightarrow \pi^0 p}{d t d\phi_{\pi^0}} \right\rangle_{\phi_{\pi^0,4}}$	=	(1.0	$\begin{array}{l} +0.4 \\ -0.3 \end{array}$	<sub>stat</sub>	$\begin{array}{l} +0.2 \\ -0.1 \end{array}$	<sub>sys</sub> )	$\frac{\text{nb}}{(\text{GeV}/c)^2}$
	$\left\langle \frac{d^2\sigma\gamma^*p \rightarrow \pi^0 p}{d t d\phi_{\pi^0}} \right\rangle_{\phi_{\pi^0,5}}$	=	(1.2	$\begin{array}{l} +0.5 \\ -0.4 \end{array}$	<sub>stat</sub>	$\begin{array}{l} +0.2 \\ -0.2 \end{array}$	<sub>sys</sub> )	$\frac{\text{nb}}{(\text{GeV}/c)^2}$
	$\left\langle \frac{d^2\sigma\gamma^*p \rightarrow \pi^0 p}{d t d\phi_{\pi^0}} \right\rangle_{\phi_{\pi^0,6}}$	=	(1.9	$\begin{array}{l} +0.5 \\ -0.4 \end{array}$	<sub>stat</sub>	$\begin{array}{l} +0.2 \\ -0.2 \end{array}$	<sub>sys</sub> )	$\frac{\text{nb}}{(\text{GeV}/c)^2}$
	$\left\langle \frac{d^2\sigma\gamma^*p \rightarrow \pi^0 p}{d t d\phi_{\pi^0}} \right\rangle_{\phi_{\pi^0,7}}$	=	(1.5	$\begin{array}{l} +0.5 \\ -0.4 \end{array}$	<sub>stat</sub>	$\begin{array}{l} +0.2 \\ -0.2 \end{array}$	<sub>sys</sub> )	$\frac{\text{nb}}{(\text{GeV}/c)^2}$
	$\left\langle \frac{d^2\sigma\gamma^*p \rightarrow \pi^0 p}{d t d\phi_{\pi^0}} \right\rangle_{\phi_{\pi^0,8}}$	=	(0.1	$\begin{array}{l} +0.2 \\ -0.1 \end{array}$	<sub>stat</sub>	$\begin{array}{l} +0.1 \\ -0.0 \end{array}$	<sub>sys</sub> )	$\frac{\text{nb}}{(\text{GeV}/c)^2}$
	$\left\langle \frac{d\sigma_T}{d t } + \varepsilon \frac{d\sigma_L}{d t } \right\rangle$	=	(8.1	$\pm 0.9$	<sub>stat</sub>	$\begin{array}{l} +1.1 \\ -1.0 \end{array}$	<sub>sys</sub> )	$\frac{\text{nb}}{(\text{GeV}/c)^2}$
BML	$\left\langle \frac{d\sigma_{TT}}{d t } \right\rangle$	=	(-6.0	$\pm 1.3$	<sub>stat</sub>	$\begin{array}{l} +0.7 \\ -0.7 \end{array}$	<sub>sys</sub> )	$\frac{\text{nb}}{(\text{GeV}/c)^2}$
	$\left\langle \frac{d\sigma_{LT}}{d t } \right\rangle$	=	(1.4	$\pm 0.5$	<sub>stat</sub>	$\begin{array}{l} +0.3 \\ -0.2 \end{array}$	<sub>sys</sub> )	$\frac{\text{nb}}{(\text{GeV}/c)^2}$
MCMC	$\left\langle \frac{d\sigma_T}{d t } + \varepsilon \frac{d\sigma_L}{d t } \right\rangle$	=	(8.2	$\pm 0.6$	<sub>stat</sub>	$\begin{array}{l} +1.2 \\ -1.0 \end{array}$	<sub>sys</sub> )	$\frac{\text{nb}}{(\text{GeV}/c)^2}$
	$\left\langle \frac{d\sigma_{TT}}{d t } \right\rangle$	=	(-4.8	$\pm 1.1$	<sub>stat</sub>	$\begin{array}{l} +0.6 \\ -0.6 \end{array}$	<sub>sys</sub> )	$\frac{\text{nb}}{(\text{GeV}/c)^2}$
	$\left\langle \frac{d\sigma_{LT}}{d t } \right\rangle$	=	(1.3	$\pm 0.5$	<sub>stat</sub>	$\begin{array}{l} +0.3 \\ -0.2 \end{array}$	<sub>sys</sub> )	$\frac{\text{nb}}{(\text{GeV}/c)^2}$

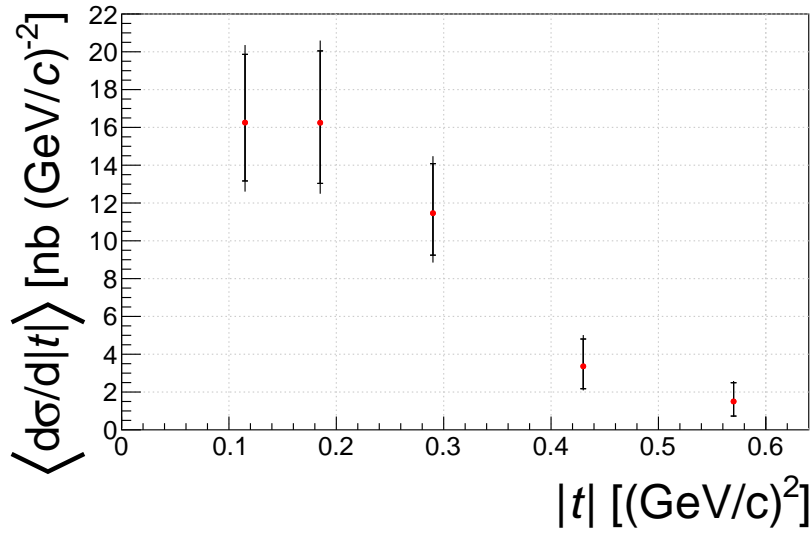


**FIGURE 6.42:** Differential virtual-photon proton cross-section for the process  $\gamma^*p \rightarrow \pi^0p$  as function of  $|t|$ . The inner error bars represent the confidence interval with exact coverage as described in Subsection 6.6.5, while the outer ones represent the square root of the quadratic sum of statistical and systematic uncertainties. The systematic uncertainties are discussed in Section 6.7.

The modulation of the cross-section as a function of  $\phi_{\pi^0}$  was fitted with two different methods as elaborated in Subsection 6.6.7 and Subsection 6.6.8. The result for the parameter values estimated with the binned maximum likelihood fit, as well as the parameter values that characterize the Bayesian result, are listed in Table 6.6. The two interpretations of the measurement are also visualized in Fig. 6.43.

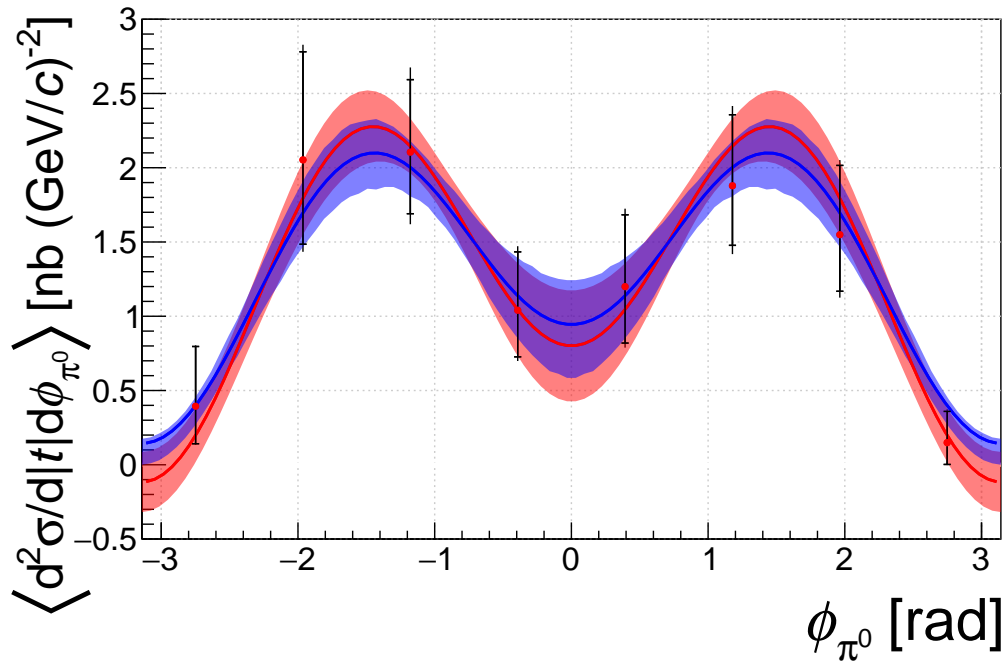


**FIGURE 6.43:** Differential virtual-photon proton cross-section for the process  $\gamma^*p \rightarrow \pi^0p$  as function of  $\phi_{\pi^0}$ . The inner error bars represent the confidence interval with exact coverage as described in Subsection 6.6.5, while the outer ones represent the square root of the quadratic sum of statistical and systematic uncertainties. The systematic uncertainties are discussed in Section 6.7. The red curve together with the red uncertainty band is the result of a binned maximum likelihood fit to the data using Eq. 6.45. The blue curve together with the blue uncertainty band is the result of sampling the log-posterior Eq. 6.58 using the MCMC sampling method.

**TABLE 6.6:** Summary of numbers involved in the cross-section extraction. The quantities  $a$  and  $b$  denote the lower and upper edge of the extraction bins, while  $\Delta = b - a$  denotes the width.  $N_{data}^{\Delta\Omega}$  gives the number of data events in the bin while  $\sum_{i=1}^{N_{data}^{\Delta\Omega}} w_i$  and  $\sum_{i=1}^{N_{BG}^{\Delta\Omega}} w_i$  denotes the sum of weights for data and “LEPTO background”. The cross-section in the bin is denoted with  $(\sum w_i)_{\Delta\Omega}$  with variance  $(\sum w_i^2)_{\Delta\Omega}$ . The confidence interval is denoted by  $[C_l, C_u]$  with width  $\Delta CI = C_u - C_l$  while the confidence interval with exact coverage is denoted by  $[C_l^*, C_u^*]$  with width  $\Delta CI^* = C_u^* - C_l^*$ . The first row shows the numbers for the unpolarized cross-section. Here, the extraction covers the full range of the analysis and no bin size is quoted. For brevity, units are omitted here.

Bin	$a$	$b$	$\Delta$	$N_{data}^{\Delta\Omega}$	$\sum_{i=1}^{N_{data}^{\Delta\Omega}} w_i$	$\sum_{i=1}^{N_{BG}^{\Delta\Omega}} w_i$	$(\sum w_i)_{\Delta\Omega}$	$(\sum w_i^2)_{\Delta\Omega}$	bootstrap $CI$			bootstrap $CI^*$		
									$C_l$	$C_u$	$\Delta CI$	$C_l^*$	$C_u^*$	$\Delta CI^*$
$\langle \frac{d\sigma_T}{d t } + \varepsilon \frac{d\sigma_L}{d t } \rangle$	-	-	-	241	11.46	3.31	8.14	0.89	-	-	-	-	-	-
$t_1$	0.08	0.15	0.07	56	21.32	5.07	16.25	11.17	12.91	19.59	6.68	13.17	19.86	6.70
$t_2$	0.15	0.22	0.07	61	20.78	4.54	16.25	12.25	12.75	19.74	6.99	13.04	20.05	7.01
$t_3$	0.22	0.36	0.14	65	14.60	3.13	11.46	5.85	9.05	13.88	4.83	9.24	14.08	4.84
$t_4$	0.36	0.50	0.14	36	6.63	3.27	3.36	1.72	2.05	4.67	2.62	2.18	4.80	2.63
$t_5$	0.50	0.64	0.14	23	3.55	2.05	1.50	0.77	0.62	2.37	1.75	0.73	2.49	1.76
$\phi_{\pi^0,1}$	-3.14	-2.36	0.79	7	0.77	0.38	0.39	0.10	0.08	0.69	0.60	0.14	0.80	0.65
$\phi_{\pi^0,2}$	-2.36	-1.57	0.79	36	2.59	0.54	2.05	0.42	1.41	2.70	1.29	1.49	2.78	1.30
$\phi_{\pi^0,3}$	-1.57	-0.79	0.79	51	2.72	0.62	2.10	0.20	1.65	2.55	0.90	1.69	2.59	0.90
$\phi_{\pi^0,4}$	-0.79	0.00	0.79	28	1.57	0.53	1.04	0.12	0.69	1.39	0.70	0.73	1.43	0.71
$\phi_{\pi^0,5}$	0.00	0.79	0.79	26	1.82	0.62	1.20	0.19	0.77	1.63	0.86	0.82	1.68	0.86
$\phi_{\pi^0,6}$	0.79	1.57	0.79	47	2.49	0.61	1.88	0.19	1.44	2.32	0.88	1.48	2.36	0.88
$\phi_{\pi^0,7}$	1.57	2.36	0.79	36	2.10	0.55	1.55	0.18	1.13	1.97	0.84	1.17	2.02	0.85
$\phi_{\pi^0,8}$	2.36	3.14	0.79	10	0.52	0.38	0.15	0.03	-0.03	0.28	0.31	0.00	0.36	0.36

## 6.7 Systematic studies

In this section, different sources of systematic uncertainties are examined. In each subsection, the effect of a variation in the cross-section extraction method is studied by comparing the modified cross-section yields with the yields of the default extraction. For most of the systematic effects, the impact is studied for each cross-section extraction bin. For brevity, the bins are labeled  $\sigma_n$  denoting the  $n$ 'th extraction bin. Furthermore, the impact of the systematic effect on the unseparated cross-section  $\langle \frac{d\sigma_{LL}}{d|t|} \rangle = \langle \frac{d\sigma_T}{d|t|} + \varepsilon \frac{d\sigma_L}{d|t|} \rangle$  and the values determined by the fit for  $\langle \frac{d\sigma_{TT}}{d|t|} \rangle$  and  $\langle \frac{d\sigma_{LT}}{d|t|} \rangle$  is studied for both the binned maximum likelihood minimization and the MCMC method.

### 6.7.1 Variation of the absolute normalization scale

As outlined in Section 6.6, the cross-section is determined from the sum of weights, where the weight of the  $i$ 'th event (*cf.* Eq. 6.34) is given by

$$w_i = \frac{\alpha}{\beta} \frac{1}{\mathcal{L} \Delta \Omega} \frac{a(\Omega_i)^{-1}}{\Gamma(\Omega_i)},$$

Here, the scaling parameters  $\alpha = \beta = 1$  are introduced. Systematic effects can influence the weight in the numerator and the denominator. A scaling of the numerator can appear for example when data events are lost due to an (unknown) inefficiency while the denominator is affected by systematic uncertainties from the luminosity and the acceptance. The systematic uncertainties discussed in the course of this section often fall back to a scaling of either the numerator or the denominator.

To illustrate the effect of a scaling of the numerator on the final result, Fig. 6.44 (Fig. 6.45) shows exemplary the influence of the scaling of the  $\mu^+$  data on the cross-section in the  $t$  ( $\phi_{\pi^0}$ ) bins. The figures are created by modifying the quantity  $\alpha$  of the weight when extracting the cross-section for  $\mu^+$  beam. The extraction is repeated for values of  $\alpha$  between 0.6 and 1.4 and the relative deviation to the nominal value in the respective bin is plotted. As expected, this results in a deviation linear in  $\alpha$ . As an exception, the first bin in  $\phi_{\pi^0}$  shows a negative slope. Here, the cross-section value extracted for  $\mu^+$  beam is negative (see Fig. 6.32), *i.e.* the estimated background exceeds the data. Since the scaling parameter  $\alpha$  is applied to the background estimation as well, the cross-section for  $\mu^+$  beam gets more negative with increasing  $\alpha$ , leading to an overall decrease of the cross-section with  $\alpha$  in this particular bin.

To depict the effect on the final result when scaling the denominator of the weight, Fig. 6.46 (Fig. 6.47) shows the effect of scaling the  $\mu^-$  flux in the bins of  $t$  ( $\phi_{\pi^0}$ ). For that, the value of  $\beta$  is modified for  $\mu^-$  data and "LEPTO background" events between 0.8 and 1.2. The resulting variation of the extracted cross-section compared to the nominal value leads to the expected  $1/\beta$  dependence.

Two systematic uncertainties that result in a scaling of the weight are discussed in the paragraphs after the figures.

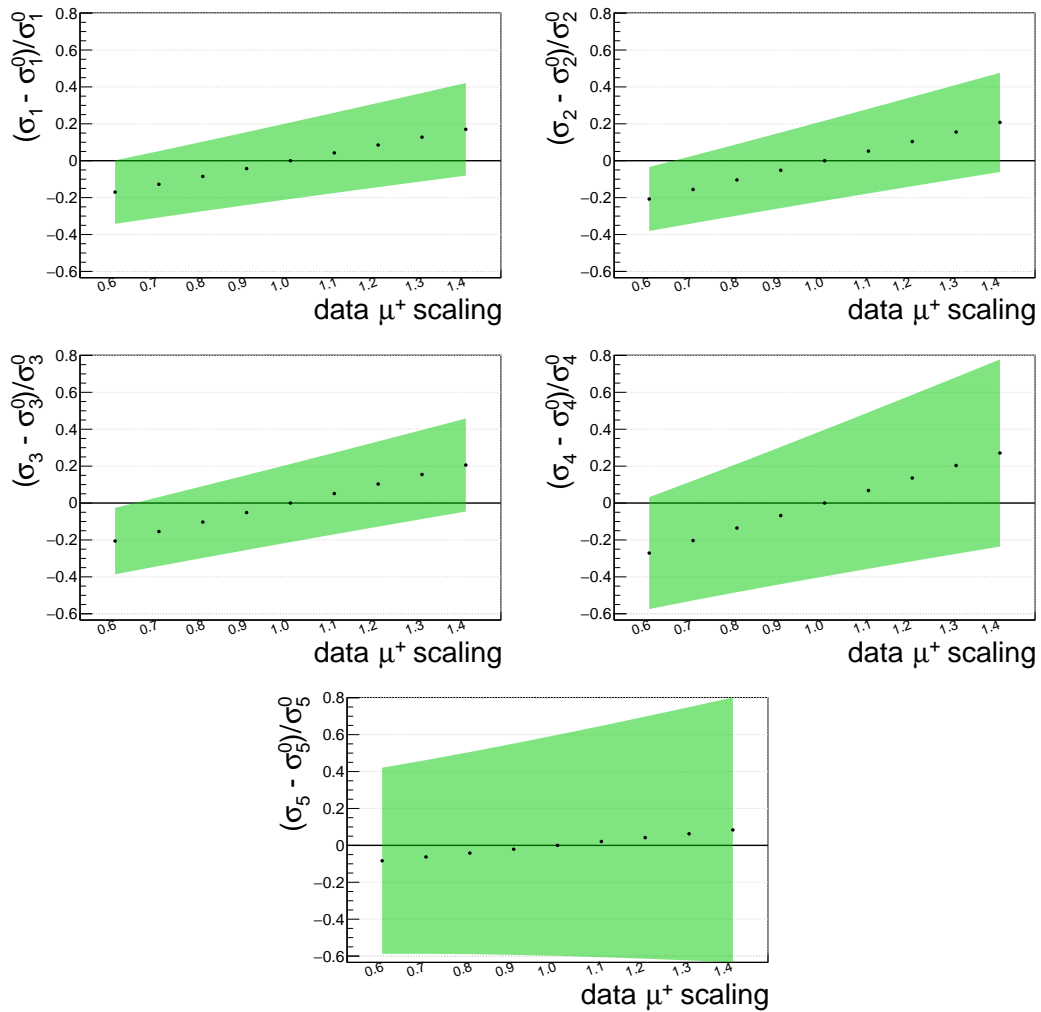
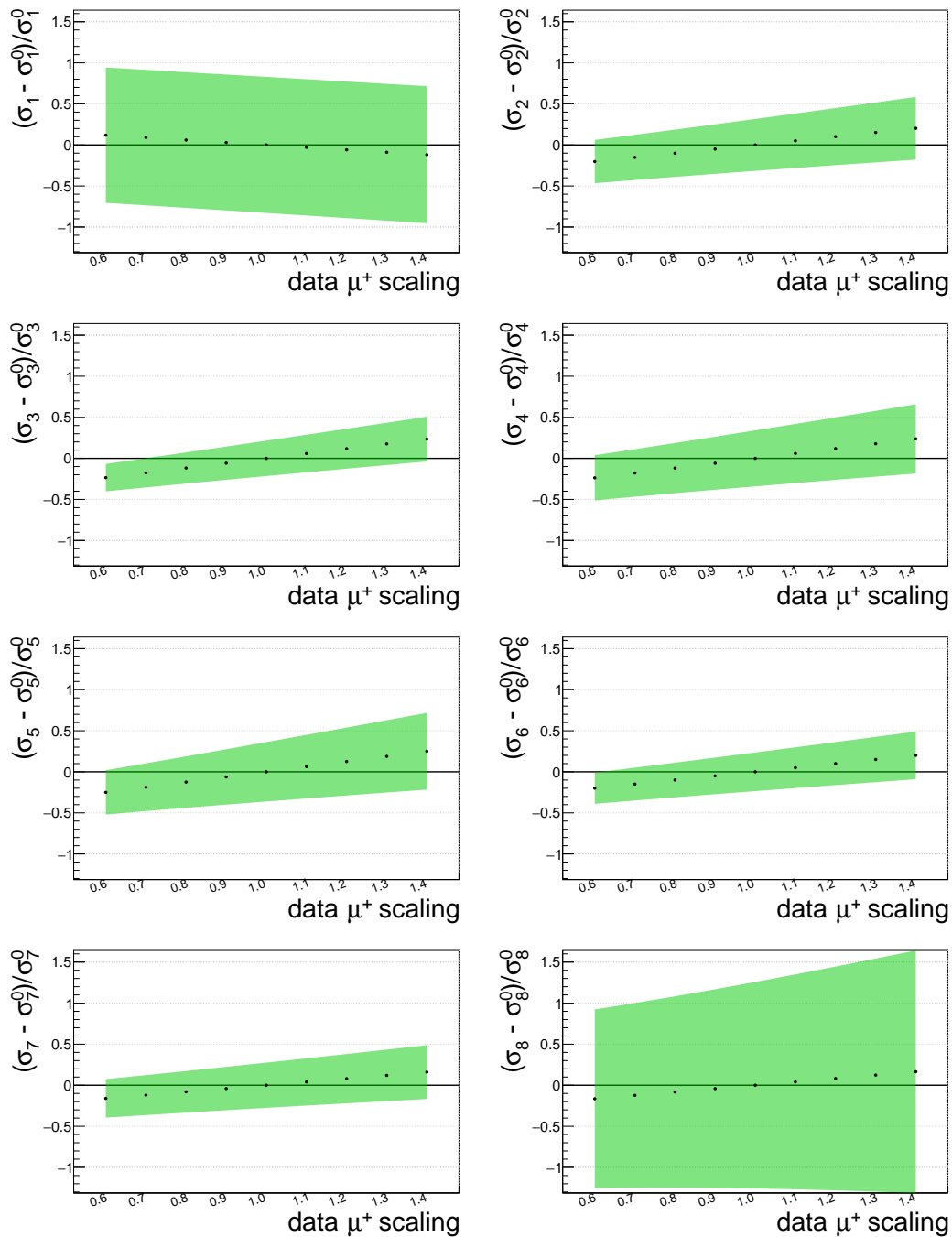
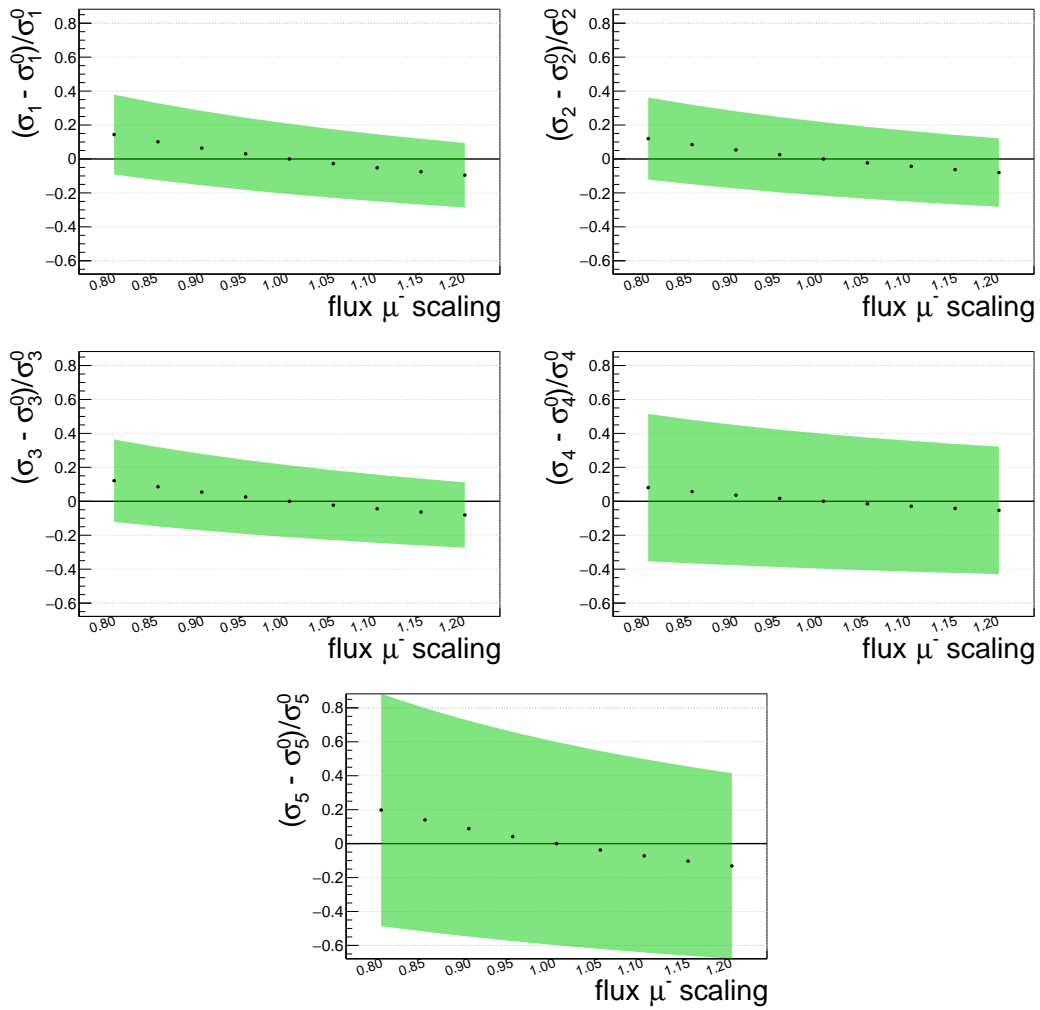


FIGURE 6.44: Influence on the extracted value of the cross-section in the 5 bins of  $t$ , originating from a scaling of the numbers of  $\mu^+$  events. The quantity  $\sigma_i^0$  denotes the preferred value of the cross-section in the corresponding  $t$ -bin with  $i \in 1,2,3,4,5$ . The green band corresponds to the relative statistical uncertainty associated to the extracted value.



**FIGURE 6.45:** Influence on the extracted value of the cross-section in the 8 bins of  $\phi_{\pi^0}$ , originating from a scaling of the numbers of  $\mu^+$  events. The quantity  $\sigma_i^0$  denotes the preferred value of the cross-section in the corresponding  $\phi_{\pi^0}$ -bin with  $i \in 1, 2, \dots, 8$ . The green band corresponds to the relative statistical uncertainty associated to the extracted value.



**FIGURE 6.46:** Influence on the extracted value of the cross-section in the 5 bins of  $t$ , originating from a scaling of the  $\mu^-$  flux. The quantity  $\sigma_i^0$  denotes the preferred value of the cross-section in the corresponding  $t$ -bin with  $i \in 1,2,3,4,5$ . The green band corresponds to the relative statistical uncertainty associated to the extracted value.

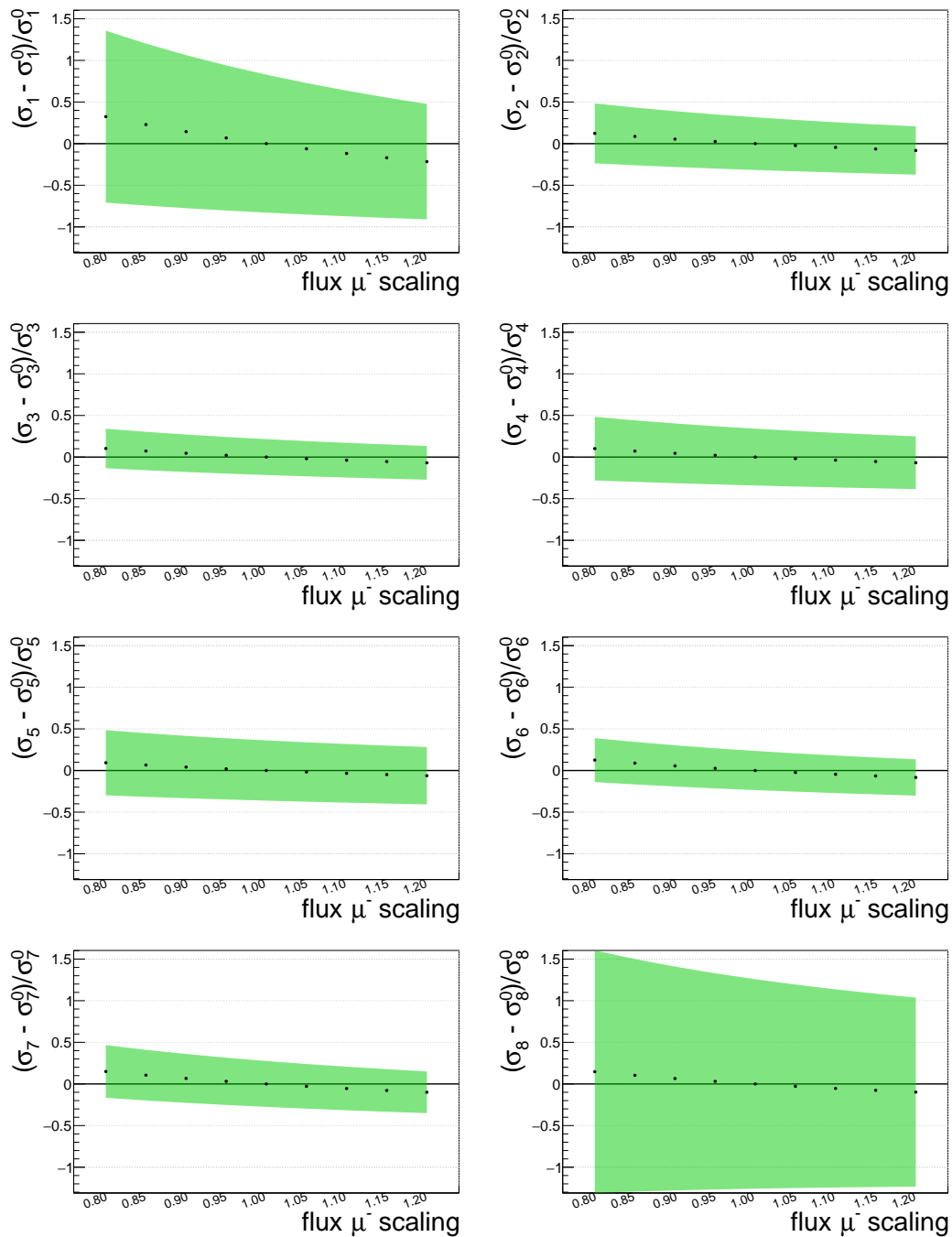


**FIGURE 6.47:** Influence on the extracted value of the cross-section in the 8 bins of  $\phi_{\pi^0}$ , originating from a scaling of the  $\mu^-$  flux. The quantity  $\sigma_i^0$  denotes the preferred value of the cross-section in the corresponding  $\phi_{\pi^0}$ -bin with  $i \in 1, 2, \dots, 8$ . The green band corresponds to the relative statistical uncertainty associated to the extracted value.

**Loss of  $\mu^+$  data:** In the course of the DVCS analysis, a loss of  $\mu^+$  data was unveiled by comparing the estimated signal yields for the Bethe-Heitler process to data in the region of  $80 \text{ GeV} < \nu < 144 \text{ GeV}$ , see [31, p. 128]. Conservatively, it is assumed that this loss of events might also be present in the analysis at hand and the uncertainty is included into the systematic uncertainties. In Table 6.7 and Table 6.8 the systematic effect of a gain of 20%  $\mu^+$  data on the cross-sections is summarized, in Table 6.9 the influence on the fit parameters is given.

**TABLE 6.7:** Summary of the estimated relative systematic uncertainty  $s_{loss}$  on the cross-section in the 5 bins of  $t$ , originating from the loss of  $\mu^+$  data. Arrows indicate an increase or decrease of the measured value due to the systematic effect.

bin	$\sigma_1$	$\sigma_2$	$\sigma_3$	$\sigma_4$	$\sigma_5$
$s_{loss}^\uparrow$	8 %	10 %	10 %	13 %	4 %

**TABLE 6.8:** Summary of the estimated relative systematic uncertainty  $s_{loss}$  on the cross-section in the 8 bins of  $\phi_{\pi^0}$ , originating from the loss of  $\mu^+$  data. Arrows indicate an increase or decrease of the measured value due to the systematic effect.

bin	$\sigma_1$	$\sigma_2$	$\sigma_3$	$\sigma_4$	$\sigma_5$	$\sigma_6$	$\sigma_7$	$\sigma_8$
$s_{loss}^\downarrow$	5 %	0 %	0 %	0 %	0 %	0 %	0 %	0 %
$s_{loss}^\uparrow$	0 %	10 %	11 %	11 %	12 %	9 %	8 %	8 %

**TABLE 6.9:** Summary of the estimated relative systematic uncertainty  $s_{loss}$  on the unpolarized cross-section and the parameters of the fit to the cross-section as a function of  $\phi_{\pi^0}$ , originating from the loss of  $\mu^+$  data. The first parameter set corresponds to the variation of the result of the binned maximum likelihood minimization while the second parameter set corresponds to the variation of the parameters characterizing the MCMC result. Arrows indicate an increase or decrease of the measured value due to the systematic effect.

parameter	$\langle \frac{d\sigma_U}{d t } \rangle$	BML			MCMC		
		$\langle \frac{d\sigma_{TT}}{d t } \rangle$	$\langle \frac{d\sigma_{LT}}{d t } \rangle$	$\langle \frac{d\sigma_U}{d t } \rangle$	$\langle \frac{d\sigma_{TT}}{d t } \rangle$	$\langle \frac{d\sigma_{LT}}{d t } \rangle$	
$s_{loss}^\uparrow$	9 %	10 %	17 %	9 %	8 %	16 %	

**Flux determination:** The estimate for the systematic uncertainty on the flux determination is 3%. The effect of scaling the total flux by 3% up or down is summarized in Table 6.10 (Table 6.11) for the bins in  $t$  ( $\phi_{\pi^0}$ ), the effect on the parameters of the fit is given in Table 6.12.

**TABLE 6.10:** Summary of the estimated relative systematic uncertainty  $s_{flux^+}$  and  $s_{flux^-}$  on the cross-section in the 5 bins of  $t$ , originating from the uncertainty on the determination of the  $\mu^+$  respectively  $\mu^-$  flux.

bin	$\sigma_1$	$\sigma_2$	$\sigma_3$	$\sigma_4$	$\sigma_5$
$s_{flux^-}$	2%	2%	2%	2%	3%
$s_{flux^+}$	2%	2%	2%	2%	1%

**TABLE 6.11:** Summary of the estimated relative systematic uncertainty  $s_{flux^+}$  and  $s_{flux^-}$  on the cross-section in the 8 bins of  $\phi_{\pi^0}$ , originating from the uncertainty on the determination of the  $\mu^+$  respectively  $\mu^-$  flux.

bin	$\sigma_1$	$\sigma_2$	$\sigma_3$	$\sigma_4$	$\sigma_5$	$\sigma_6$	$\sigma_7$	$\sigma_8$
$s_{flux^-}$	3%	2%	2%	2%	2%	2%	2%	2%
$s_{flux^+}$	1%	2%	2%	2%	2%	2%	2%	1%

**TABLE 6.12:** Summary of the estimated relative systematic uncertainty  $s_{flux^+}$  and  $s_{flux^-}$  on the unpolarized cross-section and the parameters of the fit to the cross-section as a function of  $\phi_{\pi^0}$ , originating from the uncertainty on the determination of the  $\mu^+$  respectively  $\mu^-$  flux. The first parameter set corresponds to the variation of the result of the binned maximum likelihood minimization while the second parameter set corresponds to the variation of the parameters characterizing the MCMC result.

parameter	$\langle \frac{d\sigma_U}{d t } \rangle$	BML		MCMC		
		$\langle \frac{d\sigma_{TT}}{d t } \rangle$	$\langle \frac{d\sigma_{LT}}{d t } \rangle$	$\langle \frac{d\sigma_U}{d t } \rangle$	$\langle \frac{d\sigma_{TT}}{d t } \rangle$	$\langle \frac{d\sigma_{LT}}{d t } \rangle$
$s_{flux^-}^{\downarrow}$	2%	2%	1%	2%	3%	0%
$s_{flux^+}^{\downarrow}$	2%	2%	3%	2%	2%	2%
$s_{flux^-}^{\uparrow}$	2%	2%	1%	2%	2%	1%
$s_{flux^+}^{\uparrow}$	2%	2%	2%	2%	2%	1%

### 6.7.2 Variation of the thresholds of the ECals

For the extraction of the cross-section, it is vital that the data is described well by the Monte Carlo in all variables. One critical variable is the detector threshold of the neutral clusters in the ECals.

To study the influence of the lower detector threshold on the final result, the extraction of the cross-section was performed while varying the requirement of the cut on the lower energetic photon cluster  $E_{\gamma_l}$  in the range of 0.0 GeV to 4.0 GeV in steps of 0.2 GeV. In Fig. 6.48, for each step of the  $E_{\gamma_l}$  threshold the ratio of background corrected events over the yield of the exclusive  $\pi^0$  Monte Carlo is shown. From this picture, the inferred systematic uncertainty intro-

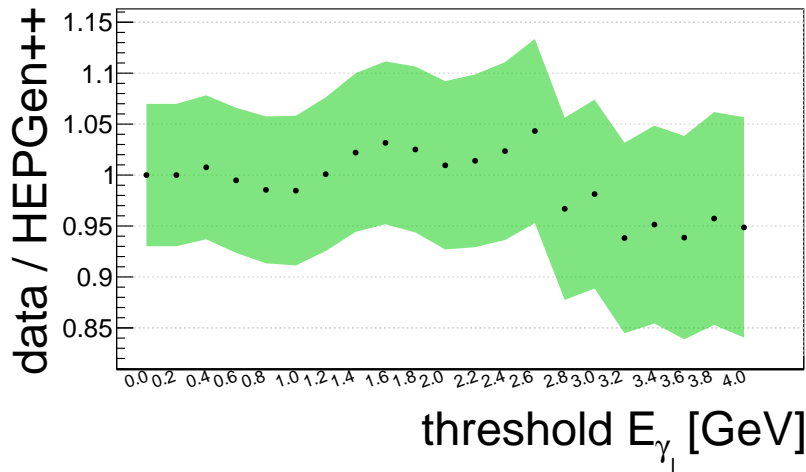


FIGURE 6.48: Ratio of background corrected data over the yield of a exclusive  $\pi^0$  Monte Carlo as a function of the threshold on the lower energetic photon energy  $E_{\gamma_l}$ . In each direction, a 5 % effect is visible.

duced by the thresholds of the ECals is estimated to be 5 % in both directions. This systematic effect is a result of a mismatch between the influence of the threshold in the real detector and its Monte Carlo description. Hence, the systematic affects the yield of either the data or the Monte Carlo, while the latter represents the worse case. A scaling of the Monte Carlo yield directly influences the acceptance and therefore modifies the event weight in the denominator. The resulting systematic uncertainties due to a scaling of the acceptance by 5 % are summarized in Table 6.13 (Table 6.14) for the extracted cross-section as a function of  $t$  ( $\phi_{\pi^0}$ ). The resulting systematic uncertainty for the parameters of the fit are summarized in Table 6.15.

TABLE 6.13: Summary of the estimated relative systematic uncertainty  $s_{thresh}$  on the cross-section in the 5 bins of  $t$ , originating from the uncertainty on the thresholds for the ECals.

bin	$\sigma_1$	$\sigma_2$	$\sigma_3$	$\sigma_4$	$\sigma_5$
$s_{thresh}$	5 %	5 %	5 %	5 %	5 %

**TABLE 6.14:** Summary of the estimated relative systematic uncertainty  $s_{thresh}$  on the cross-section in the 8 bins of  $\phi_{\pi^0}$ , originating from the uncertainty on the thresholds for the ECals.

bin	$\sigma_1$	$\sigma_2$	$\sigma_3$	$\sigma_4$	$\sigma_5$	$\sigma_6$	$\sigma_7$	$\sigma_8$
$s_{thresh}$	5 %	5 %	5 %	5 %	5 %	5 %	5 %	5 %

**TABLE 6.15:** Summary of the estimated relative systematic uncertainty  $s_{thresh}$  on the unpolarized cross-section and the parameters of the fit to the cross-section as a function of  $\phi_{\pi^0}$ , originating from the uncertainty on the thresholds for the ECals. The first parameter set corresponds to the variation of the result of the binned maximum likelihood minimization while the second parameter set corresponds to the variation of the parameters characterizing the MCMC result. Arrows indicate an increase or decrease of the measured value due to the systematic effect.

parameter	$\langle \frac{d\sigma_U}{d t } \rangle$	BML		MCMC		
		$\langle \frac{d\sigma_{TT}}{d t } \rangle$	$\langle \frac{d\sigma_{LT}}{d t } \rangle$	$\langle \frac{d\sigma_U}{d t } \rangle$	$\langle \frac{d\sigma_{TT}}{d t } \rangle$	$\langle \frac{d\sigma_{LT}}{d t } \rangle$
$s_{thresh}^\downarrow$	5 %	5 %	4 %	4 %	5 %	4 %
$s_{thresh}^\uparrow$	5 %	5 %	5 %	4 %	4 %	6 %

### 6.7.3 Variation of the acceptance binning

To investigate the stability of the result with respect to the binning of the acceptance, the reference binning (four bins in  $Q^2$ , four bins in  $\nu$ , cf. Section 6.5) was varied. First, the number of  $Q^2$  bins is varied between one and six while keeping the reference number of  $\nu$  bins. Then, the number of  $\nu$  bins is varied between one and six while keeping the reference number of  $Q^2$  bins. The results are given in Fig. 6.49 (Fig. 6.50) for the extraction as a function of  $t$  ( $\phi_{\pi^0}$ ). From the maximum and minimum shift, the numbers for the systematic uncertainties are derived, which are given in Table 6.16 (Table 6.17) for the bins in  $t$  ( $\phi_{\pi^0}$ ), and in Table 6.18 for the parameters of the fit.

**TABLE 6.16:** Summary of the estimated relative systematic uncertainty  $s_{acc}$  on the cross-section in the 5 bins of  $t$ , originating from the uncertainty from the acceptance binning. Arrows indicate an increase or decrease of the measured value due to the systematic effect.

bin	$\sigma_1$	$\sigma_2$	$\sigma_3$	$\sigma_4$	$\sigma_5$
$s_{acc}^\downarrow$	7 %	7 %	7 %	7 %	7 %
$s_{acc}^\uparrow$	4 %	4 %	4 %	4 %	4 %

**TABLE 6.17:** Summary of the estimated relative systematic uncertainty  $s_{acc}$  on the cross-section in the 8 bins of  $\phi_{\pi^0}$ , originating from the uncertainty from the acceptance binning. Arrows indicate an increase or decrease of the measured value due to the systematic effect.

bin	$\sigma_1$	$\sigma_2$	$\sigma_3$	$\sigma_4$	$\sigma_5$	$\sigma_6$	$\sigma_7$	$\sigma_8$
$s_{acc}^\downarrow$	7%	7%	7%	7%	7%	7%	7%	7%
$s_{acc}^\uparrow$	4%	4%	4%	4%	4%	4%	4%	4%

**TABLE 6.18:** Summary of the estimated relative systematic uncertainty  $s_{acc}$  on the unpolarized cross-section and the parameters of the fit to the cross-section as a function of  $\phi_{\pi^0}$ , originating from the uncertainty from the acceptance binning. The first parameter set corresponds to the variation of the result of the binned maximum likelihood minimization while the second parameter set corresponds to the variation of the parameters characterizing the MCMC result. Arrows indicate an increase or decrease of the measured value due to the systematic effect.

parameter	$\langle \frac{d\sigma_U}{d t } \rangle$	BML		MCMC		
		$\langle \frac{d\sigma_{TT}}{d t } \rangle$	$\langle \frac{d\sigma_{LT}}{d t } \rangle$	$\langle \frac{d\sigma_U}{d t } \rangle$	$\langle \frac{d\sigma_{TT}}{d t } \rangle$	$\langle \frac{d\sigma_{LT}}{d t } \rangle$
$s_{acc}^\downarrow$	7%	7%	6%	6%	7%	8%
$s_{acc}^\uparrow$	4%	4%	4%	4%	5%	6%

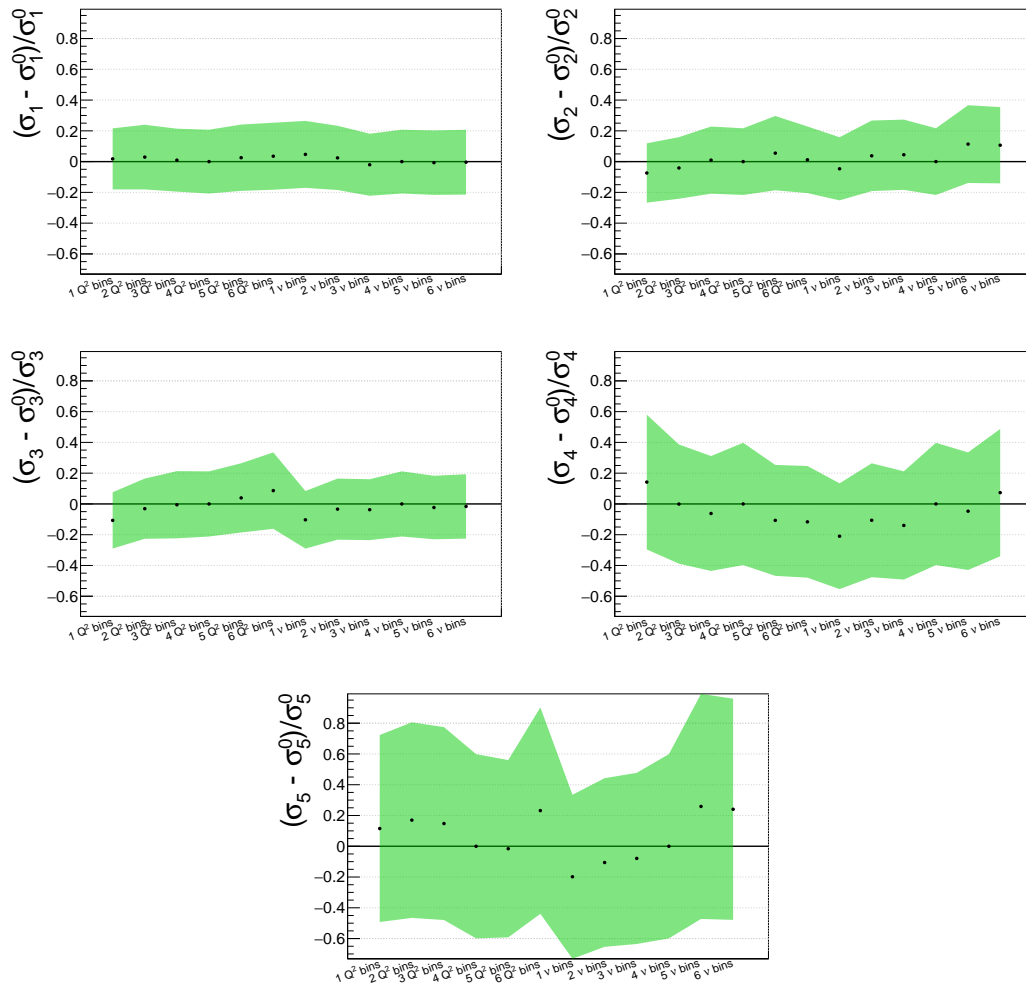


**FIGURE 6.49:** Influence on the extracted value of the cross-section in the 5 bins of  $t$ , originating from a variation of the acceptance binning. The quantity  $\sigma_i^0$  denotes the preferred value of the cross-section in the corresponding  $t$ -bin with  $i \in 1,2,3,4,5$ . The green band corresponds to the relative statistical uncertainty associated to the extracted value.

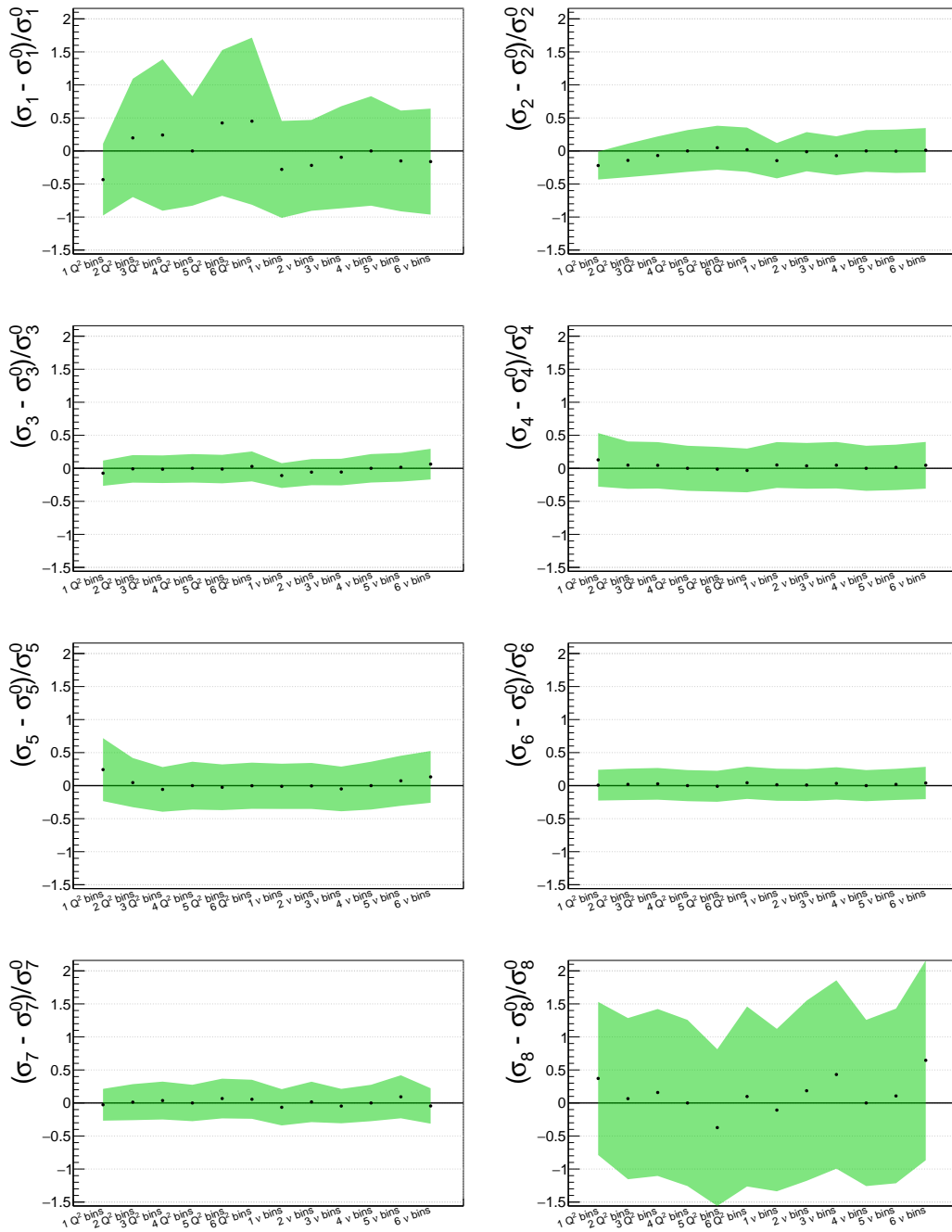


**FIGURE 6.50:** Influence on the extracted value of the cross-section in the 8 bins of  $\phi_{\pi^0}$ , originating from a variation of the acceptance binning. The quantity  $\sigma_i^0$  denotes the preferred value of the cross-section in the corresponding  $\phi_{\pi^0}$ -bin with  $i \in \{1, 2, \dots, 8\}$ . The green band corresponds to the relative statistical uncertainty associated to the extracted value.

### 6.7.4 Variation of the “LEPTO background” normalization

As concluded in Subsection 6.4.3 and summarized in Table 6.2, the “LEPTO background” normalization procedure is affected by an uncertainty that may increase or decrease the amount of non-exclusive background in the measurement. Although the normalization procedure is done independently for the beam charges, here, the maximum and minimum background scenarios are studied by taking the maximum (minimum) background for both beam charges (as opposed to adding their squared systematic). The influence on the extracted cross-section is given in Table 6.19 (Table 6.20) for the bins in  $t$  ( $\phi_{\pi^0}$ ) and in Table 6.21 for the parameters of the fit.

Exemplarily, the effect when scaling the “LEPTO background” contribution for the  $\mu^+$  beam is illustrated in Fig. 6.51 (Fig. 6.52) for each bin in  $t$  ( $\phi_{\pi^0}$ ). Comparable to the procedure in Subsection 6.7.1, here, the scaling of the event weight for the “LEPTO background” contribution  $r_{lepto}^{\mu^+}$  (cf. Table 6.2) was varied between  $r_{lepto}^{\mu^+} - 20\%$  and  $r_{lepto}^{\mu^+} + 20\%$  when extracting the cross-section for  $\mu^+$  beam.

**TABLE 6.19:** Summary of the estimated relative systematic uncertainty  $s_{norm}$  on the cross-section in the 5 bins of  $t$ , originating from the uncertainty on the normalisation of the “LEPTO background”. Arrows indicate an increase or decrease of the measured value due to the systematic effect.

bin	$\sigma_1$	$\sigma_2$	$\sigma_3$	$\sigma_4$	$\sigma_5$
$s_{norm}^{\downarrow}$	3 %	3 %	3 %	8 %	11 %
$s_{norm}^{\uparrow}$	6 %	5 %	5 %	19 %	28 %

**TABLE 6.20:** Summary of the estimated relative systematic uncertainty  $s_{norm}$  on the cross-section in the 8 bins of  $\phi_{\pi^0}$ , originating from the uncertainty on the normalisation of the “LEPTO background”. Arrows indicate an increase or decrease of the measured value due to the systematic effect.

bin	$\sigma_1$	$\sigma_2$	$\sigma_3$	$\sigma_4$	$\sigma_5$	$\sigma_6$	$\sigma_7$	$\sigma_8$
$s_{norm}^{\downarrow}$	7 %	3 %	3 %	4 %	4 %	3 %	3 %	21 %
$s_{norm}^{\uparrow}$	19 %	5 %	5 %	10 %	10 %	6 %	7 %	51 %

**TABLE 6.21:** Summary of the estimated relative systematic uncertainty  $s_{norm}$  on the unpolarized cross-section and the parameters of the fit to the cross-section as a function of  $\phi_{\pi^0}$ , originating from the uncertainty on the normalisation of the “LEPTO background”. The first parameter set corresponds to the variation of the result of the binned maximum likelihood minimization while the second parameter set corresponds to the variation of the parameters characterizing the MCMC result. Arrows indicate an increase or decrease of the measured value due to the systematic effect.

parameter	$\langle \frac{d\sigma_U}{d t } \rangle$	BML		MCMC		
		$\langle \frac{d\sigma_{TT}}{d t } \rangle$	$\langle \frac{d\sigma_{LT}}{d t } \rangle$	$\langle \frac{d\sigma_U}{d t } \rangle$	$\langle \frac{d\sigma_{TT}}{d t } \rangle$	$\langle \frac{d\sigma_{LT}}{d t } \rangle$
$s_{norm}^\downarrow$	3%	1%	2%	3%	3%	3%
$s_{norm}^\uparrow$	8%	2%	4%	7%	6%	8%

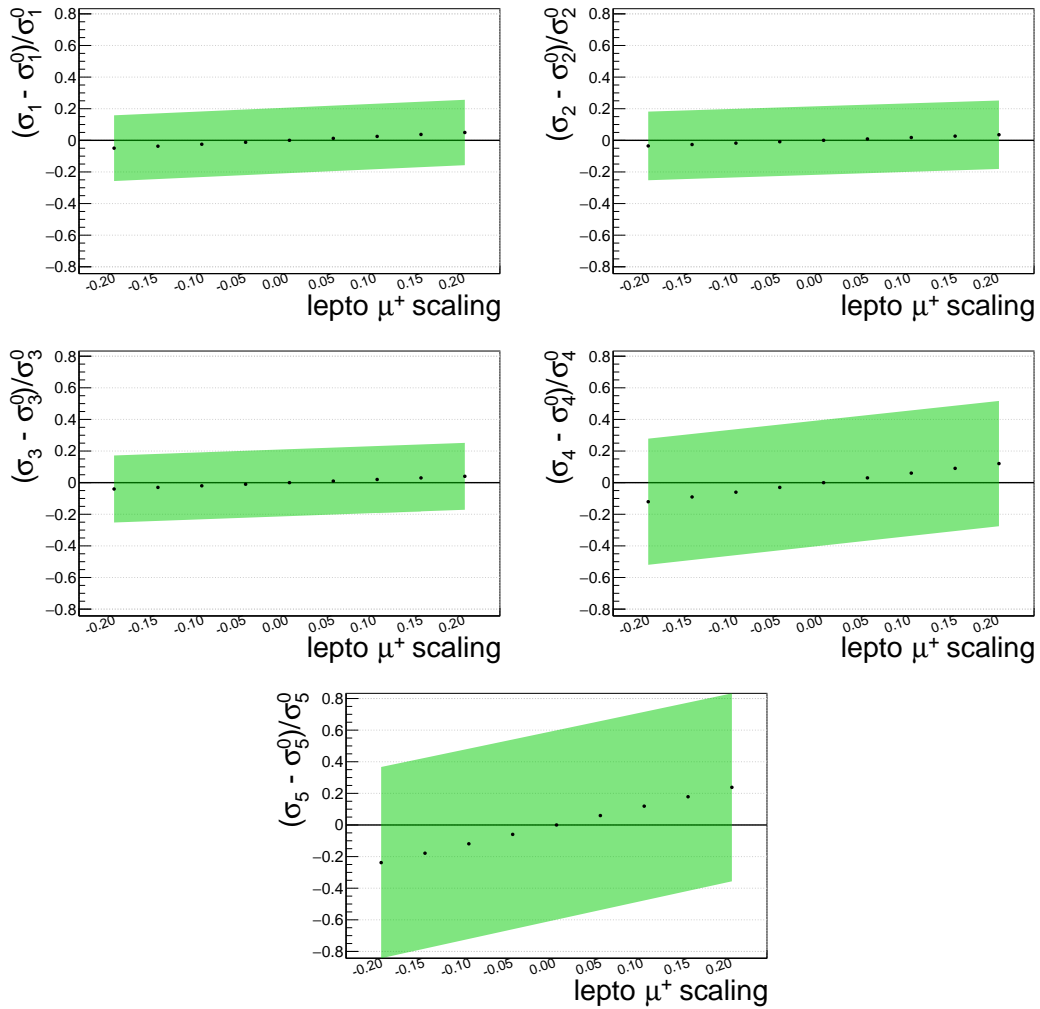


**FIGURE 6.51:** Influence on the extracted value of the cross-section in the 5 bins of  $t$ , originating from a scaling of the normalisation value for the LEPTO background in  $\mu^+$ . The quantity  $\sigma_i^0$  denotes the preferred value of the cross-section in the corresponding  $t$ -bin with  $i \in 1,2,3,4,5$ . The green band corresponds to the relative statistical uncertainty associated to the extracted value.

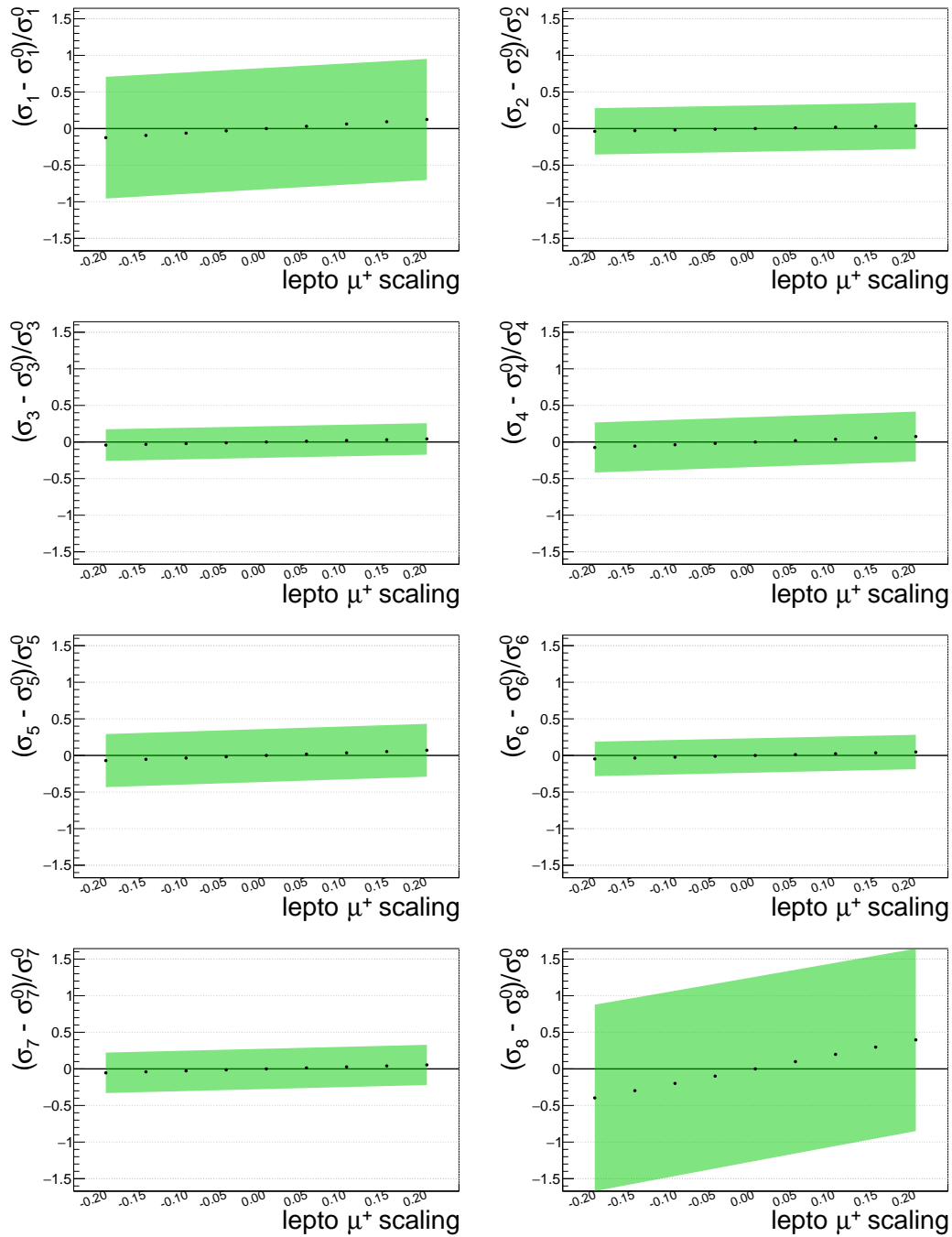


**FIGURE 6.52:** Influence on the extracted value of the cross-section in the 8 bins of  $\phi_{\pi^0}$ , originating from a scaling of the normalisation value for the LEPTO background in  $\mu^+$ . The quantity  $\sigma_i^0$  denotes the preferred value of the cross-section in the corresponding  $\phi_{\pi^0}$ -bin with  $i \in 1, 2, \dots, 8$ . The green band corresponds to the relative statistical uncertainty associated to the extracted value.



**TABLE 6.24:** Summary of the estimated relative systematic uncertainty  $s_{kin,fit}$  on the unpolarized cross-section and the parameters of the fit to the cross-section as a function of  $\phi_{\pi^0}$ , origination from the shift in the energy and momentum balance of the kinematic fit. The first parameter set corresponds to the variation of the result of the binned maximum likelihood minimization while the second parameter set corresponds to the variation of the parameters characterizing the MCMC result. Arrows indicate an increase or decrease of the measured value due to the systematic effect.

parameter	$\left\langle \frac{d\sigma_U}{d t } \right\rangle$	BML		MCMC		
		$\left\langle \frac{d\sigma_{TT}}{d t } \right\rangle$	$\left\langle \frac{d\sigma_{LT}}{d t } \right\rangle$	$\left\langle \frac{d\sigma_U}{d t } \right\rangle$	$\left\langle \frac{d\sigma_{TT}}{d t } \right\rangle$	$\left\langle \frac{d\sigma_{LT}}{d t } \right\rangle$
$s_{kin,fit}^\downarrow$	7 %	0 %	1 %	7 %	4 %	8 %
$s_{kin,fit}^\uparrow$	0 %	3 %	0 %	0 %	0 %	0 %

### 6.7.6 Contamination of exclusive $\omega$

The major source of background in the presented analysis originates from non-exclusive processes. But there are also exclusive processes which might leak into the measurement. Most prominently, a contribution from exclusive  $\omega$  muoproduction, where the  $\omega$  meson decays into a  $\pi^0$  and a photon, might exist. Events, where the photon carries away only little energy could then be mistaken with the exclusive  $\pi^0$  process<sup>8</sup>. The contribution of exclusive  $\omega$  muoproduction, where all  $\omega$  decay products are detected, is called the *detected misidentified*  $\omega$ . In this case, the mistaken exclusive  $\pi^0$  candidate can be “transformed” into an exclusive  $\omega$  candidate by combining it with the photon.

On the left-hand side in Fig. 6.53, the invariant mass of the  $\pi^0\gamma$  system is shown, where the exclusive  $\pi^0$  candidate is combined with any additional photons in the events. It is not possible to identify a signal peak at the nominal  $\omega$  mass of  $\sim 0.782 \text{ GeV}/c^2$ , *i.e.* the additional photons in the exclusive  $\pi^0$  sample seem to not originate from exclusive  $\omega$  muoproduction.

This finding is compatible with a Monte Carlo study, where the exclusive  $\pi^0$  muoproduction event selection was applied to an exclusive  $\omega$  muoproduction Monte Carlo sample. For the normalization, a dedicated exclusive  $\omega$  muoproduction  $\mu p \rightarrow \mu p \omega \rightarrow \mu p \pi^0 \gamma$  analysis was performed to extract the “true” exclusive  $\omega$  muoproduction signal yield from the 2012 data sample. This signal yield is then used to normalize the exclusive  $\omega$  muoproduction Monte Carlo, as depicted in Fig. 6.53 on the right-hand side. The event selection for the dedicated exclusive  $\omega$  muoproduction analysis follows closely the event selection outlined in Section 6.3 with the difference, that instead of  $\pi^0$  candidates,  $\omega$  candidates are formed (*cf.* Subsection 6.3.2). Only cluster pairs where the mass of the two photon system  $M_{\gamma\gamma}$  is compatible with the nominal  $\pi^0$  mass are kept. This  $\pi^0$  candidate is then combined with additional clusters in the event to form the  $\omega$  candidate. The  $\omega$  candidates are then further processed in an analogous fashion to the  $\pi^0$  candidates as described in

<sup>8</sup>Note that the event selection outlined in Section 6.3 allows any number of low energetic photons in the event.

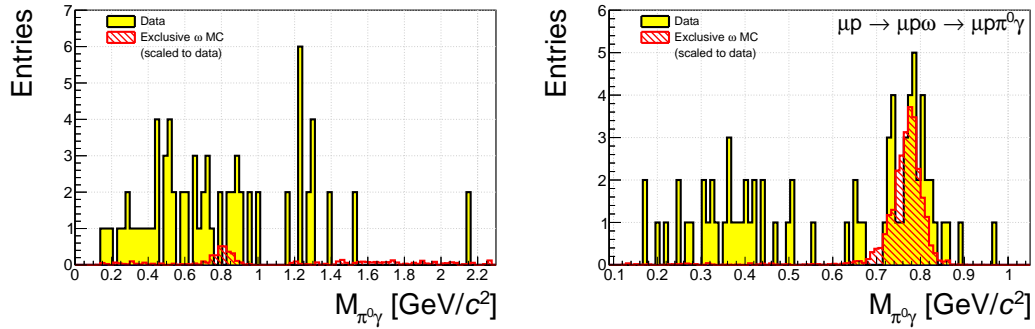


FIGURE 6.53: Left: Invariant mass spectrum for exclusive  $\pi^0$  candidates that were combined with additional photons in the event. The distribution shows no signal in the  $\omega$  mass region of  $\sim 0.782 \text{ GeV}/c^2$ . The normalization of the exclusive  $\omega$  muoproduction Monte Carlo is performed according to the plot on the right-hand side. Right: Invariant mass spectrum of the  $\pi^0\gamma$  system obtained from a dedicated exclusive  $\omega$  muoproduction,  $\mu p \rightarrow \mu p \omega \rightarrow \mu p \pi^0 \gamma$ , analysis for data and a pure exclusive  $\omega$  muoproduction Monte Carlo. The Monte Carlo is normalized to the integral of the data in the signal region.

Section 6.3<sup>9</sup>. The last step of the event selection (the conditions imposed by the kinematic fit) is not applied.

The normalized exclusive  $\omega$  muoproduction Monte Carlo allows to also estimate the contamination of *undetected misidentified*  $\omega$ , where the additional photon could not be detected. This contribution is estimated on the level of cross-sections. The virtual-photon proton cross-section for the *undetected misidentified*  $\omega$  can be estimated with the normalized Monte Carlo sample by evaluating

$$\left\langle \frac{d\sigma^{\gamma^* p \rightarrow \omega p}}{d|t|} \right\rangle_{\Delta\Omega_n} = \frac{1}{\mathcal{L}\Delta t_n \Delta Q^2 \Delta\nu} \cdot \sum_{i=1}^{N_{und.}^{\Delta\Omega_n}} \frac{a(Q^2_i, \nu_i, t_i, \phi_{\pi^0, i})^{-1}}{\Gamma(Q^2_i, \nu_i)}. \quad (6.61)$$

Here,  $N_{und.}^{\Delta\Omega_n}$  is the number of exclusive  $\omega$  muoproduction Monte Carlo events in the bin  $\Delta\Omega_n$  that comply with the exclusive  $\pi^0$  event selection and where the decay photon of the  $\omega$  was undetected. With this, the ratio of the cross-section for the *undetected misidentified*  $\omega$  over the exclusive  $\pi^0$  cross-section is calculated, leading to the systematic uncertainty of the data yield  $s_\omega$  by 1% in downwards direction.

### 6.7.7 Radiative corrections

Radiative corrections are considered to be small in the measurement of exclusive  $\pi^0$  muoproduction. Estimates for the particular case at COMPASS kinematics, however, do not yet exist. In an attempt to translate calculations done

<sup>9</sup> In essence, the difference between the *detected misidentified*  $\omega$  and the dedicated exclusive  $\omega$  muoproduction analysis is that in the latter case, the  $\omega$  is constructed *before* the exclusivity conditions.

for JLab experiments [112], reasonable estimates were provided for the measurement at COMPASS [113].

The impact of radiative corrections is estimated to lead to a systematic over-estimation of the cross-section by  $s_{rad} = 5\%$ . In the cross-section as a function of  $\phi_{\pi^0}$ , the radiative corrections are considered to be modulated leading to an additional uncertainty in the central region by  $s_{rad,mod} = 2\%$ . The effect of the relative systematic uncertainties due to radiative corrections is provided in the following summary tables.

### 6.7.8 Summary

Table 6.25 (Table 6.26) shows the compilation of all contributing systematic uncertainties to the cross-sections in the bins of  $t$  ( $\phi_{\pi^0}$ ). In Table 6.27, the systematic uncertainties for the parameters of the fit are summarized.

The individual systematic uncertainties are added in quadrature to arrive at the final systematic uncertainties. They are listed in Table 6.5 and visualized in Fig. 6.42 and Fig. 6.43 in the summary of the extraction, Subsection 6.6.9.

**TABLE 6.25:** Summary of the estimated relative systematic uncertainty on the cross-section in the 5 bins of  $t$ . Arrows indicate an increase or decrease of the measured value due to the systematic effect.

section	effect		$\sigma_1$	$\sigma_2$	$\sigma_3$	$\sigma_4$	$\sigma_5$
6.7.1	$\mu^-$ flux determ.	$s_{flux-}$	2%	2%	2%	2%	3%
6.7.1	$\mu^+$ flux determ.	$s_{flux+}$	2%	2%	2%	2%	1%
6.7.2	ECal thershold	$s_{thresh}$	5%	5%	5%	5%	5%
6.7.3	acceptance binning	$s_{acc}^{\downarrow}$	7%	7%	7%	7%	7%
6.7.5	shift in kinfit	$s_{kinfit}^{\downarrow}$	7%	7%	7%	7%	7%
6.7.4	LEPTO norm.	$s_{norm}^{\downarrow}$	3%	3%	3%	8%	11%
6.7.6	$\omega$ background	$s_{\omega}^{\downarrow}$	1%	1%	1%	1%	1%
6.7.7	rad. corr.	$s_{rad}^{\downarrow}$	5%	5%	5%	5%	5%
6.7.3	acceptance binning	$s_{acc}^{\uparrow}$	4%	4%	4%	4%	4%
6.7.1	$\mu^+$ event loss	$s_{loss}^{\uparrow}$	8%	10%	10%	13%	4%
6.7.4	LEPTO norm.	$s_{norm}^{\uparrow}$	6%	5%	5%	19%	28%
	$\sum$	$s^{\downarrow}$	12%	12%	12%	14%	16%
	$\sum$	$s^{\uparrow}$	12%	13%	13%	24%	29%

**TABLE 6.26:** Summary of the estimated relative systematic uncertainty on the cross-section in the 8 bins of  $\phi_{\pi^0}$ . Arrows indicate an increase or decrease of the measured value due to the systematic effect.

section	effect		$\sigma_1$	$\sigma_2$	$\sigma_3$	$\sigma_4$	$\sigma_5$	$\sigma_6$	$\sigma_7$	$\sigma_8$
6.7.1	$\mu^-$ flux determ.	$s_{flux-}$	3%	2%	2%	2%	2%	2%	2%	2%
6.7.1	$\mu^+$ flux determ.	$s_{flux+}$	1%	2%	2%	2%	2%	2%	2%	1%
6.7.2	ECal thershold	$s_{thresh}$	5%	5%	5%	5%	5%	5%	5%	5%
6.7.7	rad. corr. mod.	$s_{rad,mod}$	0%	0%	2%	2%	2%	2%	0%	0%
6.7.3	acceptance binning	$s_{acc}^{\downarrow}$	7%	7%	7%	7%	7%	7%	7%	7%
6.7.5	shift in kinfit	$s_{kinfit}^{\downarrow}$	7%	7%	7%	7%	7%	7%	7%	7%
6.7.1	$\mu^+$ event loss	$s_{loss}^{\downarrow}$	5%	0%	0%	0%	0%	0%	0%	0%
6.7.4	LEPTO norm.	$s_{norm}^{\downarrow}$	7%	3%	3%	4%	4%	3%	3%	21%
6.7.6	$\omega$ background	$s_{\omega}^{\downarrow}$	1%	1%	1%	1%	1%	1%	1%	1%
6.7.7	rad. corr.	$s_{rad}^{\downarrow}$	5%	5%	5%	5%	5%	5%	5%	5%
6.7.3	acceptance binning	$s_{acc}^{\uparrow}$	4%	4%	4%	4%	4%	4%	4%	4%
6.7.1	$\mu^+$ event loss	$s_{loss}^{\uparrow}$	0%	10%	11%	11%	12%	9%	8%	8%
6.7.4	LEPTO norm.	$s_{norm}^{\uparrow}$	19%	5%	5%	10%	10%	6%	7%	51%
	$\sum$	$s^{\downarrow}$	16%	12%	12%	13%	13%	12%	12%	24%
	$\sum$	$s^{\uparrow}$	20%	13%	15%	17%	17%	14%	12%	53%

**TABLE 6.27:** Summary of the estimated relative systematic uncertainty on the unpolarized cross-section and the parameters of the fit to the cross-section as a function of  $\phi_{\pi^0}$ . Arrows indicate an increase or decrease of the measured value due to the systematic effect.

section	effect		$\langle \frac{d\sigma_U}{d t } \rangle$	BML		MCMC		
				$\langle \frac{d\sigma_{TT}}{d t } \rangle$	$\langle \frac{d\sigma_{LT}}{d t } \rangle$	$\langle \frac{d\sigma_U}{d t } \rangle$	$\langle \frac{d\sigma_{TT}}{d t } \rangle$	$\langle \frac{d\sigma_{LT}}{d t } \rangle$
6.7.1	$\mu^-$ flux determ.	$s_{flux-}^\downarrow$	2 %	2 %	1 %	2 %	3 %	0 %
6.7.1	$\mu^+$ flux determ.	$s_{flux+}^\downarrow$	2 %	2 %	3 %	2 %	2 %	2 %
6.7.3	acceptance binning	$s_{acc}^\downarrow$	7 %	7 %	6 %	6 %	7 %	8 %
6.7.2	ECal thershold	$s_{thresh}^\downarrow$	5 %	5 %	4 %	4 %	5 %	4 %
6.7.5	shift in kinfit	$s_{kinfit}^\downarrow$	7 %	0 %	1 %	7 %	4 %	8 %
6.7.4	LEPTO norm.	$s_{norm}^\downarrow$	3 %	1 %	2 %	3 %	3 %	3 %
6.7.6	$\omega$ background	$s_\omega^\downarrow$	1 %	1 %	2 %	2 %	2 %	2 %
6.7.7	rad. corr.	$s_{rad}^\downarrow$	5 %	5 %	4 %	4 %	5 %	5 %
6.7.7	rad. corr. mod.	$s_{rad,mod}^\downarrow$	2 %	1 %	3 %	2 %	1 %	3 %
6.7.1	$\mu^-$ flux determ.	$s_{flux-}^\uparrow$	2 %	2 %	1 %	2 %	2 %	1 %
6.7.1	$\mu^+$ flux determ.	$s_{flux+}^\uparrow$	2 %	2 %	2 %	2 %	2 %	1 %
6.7.3	acceptance binning	$s_{acc}^\uparrow$	4 %	4 %	4 %	4 %	5 %	6 %
6.7.2	ECal thershold	$s_{thresh}^\uparrow$	5 %	5 %	5 %	4 %	4 %	6 %
6.7.5	shift in kinfit	$s_{kinfit}^\uparrow$	0 %	3 %	0 %	0 %	0 %	0 %
6.7.1	$\mu^+$ event loss	$s_{loss}^\uparrow$	9 %	10 %	17 %	9 %	8 %	16 %
6.7.4	LEPTO norm.	$s_{norm}^\uparrow$	8 %	2 %	4 %	7 %	6 %	8 %
6.7.7	rad. corr. mod.	$s_{rad,mod}^\uparrow$	2 %	1 %	3 %	2 %	1 %	4 %
	$\sum$	$s^\downarrow$	13 %	10 %	11 %	12 %	12 %	14 %
	$\sum$	$s^\uparrow$	14 %	13 %	19 %	14 %	12 %	20 %

## 6.8 Discussion of the results

In this section, the result of the exclusive  $\pi^0$  muoproduction cross-section measurement is discussed while focusing on the relation to GPDs. For this, the basic formalism was introduced in Section 2.2, where the cross-section was decomposed into helicity amplitudes which ultimately contain the GPDs. The link between the cross-section and single quark GPDs (or vice-versa) can only be drawn with the help of model descriptions, though, due to the convolution of the GPDs with the hard scattering kernel. There exists a number of parameterizations and models for GPDs, such as Goloskokov and Kroll (GK), Vanderhaeghen-Guichon-Guidal (VGG) [19], Goldstein and Liuti (GL) [35, 49, 50] or Kumerički-Mueller (KM) [114]. But not all of them implement HEMP processes and only the GK model features predictions for the COMPASS kinematics. This is why in the following only the GK model is further utilized.

A brief introduction to the GK model is given in Subsection 6.8.1 while more detailed information is available in [34, 36, 48, 115–117]. The interpretation of the measurement respectively the comparison of the measurement with the GK predictions follows in Subsection 6.8.2.

### 6.8.1 Model for GPDs by Goloskokov and Kroll

Before describing the concrete realization of GPDs in the framework of GK, a closer look into the observables of HEMP is taken. The GPDs enter in parton and nucleon helicity dependent amplitudes  $A_{S_{N'}S_{q'},S_N S_q}$  in bi-linear combinations as stated in Section 2.1, Eq. 2.3. The partonic subprocess  $\gamma^*q \rightarrow \pi^0q$  is included by taking the MPFFs for the respective GPD. In the following, the corresponding MPFFs for the GPDs  $\tilde{E}$ ,  $\tilde{H}$ ,  $E_T$ ,  $H_T$ , and  $\tilde{H}_T$  are denoted by  $\tilde{\mathcal{E}}$ ,  $\tilde{\mathcal{H}}$ ,  $\mathcal{E}_T$ ,  $\mathcal{H}_T$  and  $\tilde{\mathcal{H}}_T$ .

In the GK framework, the helicity amplitudes  $\mathcal{M}_{S_{\gamma^*}S_N,S_M S_{N'}}$  for the  $\pi^0$  production process, depending on virtual-photon, meson and nucleon helicities, are simplified and read [36, 117]

$$\begin{aligned}
 \mathcal{M}_{++,0+} &= -e \frac{\mu_\pi}{Q^2} \frac{\sqrt{-t'}}{4m} (2\tilde{\mathcal{H}}_T + \mathcal{E}_T), \\
 \mathcal{M}_{++,0-} &= e \frac{\mu_\pi}{Q^2} \sqrt{1 - \xi^2} \mathcal{H}_T, \\
 \mathcal{M}_{+-,0+} &= 0, \\
 \mathcal{M}_{+-,0-} &= -\mathcal{M}_{++,0+}, \\
 \mathcal{M}_{0+,0+} &= \sqrt{1 - \xi^2} \frac{e}{Q} \left[ \tilde{\mathcal{H}} - \frac{\xi^2}{1 - \xi^2} \tilde{\mathcal{E}} \right], \\
 \mathcal{M}_{0+,0-} &= -\xi \frac{e}{Q} \frac{\sqrt{-t'}}{2m} \tilde{\mathcal{E}},
 \end{aligned} \tag{6.62}$$

with  $e$  the positron charge,  $\mu_\pi = m_\pi/(m_u + m_d)$ ,  $m_u$  and  $m_d$  being current quark masses, and  $t' = t - t_0$ . This set of equations is obtained by combining Eq. 2.3 with Eq. 2.8 and only keeping dominating terms [117], for instance:

- terms suppressed by at least a factor of  $\frac{\sqrt{-t}}{Q}$  are neglected,
- since the model is applied in the domain of small skewness  $\xi$ , the GPD  $\tilde{E}_T$ , which is antisymmetric in  $\xi$ , is disregarded,
- $\tilde{H}_T$  is neglected since it is suppressed by  $\frac{t}{4m_p^2}$ .

The first four amplitudes in Eq. 6.62 correspond to transversely polarized virtual photons and the last two correspond longitudinally polarized virtual photons. The other helicity amplitudes follow using symmetry relations, *e.g.* parity invariance [117].

Using Eq. 6.62 and their relation with the photoabsorption cross-section or interference terms (Eq. 2.10), it is possible to infer the relation between the structure functions and the MPFFs, respectively the GPDs, where again only dominant terms are kept [46]

$$\begin{aligned}
\frac{d\sigma_T}{dt} &\propto \left[ (1 - \xi^2) |\mathcal{H}_T|^2 - \frac{t'}{8m_p^2} |\bar{\mathcal{E}}_T|^2 \right], \\
\frac{d\sigma_L}{dt} &\propto \left[ (1 - \xi^2) |\tilde{\mathcal{H}}|^2 - 2\xi^2 \text{Re} \left[ \tilde{\mathcal{H}}^* \tilde{\mathcal{E}} \right] - \xi^2 \frac{t'}{4m_p^2} |\tilde{\mathcal{E}}|^2 \right], \\
\frac{d\sigma_{TT}}{dt} &\propto t' |\bar{\mathcal{E}}_T|^2, \\
\frac{d\sigma_{LT}}{dt} &\propto \xi \sqrt{1 - \xi^2} \sqrt{-t'} \text{Re} \left[ \mathcal{H}_T^* \tilde{\mathcal{E}} \right].
\end{aligned} \tag{6.63}$$

According to Eq. 6.62 respectively Eq. 6.63, the MPFFs needed to calculate the cross-section for exclusive  $\pi^0$  production are  $\tilde{\mathcal{E}}$ ,  $\tilde{\mathcal{H}}$ ,  $\mathcal{H}_T$  and  $\mathcal{E}_T = 2\tilde{\mathcal{H}}_T + \mathcal{E}_T$ . To recall, the MPFFs are integrals over two components

$$\mathcal{F} = \sum_{S_q S_{q'}} \int_{-1}^1 dx g_{S_{\gamma^*} S_q, 0 S_{q'}}(x, \xi, t, Q^2) F(x, \xi, t),$$

where  $g_{S_{\gamma^*} S_q, 0 S_{q'}}(x, \xi, t, Q^2)$  describes the partonic subprocess and  $F(x, \xi, t)$  is the corresponding GPD. For a complete model, both parts have to be covered with appropriate descriptions. They are shortly introduced in the following. Note, that the MPFFs that involve quark helicity flip GPDs require a twist-3 meson wave function [117]. For brevity, most of the specific formulas are omitted while referring to appropriate sources. Also, only the necessary GPDs are discussed with an additional restriction to valence quark GPDs.

The partonic subprocess  $\gamma^* q \rightarrow \pi^0 q$  is calculated using the modified perturbative approach [118]. The full subprocess amplitude involves a suitable

meson waveform, the hard scattering kernel, and a Sudakov term. The infrared singularities appearing in the collinear factorization in case of transversely polarized photons are kept in control by avoiding a large separation between the quarks that form the meson [119, 120]. The Sudakov term describes the exchange of a soft gluon between these quarks and decreases for increasing transverse separation of the quarks.

The hard scattering kernel is calculated from a set of lowest order Feynman graphs [34, 115]. The twist-2, respectively twist-3 meson wave function used in the model can be found in [121, 122] and [123]. The full twist-3 subprocess amplitude is bit more complicated and its description is omitted here. One may refer to [36] for details.

In the choice of functions applicable for the parametrization of GPDs, the conditions posed by the properties of the GPDs, summarized in Section 2.1, have to be fulfilled. One approach uses double distributions  $f(\alpha, \beta, t)$  [124, 125]

$$F(x, \xi, t) = \int_{-1}^1 d\alpha \int_{-1+|\alpha|}^{1-|\alpha|} d\beta \delta(\alpha + \xi\beta - x) f(\alpha, \beta, t),$$

where  $\alpha$  and  $\beta$  are internal variables for the integration and the delta function defines the integration line in the  $(\alpha, \beta)$  plane.

It turns out, that even though the double distribution ansatz elegantly implements the polynomiality property of the GPDs, the last coefficient in the expansion can vanish. The issue of the vanishing last coefficient is ignored in the GK model, though, since the impact is expected to be negligible [115]<sup>10</sup>.

The ansatz for the functions  $f(\alpha, \beta, t)$  for  $\tilde{E}$ ,  $\bar{E}_T$  and  $H_T$  reads [124]

$$f(\alpha, \beta, t) = e^{bt} e^{-\alpha' \ln(\alpha)t} F(\alpha, \xi = t = 0) \frac{3(1-\alpha)^2 - \beta^2}{4(1-\alpha)^3} \theta(\alpha). \quad (6.64)$$

The exponentials form a Regge-like profile function with the slope of the Regge trajectory  $\alpha'$  and the slope  $b$  of the Regge residue function. The function  $F(\alpha, \xi = t = 0)$  manages the correct forward behavior for the respective GPD, see also Section 2.1. The respective forward limits are parameterized in the following fashion [36, 48]

$$\begin{aligned} H_T & : F(\alpha, \xi = t = 0) = \Delta_T q(\alpha) = N \alpha^{1/2} (1-\alpha) [q(\alpha) - \Delta q(\alpha)], \\ \tilde{E}, \bar{E}_T & : F(\alpha, \xi = t = 0) = N \alpha^{-\alpha(0)} (1-\alpha)^{\beta(0)}, \end{aligned} \quad (6.65)$$

where  $N$  is a quark flavor dependent normalization parameter. The unpolarized and polarized PDFs  $q$  and  $\Delta q$  are taken from [127, 128]. The model for the transversity PDF  $\Delta_T q$  is taken from [129]. The parameters  $\alpha(0)$  and  $\beta(0)$  in case of GPDs  $\tilde{E}$  and  $\bar{E}_T$  are obtained from fits to measurements [48] and from lattice calculations [130], respectively. The specific parameters for the GPDs are stated in Table 6.28.

For the GPD  $\tilde{H}$ , a different parametrization is used. Since the impact of GPD

<sup>10</sup>A common approach to overcome this issue is to add the so-called D-term to generate the highest order coefficient. [126]

**TABLE 6.28:** Parameters for the Regge-like behavior and the normalization of the GPDs in the GK model [48, 117]. The parameters  $N$  and  $\beta(0)$  depend on the quark flavor, which is restricted to up- and down-type here.

GPD	$\alpha(0)$	$\beta^u(0)$	$\beta^d(0)$	$\alpha'(\text{GeV}^{-2})$	$b(\text{GeV}^{-2})$	$N^u$	$N^d$
$\tilde{E}$	0.48	5	5	0.45	0.9	14.0	4.0
$\bar{E}_T$	0.3	4	5	0.45	0.5	6.83	5.05
$H_T$	-	-	-	0.45	0.3	1.1	-0.3

$\tilde{H}$  on exclusive  $\pi^0$  production is small, it shall be referred to [104] for details.

## 6.8.2 Comparison and interpretation with respect to the model for GPDs by Goloskokov and Kroll

An implementation of the GK model in HEPGEN++ [104] can be used to calculate cross-section values for the COMPASS kinematics. These values are predictions since so far, no measurement of exclusive  $\pi^0$  production exists in this kinematic domain. The implementation of the model incorporates the GK model based on [48], which corresponds to the parameter set stated in Table 6.28. In addition, the GK authors provide modified parameters [131] inspired by the measurement presented in this thesis. The aim of the modified parameters is to estimate the impact on the model needed to describe the COMPASS measurement. Most importantly, a smaller value for the parameter  $\alpha(0)$  of GPD  $\bar{E}_T$  was chosen. This modification changes the energy dependence and the strength of the GPD  $\bar{E}_T$ . The normalization and the slope parameter  $b$  of the GPD  $\bar{E}_T$  is then adjusted such that measurements at different kinematics ([46, 47]) are reproduced again.

The parameters for GPDs  $\tilde{E}$  and  $H_T$  are modified as well, but the impact of the modifications is marginal. The summary of Regge parameters and normalizations of the GPDs according to [131] is given in Table 6.29.

**TABLE 6.29:** Modified parameters for the Regge behavior and the normalization of the GPDs in the GK model. [131]

GPD	$\alpha(0)$	$b(\text{GeV}^{-2})$	$N^u$	$N^d$
$\tilde{E}$	0.32	0.6	18.2	5.2
$\bar{E}_T$	-0.1	0.67	29.23	21.61
$H_T$	-	0.04	0.68	-0.186

The implementation of the model in HEPGEN++ allows to calculate values for the cross-section that can be compared to the measurement. Similar to the measurement, the values of the model correspond to the integrated cross-sections in the domain of the COMPASS measurement, *i.e.* the value in one bin is calculated using

$$\left\langle \frac{d\sigma}{d\kappa} \right\rangle_{\Delta\kappa} = \frac{\int_{\Delta\kappa} \frac{d\sigma^{GK}}{d\kappa} d\kappa}{\Delta\kappa}, \quad (6.66)$$

where  $\frac{d\sigma^{GK}}{d\kappa}$  corresponds to the cross-section evaluated using the GK model (in analogy to what is done in case of the data, *cf.* Eq. 6.31). Like that, one can directly compare the values of the measurement and the model since they correspond to the same observables. Accordingly, the value for the unseparated cross-section ( $|t|$ -averaged cross-section) from the model, using the refined parameter set (Table 6.29), reads

$$\left\langle \frac{d\sigma_T}{d|t|} + \varepsilon \frac{d\sigma_L}{d|t|} \right\rangle = 9.47 \frac{\text{nb}}{(\text{GeV}/c)^2},$$

which is in a fair agreement with the result of the measurement of

$$\left\langle \frac{d\sigma_T}{d|t|} + \varepsilon \frac{d\sigma_L}{d|t|} \right\rangle = 8.1 \pm 0.9_{-1.0}^{+1.1} \frac{\text{nb}}{(\text{GeV}/c)^2}.$$

Further, in Fig. 6.54 and Fig. 6.55 the functional dependence of the cross-section for both model parameter sets and the measurement are compared.

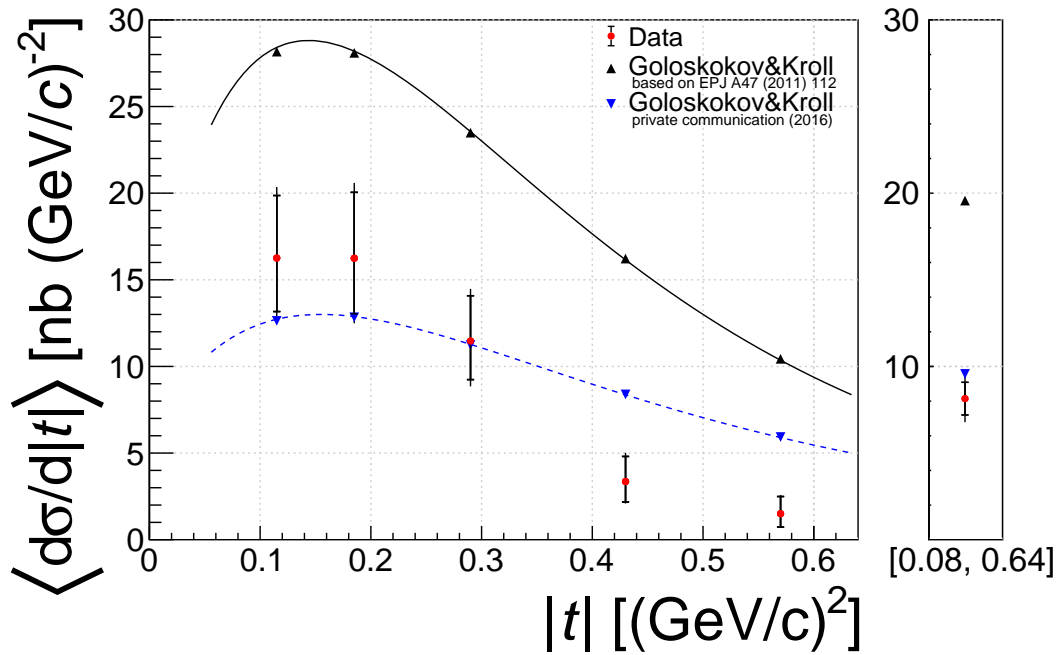


FIGURE 6.54: Cross-section as a function of  $|t|$ . The right panel corresponds to the  $t$ -averaged cross-section.

The red dots in the figures show the measured cross-sections as described in Section 6.6. The black and blue markers correspond to values obtained with the GK model, where the black markers correspond to the parameter set of Table 6.28 and the blue markers to the parameter set of Table 6.29. In order to see the behavior of the cross-section, Eq. 6.66 is evaluated at 50 positions along the abscissa and the resulting values are interpolated to form the black and blue model curves.

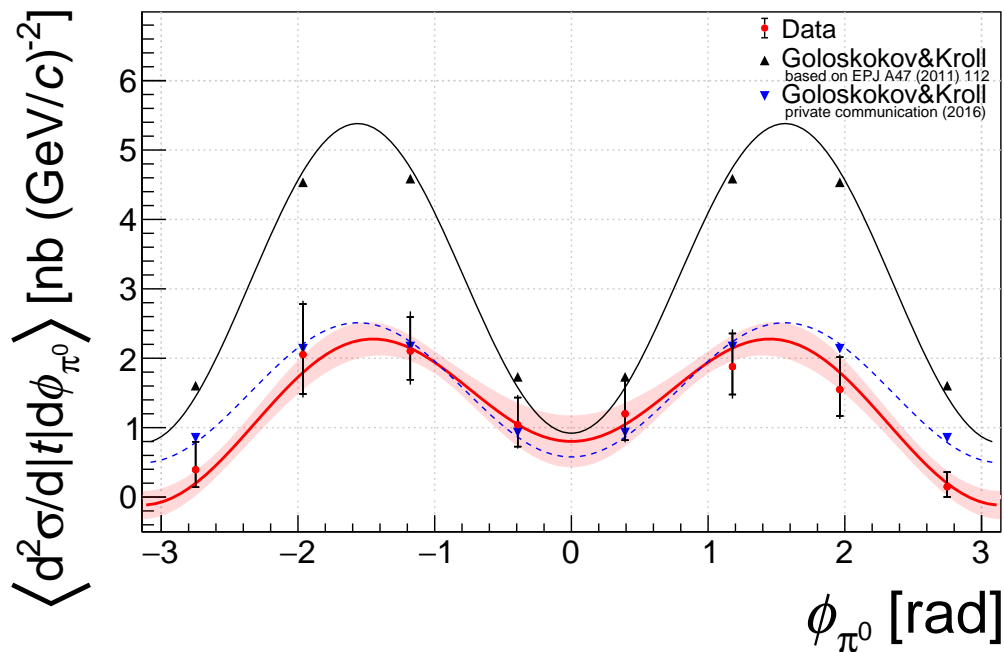


FIGURE 6.55: Cross-section as a function of  $\phi_{\pi^0}$ . The red curve and the uncertainty band, which represents the 68 % confidence interval, result from the binned maximum likelihood fit to the data (Subsection 6.6.7). A similar picture with the result of the MCMC method (Subsection 6.6.8) is available in Appendix B.4.5.

Looking at the cross-section as a function of  $|t|$  Fig. 6.54, there are a number of observations:

1. The predictions for the cross-section (black) overshoot the measurement by approximately a factor of two, leading to a modified parameter set used for the blue curve.
2. The modified parameter set (blue) has improved the compatibility of the model with the measurement. The  $|t|$ -averaged cross-section (right panel) of the model and the measurement agree now within the uncertainties. Still, the slope of the  $|t|$  dependence is more pronounced in the measurement.
3. For  $|t| \rightarrow 0$ , the model predicts a decrease of the cross-section. This is a result of the GPD  $\bar{E}_T$  as one can deduce from Eq. 6.63. In the GL model [35, 49, 50], a different shape of the small  $|t|$  dependence is advocated. Due to the large uncertainties, the measurement is inconclusive here.

For the cross-section as a function of  $\phi_{\pi^0}$  depicted in Fig. 6.55, the same general statements hold. In addition, here a binned maximum likelihood fit is used to extract the amplitudes of the structure functions (red curve). The

values of the fitted parameters are found to be

$$\begin{aligned}\left\langle \frac{d\sigma_{TT}}{d|t|} \right\rangle &= -6.0 \pm 1.3_{-0.7}^{+0.7} \frac{\text{nb}}{(\text{GeV}/c)^2}, \\ \left\langle \frac{d\sigma_{LT}}{d|t|} \right\rangle &= 1.4 \pm 0.5_{-0.2}^{+0.3} \frac{\text{nb}}{(\text{GeV}/c)^2}.\end{aligned}\quad (6.67)$$

A large contribution from  $\sigma_{TT}$  is found, which is according to Eq. 6.63 again a sign for the importance of GPD  $\bar{E}_T$ . For  $\sigma_{LT}$ , a small, positive contribution is found. It is an indication that the cross-section by transversely polarized photons is not to be neglected.

From the shape of the model one can conclude, that both findings for  $\sigma_{TT}$  and  $\sigma_{LT}$  are compatible with the model description. More precisely, the values obtained for the revised model parameter set read for the presented kinematic range

$$\begin{aligned}\left\langle \frac{d\sigma_{TT}}{d|t|} \right\rangle &= -6.19 \frac{\text{nb}}{(\text{GeV}/c)^2}, \\ \left\langle \frac{d\sigma_{LT}}{d|t|} \right\rangle &= 0.13 \frac{\text{nb}}{(\text{GeV}/c)^2}.\end{aligned}\quad (6.68)$$

Although, the sign of the quantity  $\sigma_{LT}$  is an open question. As also pointed out in Section 2.3, measurements performed at the JLab Hall A experiment favor a negative sign while model calculations favor a positive sign [46, 52]. Measurements by the CLAS experiment find both positive and negative values [47].

It is not possible to disentangle the structure functions  $\sigma_T$  and  $\sigma_L$ , which is only possible using Rosenbluth separation as it is performed at the JLab Hall A experiment [52]. Unfortunately, Rosenbluth separation is not feasible at COMPASS kinematics since a large split in the beam energies would be required.

Despite the fair agreement with the tuned GK model, the measurement also shows the importance of performing global fits including data spanning over the kinematic range of different experiments. In a recent effort, the PARTONS collaboration [132] seeks to develop a framework where different experimental observables and models for GPDs can be collected. It will give the ability to comprehensively study different models in the context of available data. All in all, the measurement of the exclusive  $\pi^0$  muoproduction cross-section already provided important input to the parametrization of GPDs and therefore helped to improve the understanding of the inner dynamics of nucleons.

---

# 7

## Summary and outlook

---

Studies of the nucleon and its substructure have prompted a number of questions. One of the most prominent question, how do the nucleons properties like spin, mass and size emerge from its constituents, still remains unanswered. In the last decades, generalized parton distribution functions (GPDs) have received rising attention. The GPDs are generalizations of both the form factors and parton distributions. The correlation of transverse spatial positions and longitudinal momentum fractions provides new insights into the nucleon and in particular into its helicity structure.

As GPDs describe long-range quantum chromodynamics, they are not calculable by perturbative quantum chromodynamics. Next to efforts to calculate GPDs from the lattice, the only possibility to find the correct functions and parameters is through measurements.

The most prominent processes that are sensitive to GPDs are exclusive scattering processes such as deeply virtual Compton scattering and hard exclusive meson production. These processes offer complementary access to GPDs while their overlap allows testing the universality of the GPDs.

Among a variety of experiments that bother with the structure of nucleons, the COMPASS experiment is (and has been) one of the cornerstones in the field. Due to its location at the end of the M2 beamline at CERN, the experiment has unique access to a high energy, polarized muon beam with the possibility to choose both charge and polarization of the beam. The experiment is a versatile setup with various detectors that are steadily updated. A big evolutionary step happened starting with the COMPASS-II phase in 2012 in which dedicated measurements for GPDs were conducted.

One of the most important upgrades for the GPD program at COMPASS was the CAMERA detector. It allows the detection of the recoiled target proton thus enabling COMPASS to reconstruct all final state particles in exclusive scattering processes. The construction and detection principles of the CAMERA detector impose challenging demands on the readout that are fulfilled by employing the GANDALF-framework.

The COMPASS-II setup, including CAMERA and the full readout, was first operated in a pilot run in 2012. The thorough analysis of the recorded data with an emphasis on the CAMERA detector together with the resulting implementation of vital hardware improvements are subjects of this thesis. Between 2012 and 2016, the FPGA firmware design was carefully refined and extensively tested leading to a flawless operation of the system during the dedicated data taking for the COMPASS GPD program in 2016 and 2017.

The thesis includes a complete description of the firmware design for the GANDALF-ADC. It is both suited for users operating the module as well as for advanced users or future developers of the system.

The extraction of first physics results from the pilot run data allows not only a glance into the prospects of the COMPASS experiment for future analysis, but has already provided valuable new information for the field.

The physics analysis necessitated a precise calibration of the CAMERA detector and the development of an easy access to the reconstructed particle tracks in the detector. The methodology for the event reconstruction of the process was developed from scratch. The analysis includes a kinematic fit that allows for the best determination of the kinematic variables and is used to improve the purity of the signal. The background was estimated using Monte Carlo techniques and systematic effects were studied to a great extent.

For the first time, the mean exclusive  $\pi^0$  muoproduction cross-section was extracted in the kinematic range

$$\begin{aligned} 0.08 (\text{GeV}/c)^2 < |t| < 0.64 (\text{GeV}/c)^2, \\ 1 (\text{GeV}/c)^2 < Q^2 < 5 (\text{GeV}/c)^2, \\ 8.5 \text{ GeV} < \nu < 28 \text{ GeV}, \end{aligned}$$

as a function of  $|t|$ , the square of the four-momentum transfer to the proton, and as a function of  $\phi_{\pi^0}$ , the angle between the lepton plane and meson production plane. The structure functions  $\sigma_L$ ,  $\sigma_T$ ,  $\sigma_{LT}$  and  $\sigma_{TT}$  were extracted in this kinematic range and determined as

$$\begin{aligned} \left\langle \frac{d\sigma_T}{d|t|} + \varepsilon \frac{d\sigma_L}{d|t|} \right\rangle &= 8.1 \pm 0.9_{-1.0}^{+1.1} \frac{\text{nb}}{(\text{GeV}/c)^2}, \\ \left\langle \frac{d\sigma_{TT}}{d|t|} \right\rangle &= -6.0 \pm 1.3_{-0.7}^{+0.7} \frac{\text{nb}}{(\text{GeV}/c)^2}, \\ \left\langle \frac{d\sigma_{LT}}{d|t|} \right\rangle &= 1.4 \pm 0.5_{-0.2}^{+0.3} \frac{\text{nb}}{(\text{GeV}/c)^2}. \end{aligned}$$

First comparisons with model predictions by Goloskokov and Kroll show, in general, a good compatibility in the functional shape. In particular the strong relative contribution of  $\left\langle \frac{d\sigma_{TT}}{d|t|} \right\rangle$  can be confirmed, which is of the order of the unseparated cross-section  $\left\langle \frac{d\sigma_T}{d|t|} + \varepsilon \frac{d\sigma_L}{d|t|} \right\rangle$ . This hints a strong contribution from transversely polarized virtual photons. In the framework of Goloskokov and Kroll, such contributions emerge in higher twist handbag calculations and can be attributed to a large contribution of the nucleon non-helicity flip/parton helicity flip GPD  $\bar{E}_T$ . In the model, this contribution manifests also in the attenuation of the cross-section for  $|t| \rightarrow 0$ . While the data show a small downwards tendency for small  $|t|$ , the large statistical uncertainties do not allow firm conclusions.

The magnitude of the cross-section predicted by Goloskokov and Kroll does

not match the measurement. On account of this fact, the measurement already lead to adjustments of the model presented in this thesis. The changes allow to both describe the presented measurement at COMPASS kinematics (sea quark region) as well as data measured by JLab (valence quark region).

The COMPASS collaboration has recorded ten times more data in 2016 and 2017 for the analysis of this interesting reaction. The techniques and methods developed in this thesis serve as a guideline for the analysis of these data. It will then be possible to study the evolution of the  $\phi_{\pi^0}$  modulations of the cross-section in bins of  $t$  and the increased statistics will also allow studying the  $t$  dependant cross-section at very small momentum transfer.

Meanwhile, the COMPASS collaboration is preparing a letter of intent for a next-generation experiment that may be realized in the early twenties, involving a polarized target.

In the long run, the field looks forward to a possible electron-ion collider which would pave the way for a comprehensive analysis of GPDs over a wide kinematic range. There are already solid studies on the performance of such a machine as well as first technical design drafts.

All in all, there is a large, growing community pushing the field forward and it seems only a matter of time when the spin puzzle will finally be solved.



## *Acknowledgements*

A special thanks goes to my supervisor Horst Fischer who gave me the opportunity to work on this interesting subject. He always had an open ear for problems and if nothing else, his continuous support and encouragement made this thesis possible.

I also want to thank all present and former colleagues in my department for the nice work relation and atmosphere. In particular, I owe Philipp Jörg a debt of gratitude, not least for proofreading this thesis. Our countless discussions were a substantial part in my ability to comprehend things, his help and advice played an important role in the success of this work. I want to acknowledge Florian Herrmann and Sebastian Schopferer for their work on the GANDALF-framework.

Further, I want to thank all present and former colleagues in the COMPASS collaboration. It was always a pleasure to present and discuss physics topics in a very friendly and open minded community and I'm grateful for taking part in it.

Special thanks goes to Andrea Ferrero, Nicole d'Hose and Andrzej Sandacz who were the driving force in the COMPASS GPD group.

Last but not least, my wholehearted thanks goes to my family. They always appreciated and encouraged my work and were a continuous source of motivation.



---

# A GANDALF-ADC firmware auxiliary material

---

## A.1 Directory structure

In Fig. A.1, the directory structure of the GANDALF-ADC project is depicted. Only the relevant directories and some relevant files are listed.

The version control system git is used to manage the project. Directories listed below the *submodules* folder are included as git submodules. Therefore, each of these folders itself represents a git repository. Each submodule roughly corresponds to a module in Fig. 4.1.

## A.2 Simulation

The simulation of the GANDALF-ADC firmware relies on *ModelSim*. The point of access is the *testbench.fdo* file, from which other important files are called. The contents of the file looks like this:

```
# compile VHDL code , create gandalf.GANDALF_env library
do testbench_compile_lib.fdo
# start the simulation
vsim -t ps -novopt +notimingchecks gandalf.GANDALF_env

# add some waveforms to the screen
do testbench_wave.fdo
# execute user directives
do testbench.udo
```

The simulation environment is configured in the *G\_PARAMETERS.vhd*. The interaction with the simulated GANDALF-module is possible using the *ModelSim* command line with the *vme\_write* command.



**FIGURE A.1:** Directory structure of the GANDALF-ADC project

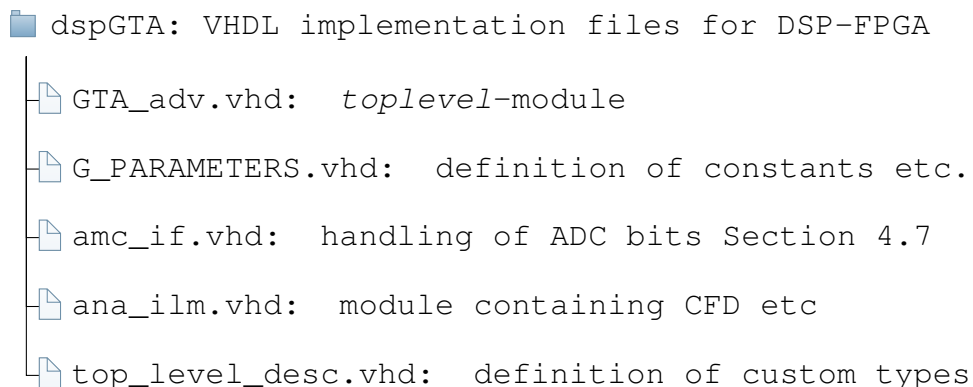


**FIGURE A.2:** Directory structure of the *dspGTA* folder, containing the VHDL implementation files for the DSP-FPGA. Only the most important files are listed.

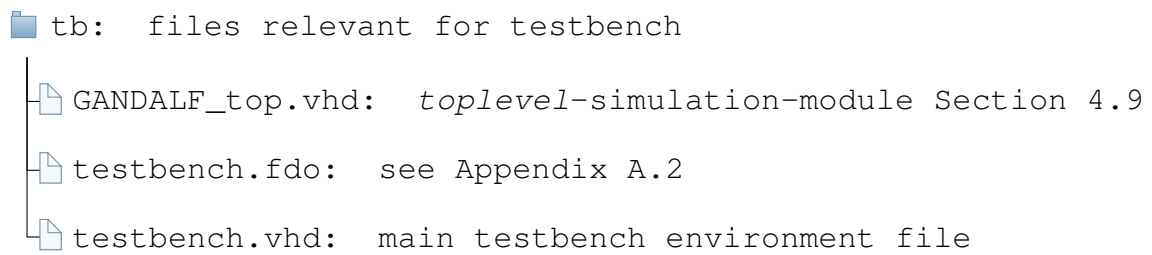


**FIGURE A.3:** Directory structure of the `tb` folder, containing the testbench files of the GANDALF-ADC project. Only the most important files are listed.

### A.3 Phase alignment

In the FPGA, the sweep process is controlled by some rather complicated logic expressed through state machines. The separation into separate state machines is not only for better style, it is mainly needed because the different processes live in different clock domains that are not related to each other. This also means, that special care has to be taken for signals crossing the clock domains.

The process to control the sweep, programming a specific phase and monitoring the phase is illustrated in Fig. A.4. To control the SI chip phase, separate state machines exist to configure fine shift (Fig. A.6) and coarse shift (Fig. A.7). The helper processes illustrated in Fig. A.5 are used to count or monitor the yields of the flip-flops and to send the results of a measurement to the *spy\_fifo*.

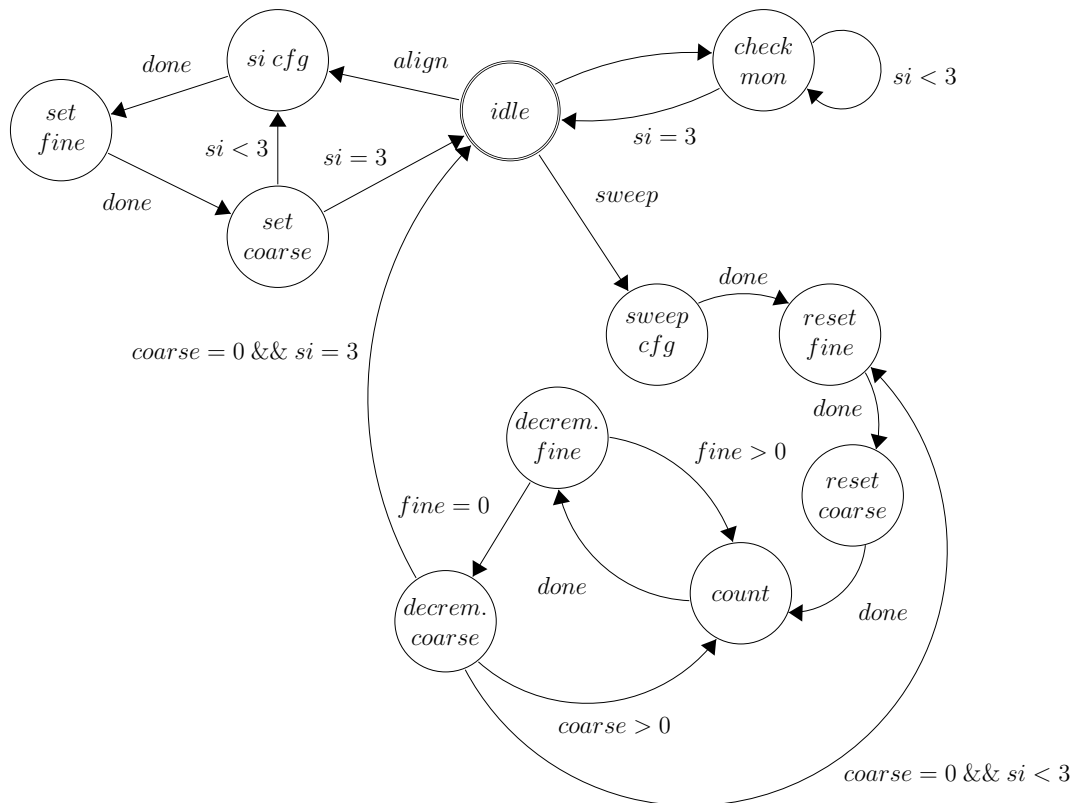


FIGURE A.4: State machine for the sweep control process. It has three tasks. First, perform the sweep, second, align the phase and third, monitor the phase. Each task is performed in sequence for each SI chip which is expressed here by the counter “si”. Following, a description of the states:

**idle:** idle state, step out on *fast-register fr\_phase\_align\_si* or *fast-register fr\_sweep\_si* to set a specific phase respectively to start the sweep process, else step to **check mon** state

**si cfg:** retrieve phase configuration from *configuration memory* (Section 4.4)

**set fine:** trigger the state machine to set a specific fine latency, see Fig. A.6

**set coarse:** trigger the state machine to set a specific fine latency, see Fig. A.7, increment “si” counter

**check mon:** check current value reading of the flip-flops, see Fig. A.5

**sweep cfg:** retrieve sweep configuration from *configuration memory* (Section 4.4)

**reset fine/coarse:** set the fine shift respectively coarse shift counter to the requested number of steps and reset the state machines that control the fine/coarse step (reset coarse step last, because only after the adjustment of a coarse step the SI chip acknowledges that the operation finished)

**count:** monitor the flip-flops and write result to *spy\_fifo*, see Fig. A.5

**decrem. fine/coarse:** decrement the fine shift respectively coarse shift counter

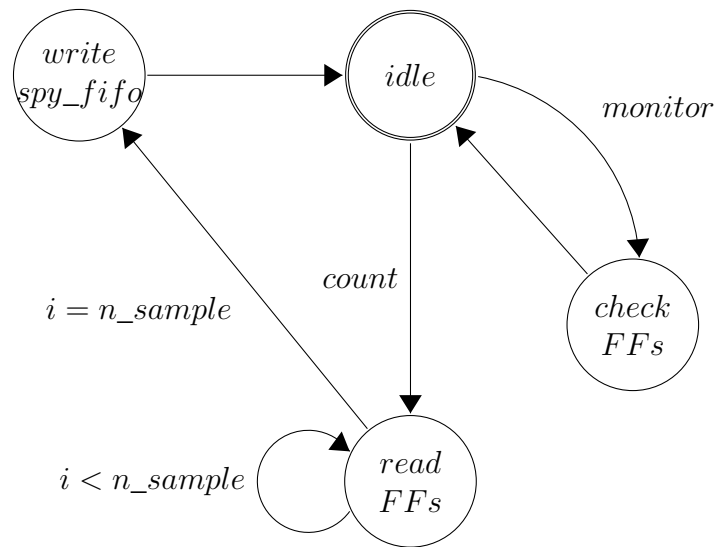


**FIGURE A.5:** Helper processes used by the sweep control process to read flip-flop values. Following, a description of the states:

**idle:** idle state, step out on signal “monitor” to check the flip-flop values once or on signal “count” to read flip-flop values for some number of clock cycles

**check FFs:** read the flip-flop values and compare to expected value; if values do not match, set the set loss-of-phase bit for the SI chip (see Subsection 4.6.2)

**read FFs:** read the values of the two flip-flop for  $n_{sample}$  clock cycles (here,  $i$  is a clock cycle counter); sum occurrences of 00, 11 and 01/10

**write spy\_fifo:** write the sums to the *spy\_fifo* with the data format specified in Table 4.1

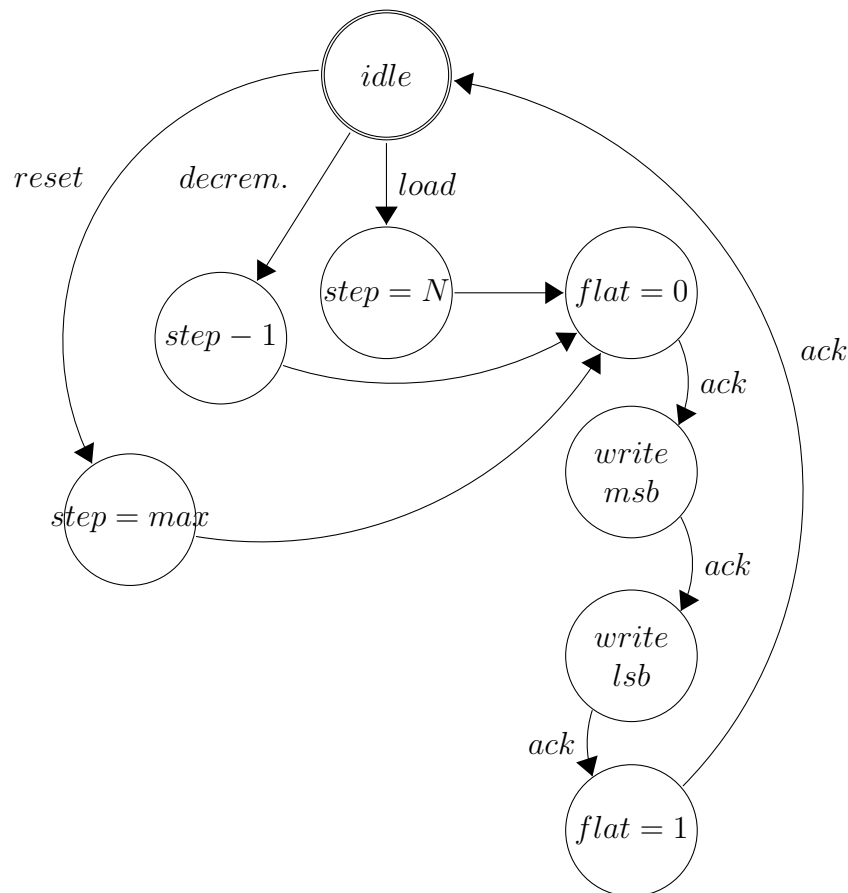


**FIGURE A.6:** State machine to control the fine shift of the SI chip. The internal scalar “step” represents the currently programmed fine shift. A positive “step” means a shift of the phase backwards while a negative value represents a shift of the phase in forward direction. Following, a description of the states:

**idle:** idle state, step out on signal “reset”, “decrem.” and “load” to the respective states setting the “step” value

**step = max:** reset the fine shift to the maximum value, which corresponds to the most backward fine shift of the phase

**step - 1:** decrement the “step” value to perform one fine shift

**step = N:** set the “step” value to the specified fine shift value N

**flat = 0:** I<sup>2</sup>C: signal SI chip that “flat” register is to be modified

**write msb:** I<sup>2</sup>C: write msb of the “step” value to the SI chip

**write lsb:** I<sup>2</sup>C: write lsb of the “step” value to the SI chip

**flat = 1:** I<sup>2</sup>C: signal SI chip that “flat” register modification ended; the SI chip will set the requested fine shift, however without acknowledging completion of the operation

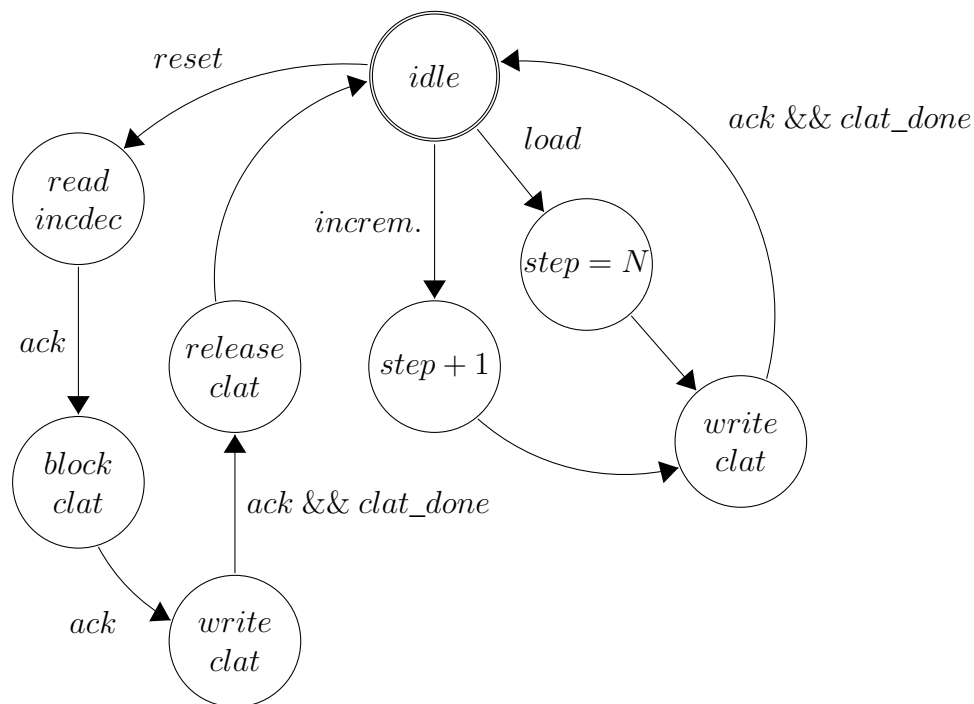


**FIGURE A.7:** State machine to control the coarse shift of the SI chip. The reset is performed such that the current phase is not modified. The internal scalar “step” represents the currently programmed fine shift. Following, a description of the states:

**idle:** idle state, step out on signal “incred.” and “load” to the respective states setting the “step” value or on signal “reset” which modifies the SI chip coarse shift register (clat) without actually altering the current phase

**read incdec:** I<sup>2</sup>C: store the current value of the register that contains the “incdec” bit, only the “incdec” bit of the register will be modified and the others shall remain

**block clat:** I<sup>2</sup>C: signal the SI chip to ignore changes done to the “clat” register

**write clat:** I<sup>2</sup>C: set “step=0” and reset “clat” register of the SI chip

**release clat:** I<sup>2</sup>C: signal the SI chip to act on changes done to the “clat” register

**step + 1:** increment the “step” value to perform one coarse shift

**step = N:** set the “step” value to the specified coarse shift value N

**write clat:** I<sup>2</sup>C: write “step” value to the SI chip; wait for the SI chip to acknowledge the completion of the operation

---

## B Additional material

---

### B.1 Photograph of CAMERA and spectrometer

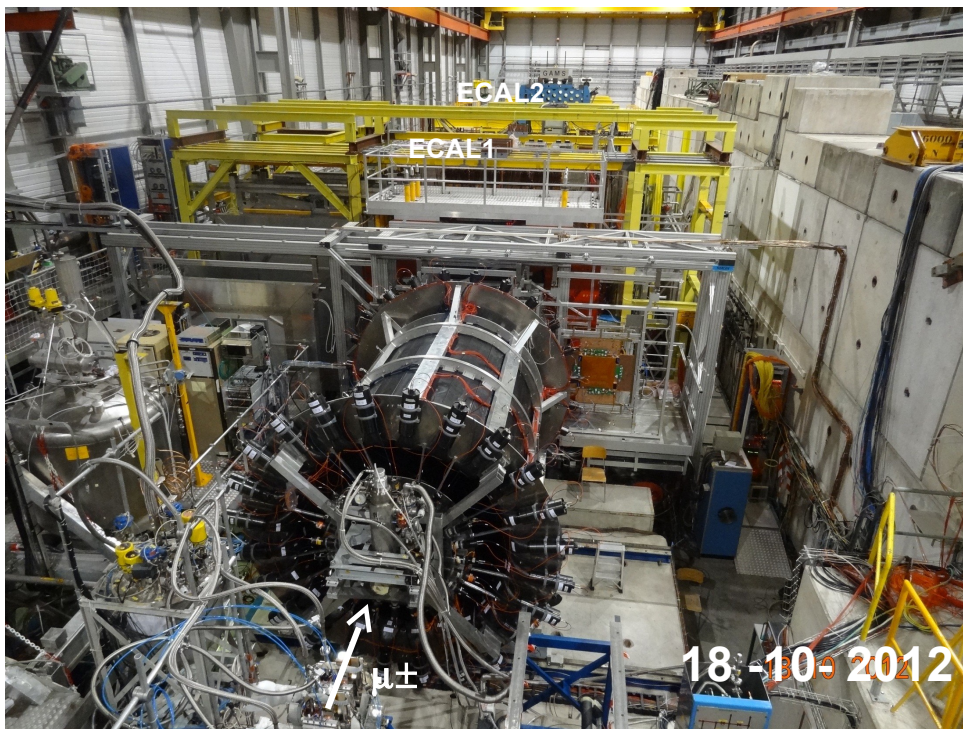


**FIGURE B.1:** Photograph of the fully assembled CAMERA detector positioned in the COMPASS beamline. The beam enters from the bottom and hits the target which is located in the center of CAMERA.

## B.2 Additional figures for event selection

### B.2.1 Kinematic and exclusive variables before cut on pulls

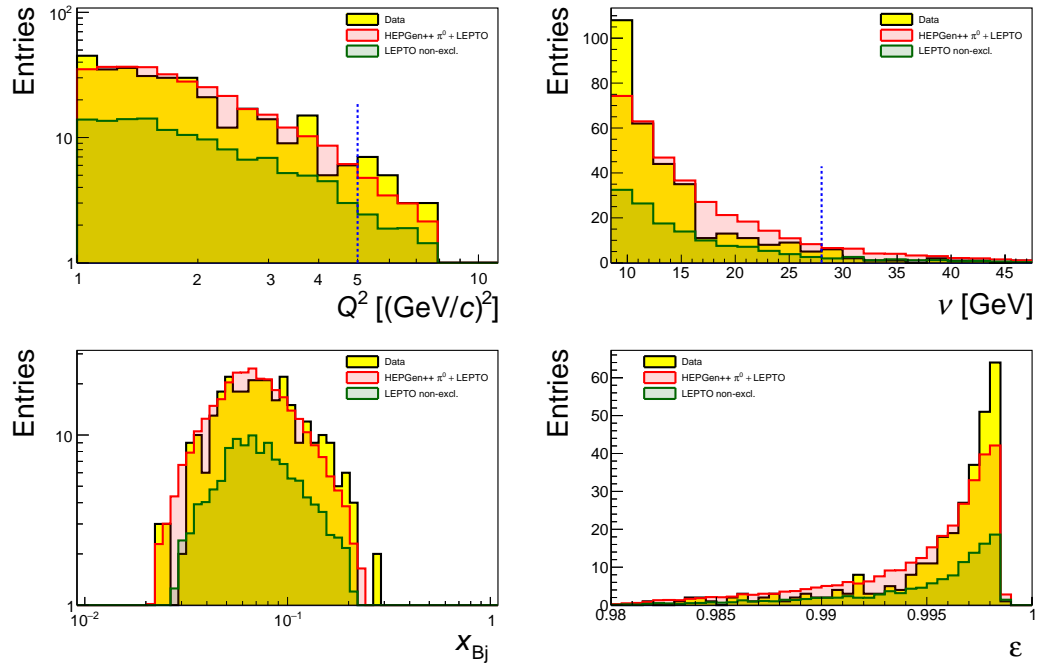


FIGURE B.2: Distribution of kinematic variables, before cut on pulls

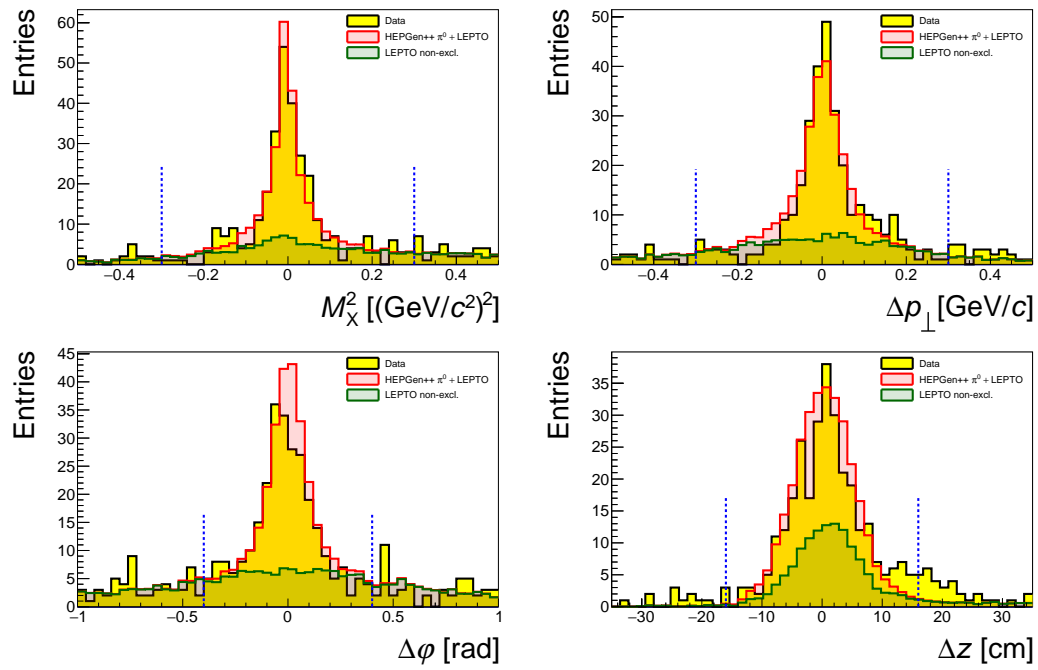


FIGURE B.3: Distribution of exclusivity variables, before cut on pulls

## B.2.2 Absolute values of pulls for measured quantities

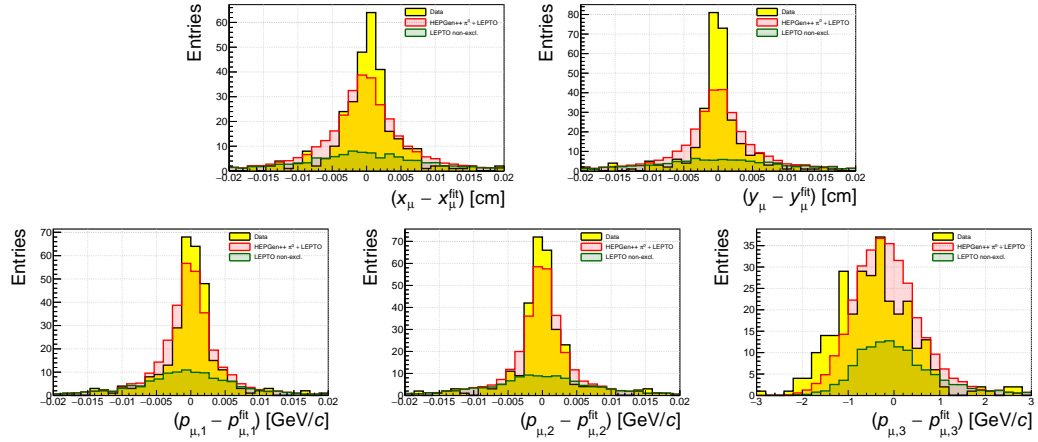


FIGURE B.4: Pull distributions for the incoming  $\mu$ . The quantities  $x$  and  $y$  denote the track position at the  $z$ -position measured at the point closest to the vertex. Here,  $p_{1,2,3}$  denote the components of the momentum vector. The distributions are shown for the full event selection while disabling all cuts imposed by the kinematic fit.

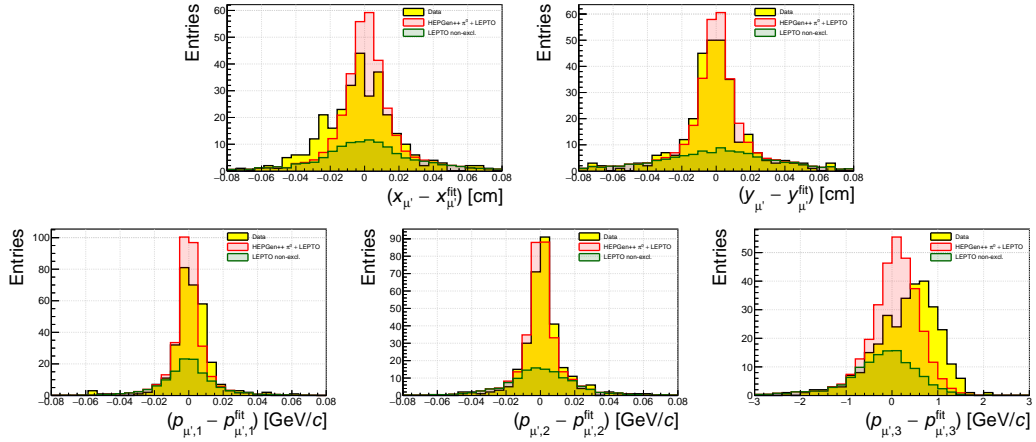
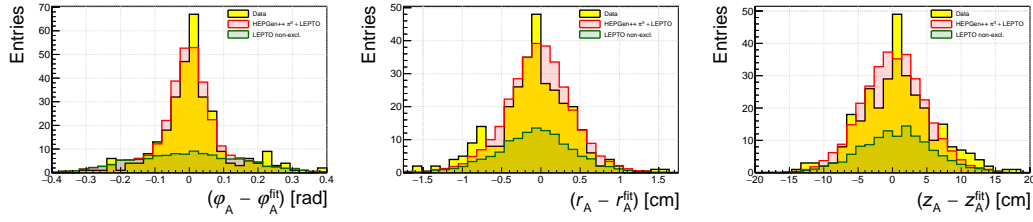
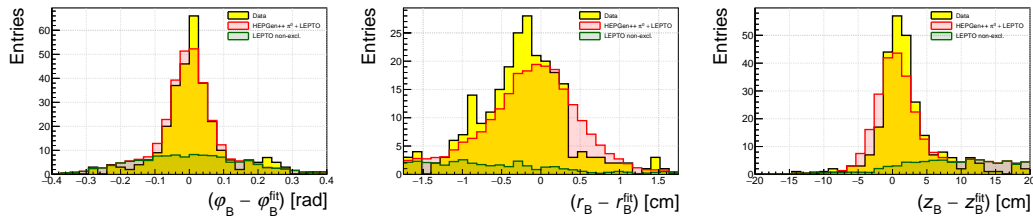


FIGURE B.5: Pull distributions for the outgoing  $\mu$ . The quantities  $x$  and  $y$  denote the track position at the  $z$ -position measured at the point closest to the vertex. Here,  $p_{1,2,3}$  denote the components of the momentum vector. The distributions are shown for the full event selection while disabling all cuts imposed by the kinematic fit.



**FIGURE B.6:** Pull distributions for the position in ring A of CAMERA. The measured quantities are the azimuth angle  $\varphi$ , the radius  $r$  and the longitudinal position  $z$  of the hit. The distributions are shown for the full event selection while disabling all cuts imposed by the kinematic fit.



**FIGURE B.7:** Pull distributions for the position in ring B of CAMERA. The measured quantities are the azimuth angle  $\varphi$ , the radius  $r$  and the longitudinal position  $z$  of the hit. The distributions are shown for the full event selection while disabling all cuts imposed by the kinematic fit.

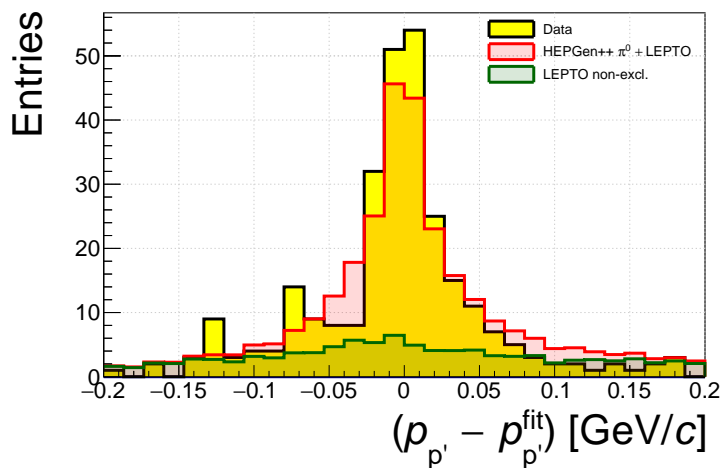


**FIGURE B.8:** Pull distribution for the magnitude of the momentum of the recoil proton. The distributions are shown for the full event selection while disabling all cuts imposed by the kinematic fit.

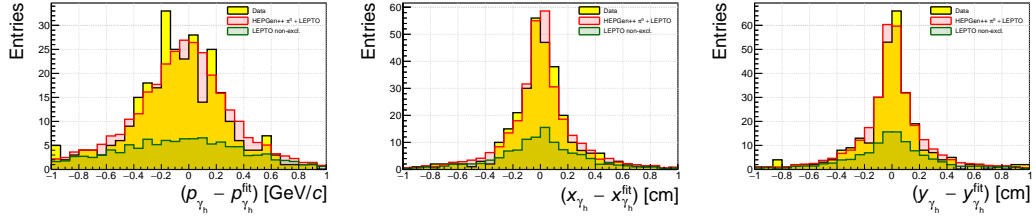


**FIGURE B.9:** Pull distributions for the higher energetic  $\gamma$ .  $x$  and  $y$  denote the track position at the  $z$ -position measured at the respective ECal,  $p$  denotes the magnitude of the momentum of the  $\gamma$ . The distributions are shown for the full event selection while disabling all cuts imposed by the kinematic fit.

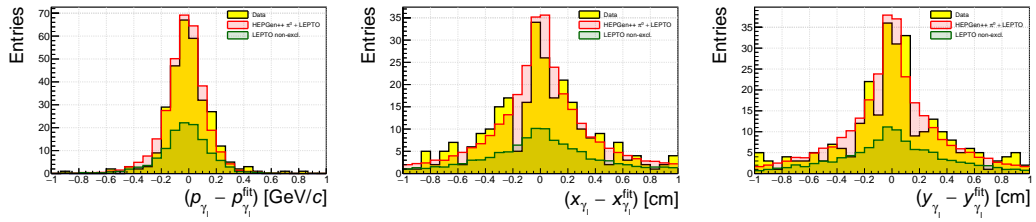


**FIGURE B.10:** Pull distributions for the lower energetic  $\gamma$ .  $x$  and  $y$  denote the track position at the  $z$ -position measured at the respective ECal,  $p$  denotes the magnitude of the momentum of the  $\gamma$ . The distributions are shown for the full event selection while disabling all cuts imposed by the kinematic fit.

## B.3 Additional material for simulation

### B.3.1 JETSET output for LEPTO event types

**FIGURE B.11:** Listing of the JETSET output for a LEPTO event with exclusive  $\pi^0$  signature and a recoiling proton (type 1). Notice, that the recoil proton (I=8) has the incoming proton (I=2) as its origin.

I	particle/jet	KS	KF orig	p_x	p_y	p_z	E	m	
1	!mu+	21	-13	0	-0.208	-0.031	155.717	155.717	0.106
2	!p+	21	2212	0	-0.000	-0.000	-0.000	0.938	0.938
3	!gamma!	21	22	1	1.013	0.269	-8.524	8.519	-1.085
4	mu+	1	-13	1	-1.221	-0.299	147.193	147.198	0.106
5	!u~!	21	-2	2	0.598	0.457	1.238	1.449	0.000
6	!u~!	21	-2	5	0.598	0.457	1.238	1.449	0.000
7	!u~!	21	-2	6	1.322	0.666	7.113	7.265	0.006
8	p+	1	2212	2	-0.485	-0.825	0.908	1.619	0.938
9	(u~)	A 12	-2	0	1.322	0.666	7.113	7.265	0.006
10	(u)	V 11	2	2	0.182	0.370	0.879	1.024	0.325
11	(cluster)	11	91	9	1.503	1.036	7.992	8.290	1.227
12	(pi0)	11	111	11	1.568	1.129	7.997	8.228	0.135
13	gamma	1	22	12	0.666	0.556	3.477	3.584	0.000
14	gamma	1	22	12	0.902	0.573	4.520	4.645	0.000
	sum:	2.00			-0.137	0.005	156.098	157.045	17.222

**FIGURE B.12:** Listing of the JETSET output for a LEPTO event with exclusive  $\pi^0$  signature and a proton originating from hadronization (type 2).

I	particle/jet	KS	KF orig	p_x	p_y	p_z	E	m	
1	!mu+	21	-13	0	-0.117	-0.072	161.834	161.834	0.106
2	!p+	21	2212	0	0.000	0.000	-0.000	0.938	0.938
3	!gamma!	21	22	1	0.686	0.705	27.857	27.852	-1.102
4	mu+	1	-13	1	-0.803	-0.777	133.977	133.982	0.106
5	!g!	21	21	2	-0.022	-0.408	0.054	0.412	-0.000
6	!g!	21	21	5	-0.022	-0.408	0.054	0.412	-0.000
7	!u!	21	2	6	0.636	0.193	0.478	0.819	0.006
8	!u~!	21	-2	6	-0.129	-0.055	21.058	21.059	0.006
9	(u)	A 12	2	6	0.581	0.176	0.437	0.748	0.006
10	(ud_0)	V 11	2101	2	0.520	0.751	0.823	1.391	0.650
11	(u~)	A 12	-2	6	0.473	0.051	14.121	14.129	0.006
12	(g)	I 12	21	6	-0.546	-0.090	6.999	7.021	0.000
13	(u)	V 11	2	2	-0.342	-0.182	5.470	5.494	0.325
14	(cluster)	11	91	9	1.102	0.927	1.260	2.139	0.957
15	p+	1	2212	14	1.161	0.977	1.255	2.181	0.938
16	(cluster)	11	91	11	-0.416	-0.221	26.591	26.644	1.616
17	(pi0)	11	111	16	-0.476	-0.271	26.575	26.581	0.135
18	gamma	1	22	17	-0.187	-0.092	13.293	13.295	0.000
19	gamma	1	22	17	-0.289	-0.179	13.281	13.286	0.000
	sum:	2.00			-0.118	-0.071	161.807	162.744	17.436

### B.3.2 Pull distributions for LEPTO event types

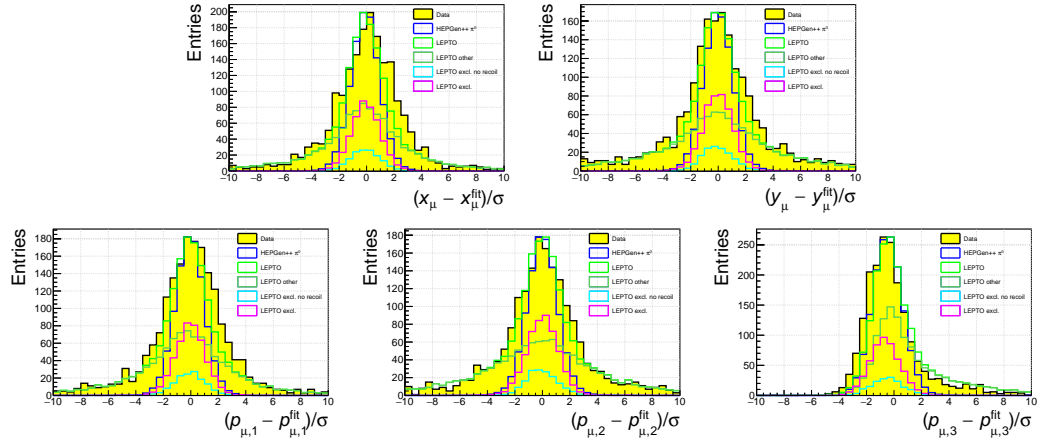


**FIGURE B.13:** Pull distributions for the incoming  $\mu$ . The quantities  $x$  and  $y$  denote the track position at the  $z$ -position measured at the point closest to the vertex. Here,  $p_{1,2,3}$  denote the components of the momentum vector. The normalization factor  $\sigma$  denotes the difference of the error on the quantity before and after the fit. The distributions for HEPGEN++ and LEPTO are normalized to data using the integral. The kinematic range is specified in Section 6.4.

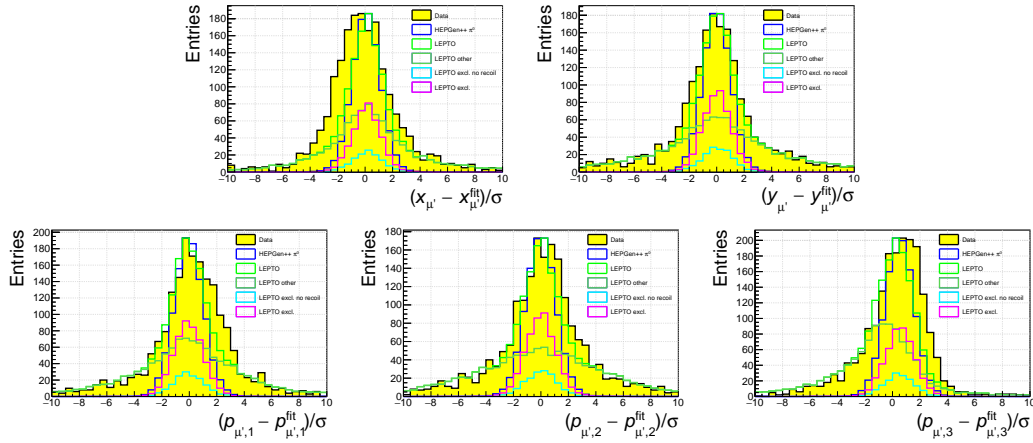


**FIGURE B.14:** Pull distributions for the outgoing  $\mu$ . The quantities  $x$  and  $y$  denote the track position at the  $z$ -position measured at the point closest to the vertex. Here,  $p_{1,2,3}$  denote the components of the momentum vector. The normalization factor  $\sigma$  denotes the difference of the error on the quantity before and after the fit. The distributions for HEPGEN++ and LEPTO are normalized to data using the integral. The kinematic range is specified in Section 6.4.

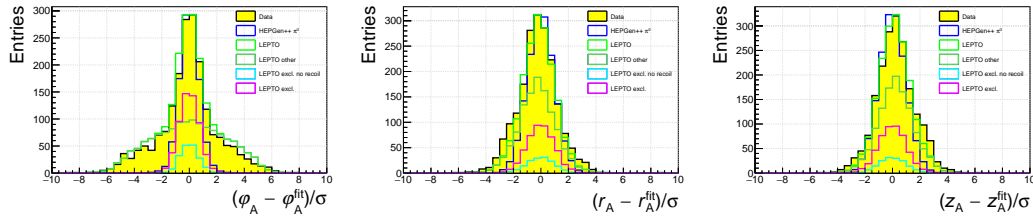


**FIGURE B.15:** Pull distributions for the position in ring A of CAMERA. The measured quantities are the azimuth angle  $\varphi$ , the radius  $r$  and the longitudinal position  $z$  of the hit. The normalization factor  $\sigma$  denotes the difference of the error on the quantity before and after the fit. The distributions for HEPGEN++ and LEPTO are normalized to data using the integral. The kinematic range is specified in Section 6.4.

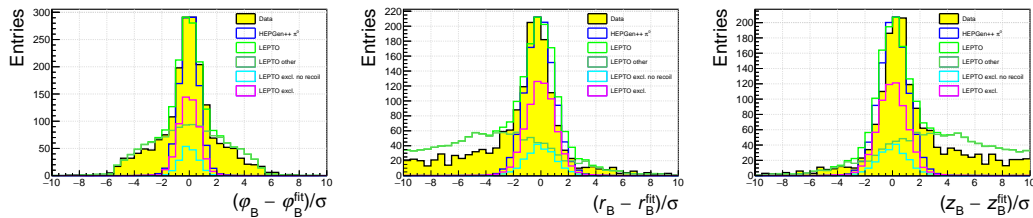


**FIGURE B.16:** Pull distributions for the position in ring B of CAMERA. The measured quantities are the azimuth angle  $\varphi$ , the radius  $r$  and the longitudinal position  $z$  of the hit. The normalization factor  $\sigma$  denotes the difference of the error on the quantity before and after the fit. The distributions for HEPGEN++ and LEPTO are normalized to data using the integral. The kinematic range is specified in Section 6.4.

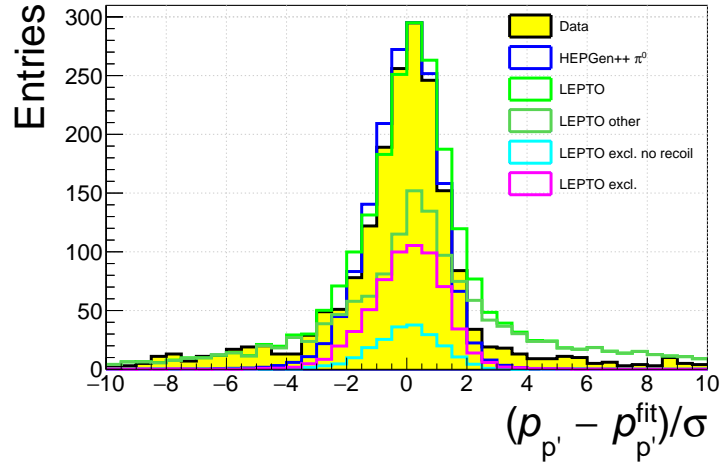


**FIGURE B.17:** Pull distribution for the magnitude of the momentum of the recoil proton. The normalization factor  $\sigma$  denotes the difference of the error on the quantity before and after the fit. The distributions for HEPGEN++ and LEPTO are normalized to data using the integral. The kinematic range is specified in Section 6.4.

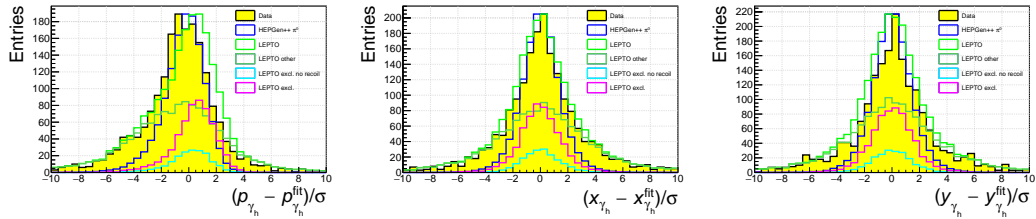


**FIGURE B.18:** Pull distributions for the higher energetic  $\gamma$ .  $x$  and  $y$  denote the track position at the  $z$ -position measured at the respective ECal,  $p$  denotes the magnitude of the momentum of the  $\gamma$ . The normalization factor  $\sigma$  denotes the difference of the error on the quantity before and after the fit. The distributions for HEPGEN++ and LEPTO are normalized to data using the integral. The kinematic range is specified in Section 6.4.

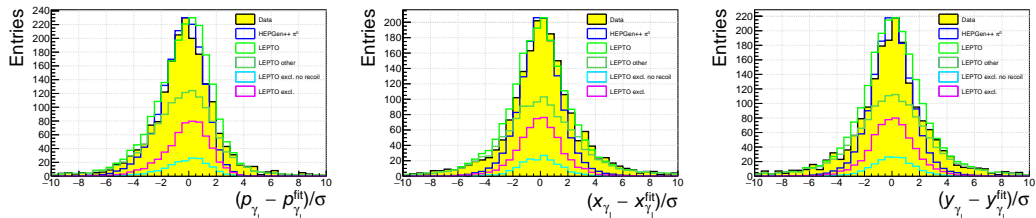


**FIGURE B.19:** Pull distributions for the lower energetic  $\gamma$ .  $x$  and  $y$  denote the track position at the  $z$ -position measured at the respective ECal,  $p$  denotes the magnitude of the momentum of the  $\gamma$ . The normalization factor  $\sigma$  denotes the difference of the error on the quantity before and after the fit. The distributions for HEPGEN++ and LEPTO are normalized to data using the integral. The kinematic range is specified in Section 6.4.

### **B.3.3 Acceptance for each extraction bin**

The following Figures B.20 to B.24 display the acceptance for each  $t$  bin while Figures B.25 to B.32 display the acceptance for each  $\phi_{\pi^0}$  bin. They are plotted in full page and landscape for better visibility.

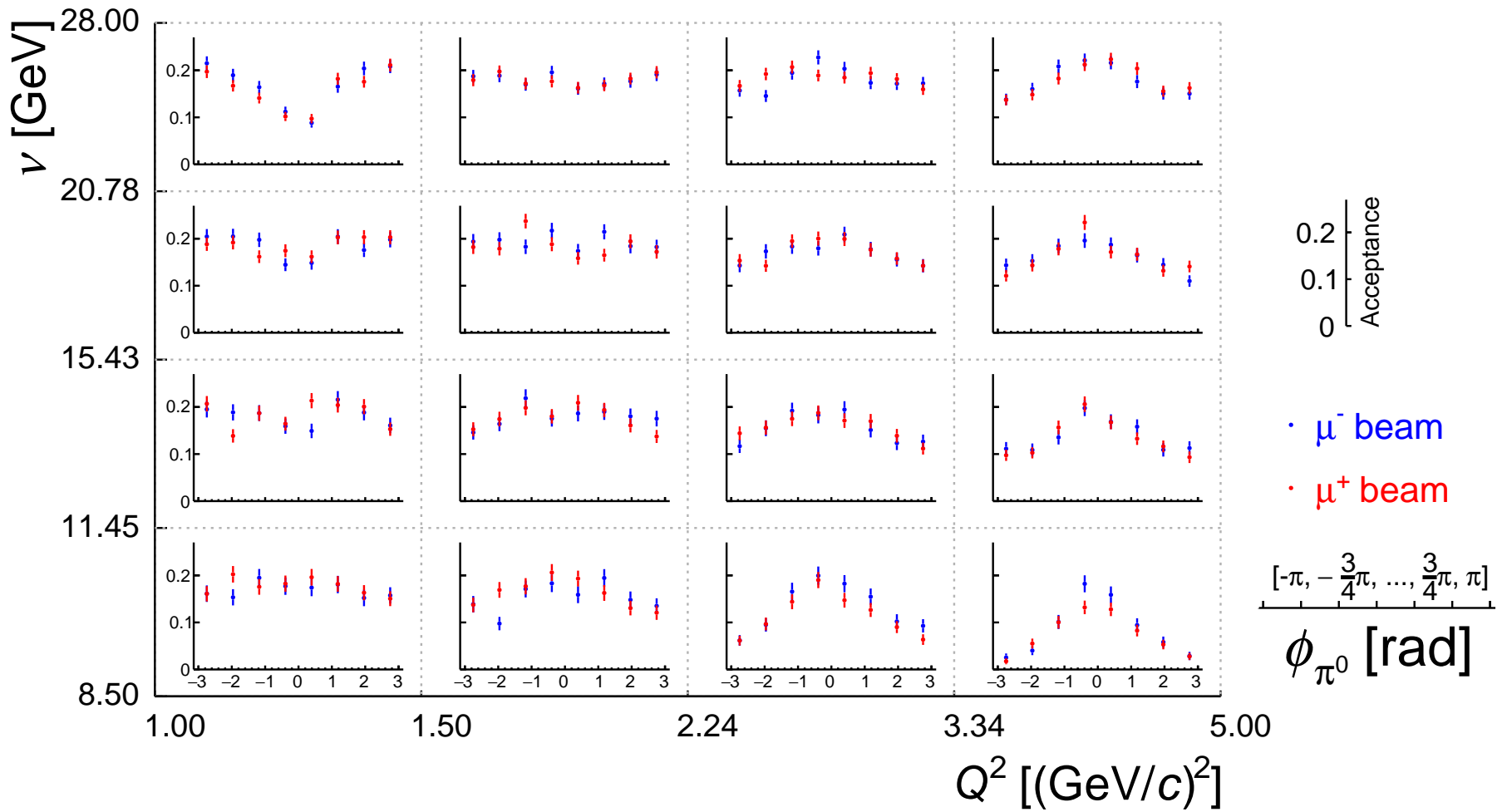


FIGURE B.20: Acceptance as function of  $\phi_{\pi^0}$  for bins in  $\nu$  and  $Q^2$  for the 0th  $t$ -bin.

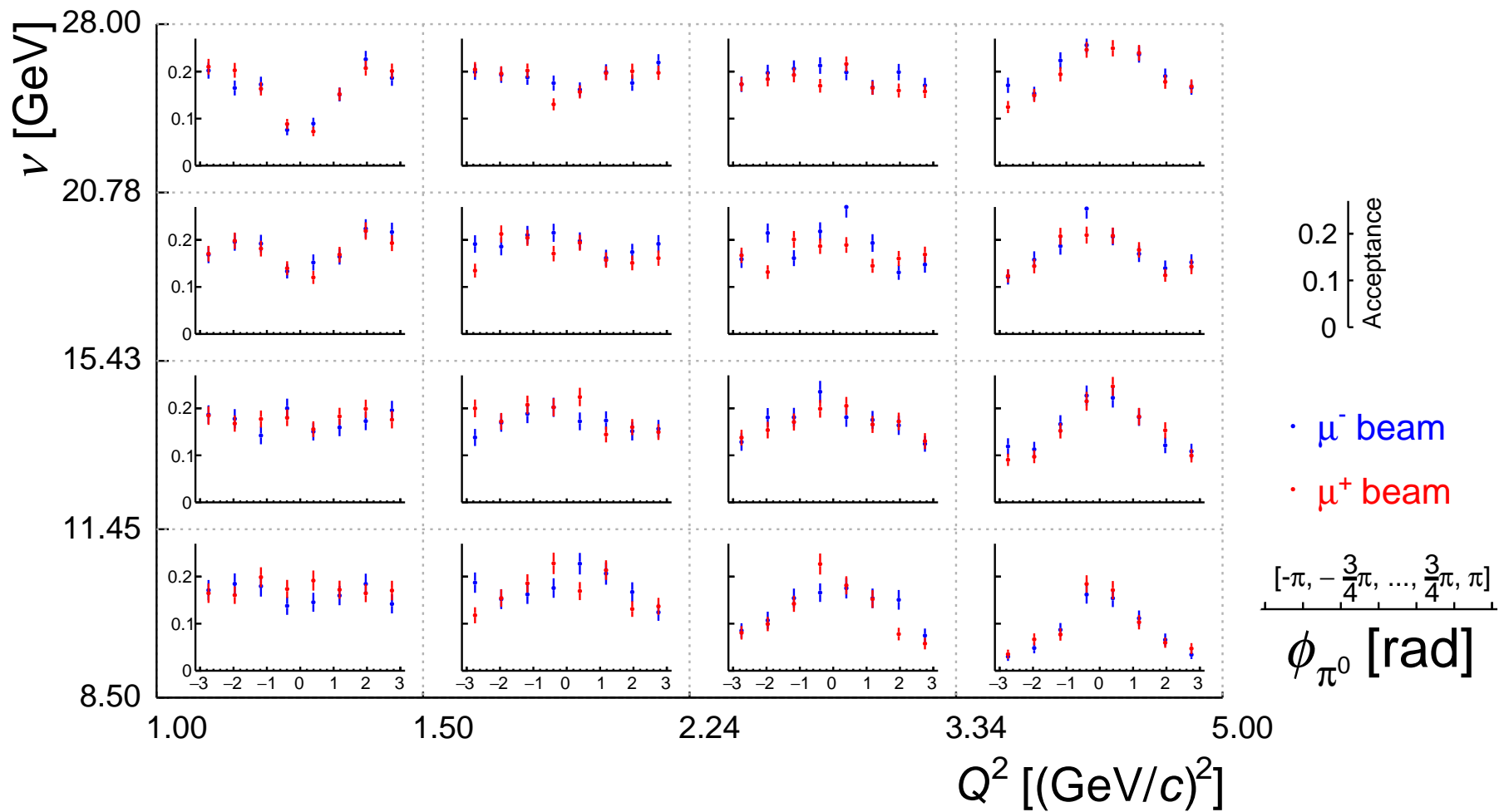


FIGURE B.21: Acceptance as function of  $\phi_{\pi^0}$  for bins in  $\nu$  and  $Q^2$  for the 1st  $t$ -bin.

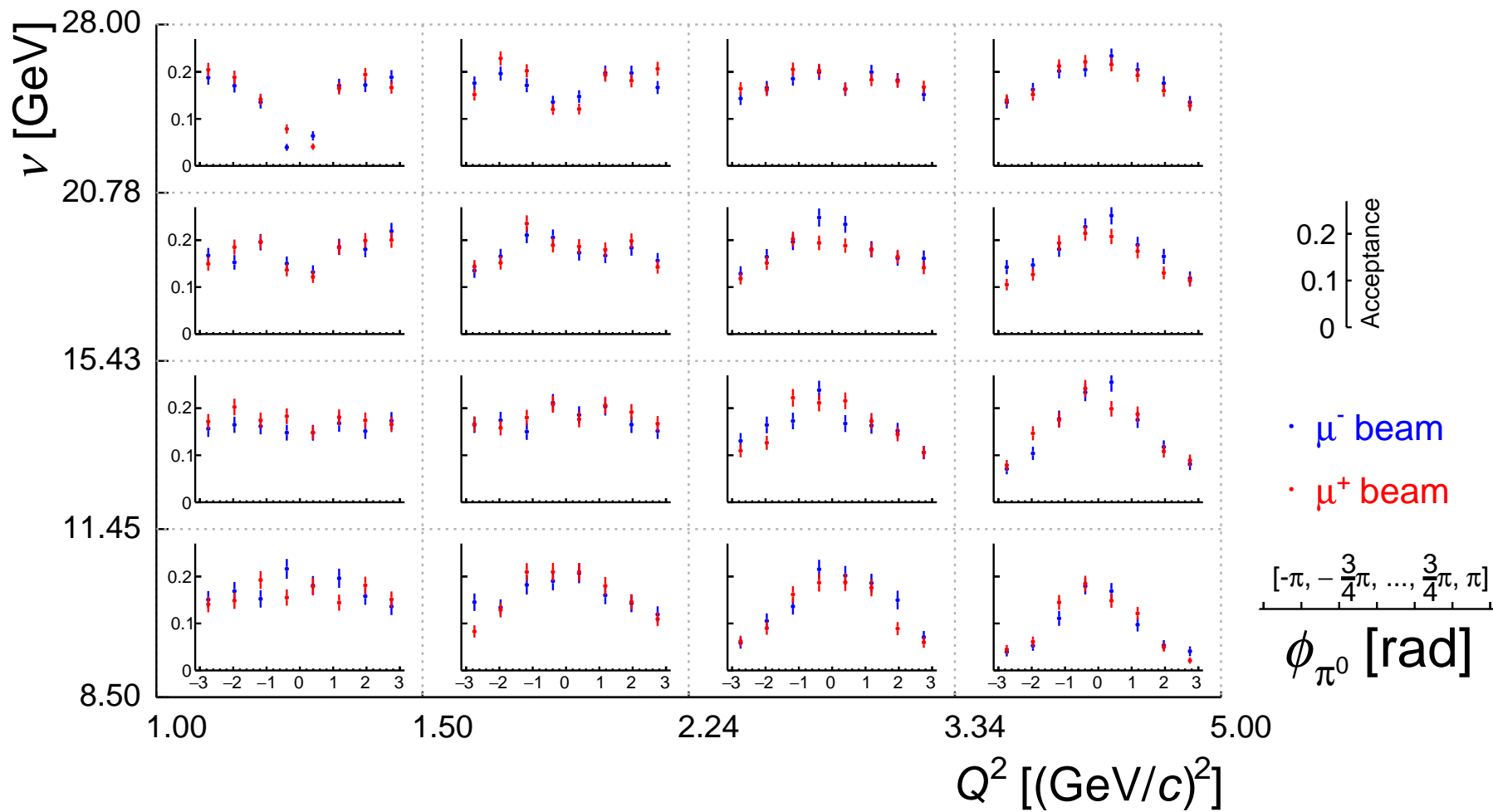


FIGURE B.22: Acceptance as function of  $\phi_{\pi^0}$  for bins in  $\nu$  and  $Q^2$  for the 2nd  $t$ -bin.

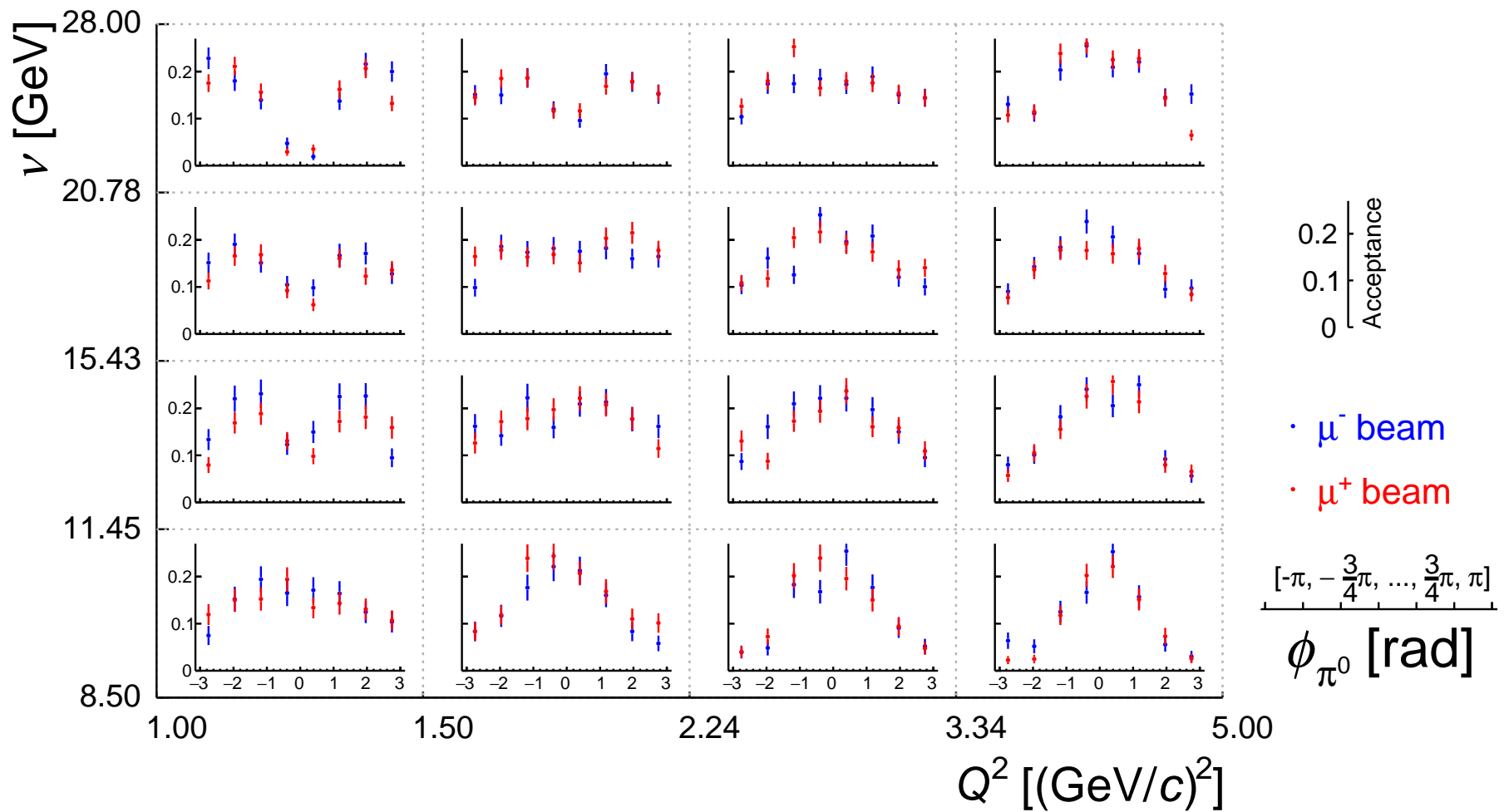


FIGURE B.23: Acceptance as function of  $\phi_{\pi^0}$  for bins in  $\nu$  and  $Q^2$  for the 3rd  $t$ -bin.

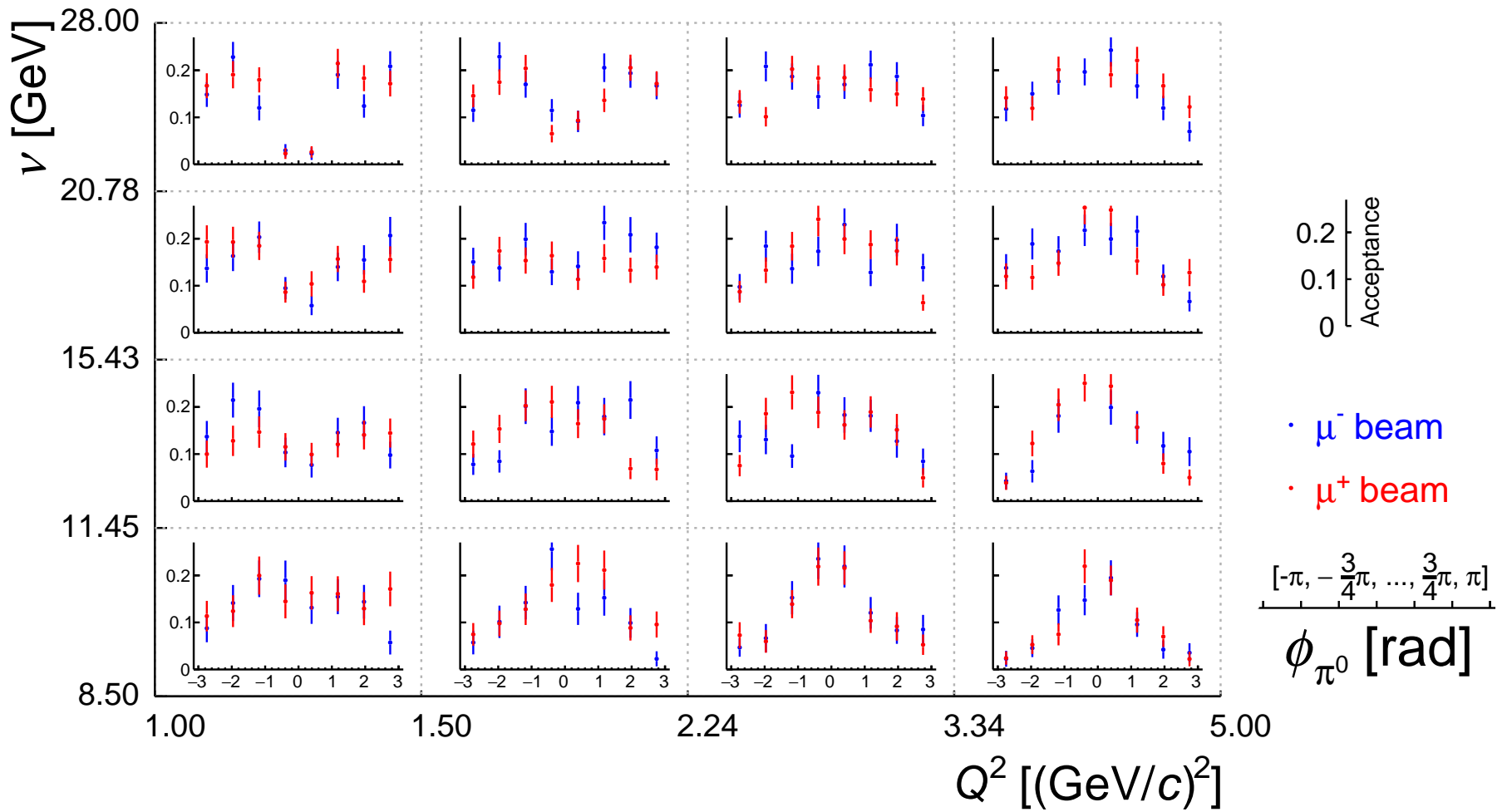


FIGURE B.24: Acceptance as function of  $\phi_{\pi^0}$  for bins in  $\nu$  and  $Q^2$  for the 4th  $t$ -bin.

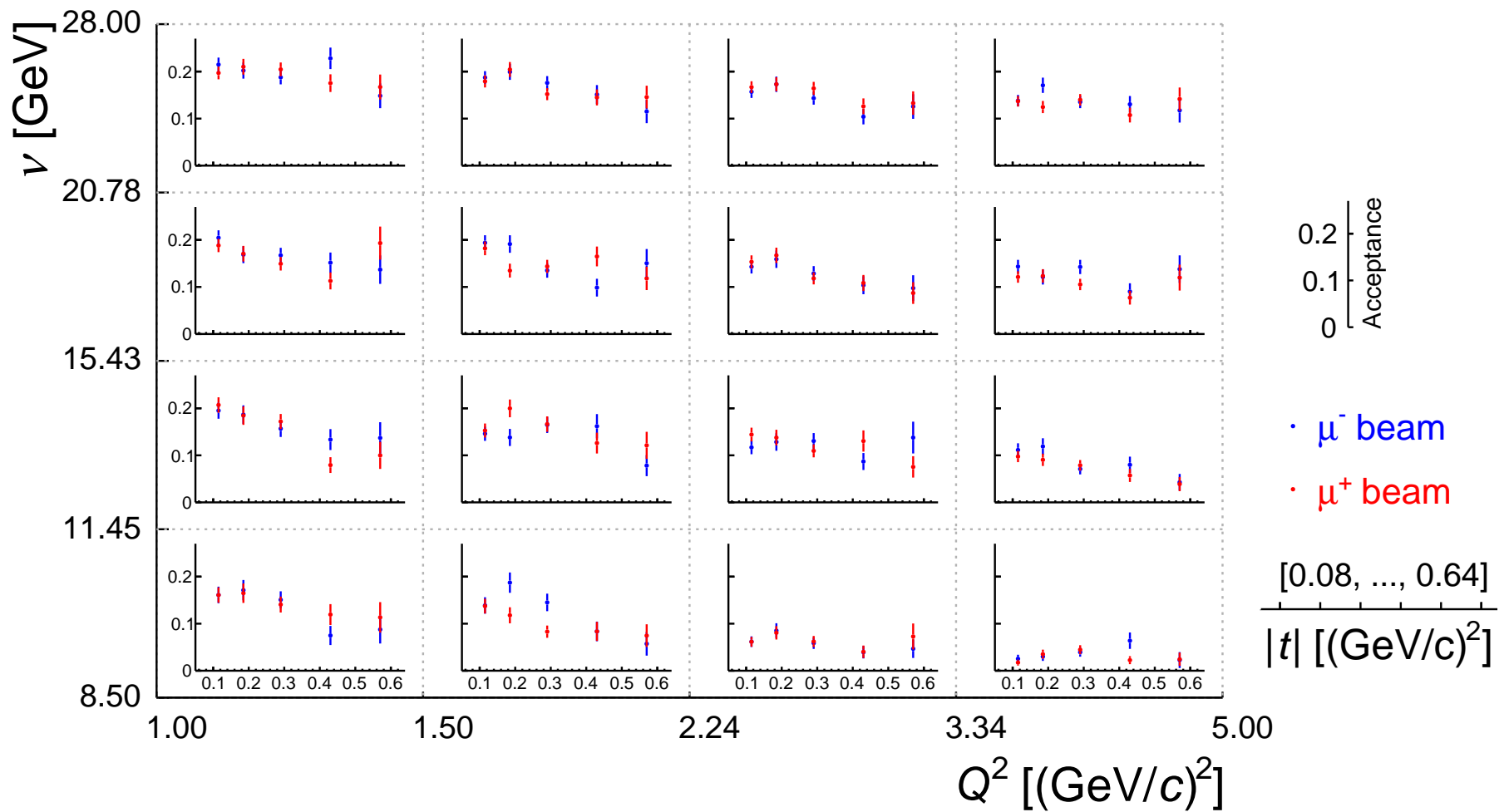


FIGURE B.25: Acceptance as function of  $t$  for bins in  $\nu$  and  $Q^2$  for the 0th  $\phi_{\pi^0}$ -bin.

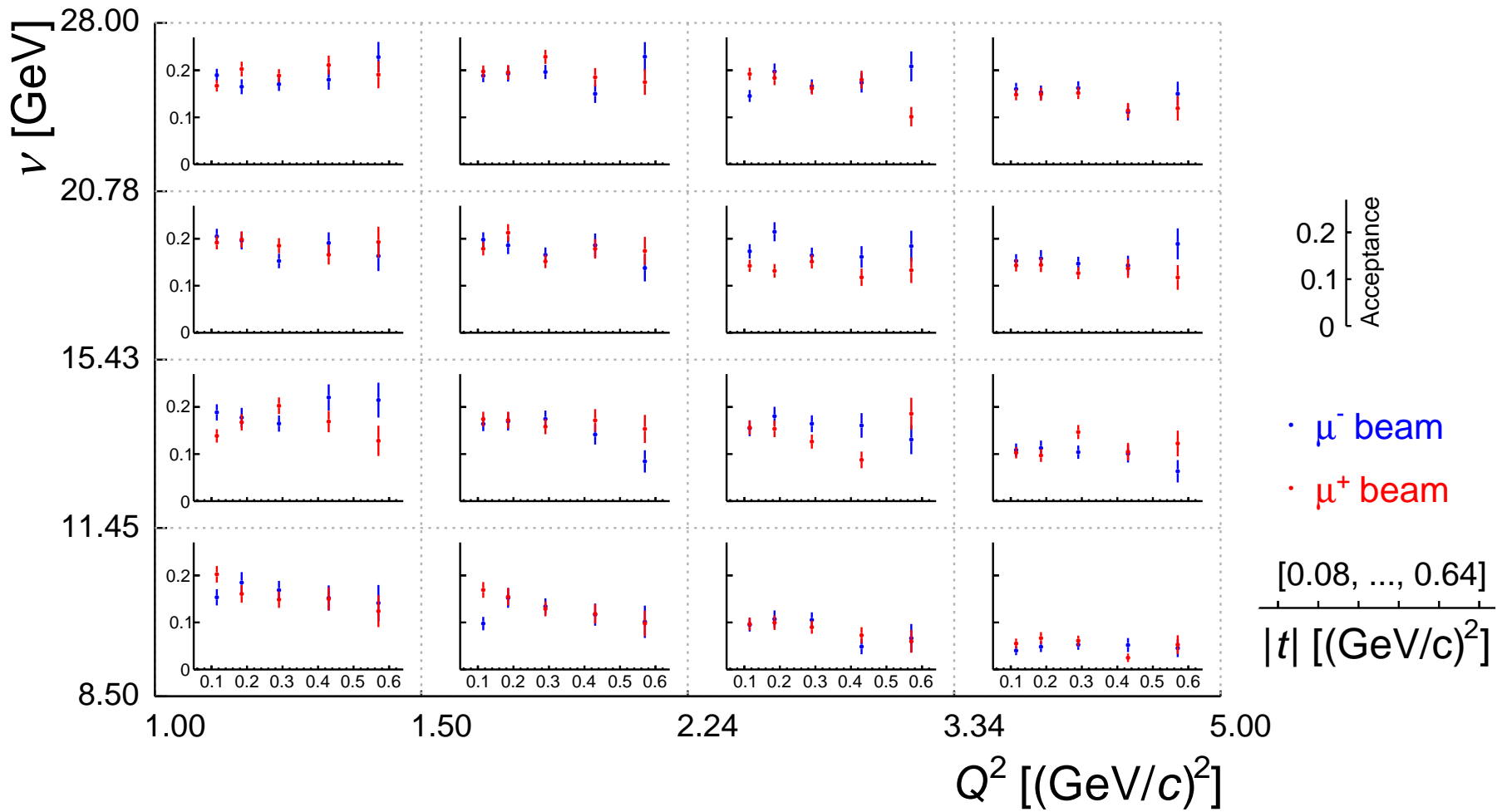


FIGURE B.26: Acceptance as function of  $t$  for bins in  $\nu$  and  $Q^2$  for the 1st  $\phi_{\pi^0}$ -bin.

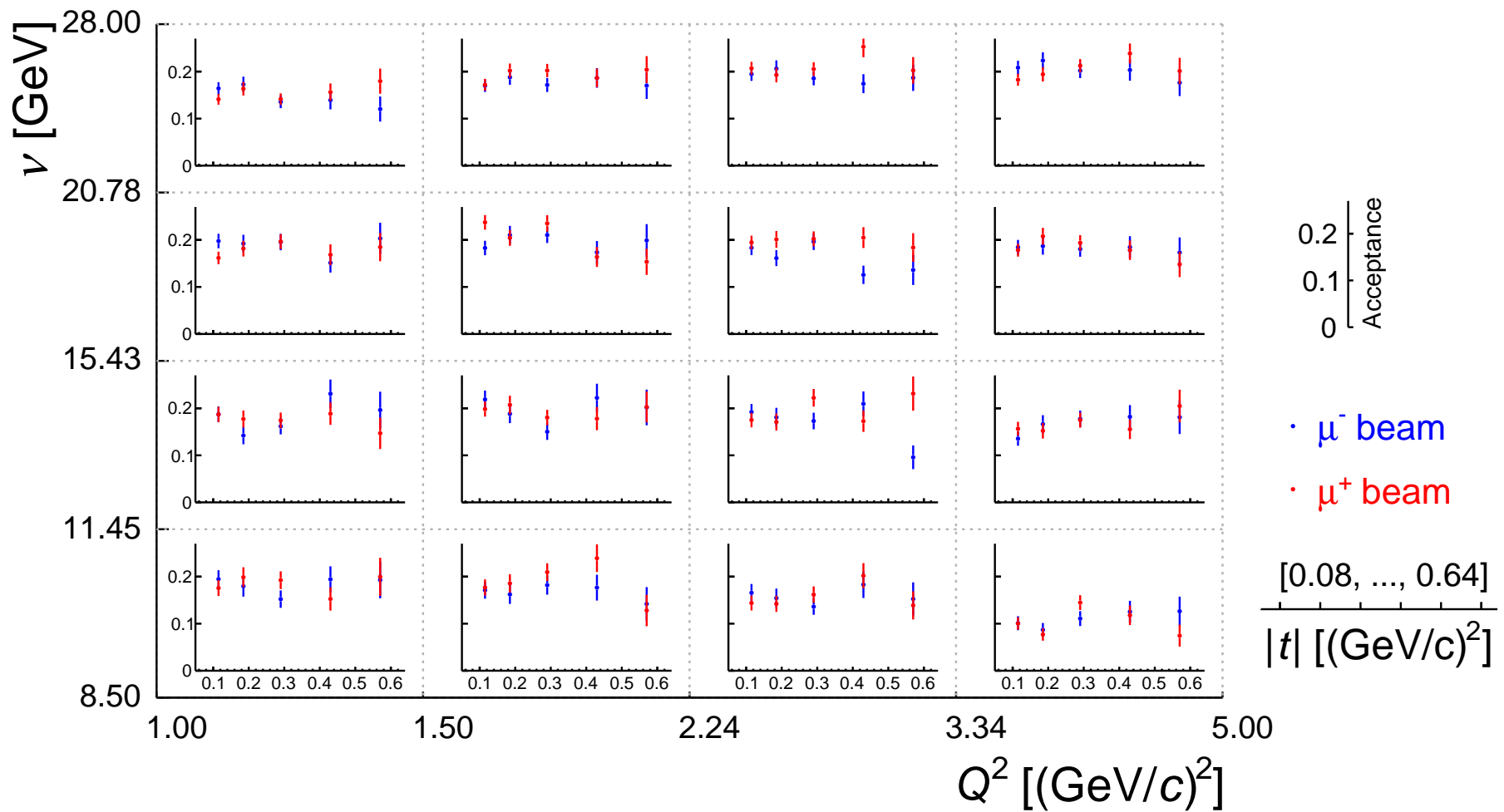


FIGURE B.27: Acceptance as function of  $t$  for bins in  $\nu$  and  $Q^2$  for the 2nd  $\phi_{\pi^0}$ -bin.

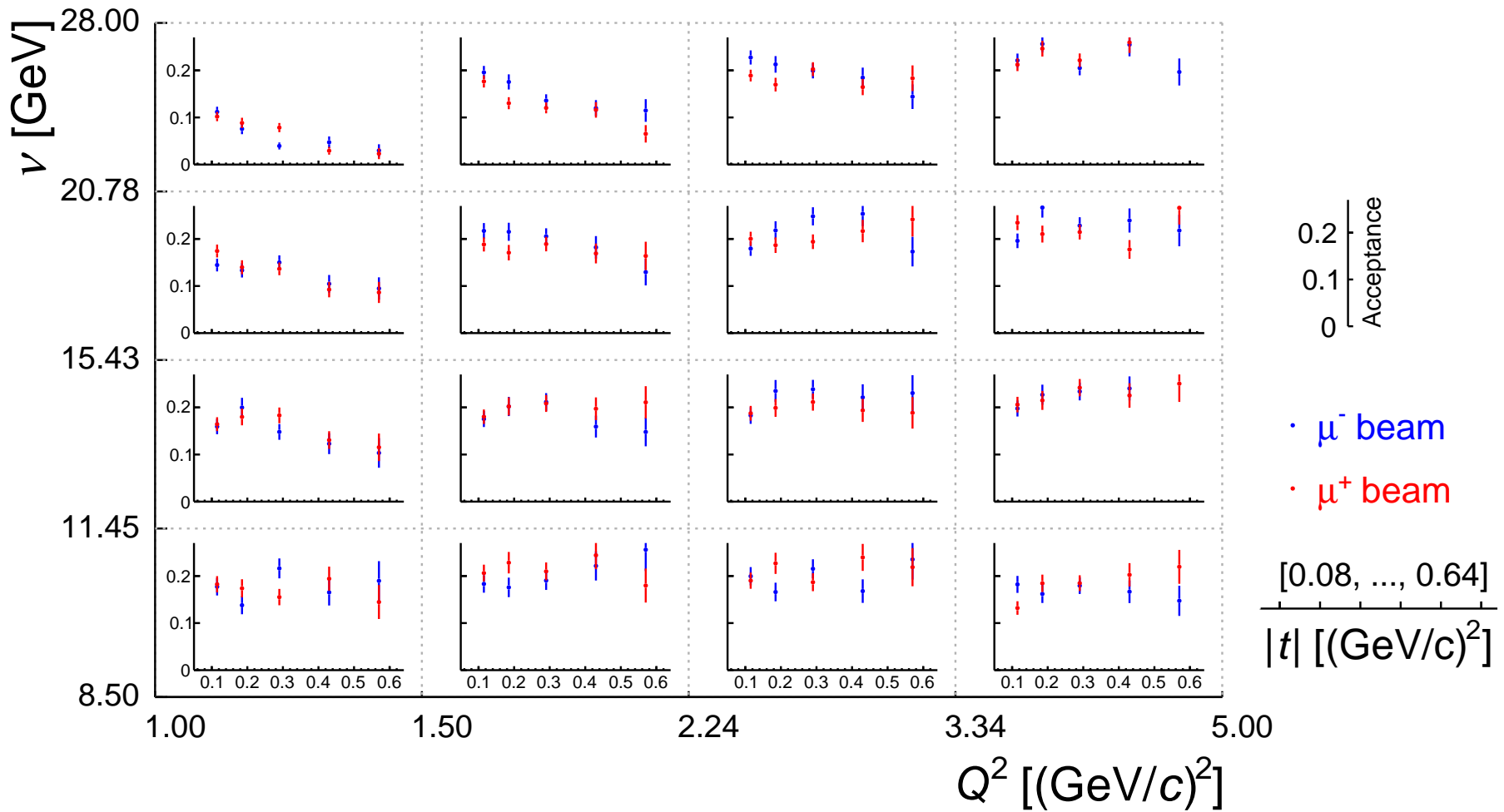


FIGURE B.28: Acceptance as function of  $t$  for bins in  $\nu$  and  $Q^2$  for the 3rd  $\phi_{\pi^0}$ -bin.

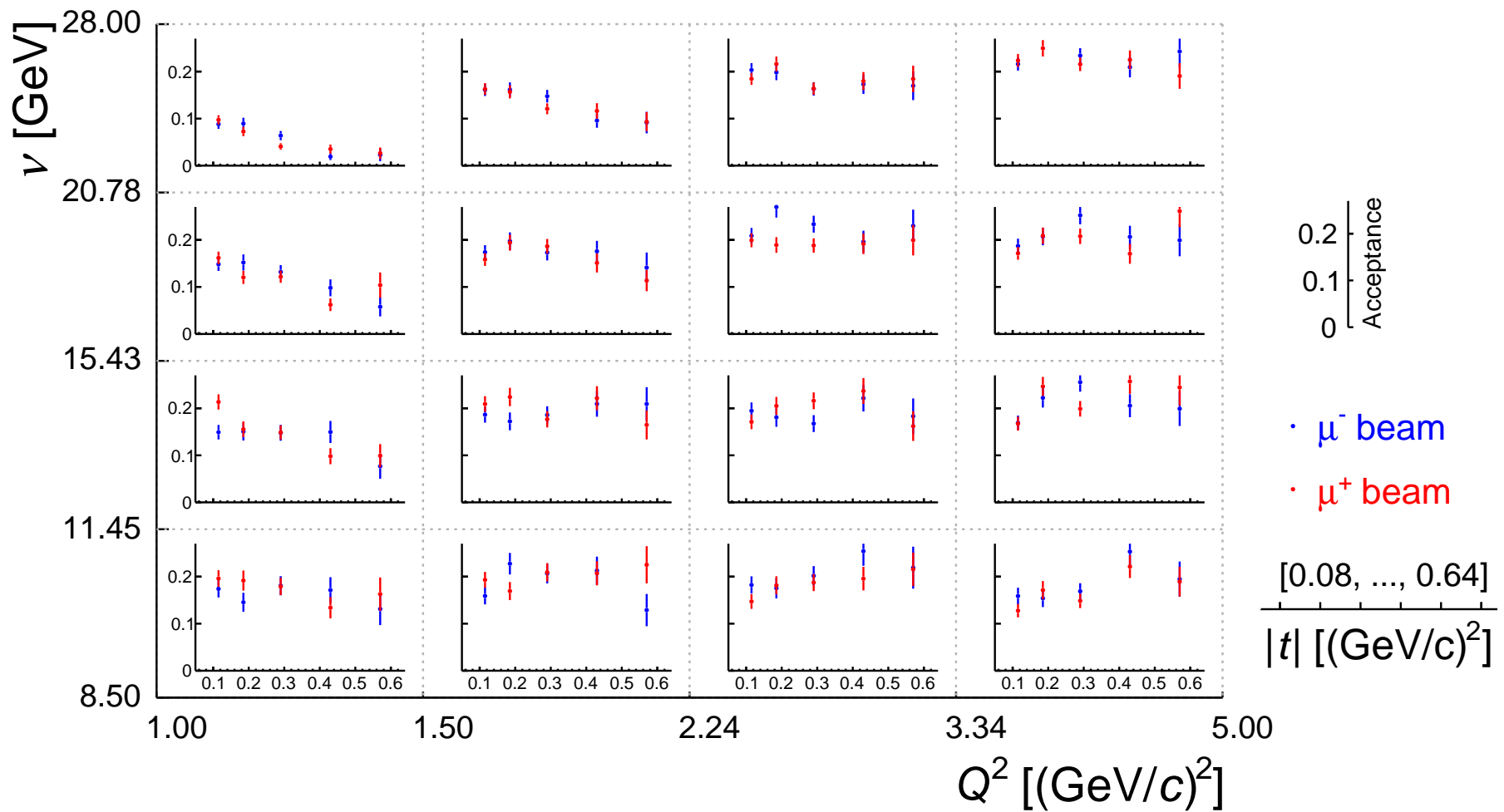


FIGURE B.29: Acceptance as function of  $t$  for bins in  $\nu$  and  $Q^2$  for the 4th  $\phi_{\pi^0}$ -bin.

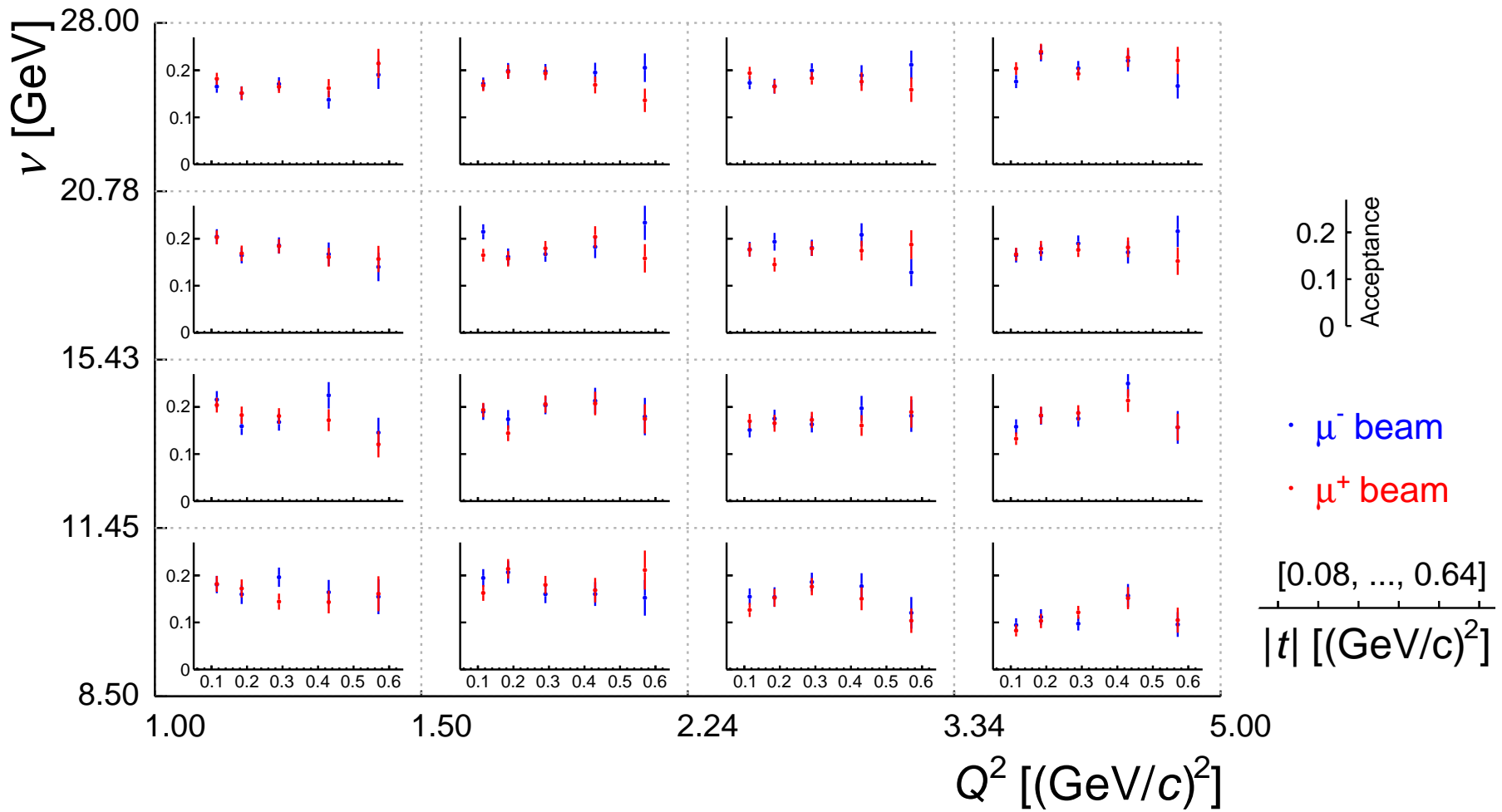


FIGURE B.30: Acceptance as function of  $t$  for bins in  $\nu$  and  $Q^2$  for the 5th  $\phi_{\pi^0}$ -bin.

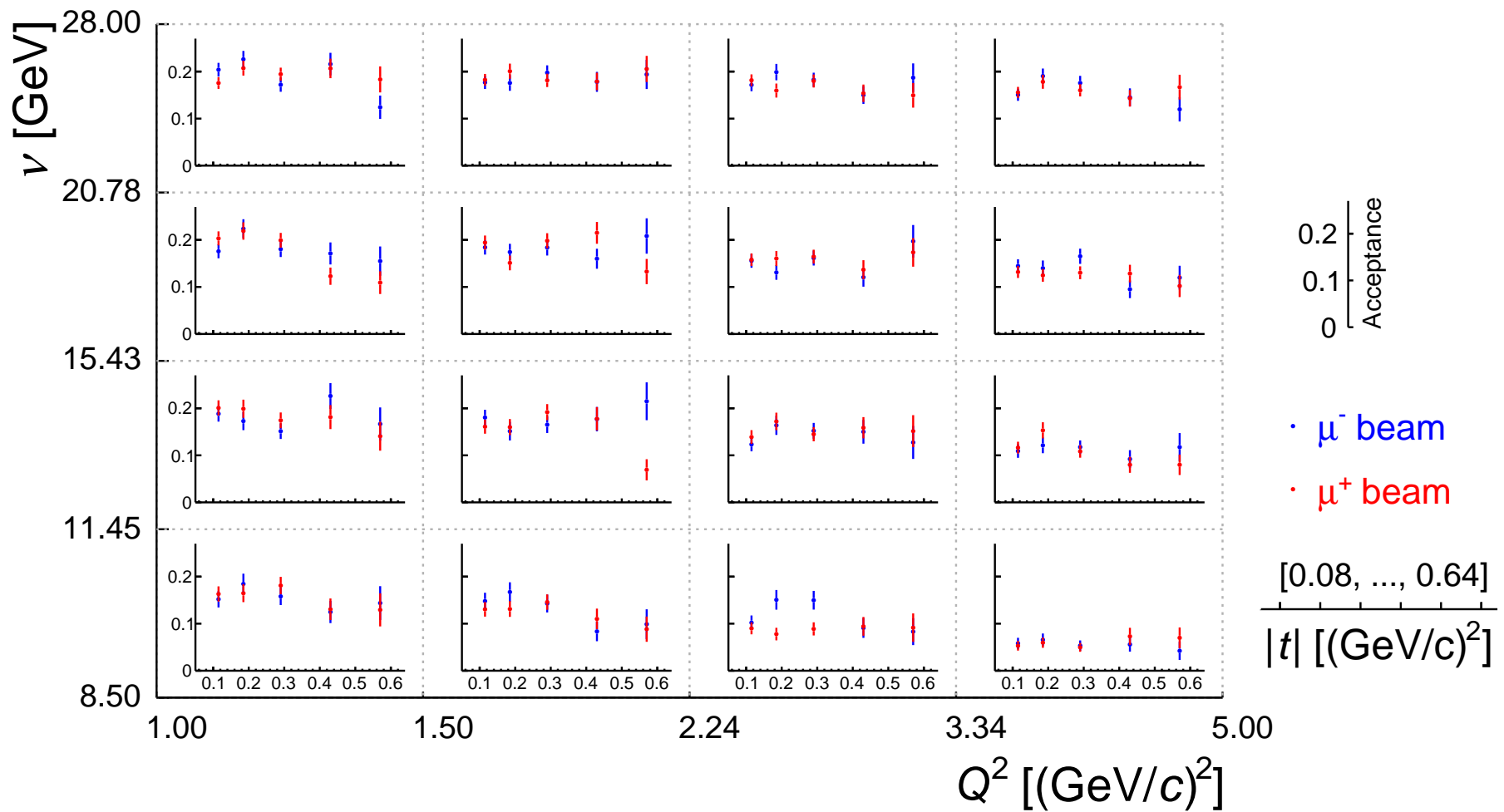


FIGURE B.31: Acceptance as function of  $t$  for bins in  $\nu$  and  $Q^2$  for the 6th  $\phi_{\pi^0}$ -bin.

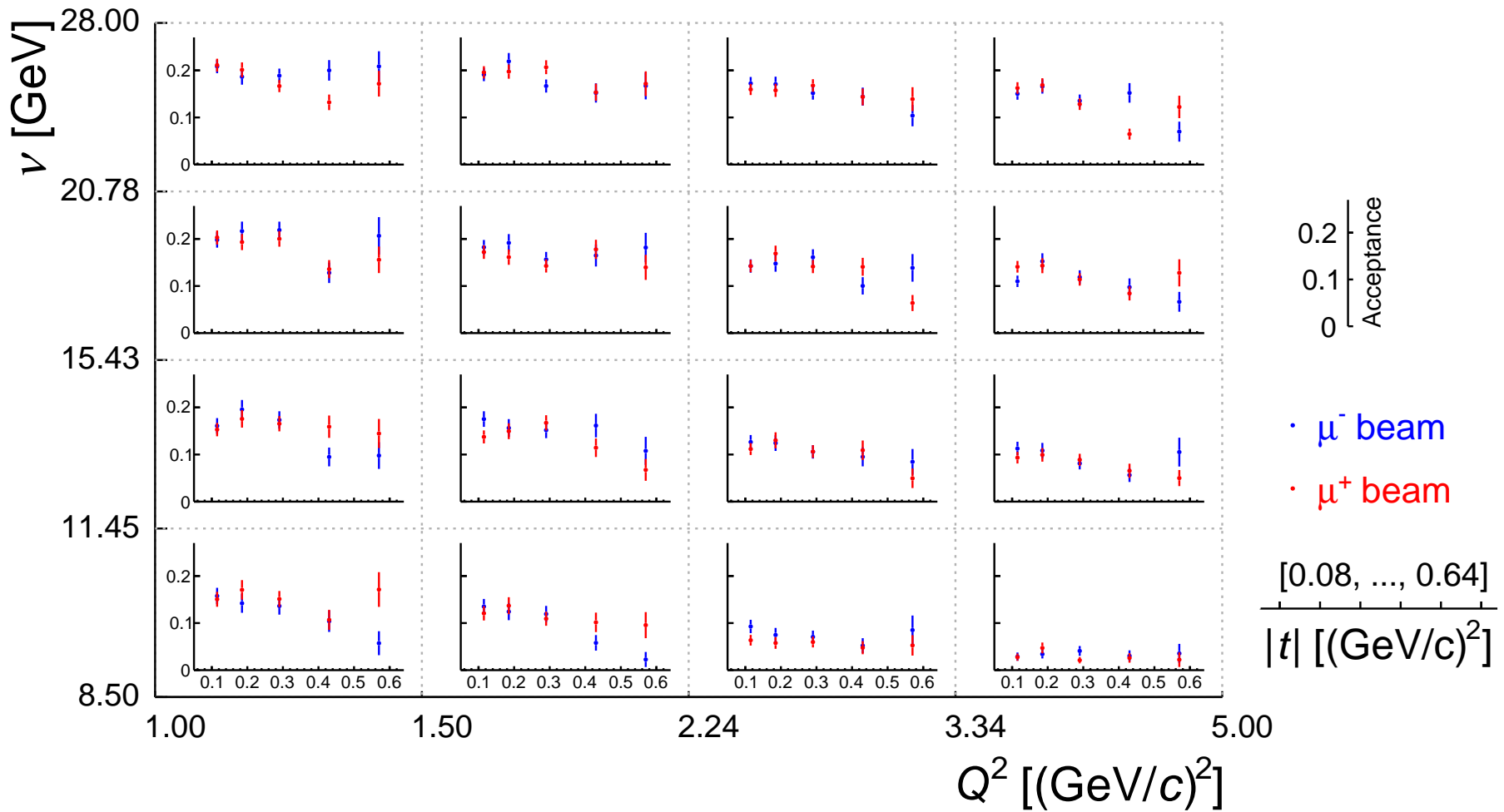
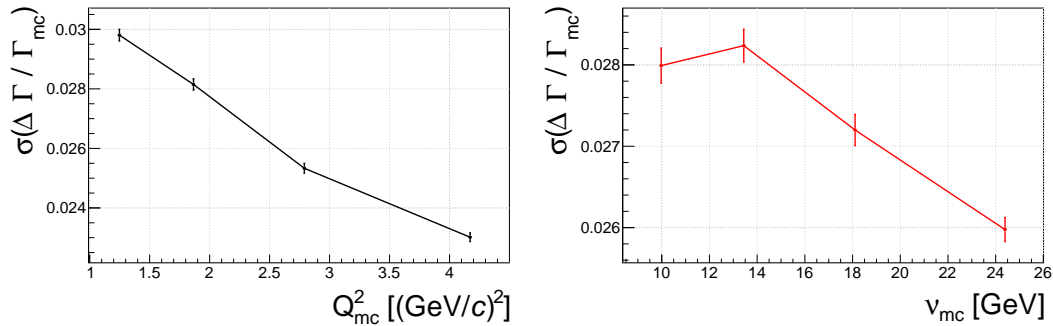


FIGURE B.32: Acceptance as function of  $t$  for bins in  $\nu$  and  $Q^2$  for the 7th  $\phi_{\pi^0}$ -bin.

## B.4 Additional material for extraction of cross-section

### B.4.1 Resolution effects on virtual-photon flux



**FIGURE B.33:** Relative resolution for evaluation of the virtual-photon flux  $\Gamma(Q^2, \nu)$  using an exclusive  $\pi^0$  muoproduction Monte Carlo. The quantity  $\Delta\Gamma = \Gamma - \Gamma_{mc}$  denotes the difference between the value of  $\Gamma$  with reconstructed kinematic and the generator truth denoted by  $\Gamma_{mc}$ . The resolution  $\sigma$  is plotted as a function of the generator truth for  $Q_{mc}^2$  (left) and  $\nu_{mc}$  (right).

### B.4.2 Study of binned maximum likelihood fit using a bootstrap/replica method

Next to the uncertainties for the cross-section values, the Poisson bootstrap method introduced in Subsection 6.6.5 allows to examine the binned maximum likelihood fit as well. Here, a bootstrap sample is the combination of bootstrap samples for each  $\phi_{\pi^0}$  bin, each created according to Eq. 6.41. The Poisson bootstrap distribution of the fit parameters follow from fitting the binned maximum likelihood for a large number of bootstrap samples. The resulting distribution is displayed in Fig. B.34. In the plots, the best fit value determined by the minimizer is indicated by the blue line. One can observe, that the mean of the bootstrap distributions are slightly shifted with respect to the best fit value. It seems therefore, that the minimizer tends to favor another minimum when the input is modified. The  $\sigma$  of the bootstrap distributions is very much compatible with the errors estimated by the minimizer while the covariance matrix reads

$$C = \begin{pmatrix} 2.23 & 0.22 \\ 0.22 & 0.29 \end{pmatrix}.$$

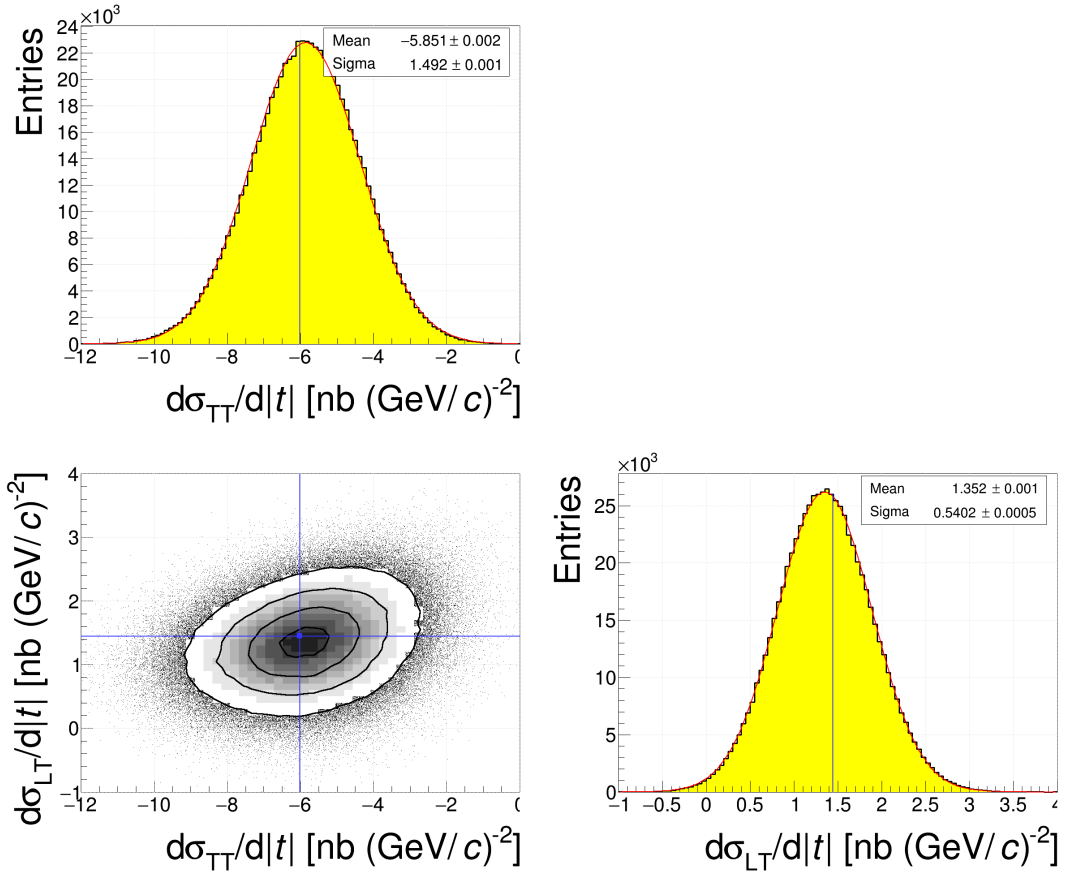


FIGURE B.34: Poisson bootstrap distributions for binned maximum likelihood fit parameters. The blue line indicates the best fit value determined by the minimizer.

### B.4.3 Alternative likelihood using parameterized PDFs

When setting up the likelihood function Eq. 6.51 it was assumed that the number of events in a bin is described by a Poisson distribution. As a result, a correction for the covariance matrix reported by the minimizer is needed. In Subsection 6.6.8, the likelihood is expressed using the parameterization of the PDFs in the extraction bins, Eq. 6.58. This likelihood can also be fed to the minimizer. Now, the covariance matrix correction is not needed since the likelihood is properly normalized. The result of the minimization reads

$$\begin{aligned} \left\langle \frac{d\sigma_{TT}}{d|t|} \right\rangle &= -6.02 \pm 1.31 \frac{\text{nb}}{(\text{GeV}/c)^2}, \\ \left\langle \frac{d\sigma_{LT}}{d|t|} \right\rangle &= 1.54 \pm 0.52 \frac{\text{nb}}{(\text{GeV}/c)^2}, \end{aligned}$$

while the reported covariance matrix reads

$$C = \begin{pmatrix} 1.71 & 0.29 \\ 0.29 & 0.27 \end{pmatrix},$$

which is to be compared to (Eq. 6.54)

$$\left\langle \frac{d\sigma_{TT}}{d|t|} \right\rangle = -6.02 \pm 1.31 \frac{\text{nb}}{(\text{GeV}/c)^2},$$

$$\left\langle \frac{d\sigma_{LT}}{d|t|} \right\rangle = 1.44 \pm 0.49 \frac{\text{nb}}{(\text{GeV}/c)^2},$$

with covariance matrix (Eq. 6.53)

$$C = \begin{pmatrix} 1.73 & 0.49 \\ 0.49 & 0.24 \end{pmatrix},$$

The value for  $\frac{d\sigma_{LT}}{dt}$  slightly differs which means that the different choice of PDFs creates a slightly different minimum. Also, the correlation between the two parameters seems to be slightly reduced.

Again, the fit with the modified can be studied using the replica/bootstrap method as explained in Appendix B.4.2. The results are presented in Fig. B.35. Again, the bootstrap samples are slightly shifted with respect to

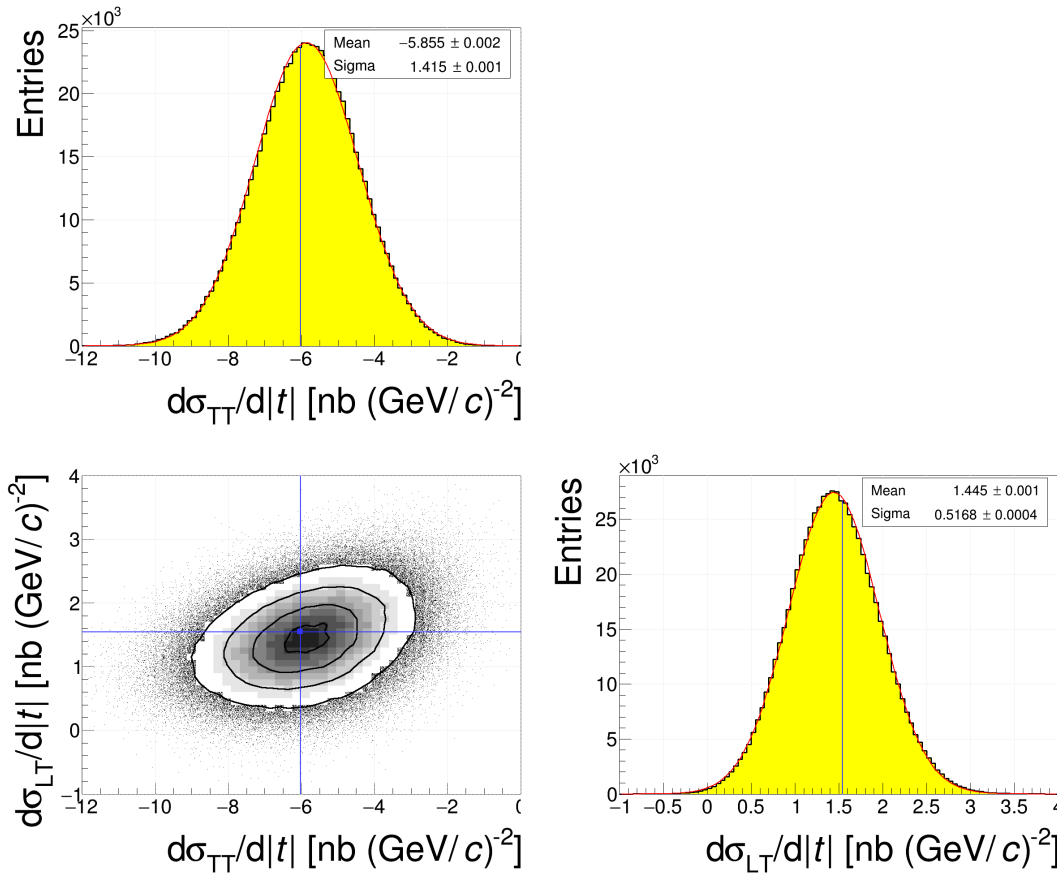


**FIGURE B.35:** Poisson bootstrap distributions for binned maximum likelihood fit parameters, using the parameterized PDFs to define the likelihood (Eq. 6.58). The blue line indicates the best fit value determined by the minimizer.

the best fit value of the minimizer while the widths of the distributions vary

much resemble the uncertainties reported by the minimizer. The corresponding covariance matrix results in

$$C = \begin{pmatrix} 2.01 & 0.24 \\ 0.24 & 0.28 \end{pmatrix}.$$

One can further utilize the likelihood used in the MCMC sampling method (Eq. 6.58) with a flat prior  $\pi(\vec{\beta}) = 1$  (see also Appendix B.4.4). Now, the normalization parameter (unseparated cross-section) is a free parameter. The result of the minimizing process reads

$$\begin{aligned} \left\langle \frac{d\sigma_T}{d|t|} + \varepsilon \frac{d\sigma_L}{d|t|} \right\rangle &= \left\langle \frac{d\sigma_U}{d|t|} \right\rangle = 8.08 \pm 0.64 \frac{\text{nb}}{(\text{GeV}/c)^2}, \\ \left\langle \frac{d\sigma_{TT}}{d|t|} \right\rangle &= -5.98 \pm 1.36 \frac{\text{nb}}{(\text{GeV}/c)^2}, \\ \left\langle \frac{d\sigma_{LT}}{d|t|} \right\rangle &= 1.53 \pm 0.53 \frac{\text{nb}}{(\text{GeV}/c)^2}, \end{aligned}$$

with covariance matrix

$$C = \begin{pmatrix} 0.42 & -0.26 & 0.06 \\ -0.26 & 1.86 & 0.25 \\ 0.06 & 0.25 & 0.28 \end{pmatrix}.$$

#### B.4.4 MCMC with flat prior

As a test of the MCMC method, Fig. B.36 and Fig. B.37 show the corresponding figures to Fig. 6.39 and Fig. 6.40 for a log-posterior with a flat prior  $\pi(\vec{\beta}) = 1$ .

Here, the most probable parameter set extracted from the three dimensional parameter density reads

$$\begin{aligned} \left\langle \frac{d\sigma_T}{d|t|} + \varepsilon \frac{d\sigma_L}{d|t|} \right\rangle &= \left\langle \frac{d\sigma_U}{d|t|} \right\rangle = 8.07 \frac{\text{nb}}{(\text{GeV}/c)^2}, \\ \left\langle \frac{d\sigma_{TT}}{d|t|} \right\rangle &= -6.00 \frac{\text{nb}}{(\text{GeV}/c)^2}, \\ \left\langle \frac{d\sigma_{LT}}{d|t|} \right\rangle &= 1.53 \frac{\text{nb}}{(\text{GeV}/c)^2}. \end{aligned}$$

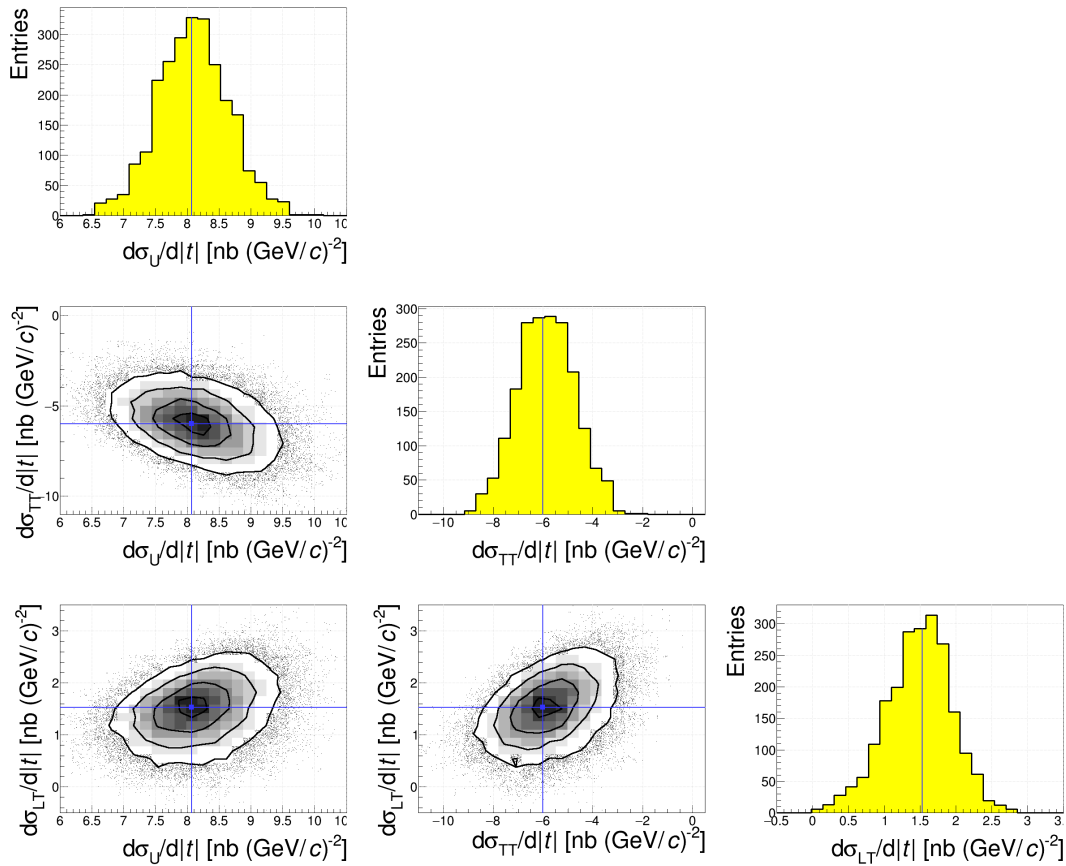


**FIGURE B.36:** Visualization of the most probable parameter set obtained using the MCMC sampling method. The histograms show the values for the respective parameter or parameter combination when slicing the other parameters. For instance, the lower left shows the samples for  $\langle \frac{d\sigma_{LT}}{d|t|} \rangle$  and  $\langle \frac{d\sigma_U}{d|t|} \rangle$  for a slice in  $\langle \frac{d\sigma_{TT}}{d|t|} \rangle$ . The blue lines and marker indicate the position of the most probable parameter set. The contours contain from dark to light  $\{10, 40, 70, 90\}\%$  of the most probable parameters.

The mean and RMS of the of the projections to the respective parameter results in the following values

$$\begin{aligned} \left\langle \frac{d\sigma_T}{d|t|} + \varepsilon \frac{d\sigma_L}{d|t|} \right\rangle &= \left\langle \frac{d\sigma_U}{d|t|} \right\rangle = 8.16 \pm 0.66 \frac{\text{nb}}{(\text{GeV}/c)^2}, \\ \left\langle \frac{d\sigma_{TT}}{d|t|} \right\rangle &= -5.87 \pm 1.41 \frac{\text{nb}}{(\text{GeV}/c)^2}, \\ \left\langle \frac{d\sigma_{LT}}{d|t|} \right\rangle &= 1.53 \pm 0.54 \frac{\text{nb}}{(\text{GeV}/c)^2}, \end{aligned}$$

and the corresponding covariance matrix reads

$$C = \begin{pmatrix} 0.43 & -0.23 & 0.05 \\ -0.23 & 2.01 & 0.20 \\ 0.05 & 0.20 & 0.30 \end{pmatrix}.$$

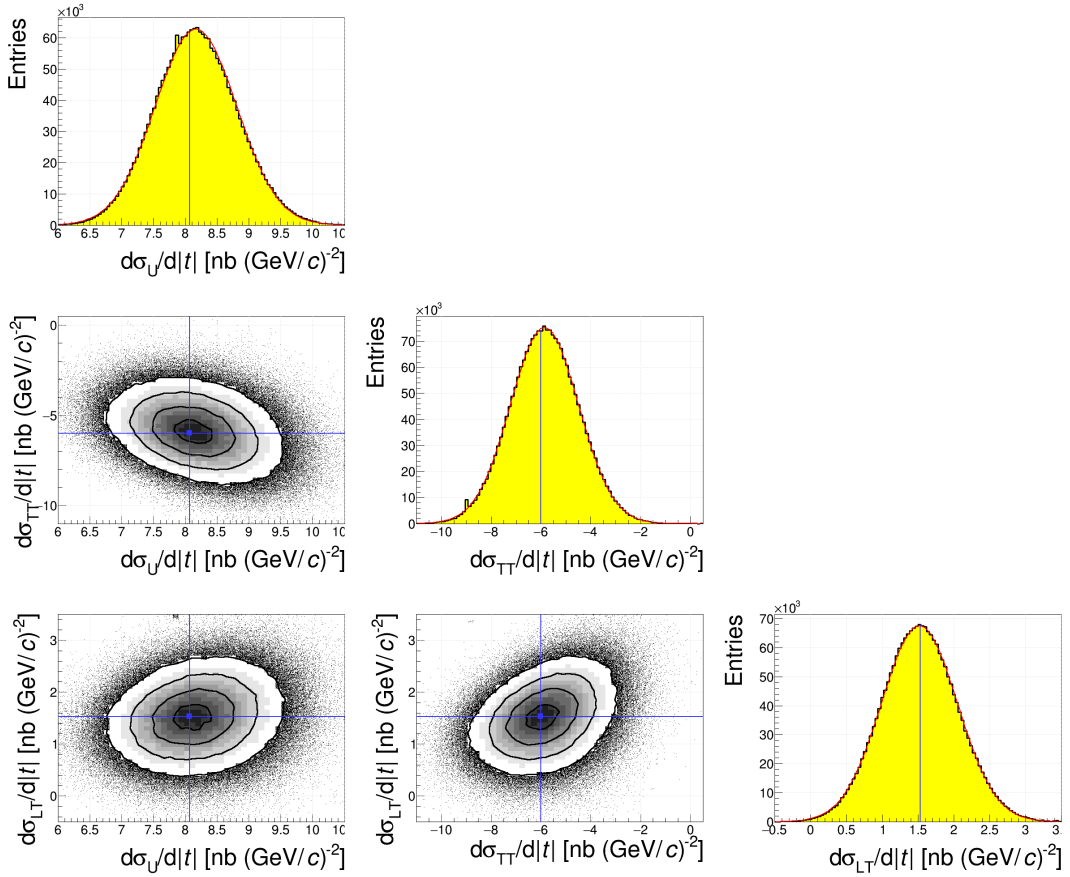


**FIGURE B.37:** Visualization of the distribution of parameters obtained with the MCMC. The histograms show the values for the respective parameter or parameter combination when integrating the other parameters. For instance, the lower left shows the values for  $\langle \frac{d\sigma_{LT}}{d|t|} \rangle$  and  $\langle \frac{d\sigma_U}{d|t|} \rangle$  when integrating over  $\langle \frac{d\sigma_{TT}}{d|t|} \rangle$ . The blue lines and marker indicate the position of the most probable parameter set. The contours contain from dark to light  $\{10, 40, 70, 90\}\%$  of the most probable parameters.

### B.4.5 MCMC result with model curves

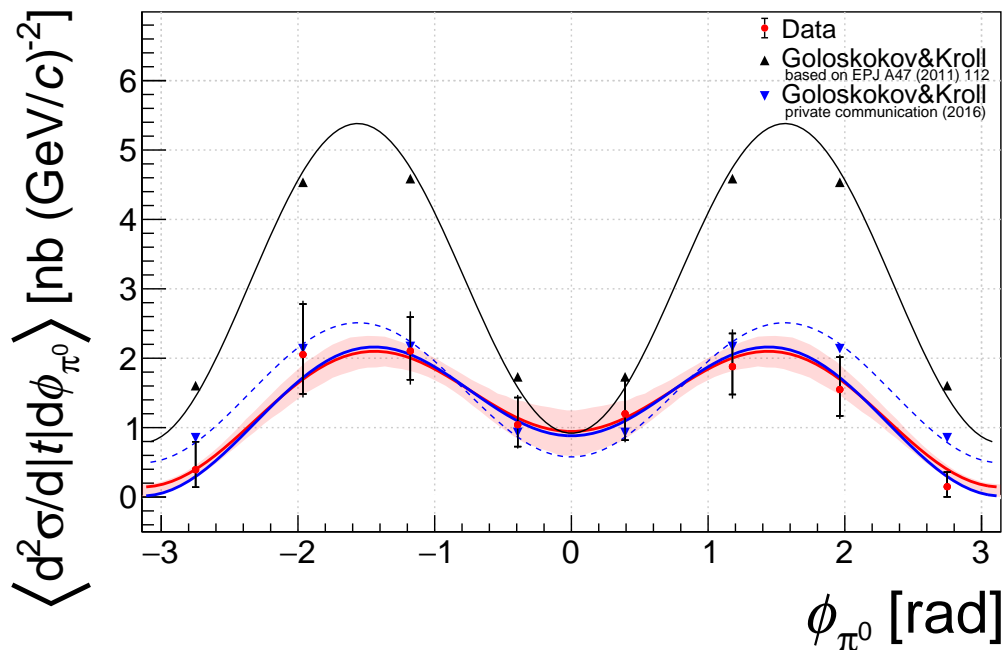


FIGURE B.38: Cross-section as a function of  $\phi_{\pi^0}$ . The red curve and the uncertainty band, which represents the 68% confidence interval, result from the MCMC method (Subsection 6.6.8).

## B.5 Various systematic tests

The Fig. B.39 (Fig. B.40) summarizes the result of various systematic tests and their influence on the extracted cross-section as a function of  $t$  ( $\phi_{\pi^0}$ ). The labels of the points are explained in the following.

- no fit:** Extraction using the event kinematics determined without the kinematic fit (*cf.* Section 6.3).
- kinfit shift:** Extraction with modified energy and momentum balance constraints (*cf.* Subsection 6.7.5).
- 3d acc:** Extraction with a three dimensional acceptance, *cf.* Section 6.5. The dimensions are  $Q^2$  and  $\nu$  and the respective extraction variable ( $t$  respectively  $\phi_{\pi^0}$ ).
- 3d acc, no fit:** Same as “3d acc” but using the event kinematics determined without the kinematic fit (*cf.* Section 6.3).
- 3d acc, kinfit shift** Same as “3d acc” but with modified energy and momentum balance constraints (*cf.* Subsection 6.7.5).

**alternate:** Extraction was modified by estimating the virtual photon flux using Monte Carlo, as explained in Subsection 6.6.1.

**alternate no fit:** Same as “alternate” but using the event kinematics determined without the kinematic fit (*cf.* Section 6.3).

**alternate shifted:** Same as “alternate” but with modified energy and momentum balance constraints (*cf.* Subsection 6.7.5).

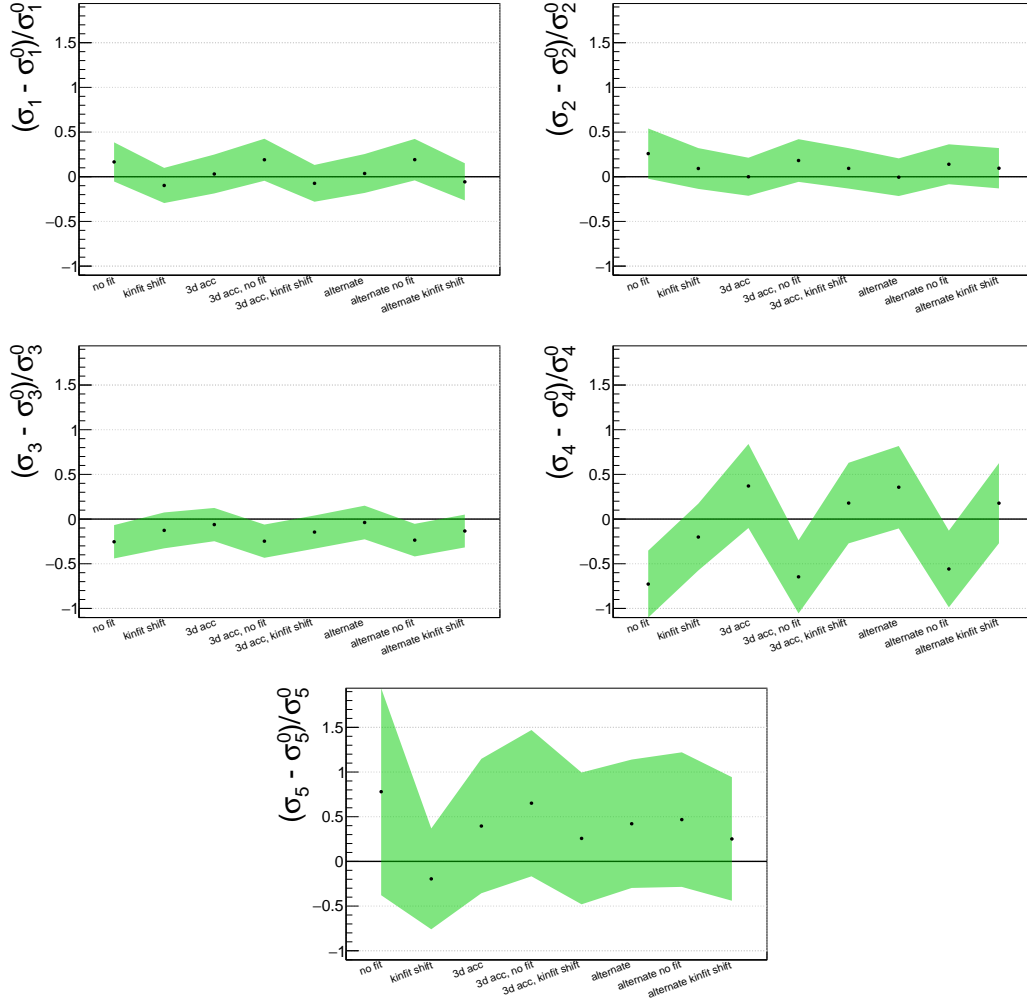


**FIGURE B.39:** Influence on the extracted value of the cross-section in the 5 bins of  $t$ , originating from various studies, see Appendix B.5 for the explanation of the labels. The quantity  $\sigma_i^0$  denotes the preferred value of the cross-section in the corresponding  $t$ -bin with  $i \in 1,2,3,4,5$ . The green band corresponds to the relative statistical uncertainty associated to the extracted value.

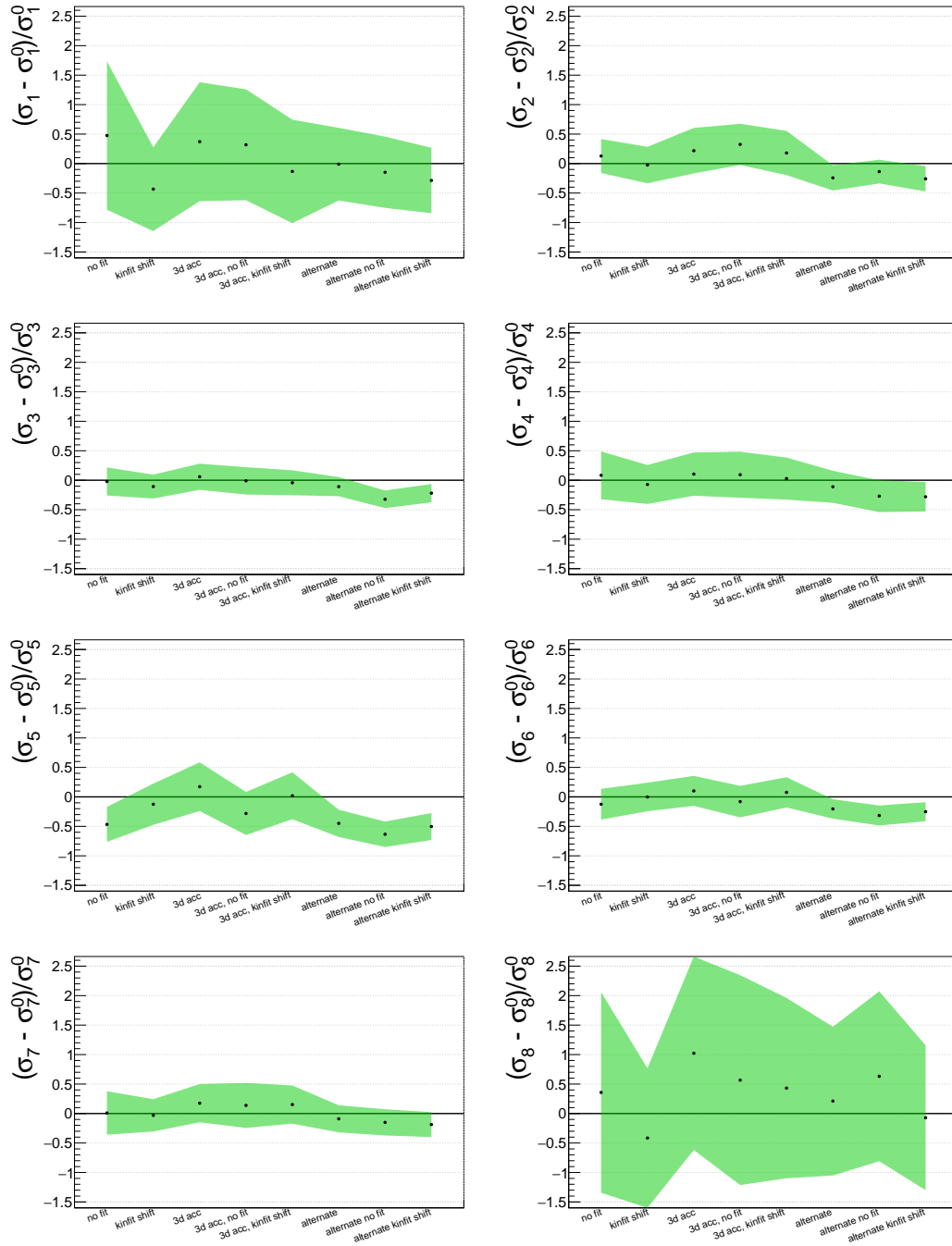


**FIGURE B.40:** Influence on the extracted value of the cross-section in the 8 bins of  $\phi_{\pi^0}$ , originating from various studies, see Appendix B.5 for the explanation of the labels. The quantity  $\sigma_i^0$  denotes the preferred value of the cross-section in the corresponding  $\phi_{\pi^0}$ -bin with  $i \in 1, 2, \dots, 8$ . The green band corresponds to the relative statistical uncertainty associated to the extracted value.



# Acronyms

**ADC** analog-to-digital converter. v, 22, 27–29, 33, 36, 37, 51–56, 73, 77, 78, 80, 180, 221, 225, *Glossary*: ADC

**AMC** ADC mezzanine-card. 28, 29, 33, 34, 36–39, 41, 46, 51–55, 226, *Glossary*: AMC

**BMS** beam momentum station. 20, 88, 108

**BoPET** Biaxially-oriented polyethylene terephthalate. 21, *Glossary*: BoPET

**BoS** Begin of Spill. 48, 74, 76, 89, *Glossary*: BoS

**BRAM** block random-access memory. 35, 49, 57, 225, 226, *Glossary*: BRAM

**BT** beam telescope. 20, 89

**CAMERA** Apparatus for Measurement of Exclusive ReActions. 21, 22, 24, 25, 27, 33, 62, 65, 67, 68, 72–76, 78–85, 87, 88, 93, 94, 96, 101, 105, 108, 109, 173, 174, *Glossary*: CAMERA

**CASTOR** CERN advanced storage manager. 28

**CERN** Conseil Européen pour la Recherche Nucléaire. 1, 2, 19, 28, 173, 221, 226

**CFD** constant fraction discriminator. 56, 57, 59, 80, 180

**CFFs** Compton form factors. 12

**COMPASS** Common Muon and Proton Apparatus for Structure and Spectroscopy. 2, 3, 5, 10, 14, 17, 19, 20, 22–28, 62, 63, 66–68, 70, 74, 78, 81, 87, 88, 91, 92, 97, 108, 110, 162, 163, 166, 169, 172–175, 177, 187, 227

**DA** distribution amplitude. 11

**DAC** digital-to-analog converter. 36, 37, 52, 55, *Glossary*: DAC

**DAQ** data acquisition system. 28, 57, 59, 60, 63

**DCs** drift chambers. 25

**DDR** double data rate. xvi, 46, 52–54, 57, 59, 60, 62

**DIS** deep inelastic scattering. xvii, 1, 3, 20, 24, 97, 108

- DMC** digital mezzanine-card. 28, 226, *Glossary*: DMC
- DoF** distance-of-flight. xvi, 66, 67, 72, 73, 81–83
- DVCS** deeply virtual Compton scattering. 3, 10, 12, 14, 19–22, 25, 28, 33, 66, 67, 84, 87, 88, 90, 91, 102, 150, 173
- EEPROM** electrically erasable programmable read-only memory. 36, 55
- EMC** European Muon Collaboration. 2, 19
- EoS** End of Spill. 48, *Glossary*: EoS
- FFT** fast Fourier transform. 79–81
- FLT** First Level Trigger. 25, 51, 57, 74, *Glossary*: FLT
- GANDALF-module** Generic Advanced Numerical Device for Analytic and Logic Functions. v, 3, 22, 27–31, 33–35, 37, 40, 41, 46–49, 51–55, 57, 59–62, 73–75, 78, 79, 179, 223, 226
- GEANT4** GEometry ANd Tracking. 108, 227
- GEM** gas electron multiplier. 25
- GK** Goloskokov and Kroll. 16–18, 166, 168–170, 172, 174
- GL** Goldstein and Liuti. 16–18, 166, 171
- GPDs** generalized parton distribution functions. 2, 3, 5–12, 14–17, 87, 166–169, 172, 173, 175
- GPU** graphics processing unit. 30
- HEMP** hard exclusive meson production. 3, 10, 17, 166, 173
- JLab** Jefferson Lab. 15, 16, 18, 163, 172, 175
- LAS** LAS Trigger. 26
- LAS** Large Angle Spectrometer. 22, 24, 26, 222
- LAT** Large Area Tracker. 22, 25
- LH<sub>2</sub>** liquid hydrogen. 3, 20, 21, 23, 24, 67, 81, 88, 108
- LT** Ladder Trigger. 26, 97
- LVDS** low-voltage differential signaling. 28
- MCMC** Markov chain Monte Carlo. 137–140, 143, 145, 150, 151, 153, 154, 158, 161, 165, 171, 214–217

- MPFFs** meson production form factors. 12, 166, 167
- MT** Middle Trigger. 26, 97
- MWPC** multi wire proportional chamber. 25
- OMC** optical mezzanine-card. 28, *Glossary: OMC*
- OT** Outer Trigger. 26, 97
- PCIe** Peripheral Component Interconnect Express. 30
- PDF** probability density function. 128, 129, 132, 134, 135, 137, 139, 212, 213
- PDFs** parton distribution functions. 5, 7, 168
- PMT** photomultiplier tube. 21, 22
- QCD** quantum chromodynamics. 97, 173
- QDR** quad data rate. 60, 62
- RICH** ring-imaging Cherenkov. 22, 23
- SAS** Small Angle Spectrometer. 22, 24
- SAT** Small Area Tracker. 22, 25
- SLAC** Stanford Linear Accelerator Center. 1
- SPS** Super Proton Synchrotron. 19, 20, 88, 227
- TCS** Trigger Control System. 25, 27, 34, 35, 40, 46–48, 51, 57, 60, 62, 74, 76, 79, 88, 225, *Glossary: TCS*
- TDC** time-to-digital converter. 27, 29, *Glossary: TDC*
- TIGER-module** Trigger Implementation for GANDALF-module Electronic Read-out. v, 27, 29–31, 36, 46, 47, 59, 62, 226
- ToF** time-of-flight. xvi, 3, 21, 65–67, 72, 73, 81–84, 225
- USB** Universal Serial Bus. 28, 36, 49, 60
- VDT** veto dead time. 26, 89, 90
- VSAT** very small area tracker. 22, 25
- VT** Veto Trigger. 26



# Glossary

- ADC** analog-to-digital converter (ADC), converts analog signals into digital data. v, 22, 27
- AMC** GANDALF ADC mezzanine-card with up to eight analog inputs. 28, 29, 33, 36
- baseline** The digitized value output of an ADC without load on the input. 36, 55
- BoPET** Biaxially-oriented polyethylene terephthalate (BoPET) is a polyester film made from stretched polyethylene terephthalate. Available under trade names Mylar, Melinex and Hostaphan.. 21
- BoS** Begin of Spill (BoS), TCS signal to mark the start of a spills. 48, 74
- BRAM** logic unit of FPGAs used to store volatile data. 35
- CAMERA** Apparatus for Measurement of Exclusive ReActions (CAMERA), target ToF system used in the COMPASS-II program. 21, 65
- CORAL** reconstruction software used by the COMPASS experiment. 67, 97
- CPLD** *Complex Programmable Logic Device*, array of programmable logic blocks, somewhat similar to FPGAs but with non-volatile configuration memory. 28, 35, 36, 46, 49, 57, 59, 60, 62, 180
- DAC** digital-to-analog converter (DAC), converts a digital signal into an analog signal. 36
- DMC** GANDALF mezzanine-card with 64 digital inputs. 28
- DSP** *Digital-Signal-Processing*, logic unit of FPGAs, used to perform complex arithmetic operations. 226
- EoS** End of Spill (EoS), TCS signal to mark the end of a spills. 48
- FIFO** *First-In-First-Out*, data buffer which dispenses the oldest word in the buffer first. In a FPGA, FIFOs are implemented using BRAMs.. 36, 57, 58
- FLT** First Level Trigger (FLT), lowest trigger level of the COMPASS TCS. 25, 74

- FPGA** *Field Programmable Gate Array*, array of programmable logic blocks which can be variably interconnected; main components are slices, BRAMs and DSPs. 3, 28–30, 33, 34, 42–44, 46, 49, 52, 53, 56, 60, 61, 173, 182, 225–227
- GANDALF-ADC** GANDALF-module equipped with AMC cards. v, vi, viii, 22, 33, 34, 40, 46, 49, 57, 59–62, 65, 73, 74, 76, 78, 80, 174, 179–181
- GANDALF-framework** system for detector readout comprising of GANDALF-modules and TIGER-modules, interconnected using the VXS-backplane. 3, 36, 62, 67, 173, 177, 226
- GANDALF-TDC** GANDALF-module equipped with DMC cards. 88
- GIMLI** Mezzanine card used in the GANDALF-framework. Used for clock distribution on the modules.. v, 34, 46–48, 51, 60
- git** a version control system for files, used for collaborative working on projects. 179
- I<sup>2</sup>C** a serial computer bus, commonly used for intra-board communication. v, 33, 34, 36–39, 41, 49, 50, 55, 185, 186
- IODelay** *Input-Output delay*, unit at the input of FPGAs used to delay the input or output signal by means of delay tabs with a certain size. 53, 54, 77, 78
- LEMO** push-pull connectors made by the company with the same name. 48
- mezzanine-card** daughter-card to extend the functionality of its motherboard. 28, 29, 33, 36, 40, 221–223, 225, 226
- OMC** GANDALF mezzanine-card with four optical transceivers. 28
- PLL** *Phase-locked loop*, here, unit inside the FPGA which generates an output signal with a fixed phase relation to the input, commonly used for clock multiplication. 46
- ROOT** Data analysis framework. 129
- scaler** counts occurrences of logical signals on its input. 27, 29
- SI chip** here: Si5326 chip that is mounted on the GANDALF-module and on the AMC for clock multiplication and jitter attenuation. viii, 33, 34, 36–41, 43–46, 48, 51, 52, 54, 77, 79, 182–186
- slice** Building block of an FPGA. Each slice contains flip-flops and Look-up-Tables, which are interconnected to implement a specific logic task. 226
- S-LINK** CERN protocol for optical data transmission. 36

- spill** period of arrival of particle beam dispensed from the SPS in the COMPASS hall. 27, 48, 74, 78, 88–90, 221, 222, 225
- TCS** Trigger Control System (TCS), system for the generation and distribution of trigger information. 25, 46
- TDC** time-to-digital converter (TCS), measurement of time intervals of logical signals. 27
- TGEANT** Total GEometry ANd Tracking, full description of the COMPASS experiment using the GEANT4 framework. 108
- VHDL** *Very High Speed Integrated Circuit Hardware Description Language*, programming language to describe the behaviour of an electronic circuit of logic units. viii, 33–36, 61, 180
- Virtex** FPGA family manufactured by XILINX. 28, 29
- VME** *VERSA Module Eurocard Bus*, computer bus standard. 28, 60, 62, 227
- VME-backplane** see VME. 28, 36, 49, 57, 59, 60, 227
- VME-CPU** PC module placed into a dedicated slot of the VME-backplane. 28, 30, 36, 60, 62
- VXS** *VME Switched Serial*, extension of VME-standard by serial high-speed connections. v, xvi, 28, 31, 36, 46, 47, 54, 57, 59, 60, 62, 227
- VXS-backplane** see VXS. v, 27, 28, 30, 31, 47, 57, 226



# Bibliography

- [1] P. J. Mohr et al., “CODATA recommended values of the fundamental physical constants: 2014”, *Reviews of Modern Physics* **88**, 035009 (2016) DOI: 10.1103/RevModPhys.88.035009.
- [2] K.A. Olive et al. (Particle Data Group), “Review of particle physics”, *Chinese Physics C* **38**, 090001 (2014) DOI: 10.1088/1674-1137/38/9/090001.
- [3] **COMPASS** Collaboration, E. Bielert et al., “A 2.5 m long liquid hydrogen target for COMPASS”, *Nuclear Instruments and Methods in Physics Research Section A* **746**, 20–25 (2014) DOI: 10.1016/j.nima.2014.01.067.
- [4] E. Leader and M. Anselmino, “A crisis in the parton model: where, oh where is the proton’s spin?”, *Zeitschrift für Physik C* **41**, 239–246 (1988) DOI: 10.1007/BF01566922.
- [5] M. Gell-Mann, “A schematic model of baryons and mesons”, *Physics Letters* **8**, 214–215 (1964) DOI: 10.1016/S0031-9163(64)92001-3.
- [6] G. Zweig, “An  $SU_3$  model for strong interaction symmetry and its breaking.”, CERN-TH-401 (1964), <https://cds.cern.ch/record/352337>.
- [7] A. Petermann, “Propriétés de l’étrangeté et une formule de masse pour les mésons vectoriels”, *Nuclear Physics* **63**, 349–352 (1965) DOI: 10.1016/0029-5582(65)90348-2.
- [8] R. Pohl et al., “Laser spectroscopy of muonic deuterium”, *Science* **353**, 669–673 (2016) DOI: 10.1126/science.aaf2468.
- [9] **EMC** Collaboration, J. Ashman et al., “A measurement of the spin asymmetry and determination of the structure function  $g_1$  in deep inelastic muon-proton scattering”, *Physics Letters B* **206**, 364–370 (1988) DOI: 10.1016/0370-2693(88)91523-7.
- [10] **COMPASS** Collaboration, C. Adolph et al., “Leading-order determination of the gluon polarisation from semi-inclusive deep inelastic scattering data”, *The European Physical Journal C* **77**, 209 (2017) DOI: 10.1140/epjc/s10052-017-4716-x.
- [11] D. de Florian et al., “Evidence for polarization of gluons in the proton”, *Physical Review Letters* **113**, 012001 (2014) DOI: 10.1103/PhysRevLett.113.012001.

- [12] X. Ji, "Gauge-invariant decomposition of nucleon spin", *Physical Review Letters* **78**, 610–613 (1997) DOI: 10.1103/PhysRevLett.78.610.
- [13] M. Burkardt, "Impact parameter dependent parton distributions and off-forward parton distributions for  $\zeta \rightarrow 0$ ", *Physical Review D* **62**, 071503 (2000) DOI: 10.1103/PhysRevD.62.071503.
- [14] X. Ji, "Generalized parton distributions", *Annual Review of Nuclear and Particle Science* **54**, 413–450 (2004) DOI: 10.1146/annurev.nucl.54.070103.181302.
- [15] M. Diehl, "Generalized parton distributions with helicity flip", *The European Physical Journal C* **19**, 485–492 (2001) DOI: 10.1007/s100520100635.
- [16] X. Ji, "Deeply virtual Compton scattering", *Physical Review D* **55**, 7114–7125 (1997) DOI: 10.1103/PhysRevD.55.7114.
- [17] A. V. Radyushkin, "Asymmetric gluon distributions and hard diffractive electroproduction", *Physics Letters B* **385**, 333–342 (1996) DOI: 10.1016/0370-2693(96)00844-1.
- [18] D. Müller et al., "Wave functions, evolution equations and evolution kernels from light-ray operators of QCD", *Progress of Physics* **42**, 101–141 (1994) DOI: 10.1002/prop.2190420202.
- [19] K. Goeke et al., "Hard exclusive reactions and the structure of hadrons", *Progress in Particle and Nuclear Physics* **47**, 401–515 (2001) DOI: 10.1016/S0146-6410(01)00158-2.
- [20] M. Diehl et al., "Generalized parton distributions", *Physics Reports* **388**, 41–277 (2003) DOI: 10.1016/j.physrep.2003.08.002.
- [21] S. Boffi et al., "Generalized parton distributions and the structure of the nucleon", *Rivista del Nuovo Cimento* **30**, 387 (2007) DOI: 10.1393/ncr/i2007-10025-7.
- [22] V.N. Gribov and L.N. Lipatov, "Deep inelastic e p scattering in perturbation theory", *Soviet Journal of Nuclear Physics* **15**, 438–450 (1972), [*Yad. Fiz.*15, 781 (1972)].
- [23] L.N. Lipatov, "The parton model and perturbation theory", *Soviet Journal of Nuclear Physics* **20**, 94–102 (1975), [*Yad. Fiz.*20, 181 (1974)].
- [24] G. Altarelli and G. Parisi, "Asymptotic freedom in parton language", *Nuclear Physics* **126**, 298–318 (1977) DOI: 10.1016/0550-3213(77)90384-4.
- [25] Y.L. Dokshitzer, "Calculation of the structure functions for deep inelastic scattering and e+ e- annihilation by perturbation theory in quantum chromodynamics.", *Soviet Physics JETP* **46**, 641–653 (1977), [*Zh. Eksp. Teor. Fiz.*73, 1216 (1977)].
- [26] A. V. Efremov and A. V. Radyushkin, "Factorization and asymptotic behaviour of pion form factor in QCD", *Physics Letters B* **94**, 245–250 (1980) DOI: 10.1016/0370-2693(80)90869-2.

- [27] G. P. Lepage and S. J. Brodsky, "Exclusive processes in quantum chromodynamics: Evolution equations for hadronic wavefunctions and the form factors of mesons", *Physics Letters B* **87**, 359–365 (1979) DOI: 10.1016/0370-2693(79)90554-9.
- [28] M. Burkardt, "Impact parameter space interpretation for generalized parton distributions", *International Journal of Modern Physics A* **18**, 173–207 (2003) DOI: 10.1142/S0217751X03012370.
- [29] Jefferson Lab, "Conceptual design report (CDR) for the science and experimental equipment for the 12 GeV upgrade of CEBAF", (2005), [https://www.jlab.org/div\\_dept/physics\\_division/GeV/doe\\_review/CDR\\_for\\_Science\\_Review.pdf](https://www.jlab.org/div_dept/physics_division/GeV/doe_review/CDR_for_Science_Review.pdf).
- [30] M. Strikman and C. Weiss, "Chiral dynamics and the growth of the nucleon's gluonic transverse size at small  $x$ ", *Physical Review D* **69**, 054012 (2004) DOI: 10.1103/PhysRevD.69.054012.
- [31] P. Joerg, "Deeply virtual Compton scattering at CERN - What is the Size of the Proton?", Dissertation (Albert Ludwigs Universität Freiburg, Feb. 2017), DOI: 10.6094/UNIFR/12397.
- [32] COMPASS Collaboration, R. Akhunzyanov et al., "Transverse extension of partons in the proton probed by deeply virtual Compton scattering", (2018), <http://arxiv.org/abs/1802.02739>.
- [33] J. C. Collins et al., "Factorization for hard exclusive electroproduction of mesons in QCD", *Physical Review D* **56**, 2982–3006 (1997) DOI: 10.1103/PhysRevD.56.2982.
- [34] S. V. Goloskokov and P. Kroll, "Vector-meson electroproduction at small Bjorken- $x$  and generalized parton distributions", *The European Physical Journal C* **42**, 281–301 (2005) DOI: 10.1140/epjc/s2005-02298-5.
- [35] S. Ahmad et al., "Nucleon tensor charge from exclusive  $\pi^0$  electroproduction", *Physical Review D* **79**, 054014 (2009) DOI: 10.1103/PhysRevD.79.054014.
- [36] S. V. Goloskokov and P. Kroll, "An attempt to understand exclusive  $\pi^+$  electroproduction", *The European Physical Journal C* **65**, 137–151 (2010) DOI: 10.1140/epjc/s10052-009-1178-9.
- [37] M. Diehl et al., "On the analysis of lepton scattering on longitudinally or transversely polarized protons", *The European Physical Journal C* **41**, 515–533 (2005) DOI: 10.1140/epjc/s2005-02242-9.
- [38] T. Arens et al., "Some tests for the helicity structure of the pomeron in ep collisions", *Zeitschrift für Physik C* **74**, 651–669 (1997) DOI: 10.1007/s002880050430.
- [39] J. Pretz, *Virtual photon flux factor, not neglecting the lepton mass*, COMPASS Note 2002-11, 2002.
- [40] L. N. Hand et al., "Experimental investigation of pion electroproduction", *Physical Review* **129**, 1834–1846 (1963) DOI: 10.1103/PhysRev.129.1834.

- [41] **MAMI** Collaboration, S. Stave et al., “Measurements of the  $\gamma^*p \rightarrow \Delta$  reaction at low  $Q^2$ : Probing the mesonic contribution”, *Physical Review C* **78**, 025209 (2008) DOI: 10.1103/PhysRevC.78.025209.
- [42] **HERMES** Collaboration, H. Collaboration et al., “Single-spin azimuthal asymmetry in exclusive electroproduction of  $\pi^+$  mesons”, *Physics Letters B* **535**, 85–92 (2002) DOI: 10.1016/S0370-2693(02)01780-X.
- [43] **HERMES** Collaboration, A. Airapetian et al., “Single-spin azimuthal asymmetry in exclusive electroproduction of  $\pi^+$  mesons on transversely polarized protons”, *Physics Letters B* **682**, 345–350 (2010) DOI: 10.1016/j.physletb.2009.11.039.
- [44] **HERMES** Collaboration, A. Airapetian et al., “Cross sections for hard exclusive electroproduction of  $\pi^+$  mesons on a hydrogen target”, *Physics Letters B* **659**, 486–492 (2008) DOI: 10.1016/j.physletb.2007.11.079.
- [45] **CLAS** Collaboration, R. D. Masi et al., “Measurement of  $ep \rightarrow ep\pi^0$  beam spin asymmetries above the resonance region”, *Physical Review C* **77**, 042201 (2008) DOI: 10.1103/PhysRevC.77.042201.
- [46] **CLAS** Collaboration, I. Bedlinskiy et al., “Measurement of exclusive  $\pi^0$  electroproduction structure functions and their relationship to transverse generalized parton distributions”, *Physical Review Letters* **109**, 112001 (2012) DOI: 10.1103/PhysRevLett.109.112001.
- [47] **CLAS** Collaboration, I. Bedlinskiy et al., “Exclusive  $\pi^0$  electroproduction at  $W > 2$  GeV with CLAS”, *Physical Review C* **90** (2014) DOI: 10.1103/PhysRevC.90.025205.
- [48] S. V. Goloskokov et al., “Transversity in hard exclusive electroproduction of pseudoscalar mesons”, *The European Physical Journal A* **47**, 112 (2011) DOI: 10.1140/epja/i2011-11112-6.
- [49] G. R. Goldstein et al., “Flexible parametrization of generalized parton distributions from deeply virtual Compton scattering observables”, *Physical Review D* **84**, 034007 (2011) DOI: 10.1103/PhysRevD.84.034007.
- [50] G. R. Goldstein et al., “Easy as  $\pi^0$ : on the interpretation of recent electroproduction results”, *Journal of Physics G: Nuclear and Particle Physics* **39**, 115001 (2012) DOI: 10.1088/0954-3899/39/11/115001.
- [51] **Jefferson Lab Hall A** Collaboration, E. Fuchey et al., “Exclusive neutral pion electroproduction in the deeply virtual regime”, *Physical Review C* **83**, 025201 (2011) DOI: 10.1103/PhysRevC.83.025201.
- [52] **Jefferson Lab Hall A** Collaboration, M. Defurne et al., “Rosenbluth separation of the  $\pi^0$  electroproduction cross section”, *Physical Review Letters* **117** (2016) DOI: 10.1103/PhysRevLett.117.262001.

- [53] M. Vanderhaeghen et al., “Deeply virtual electroproduction of photons and mesons on the nucleon: Leading order amplitudes and power corrections”, *Physical Review D* **60**, 094017 (1999) DOI: 10.1103/PhysRevD.60.094017.
- [54] **Jefferson Lab Hall C Collaboration**, T. Horn et al., “Scaling study of the pion electroproduction cross sections”, *Physical Review C* **78**, 058201 (2008) DOI: 10.1103/PhysRevC.78.058201.
- [55] **Jefferson Lab Hall C Collaboration**, A. N. Villano et al., “Neutral pion electroproduction in the resonance region at high  $Q^2$ ”, *Physical Review C* **80**, 035203 (2009) DOI: 10.1103/PhysRevC.80.035203.
- [56] **COMPASS Collaboration**, C. Adolph et al., “Transverse target spin asymmetries in exclusive  $\rho^0$  muoproduction”, *Physics Letters B* **731**, 19–26 (2014) DOI: 10.1016/j.physletb.2014.02.005.
- [57] **COMPASS Collaboration**, C. Adolph et al., “Exclusive  $\omega$  meson muoproduction on transversely polarised protons”, *Nuclear Physics* **915**, 454–475 (2017) DOI: 10.1016/j.nuclphysb.2016.12.015.
- [58] **COMPASS Collaboration**, P. Abbon et al., “The COMPASS experiment at CERN”, *Nuclear Instruments and Methods in Physics Research Section A* **577**, 455–518 (2007) DOI: 10.1016/j.nima.2007.03.026.
- [59] T. Szameitat, “New geant4-based Monte Carlo software for the COMPASS-II experiment at CERN”, Dissertation (Albert Ludwigs Universität Freiburg, Jan. 2017), DOI: 10.6094/UNIFR/11686.
- [60] Hamamatsu Photonics, *Hamamatsu R10533 series data sheet* (2014), [https://www.hamamatsu.com/resources/pdf/etd/R10533\\_TPMH1314E.pdf](https://www.hamamatsu.com/resources/pdf/etd/R10533_TPMH1314E.pdf).
- [61] ET Enterprises electron tubes, *9823B series data sheet*, ET Enterprises Limited (45 Riverside Way, Uxbridge UB8 2YF, United Kingdom, 2012), <http://my.et-enterprises.com>.
- [62] J. Novy, *Compass daq beyond 2020*, Conference talk presented at the “DAQ/FEE/Trigger for COMPASS beyond 2020 workshop”, Prague, Nov. 2017.
- [63] F. Herrmann, “Development and verification of a high performance electronic readout framework for high energy physics”, Dissertation (Albert Ludwigs Universität Freiburg, Aug. 2011), URN:nbn:de:bsz:25-opus-83709.
- [64] S. Schopferer, “An FPGA-based trigger processor for a measurement of deeply virtual Compton scattering at the COMPASS-II experiment”, Dissertation (Albert Ludwigs Universität Freiburg, Oct. 2013), URN:nbn:de:bsz:25-opus-83709.
- [65] M. Gorzellig, “Entwicklung eines digitalen Triggersystems für Rückstoßproton Detektoren”, Diploma thesis (Albert Ludwigs Universität Freiburg, Mar. 2013).

- [66] COMPASS Collaboration, C. Bernet et al., “The COMPASS trigger system for muon scattering”, *Nuclear Instruments and Methods in Physics Research Section A* **550**, 217–240 (2005) DOI: 10.1016/j.nima.2005.05.043.
- [67] T. Baumann, “Entwicklung einer Schnittstelle zur Übertragung von Pulsinformationen von einem Rückstoßdetektor an ein digitales Triggersystem”, Diploma thesis (Albert Ludwigs Universität Freiburg, Jan. 2013).
- [68] Xilinx Inc., *Virtex-5 family overview*, v5.0, **DS100** (2009), <http://www.xilinx.com>.
- [69] C. Michalski, “Entwicklung eines Echtzeit-Strahlprofil-Monitoring-Systems für das COMPASS-II Experiment”, Diploma thesis (Albert Ludwigs Universität Freiburg, Feb. 2013).
- [70] M. Büchele, “Entwicklung eines FPGA-basierten 128-Kanal Time-to-Digital Converter für Teilchenphysik-Experimente”, Diploma thesis (Albert Ludwigs Universität Freiburg, Jan. 2012).
- [71] S. Schopferer, “Entwicklung eines hochauflösenden Transientenrekorders”, Diploma thesis (Albert Ludwigs Universität Freiburg, Feb. 2009).
- [72] P. Jörg, “Untersuchung von Algorithmen zur Charakterisierung von Photomultiplierpulsen in Echtzeit”, Diploma thesis (Albert Ludwigs Universität Freiburg, Jan. 2013).
- [73] Xilinx Inc., *Virtex-6 family overview*, v2.4, **DS150** (2012), <http://www.xilinx.com>.
- [74] F. Herrmann, “The GANDALF framework”, (COMPASS Collaboration Meeting at CERN, Nov. 2012).
- [75] Texas Instruments, *ADS5463 12-bit, 500-/550-MSPS analog-to-digital converters*, SLAS515E (July 2009), <http://www.ti.com/general/docs/lit/getliterature.tsp?genericPartNumber=ads5463&fileType=pdf>.
- [76] Analog Devices, *Quad, 12-/14-/16-bit nanoDACs*, Rev. D (2015), [http://www.analog.com/media/en/technical-documentation/data-sheets/AD5625R\\_5645R\\_5665R\\_5625\\_5665.pdf](http://www.analog.com/media/en/technical-documentation/data-sheets/AD5625R_5645R_5665R_5625_5665.pdf).
- [77] Texas Instruments, *TMPx75 temperature sensor* (2014), <http://www.ti.com/product/TMP175/datasheet/>.
- [78] R. Herveille and F. Renet, *I2C-master core*, <https://opencores.org/project,i2c> (visited on 10/18/2017).
- [79] W. D. Peterson, *SoC interconnection: WISHBONE*, <https://opencores.org/opencores,wishbone> (visited on 10/18/2017).
- [80] Silicon Laboratories, *Si5326 any-frequency precision clock multiplier/jitter attenuator*, 1.0 9/10 (2010), <https://www.silabs.com/documents/public/data-sheets/Si5326.pdf>.

- [81] Silicon Laboratories, *DSPLLsim precision clock EVB software* (2014), <https://www.silabs.com/products/development-tools/software/clock>.
- [82] V. Lopez Lorenzo, *Sp\_ram to 3p\_ram WISHBONE wrapper*, [https://opencores.org/project,w\\_b\\_3p\\_spram\\_wrapper](https://opencores.org/project,w_b_3p_spram_wrapper) (visited on 10/18/2017).
- [83] Xilinx Inc., *Virtex-5 FPGA system monitor user guide*, v1.7.1 (Feb. 2011), [https://www.xilinx.com/support/documentation/user\\_guides/ug192.pdf](https://www.xilinx.com/support/documentation/user_guides/ug192.pdf).
- [84] P. Kremser, "Optimierung und Charakterisierung eines Transientenrekorders für Teilchenphysikexperimente", Diploma thesis (Albert Ludwigs Universität Freiburg, Feb. 2014).
- [85] H. Fischer et al., *The COMPASS online data format*, "COMPASS Note 2000-8", June 2000.
- [86] T. Grussenmeyer, "Entwicklung eines modularen und verteilten Datenaufnahmesystems für Testexperimente", Diploma thesis (Albert Ludwigs Universität Freiburg, Dec. 2013).
- [87] S. Stephan, "Entwicklung einer speicheroptimierten Auslese für einen Sampling-ADC", Bachelor thesis (Albert Ludwigs Universität Freiburg, Feb. 2017).
- [88] R. Schäfer, "Charakterisierung eines Detektors zum Nachweis von Rückstoßprotonen am COMPASS Experiment", Diploma thesis (Albert Ludwigs Universität Freiburg, Sept. 2013).
- [89] E. J. Dorbath, "Kalibrierung des CAMERA-Detektors am COMPASS-Experiment", Bachelor thesis (Albert Ludwigs Universität Freiburg, Aug. 2017).
- [90] Xilinx Inc., *Virtex-5 FPGA data sheet: DC and switching characteristics*, v5.5, **DS202** (June 2016), <http://www.xilinx.com>.
- [91] A. Ferrero, *Algorithm for clusterization and association of hits with the beam muon*, private communications, 2014.
- [92] A. Ferrero, *Extraction of the target position from the 2012 DVCS data*, private communications, 2014.
- [93] H. Wollny, "Measuring azimuthal asymmetries in semi-inclusive deep-inelastic scattering off transversely polarized protons", Dissertation (Albert Ludwigs Universität Freiburg, Apr. 2010), URN:nbn:de:bsz:25-opus-75589.
- [94] O. Kouznetsov, *Extraction of the bad spill lists for the 2012 DVCS data*, private communications, 2015.
- [95] E. Fuchey, *Extraction of the bad spill list for the fiber station time jumps for the 2012 DVCS data*, private communications, 2015.
- [96] E. Fuchey, *Beam flux determination for the 2012 data using random triggers*, private communications, 2015.

- [97] **NMC** Collaboration, M. Arneodo et al., “Measurement of the proton and deuteron structure functions,  $F_2^p$  and  $F_2^d$ , and of the ratio  $\sigma_L/\sigma_T$ ”, *Nuclear Physics B* **483**, 3–43 (1997) DOI: 10.1016/S0550-3213(96)00538-X.
- [98] **SMC** Collaboration, B. Adeva et al., “Spin asymmetries  $A_1$  and structure functions  $g_1$  of the proton and the deuteron from polarized high energy muon scattering”, *Physical Review D (Particles and Fields)* **58**, 112001 (1998) DOI: 10.1103/PhysRevD.58.112001.
- [99] **E143** Collaboration, K. Abe et al., “Measurements of  $R = \sigma_L/\sigma_T$  for  $0.03 < x < 0.1$  and fit to world data”, *Physics Letters B* **452**, 194–200 (1999) DOI: 10.1016/S0370-2693(99)00244-0.
- [100] S. Landgraf, “Luminosity Calculation for the COMPASS Experiment using the F2 Structure Function”, Addendum to Luminosity Calculation for the COMPASS Experiment using the F2 Structure Function, Master thesis (Albert Ludwigs Universität Freiburg, Nov. 2015).
- [101] E. Fuchey, *Extraction of the cluster time with respect to the trigger as a function of the cluster energy*, private communications, 2014.
- [102] G. Ingelman et al., “LEPTO 6.5 - A Monte Carlo generator for deep inelastic lepton-nucleon scattering”, *Computer Physics Communications* **101**, 108–134 (1997) DOI: 10.1016/S0010-4655(96)00157-9.
- [103] **COMPASS** Collaboration, C. Adolph et al., “Leading order determination of the gluon polarisation from DIS events with high- $p_T$  hadron pairs”, *Physics Letters B* **718**, 922–930 (2013) DOI: 10.1016/j.physletb.2012.11.056.
- [104] C. Regali, “Exclusive event generation for the COMPASS-II experiment at CERN and improvements for the Monte-Carlo chain”, Dissertation (Albert Ludwigs Universität Freiburg, Dec. 2016), DOI: 10.6094/UNIFR/11449.
- [105] A. Sandacz and P. Sznajder, “HEPGEN - generator for hard exclusive lepton production”, (2012), <http://arxiv.org/abs/1207.0333>.
- [106] C. Regali and T. Szameitat, *TGEANT, a Geant4 based Monte Carlo simulation for the COMPASS-II experiment*, (2016) <https://na58-project-tgeant.web.cern.ch/> (visited on 10/11/2017).
- [107] S. Agostinelli et al., “Geant4 - a simulation toolkit”, *Nuclear Instruments and Methods in Physics Research Section A* **506**, 250–303 (2003) DOI: [https://doi.org/10.1016/S0168-9002\(03\)01368-8](https://doi.org/10.1016/S0168-9002(03)01368-8).
- [108] C. Regali and T. Szameitat, *TGEANT productions*, (2016) <https://na58-project-tgeant.web.cern.ch/content/productions> (visited on 10/11/2017).
- [109] G. Bohm and G. Zech, “Statistics of weighted Poisson events and its applications”, *Nuclear Instruments and Methods in Physics Research A* **748**, 1–6 (2014) DOI: 10.1016/j.nima.2014.02.021.

- [110] R. Brun and F. Rademakers, "ROOT - An Object Oriented Data Analysis Framework", *Nuclear Instruments and Methods in Physics Research A* **389**, 81–86 (1997), Proceedings AIHENP'96 Workshop, Lausanne, Sep. 1996, see also: <http://root.cern.ch/>.
- [111] J. Goodman and J. Weare, "Ensemble samplers with affine invariance", *Communications in Applied Mathematics and Computational Science* **5**, 65–80 (2010) DOI: 10.2140/camcos.2010.5.65.
- [112] A. Afanasev et al., "QED radiative corrections in processes of exclusive pion electroproduction", *Physical Review D* **66**, 074004 (2002) DOI: 10.1103/PhysRevD.66.074004.
- [113] A. Afanasev, *Radiative corrections for exclusive pion lepto-production*, private communications, 2016.
- [114] K. Kumerički and D. Müller, "Deeply virtual Compton scattering at small  $x$  and the access to the GPD  $H$ ", *Nuclear Physics B* **841**, 1–58 (2010) DOI: 10.1016/j.nuclphysb.2010.07.015.
- [115] S. V. Goloskokov and P. Kroll, "The role of the quark and gluon GPDs in hard vector-meson electroproduction", *The European Physical Journal C* **53**, 367–384 (2007) DOI: 10.1140/epjc/s10052-007-0466-5.
- [116] S. V. Goloskokov et al., "The target asymmetry in hard vector-meson electroproduction and parton angular momenta", *The European Physical Journal C* **59**, 809–819 (2009) DOI: 10.1140/epjc/s10052-008-0833-x.
- [117] S. V. Goloskokov et al., "Transversity in exclusive vector-meson lepto-production", *The European Physical Journal C* **74** (2014) DOI: 10.1140/epjc/s10052-014-2725-6.
- [118] J. Botts and G. Sterman, "Hard elastic scattering in QCD: leading behavior", *Nuclear Physics* **325**, 62–100 (1989) DOI: 10.1016/0550-3213(89)90372-6.
- [119] L. Mankiewicz and G. Piller, "Remarks on exclusive electroproduction of transversely polarized vector mesons", *Physical Review D* **61**, 074013 (2000) DOI: 10.1103/PhysRevD.61.074013.
- [120] I. Anikin and O. Teryaev, "Genuine twist 3 in exclusive electroproduction of transversely polarized vector mesons", *Physics Letters B* **554**, 51–63 (2003) DOI: 10.1016/S0370-2693(02)03195-7.
- [121] R. Jacob and P. Kroll, "The pion form factor. Sudakov suppressions and intrinsic transverse momentum", *Physics Letters B* **315**, 463–470 (1993) DOI: 10.1016/0370-2693(93)91642-Z, Erratum in [133].
- [122] P. Kroll and M. Raulfs, "The  $\pi\gamma$  transition form factor and the pion wave function", *Physics Letters B* **387**, 848–854 (1996) DOI: 10.1016/0370-2693(96)01101-X.
- [123] X. Ji et al., "Classification and asymptotic scaling of the light-cone wave-function amplitudes of hadrons", *The European Physical Journal C* **33**, 75–90 (2004) DOI: 10.1140/epjc/s2003-01563-y.

- [124] I. V. Musatov and A. V. Radyushkin, "Evolution and models for skewed parton distributions", *Physical Review D* **61** (2000) DOI: 10.1103/PhysRevD.61.074027.
- [125] A. V. Radyushkin, "Symmetries and structure of skewed and double distributions", *Physics Letters B* **449**, 81–88 (1999) DOI: 10.1016/S0370-2693(98)01584-6.
- [126] L. L. Frankfurt et al., "Hard exclusive pseudoscalar meson electroproduction and spin structure of the nucleon", *Physical Review D* **60** (1999) DOI: 10.1103/PhysRevD.60.014010.
- [127] J. Blümlein and H. Böttcher, "QCD analysis of polarized deep-inelastic scattering data and parton distributions", *Nuclear Physics B* **636**, 225–263 (2002) DOI: 10.1016/S0550-3213(02)00342-5.
- [128] J. Pumplin et al., "New generation of parton distributions with uncertainties from global QCD analysis", *Journal of High Energy Physics* **07**, 012 (2002) DOI: 10.1088/1126-6708/2002/07/012.
- [129] M. Anselmino et al., "Update on transversity and Collins functions from SIDIS and ee data", *Nuclear Physics B (Proceedings Supplements)* **191**, 98–107 (2009) DOI: 10.1016/j.nuclphysbps.2009.03.117.
- [130] **Qcdsf/UKQCD** Collaboration, M. Göckeler et al., "Quark helicity flip generalized parton distributions from two-flavor lattice QCD", *Physics Letters B* **627**, 113–123 (2005) DOI: 10.1016/j.physletb.2005.09.002.
- [131] P. Kroll, *Adjusted model parameters for COMPASS exclusive  $\pi^0$  muoproduction*, private communications, 2016.
- [132] **PARTONS** Collaboration, B. Berthou et al., "PARTONS: PARTonic tomography of nucleon software. a computing platform for the phenomenology of generalized parton distributions", (2015), <http://arxiv.org/abs/1512.06174>.
- [133] R. Jacob and P. Kroll, "The pion form factor. Sudakov suppressions and intrinsic transverse momentum", *Physics Letters B* **319**, 545–545 (1993) DOI: 10.1016/0370-2693(93)91770-N.

## Declaration of Authorship

I, Matthias GORZELLIK, declare that this thesis titled, “Cross-section measurement of exclusive  $\pi^0$  muoproduction and firmware design for an FPGA-based detector readout ” and the work presented in it are my own. I confirm that:

- This work was done wholly or mainly while in candidature for a research degree at this University.
- Where any part of this thesis has previously been submitted for a degree or any other qualification at this University or any other institution, this has been clearly stated.
- Where I have consulted the published work of others, this is always clearly attributed.
- Where I have quoted from the work of others, the source is always given. With the exception of such quotations, this thesis is entirely my own work.
- I have acknowledged all main sources of help.
- Where the thesis is based on work done by myself jointly with others, I have made clear exactly what was done by others and what I have contributed myself.

Signed:

---

Date:

---